Nanostructure Formation on Rutile TiO_2 and Ta surfaces by Ion Beam Irradiation : Photoabsorption, Magnetism, Scaling and KMC Studies

By

Shalik Ram Joshi

PHYS07201004004

Institute of Physics, Bhubaneswar

A thesis submitted to the
Board of Studies in Physical Sciences

In partial fulfillment of requirements
For the Degree of

DOCTOR OF PHILOSOPHY
of
HOMI BHABHA NATIONAL INSTITUTE

December, 2016

STATEMENT BY AUTHOR

This dissertation has been submitted in partial fulfillment of requirements for an advanced degree at Homi Bhabha National Institute (HBNI) and is deposited in the Library to be made available to borrowers under rules of the HBNI.

Brief quotations from this dissertation are allowable without special permission, provided that accurate acknowledgment of source is made. Requests for permission for extended quotation from or reproduction of this manuscript in whole or in part may be granted by the Competent Authority of HBNI when in his or her judgment the proposed use of the material is in the interests of scholarship. In all other instances, however, permission must be obtained from the author.

(Shalik Ram Joshi)

CERTIFICATE

This is to certify that the thesis entitled “**Nanostructure Formation on Rutile TiO_2 and Ta surfaces by Ion Beam Irradiation : Photoabsorption, Magnetism, Scaling and KMC Studies**”, which is being submitted by **Mr. Shalik Ram Joshi**, in partial fulfillment of the degree of **Doctor of Philosophy in Physics** of **Homi Bhabha National Institute** is a record of his own research work carried by him. He has carried out his investigations for the last five years on the subject matter of the thesis under my supervision at **Institute of Physics, Bhubaneswar**. To the best of our knowledge, the matter embodied in this thesis has not been submitted for the award of any other degree.

Signature of the Candidate **Signature of the Supervisor**

Shalik Ram Joshi
Institute of Physics
Bhubaneswar

Prof. Shikha Varma
Professor
Institute of Physics
Bhubaneswar

DECLARATION

I, hereby declare that the investigation presented in the thesis has been carried out by me. The work is original and has not been submitted earlier as a whole or in part for a degree/diploma at this or any other Institution/University.

(Shalik Ram Joshi)

To my Parents
&
Ramanpreet Virdi

Contents

Acknowledgement

This thesis is a culmination of research work that I have carried out at IOP for last five years. This would not have been possible without the guidance and the help of several individuals who directly or indirectly have contributed and extended their valuable assistance whenever was required. I am incredibly indebted to all of them.

First and foremost, I offer my utmost gratitude to my supervisor Prof. Shikha Varma for her supervision, advice and guidance during my research. Above all and the most needed, she provided me with unflinching encouragement and support in various ways with allowing me the room to work in my own way. Without her this thesis would not have been completed. The other person whom I would like to offer my gratitude is Prof. Ajit Mohan Srivastava. I will remember him as a savior, an excellent physicist, and a great speaker whom I always love to listen. The aura that he carries along with him is something magical which rejuvenates everyone. They both have really made me feel like home during my stay at IOP.

The next name that immediately comes to my mind is Dr. Anurag Sahay and Ms. Ritu. They both have joined me when i was having the touhgest time of my PhD. Anurag Bhaiya has helped me personally and professionally as well. Because of him only, I got a chance to interact with Dr. Neeraj Shukla and Dr. Shyam Kumar Choudhary. They both have played a very major role, for pursuing my research and have molded my career into a decent shape. I would also like to pay my gratitude to Dr. Anupama Chanda with whom I wanted to work from my initial years of PhD. She has walked along with me, guided me step by step, during all my research work at IOP. I would like to acknowledge Dr. Trilochan Bagarti who taught me the basics of numerical simulation and the most crucial thing for a PhD, the scientific temperament. I wish to pay my gratitude to Dr. D. Kanjilal, Dr. Sunil Ojha and Devrani Devi for their help and guidance during my experiments at IUAC, New Delhi. I am very thankful to Dr. Padmanabhan Balasubramanian who has helped me both professionally and financially, whenever required. I am also very thankful to Dr. Pramita Mishra for her constant support and guidance all throughout my stay at IOP.

I must acknowledge Indrani Mishra, especially her parents and her daughter, who have made me feel like home at Jamshedpur. I also pay my utmost gratitude to Santosh sir who has taught me both XPS and lessons of life in several ways. He has paid his part extremely well to make me a better person. I also want to thank Shreyansh S. Dave, Amit Kumar for their overwhelming support. I am also grateful to Himanshu Lohani who have helped me during my tough times on several occasions. I would like to take this opportunity to thank my teachers, Dr. R. K. Sharma(Principal, KVTG). Dr. A. K. Gupta(PGT Physics, KVTG), Alok Upadhyay(MTech, IIT-K), Dr. Geetanjali Sethi(Professor, St. Stephen) for reviving my interest in physics at regular intervals. I also want to thank Suryanarayan Balasubramanian who has given me an opportunity to work for underprivileged kids at IOP. I would also like to thank all library staff, especially Hans Da and Ravaneswar Nayak for their help and overwhelming support. I would also like to acknowledge A. S. Lokhande and Makrand Siddhabhatti with whom i got a chance to interact only during my last a few days at IOP.

I am extremely grateful to my dearest parents who have supported me all throughout my life and have allowed to me pursue whatever I wanted. I must say because of their blessings only, i have found so many excellent people who have supporter me whenever required. I don't have words to pay my tribute to Deepak Dalal and Bharati Tripathi for there immense support and uncondtional love. I am also thankful to Ramanpreet Virdi who has handled me so nicely, whenever I was having a tough time in my life. I do not have words to pay tribute to her as well.

Date: **Shalik Ram Joshi**

Synopsis

Low dimensional materials exhibit many exceptional and fascinating properties which have numerous technological applications [1–4]. Several top- down and bottom- up approaches have been employed to develop wide variety of nanostructures for achieving desired functional properties [5–7]. Surface engineering by ion beam irradiation (IBI) has become a very promising candidate for the top down production of self organized nanostructures. The evolution of these nanostructures is a result of interplay between surface erosion which creates instability and surface diffusion which acts as a stabilizing mechanism [8–10]. During this process, the host lattice also undergoes structural modifications, which play pivotal role in the modification of several properties [5–7]. Implantation can also produce defects and damage in the lattice. Thus, it is immensely important to investigate and understand the parameters influencing the surface evolution and generation of defects in the host material after ion beam irradiation [11]. Understanding the role of residual damage and amorphicity is essential for producing desired surfaces. Further, it can also impart insight into the factors responsible for these modifications [12].

In general, surfaces modified by IBI methods produce rough interfaces, with fluctuations that display kinetic roughening [13] analogous to those seen during film growth [13, 14] or in more general context of non-equilibrium interface growth phenomenon [15]. Dynamical scaling models, based on the general idea that the width of an interface depends in a self affine fashion, on length and time, have been also applied to surfaces eroded by IBI [16]. The formation of nanoscale patterns during low energy ion sputtering is governed by non-equilibrium processes and is essentially described by non-linear KS equation [17].

TiO_2 is a wide wide bandgap semiconductor and is being very actively explored for many remarkable properties such as photocatalysis, photovoltaics, bio-compatible nature, etc. [18]. It shows paramagnetic behavior but with the incorporation of a material like Cobalt it is expected to belong to the class of dilute magnetic semiconductor which exhibits room temperature ferromagnetism [19]. Tantalum is a metal and displays many exciting applications as thin film resistor materials with low temperature coefficient of resistivity, oxygen sensors, high dielectric material in metal-oxide semiconductor devices, etc. [20–23]. Both these materials, in nanostructure form, exhibit many enhanced fascinating and modified properties making them important candidates for advanced materials in frontier research [20, 24].

The present thesis discusses the fabrication of nanostructures on rutile TiO_2 single crystals and Tantalum surfaces via ion beam irradiation. TiO_2 (110) have been implanted with 200 keV Co ions and Tantalum has been irradiated with 3 keV Ar ions. Both the surfaces have been investigated by scaling studies which provide crucial scaling exponents necessary for understanding the universal behavior of the surfaces. The nano-patterned TiO_2 (110) surfaces have been investigated for modification in photo- absorption and magnetic properties. The bandgap modification, generation of vacancy states and formation of Ti- rich nanostructures, after irradiation, produce the enhanced photo-absorption behavior observed here. These TiO_2 (110) single crystals also exhibit unexpected super-paramagnetic behavior which is anisotropic along the two crystallographic axes of the crystal. The Rutherford backscattering/ channeling (RBS/C) technique has been utilized to extract the depth distribution of damage in the lattice after IBI. Kinetic Monte Carlo (KMC) simulations in 1+1 dimension have been developed here for understanding the nano-pattern formation, after IBI, on Tantalum surfaces. A non-linearity in the Hamiltonian has been shown to play an essential role in the generation of nano-patterns after ion beam irradiation.

The first part of the thesis investigates of the morphological modifications, photo absorption properties, magnetic response and lattice disorder of rutile TiO_2 after implantation with 200 keV cobalt ions. The morphological evolution of the surface takes place due to the interplay of various processes, like roughening, smoothening, material transport through diffusion, etc. These processes also become responsible for the generation of vacancies, interstitial atoms and other type of lattice disorder in the TiO_2 lattice. Modifications due to the ion beam irradiation have been investigated here using several techniques, like Atomic force Microscopy (AFM), X-ray Photoelectron Spectroscopy (XPS), X-ray Diffraction (XRD), UV-Vis Spectroscopy, Raman Spectroscopy and Rutherford backscattering/Channeling (RBS/C). Ion implantation of oxides such as TiO_2 produces preferential sputtering of oxygen atoms where the associated 2p electrons get transferred to the empty 3d orbitals of the neighboring Ti atoms on the surface leading to the development of two

Ti^{3+} oxygen vacancy states. Presence of oxygen vacancies also leads to the formation of Ti rich zones which become the nucleation centers for the nanostructure formation. Development of secondary phases of cobalt, such as $Ti_{1-x}Co_xO_2$ and $CoTiO_3$, have been observed by XPS, XRD and Raman Spectroscopy techniques [25, 26]. The results show an enhanced photo- absorption in the visible as well as in UV ranges along with a reduction in the bandgap, with increasing fluence. Formation of cobalt clusters, development of Ti rich zones and creation of oxygen vacancy states, during implantation, are crucial for these observations. The enhanced absorption is caused by the sp-d exchange interactions between the band electrons and the localized d electrons of Co^{2+} ions. These results can have potential applications in photocatalysis.

The magnetic response of rutile TiO_2 has been investigated here at several fluences after implantation with 200 keV cobalt ions. These studies have been performed at various temperatures and fields by utilizing a Superconducting Quantum Interference Device (SQUID). The results surprisingly display a super paramagnetic (SPM) behavior instead of a room temperature ferromagnetism [27]. This SPM behavior is caused by the development of cobalt nano-clusters in the system after implantation. The magnetic moment has been observed to increase with the ion fluence indicating an increase in the size of these nano-clusters. Scaling studies have been undertaken and display an anisotropic nature of SPM above blocking temperature. Such an anisotropy is very unexpected and the results presented here show that for field along $[1\bar{1}0]$ direction ($H \parallel H_\perp$), magnetic moments are easily rotatable whereas for field applied along [001] ($H \parallel H_\parallel$) considerable fraction of spins remain blocked. The cobalt nanoclusters, thus, display an easy and hard axis of magnetization coupled with the magnetocrystalline anisotropy of $Ti_{1-x}Co_xO_2$. In addition, at T= 2K, surprisingly a crossover in the magnetization for two field direction has also been observed. The origin of this crossover is the anisotropic paramagnetism arising from the +2 ionic state of cobalt [27]. Role of dipole-dipole interaction and inter-cluster exchange interactions have also been explored. The results observed here can have potential applications in spintronic devices.

Ion implantation can also produce lattice disorder due to the interactions of the energetic ions with the atoms of the host lattice. This can in turn generate defects, vacancies, interstitials, etc. which affect the intrinsic properties of the host lattice. RBS/C technique is a powerful technique to understand the disorder and depth dependent damage in the lattice. This thesis discusses the surface to deep layer modifications in TiO_2 after implantation with Co ions, as a function of ion fluence [28]. The depth dependent damage profiles have been derived here using the RBS/C spectra [28] by applying multiple scattering formalism developed by Feldman and Rodgers [29]. Results display that ion beam induced dynamical annealing, that increases with fluence, plays a pivotal role in reducing the damage in deep layers. Grazing incidence XRD data also confirm this. In the surface region, an increase in damage with fluence is observed. This is related to several factors including nanostructure formation and presence of vacancies.

The second part of the thesis discusses the nanopatterns generated by IBI and their scaling studies. Scaling theories have proven to be a powerful tool for understanding non-equilibrium growth processes. These have been applied here on TiO_2 as well as Tantalum surfaces to understand the mechanisms controlling the pattern formation after IBI as well as the universal nature of the surfaces. The TiO_2 surface displays formation of nanostructures which initially nucleate on the steps. After a critical fluence, a large density of nanostructures are observed to be aligned along the [001] crystallographic direction of the lattice. These nanostructures have been generated at various fluence ranging from 1×10^{16} to 1×10^{17} $ions/cm^2$ and have been investigated by Atomic Force Microscopy (AFM). The average diameter and height of these nanostructures varies from 25 to 40 nm and 1.0 to 1.6 nm, respectively. The surfaces display an increase in smaller sized nanostructures as a function of fluence. This is attributed to the systematic fragmentation of nanostructures, created at lower fluences, along with predominant fabrication of smaller nanostructures at later stages. To understand the nature of the surface modifications and to compare the results with the existing theoretical models, roughness exponent (α), growth exponent (β), dynamic exponent (z) and structure factor constant (γ) have been measured for these nanopatterned surfaces using height-height correlation (HHC) and structure factor techniques [30]. The observed scaling exponents suggest that the surface evolution is diffusion dominated and comes under Edward-Wilkinson (EW) class.

Tantalum surfaces exhibit formation of ripple patterns after Ion beam irradiation with 3 keV Ar^+. To understand the underlying mechanisms behind the ripple formation on this surface, 1+1 dimensional Kinetic Monte Carlo (KMC) simulations are presented here. The earlier work by Cuerno et.al [31] was based on a linear Hamiltonian which cannot explain the ripple- pattern formation on a metallic Tantalum. The line profiles, in AFM images here, display a groove like structures for these surfaces that indicate the presence of Schwoebel effect during pattern formation. The earlier discussed models, for ion irradiated surfaces, did not take this effect in account. Hence, in the model presented in this thesis, the effect of this Schwoebel barrier has been modeled by proposing a nonlinear term in the Hamiltonian [32]. The simulation results produce the surface morphology and scaling exponents that are consistent with our experimental observations. Moreover, the results show that the non-linearity term, related to the diffusing atoms after ion irradiation, is weak on Tantalum surfaces. The scaling exponents indicate that the morphology of ion irradiated Tantalum surfaces may belong to a universality class other than Edward- Wilkinson (EW) and Kardar- Parisi- Zhang (KPZ).

Thus, the present thesis discusses the generation of nano-patterns on single crystal semiconducting rutile TiO_2 surfaces and metallic Tantalum surfaces via the technique of ion irradiation. In both the cases the nanostructures are generated through the competition between the erosion and diffusion processes. The scaling studies on these non-equilibrium surfaces as well as the scaling exponents show that these surfaces belong to different universal classes. Results presented here further show that the inclusion of Schwoebel barrier in the metallic tantalum is important for understanding pattern formation. On the $TiO_2(110)$ surface, preferential sputtering of oxygen atoms leads to the formation of Ti rich zones that become the nucleation sites for the development of nanostructures. The results show an enhanced photoabsorption from these nano-patterned surfaces. Development of nanostructures on the surface and creation of vacancy sites along with the formation of $Ti_{1-x}Co_xO_2$, $CoTiO_3$ and Co nanoclusters, upon ion irradiation, promote the high photoabsorption and the reduced band gaps observed here. Formation of the cobalt nanoclusters, after implantation, also manifests in unusual superparamagnetic properties in this system. The observed SPM is in-equivalent along the two crystallographic axes of the TiO_2 lattice as demonstrated by the behavior of magnetic moments, above and below the *blocking temperature*. Scaling studies above blocking temperature also display this anisotropy. Presence of nanoclusters, with dipole-

dipole interactions and inter-cluster exchange interactions, produce these anisotropies. RBS/C results also display presence of these Cobalt-clusters along with an increase in depth dependent damage below the surface. Multiple scattering formalism has been applied to obtain the depth dependent damage profiles which indicate dynamical annealing of defects at the End-of-range. Scaling studies of TiO_2 surfaces, based on the non-equilibrium growth models, indicate that these surfaces after irradiation belong to the EW class. In the nanopatterns created on the metallic Tantalum surfaces, Schwoebel barrier plays an important role as has been demonstrated here through 1+1 dimensional KMC simulations. The Schwoebel effect has been incorporated here via a weak non linearity in the Hamiltonian. Comparison of simulations with experimental results show that the morphology of ion irradiated Tantalum surfaces belongs to a universality class other than EW and KPZ.

Bibliography

[1] A. Fujishima, and K. Honda, Nature **238**, 37 (1972).

[2] X. Chen, and S. S. Mao, Chem. Rev. **107**, 2891 (2007).

[3] D. Caruntu, G. Caruntu, and C. J. O'Connor, J. Phys. D: Appl. Phys. **40**, 5801 (2007).

[4] J. Zhu, Z. Gui, Y. Ding, Z. Wang, Y. Hu, and M. Zou, J. Phys. Chem. C **111**, 5622 (2007).

[5] S. Majumder, D. Paramanik, V. Solanki, B. P. Bag, and S. Varma, Applied Physics Letters **98**, 053105 (2011).

[6] F. Frost, A. Schindler, and F. Bigl, Phys. Rev. Lett. **85**, 4116 (2000).

[7] V. Solanki, S. Majumder, I. Mishra, P. Dash, C. Singh, D. Kanjilal, and S. Varma, Journal of Applied Physics **115**, 124306 (2014).

[8] U. Valbusa, C. Boragno, and F. B. de Mongeot, J. Phys. Cond. Mat. **14**, 8153 (2002).

[9] R. M. Bradley, and J. M. E. Harper, J. Vac. Sci. Technol. A **6**, 2390 (1988).

[10] M. A. Makeev, R. Cuerno, and A. L. Barabasi, Nucl. Instrum. Methods Phys. Res. B **197**, 185 (2002).

[11] P. Sigmund, Phys. Rev. B **184**, 383 (1969).

[12] M. Tamura an T. Suzuki, Nucl. Instr. Meth. **B 39**, 318 (1989).

[13] A.L. Barabasi and H.E. Stanley, Fractal Concepts of Surface Growth Cambridge University Press, Cambridge, 1995.

[14] C.A. Lang, C.F. Quate and J. Nogami, Appl. Phys. Lett. **59**, 1696 (1991).

[15] E. Chasen etal. Phys. Rev. Lett. **72**, 3040 (1994); T. M. Mayer et al. J. Appl. Phys.**76**, 1633 (1994).

[16] E. A. Eklund etal. Phys. Rev. Lett. **67**, 1759 (1991); E. A. Eklund etal. Surf. Sci. **285**, 157 (1993); J. Krim etal. Phys. Rev. Lett. **70**, 57 (1993), H.N. Yang etal. Phys. Rev. B. **50**, 7635 (1994).

[17] S. Habenicht, W. Bolse, K. Reimann, and U. Geyer, Phys. Rev. B **60**, 2200 (1999).

[18] A. Fujishima, T. N. Rao, and D. A. Tryk, J. Photochem. Photobiol. C **1**, 1 (2000).

[19] Y. Matsumoto, M. Murakami, T. Shono, T. Hasegawa, T. Fukumura, M. Kawasaki, P. Ahmet, T. Chikyow, S. Y. Koshihara, and H. Koinuma, Science **291**, 854 (2001).

[20] P. Kofstad, J. Electrochem. Soc. **109**, 776 (1962).

[21] G.M. Choi, H.L. Tuller, J.S. Haggerty, J. Electrochem. Soc. **136**, 835 (1989).

[22] S. Maeng, L. Axe, T.A. Tyson, L. Gladczuk, M. Sosnowski, Corros. Sci. **48**, 2154 (2006).

[23] S. Kimura, Y. Nishioka, A. Shintani, K. Mukai, J. Electrochem. Soc. **130**, 2414 (1983).

[24] X. Chen, and S. S. Mao, Chem. Rev. **107**, 2891 (2007).

[25] Shalik Ram Joshi, B. Padmanabhan, A. Chanda, V. K. Malik, N. C. Mishra, D. Kanjilal, and Shikha Varma, Appl. Phys. A. **122**, 713 (2016).

[26] Shalik Ram Joshi, B. Padmanabhan, A. Chanda, I. Mishra, V. K. Malik, N. C. Mishra, D. Kanjilal, and Shikha Varma, Appl. Surf. Sci. **387**, 938-943 (2016).

[27] Shalik Ram Joshi, B. Padmanabhan, Anupama Chanda, N. Shukla, R. Chandra, V. K. Malik, D. Kanjilal and Shikha Varma, (to be submitted).

[28] Shalik Ram Joshi, B. Padmanabhan, Anupama Chanda, V. K. Malik, S. Ojha, D. Kanjilal and Shikha Varma, (to be submitted).

[29] L. C. Feldman and J. W. Rodgers, J. Appl. Phys. **41**, 3776 (1970).

[30] Shalik Ram Joshi, Anupama Chanda, D. Kanjilal and Shikha Varma, (to be submitted).

[31] R. Cuerno, H. A. Makse, S. Tomassone, S. T. Harrington, and H. E. Stanley, Phys. Rev. Lett. **75**, 4464 (1995).

[32] Shalik Ram Joshi, Trilochan Bagarti, and Shikha Varma, Surf. Science **641**, 170, (2015).

List of Publications :

1. * Effect of Cobalt Implantation on Structural and Optical Properties of Rutile TiO2(110), **Shalik Ram Joshi**, B. Padmanabhan, Anupama Chanda, V. K. Malik, N. C. Mishra, D. Kanjilal and Shikha Varma, Applied Physics A, **122**, 713, (2016).

2. * Optical Studies of Cobalt Implanted Rutile TiO2(110) Surface, **Shalik Ram Joshi**, B. Padmanabhan, Anupama Chanda, Indrani Mishra, V. K. Malik, N. C. Mishra, D. Kanjilal and Shikha Varma Applied Surface Science, **387**, 938-943 (2016).

3. * Kinetic Monte Carlo Simulations of Self Organized Nanostructures on Tantalum Surface Fabricated by Low Energy Ion Sputtering, **Shalik Ram Joshi**, Trilochan Bagarti and Shikha Varma, Surface Science **641**, 170-173 (2015).

4. Ion-beam-induced nanodots formation from Au/Si thin films on quartz surface, D. P. Datta, V. Siva, A. Singh, **Shalik Ram Joshi**, D. Kanjilal, P. K. Sahoo, Nuclear Instruments and Methods in Physics Research B, **379**, 48-51, (2015).

5. Room Temperature Superparamagnetism in Rutile TiO_2 Quantum Dots : Produced via ECR Sputtering, Vanaraj Solanki, I. Mishra, **Shalik Ram Joshi**, P. Mishra, P. Dash, N. C. Mishra, D. Kanjilal, and Shikha Varma, Nuclear Instruments and Methods in Physics Research B **365**, 82-85 (2015).

6. Size-dependent optical properties of TiO_2 nanostructures, Vanaraj Solanki, Subrata Majumder, Indrani Mishra, **Shalik Ram Joshi**, Dinakar Kanjilal, and Shikha Varma, Radiation Effects and Defects in Solids **168**, 518 (2013).

7. Oxygen vacancy mediated enhanced photo-absorption from ZnO(0001) nanostructures fabricated by atom beam sputtering,

Vanaraj Solanki, **Shalik Ram Joshi**, Indrani Mishra, D. Kabiraj, N. C. Mishra, D. K. Avasthi, and Shikha Varma, Journal of Applied Physics **120**, 054303 (2016).

8. Scaling Studies of Nanopatterned TiO2(110) Surfaces Created via Low Energy Ion Irradiation,
   Indrani Mishra, **Shalik Ram Joshi**, Subrata Majumder, Ashis Kumar Manna and Shikha Varma, Radiation Effects and Defects in Solids, (DOI: 10.1080/10420150.2016.1225067).

9. Effect of Self Affine Morphology of Natively oxidised Silicon(100) on Wetting, Scaling Properties and DNA Fractal Dimension,
   Indrani Mishra, **Shalik Ram Joshi**, Subrata Majumder, U. Subudhi and Shikha Varma, Physics Letters A (Under Review).

10. Conducting Polymer PEDOT:PSS: An Emerging Material,
    Anupama Chanda, **Shalik Ram Joshi**, Rakesh Sahoo, Shikha Varma, and Kwangsoo No, Sensors and Transducers (Under Review).

11. * Unusual Superparamagnetism in Cobalt Implanted Rutile TiO2(110),
    Shalik Ram Joshi, B. Padmanabhan, Anupama Chanda, Neeraj Shukla, V. K. Malik, D. Kanjilal and Shikha Varma, (to be submitted).

12. * Damage Studies of Cobalt Implanted Rutile TiO_2 (110) Lattice via. RBS/C,
    Shalik Ram Joshi, B. Padmanabhan, Anupama Chanda, V. K. Malik, S. Ojha, D. Kanjilal and Shikha Varma, (to be submitted)

13. * Scaling Studies of Self Affine Nanostructures on TiO_2 (110) surfaces via. Ion Irradiation,
    Shalik Ram Joshi, Anupama Chanda, D. Kanjilal and Shikha Varma, (to be submitted)

14. Photo-Absorbance Properties of Constrained Nanostructures on rutile TiO_2 (110) surfaces,
    Vanaraj Solanki, **Shalik Ram Joshi**, Indrani Mishra, D. Kanjilal, and Shikha Varma, (to be submitted).

Conference Proceedings :

1. Bandgap Engineering, Enhanced UV-Vis Absorbance and Higher PL Emission from Ion Beam Modified and Nanodot Patterned Rutile TiO_2(110) Surfaces, Subrata Majumder, Vanaraj Solanki, Indrani Mishra, **Shalik Ram Joshi**, Dinakar Kanjilal, Shikha Varma.AES-ATEMA 2012 Conference Proceedings pp 131-138, (2012).

* indicates papers on which this thesis is based

List of Figures

Chapter 1

Introduction

Nano- dimensional materials are the foundation of frontier research in many advanced systems and in numerous applications. Characterized by dimensions of few atoms, materials in low dimension exhibit many unique and interesting properties [1,2], not observed in their bulk counterpart. Significance of these observations are at the forefront of enormous technological applications in the fields of nano-optics, nano-electronics, nano-devices, nano-photonics, spintronics, photo-catalysis, solar cells, optoelectronics, gas sensing etc. [2]. Fabrication of nanostructures, with well-defined properties and sizes, is the first crucial step in this direction. Top down and bottom up are two widely used approaches for the fabrication of nano-dimensional structures. With control at the nanoscale during material synthesis process, these methods offer the possibility of designing structures with desirable characteristics and improved performances [3, 4].

Top down approach refers to slicing or successive cutting of bulk materials to get a nanosized particle while bottom up refers to the build up of a material from atom by atom, molecule by molecule or cluster by cluster. Both approaches play very important role in modern technology. In top down approach any material is engineered by scaling down a complex entity into its component, such as creating a small nano crystals from a bulk material via variety of processes [2–7]. By contrast, the bottom up approach assembles materials from nanoscale molecules and atoms, to form larger structures. Examples of bottom up approach include self assembly of molecular patterning [8, 9]. The top down approach often uses the traditional fabrication methods such as lithography where extremely controllable tools are used to shape the materials . Formation of self organized nanostructures on large areas using ion beam irradiation is also an example of top down approach.

Transition metal oxide semiconductors are one of the most versatile class of semiconducting materials due to their diverse properties and functionalities [10–17]. Metal oxide nanostructures exhibit unique properties which can be used in variety of applications for the fabrication of efficient devices. Therefore, rapid research is being undertaken in the field of metal oxide nanostructures in terms of their growth and applications. TiO_2 has attracted a great deal of interest due to the importance of size and shape dependent properties in electronics and optoelectronics, photo catalysis, water splitting, photo voltaic cells, self cleaning surfaces, dye sensitized solar cells, etc [17–24]. Nanostructured Tantalum, however, have been extensively investigated due to their large technological application in thin film resistor materials with low temperature co-efficient of resistivity, oxygen sensors, erosion and corrosion resistance coatings [25–28]. Superfine and pliable tantalum powders can also be utilized to improve the quality and reduce the package size of capacitors in many devices [29–31].

Ion irradiation of solids generally give rise to well ordered nanostructures whose properties depend on several ion beam parameters such as substrate temperature, flux, energy, mass and incident angle *wrt.* surface normal [32–40]. These patterns may align either in the direction of ion beam or along the crystallographic direction of the surface. Non metallic surfaces result in an interlocking grids of hillocks and depression when the direction of incident ion beam is normal to the surface [38]. However, for off normal incidence, it gives rise to the formation of quasi periodic ripple patterns. On the contrary, ripple patterns are observed at normal incidence on metallic substrates [40]. These self organized nanopatterns are a result of competition between curvature dependent erosive process that roughens the surface and creates instability, and the diffusive process which reduces the instability *via* surface relaxation mechanism [38]. Sample rotation may also change the qualitative and quantitative characteristics of quasi periodic ripple patterns. Fig. 1.1(a) displays the ripple pattern formation on rutile TiO_2 (110) single crystals using 60 keV Ar^+ ion irradiation when it is being irradiated at 60° *wrt.* surface normal. However, evolution of nano dots have been observed on Muscovite mica (see fig. 1.1(b)), after it has been irradiated with 3 keV Ar^+ ion at incidence angle of 15° *wrt.* surface normal.

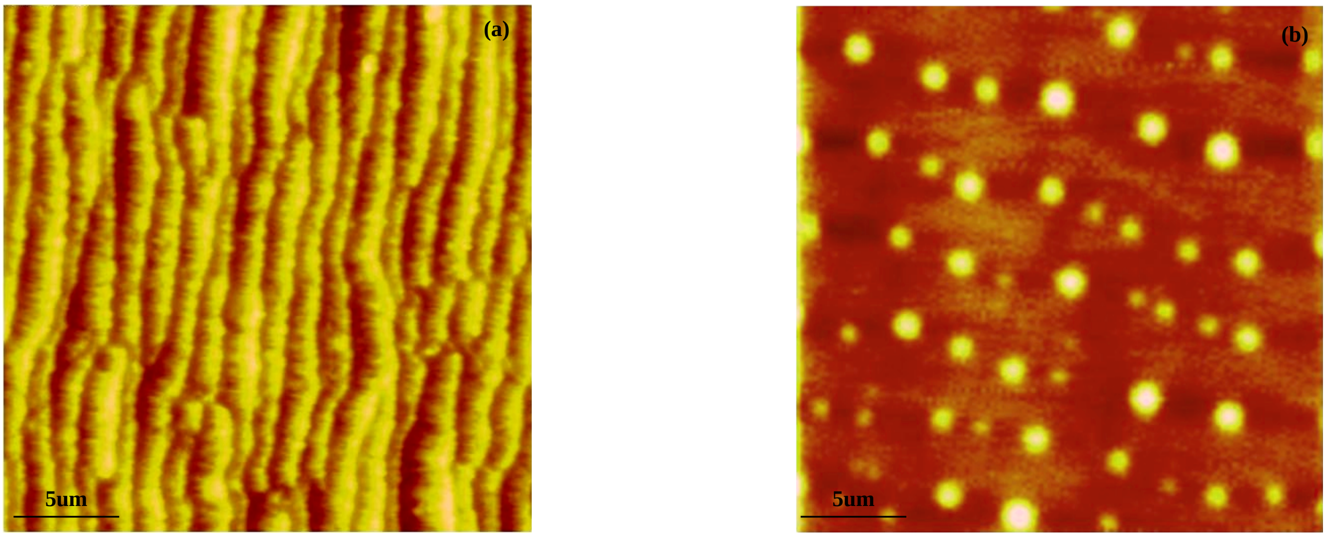

Figure 1.1: Self-organized (a) ripple pattern on $TiO_2(110)$ after irradiation with 60 eV Ar^+ ion beam at an incident angle of 60°, measured from surface normal [41] while (b) nano dots on Muscovite mica surface after irradiation with 3 keV Ar^+ ion at an incident angle of 15° *wrt.* surface normal.

The present work discusses the fabrication of TiO_2 and Tantalum nanostructures using ion beam irradiation technique. These nanostructured surfaces have tremendous applications in photo catalysis, photo voltaics, spintronics, memory devices, etc. As oxide nanostructures have been used for optical as well as magnetic application, their photo absorption response along with magnetic behavior, post ion irradiation, have been investigated. By controlling the compositional properties, oxidation states, vacancy states and dopant concentration, etc., at nanoscale during the synthesis process, it is possible to design high quality devices with improved predefined performances.

This chapter is organized as follows. Section 1.1 discuses ion implantation while Section 1.2 discuses basics of ion-solid interaction and energy losses. The damage distribution due to the interaction of the energetic ions with the host lattice has been discussed in Section 1.3. In Section 1.4, we discuss about the sputtering process along with the theoretical aspects of pattern formation due to the ion beam sputtering. Section 1.5 discusses the scaling theory to determine the universality class of patterned surfaces. Importance of Photo absorption response and magnetic behavior, in current research, and their utilization for technological application is discussed in Section 1.6 and 1.7, respectively. The modeling of patterned surfaces via of Kinetic Monte Carlo (KMC) simulation has been explored in Section 1.8.

1.1 Implantation

Ion implantation is an excellent method for modifying surface properties of materials since it offers precise control of dopant composition and structural modification at any selected temperature [40, 42–44]. Modern semiconductor industry has also embraced the ion implantation process as a key element in chip production [45, 46]. The incident ions of energy few hundred keV, lead to a penetration depth of few microns. Hence, only top surface layers, up to ion range, exhibit change in properties. The high rate of energy transfer of the ions to the target during implantation results in the displacement of atoms from their lattice sites. The displaced atom further collide with other atoms, thereby creating a collision cascade within the solid. This generates vacancies, interstitial atoms and other type of lattice disorder in the region around the ion track. Increasing ion fluence causes generation of an amorphous layer at the surface due to the overlapping of individual disordered region. The total amount of damage and its depth distribution depend on the implanted species, energy and flux of the incident ion, substrate temperature, and the channeling effects.

1.2 Basics of Ion-Solid Interaction

Ion irradiation of metals and semiconductors have shown numerous technological application [47]. The ability to improve the physical and chemical properties of the host lattice depends on the nature of ion-solid interaction. Fig. 1.2 displays the schematic diagram illustrating some of the possible ion beam interactions that result from ion bombardment of solid. Irradiation causes change in the chemical composition of host matrix which can be tailored using implantation dose. The spatial distribution of the implanted ions depends on the energy of the incident ions and the stopping processes. When a target atom gets knocked-off from its position, it can contribute to the collision cascade, as shown in fig. 1.2(b), within the solid under ion irradiation. This can cause sputtering if sufficient momentum and kinetic energy is transferred from the collision cascade to the surface or to near surface atoms. The main parameter that governs the conservation laws are the energy,

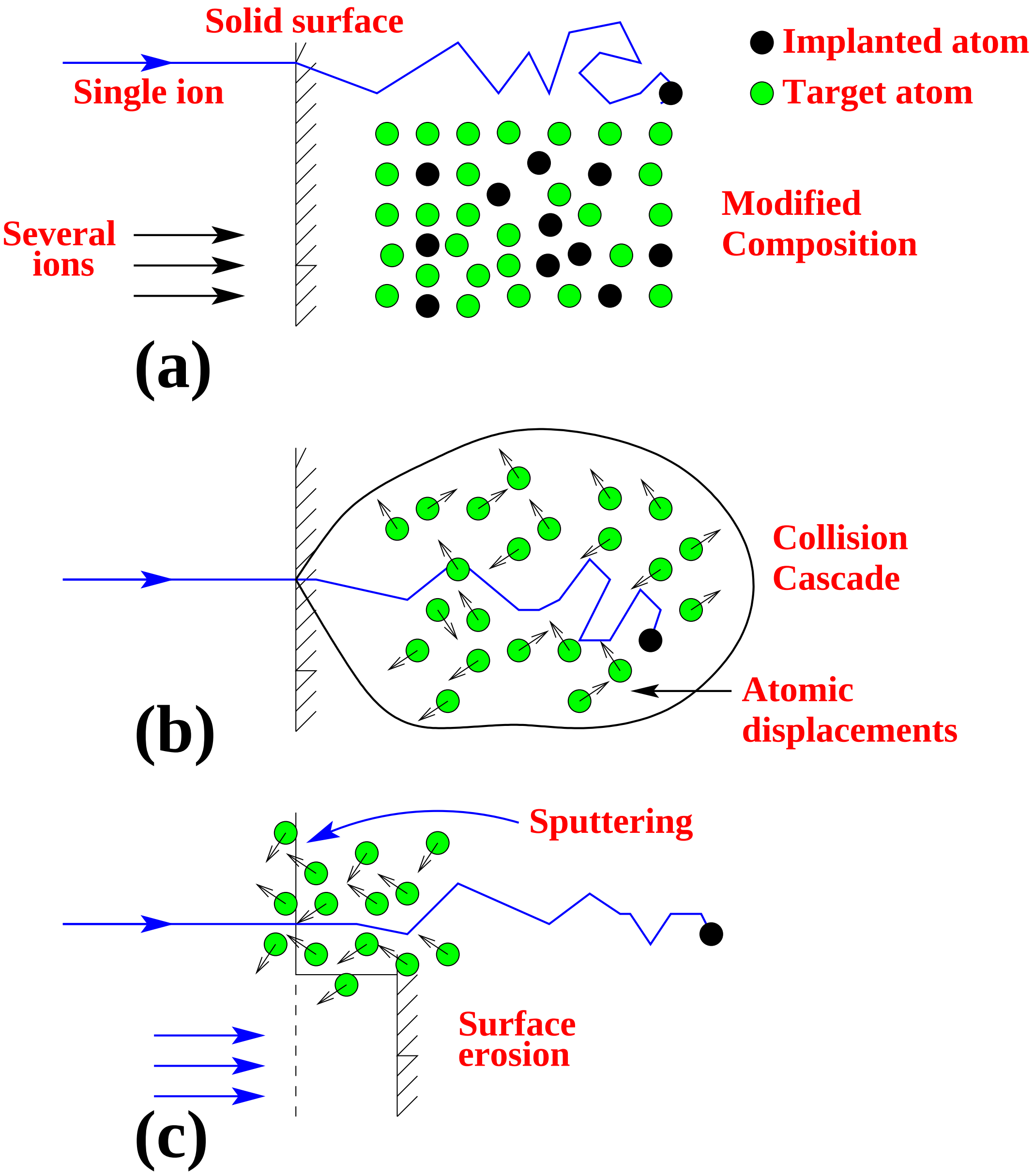

Figure 1.2: Schematic diagram to represent (a) ion implantation (b) collision cascade and atomic displacements which finally leads to (c) surface erosion (from ref [48]).

atomic masses and numbers, respectively, for both target and incident atoms. Depending on the energy of the incident ion, a collision cascade can be divided into three regimes. Regime I is called the single knock-off regime, and occurs at very low incident ion energy and $M_1 << M_2$, where M_1, and M_2 are the mass of the incident ion and target atoms, respectively. In this regime,

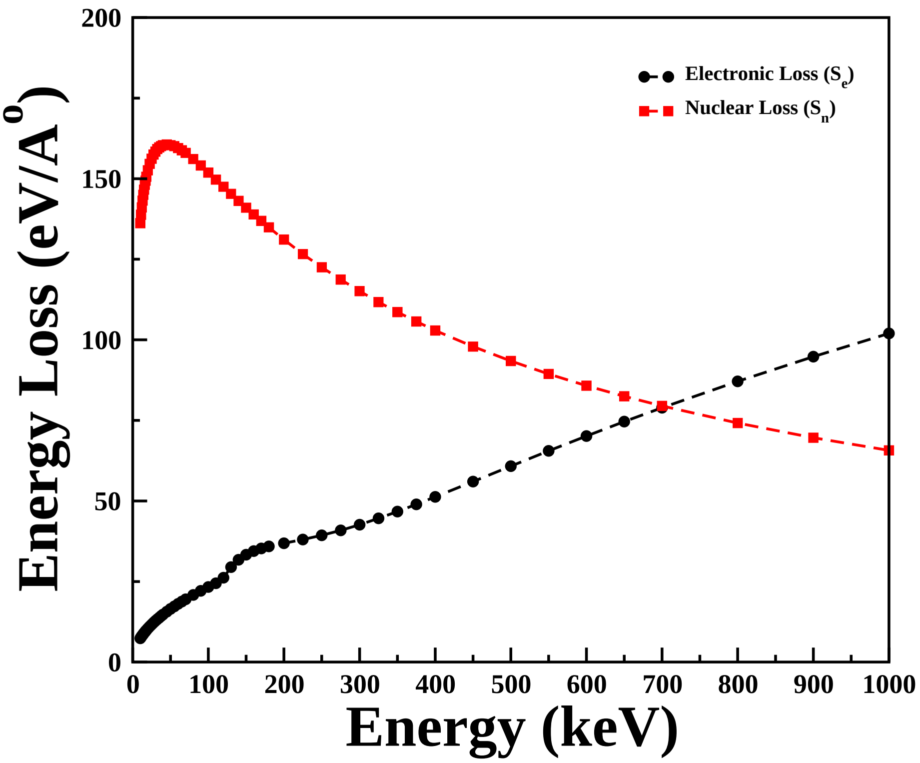

Figure 1.3: Variation of Nuclear S_n, and Electronic S_e energy losses, respectively, as a function of ions kinetic energy via SRIM simulation code [49], for cobalt ions in TiO_2 target.

the recoil atom does not receive enough energy to generate a cascade and sputtering is minimal. This is the region where only nuclear loss dominates. Regime II is a linear cascade region where $M_1 \approx M_2$ and the incident ion energy lies within few hundreds of keV. Here, the recoil atom receives enough energy to generate a cascade but the density of moving atoms are dilute enough to disregard both multiple collisions and collisions between moving atoms. Here, the loss is a combination of electronic as well as nuclear, but the contribution of electronic energy loss can be neglected. Regime III is called the spike regime, where $M_1 >> M_2$ and the incident ion energy is also very large. This results in majority of the target atoms within the spike volume to diffuse during the collision cascade. The loss in this regime is perfectly electronic.

1.2.1 Nuclear Energy Loss

It involves discrete energy transfer along with significant angular deflection of ions from their initial trajectory. These energetic ions in turn produce lattice disorder by the displacement of atoms from their equilibrium position due to collision with the target atom. These displaced atoms sometimes have significant energy to disturb the nearby atoms and form collision cascade. When the concentration of displaced atom per unit volume approaches the atomic density of the semiconductors, the material becomes amorphous. The process of nuclear stopping can also be visualized as a binary collision approximation which considers a series of elastic collision between the incident ion with energy E_0 and mass M_1 with a target atom which is initially at rest. The energy transfer (T) from the incident ion to the target atom can be derived as a function of scattering angle θ, using laws of conservation of energy and momentum, respectively [49,50].

$$T = T_{max}\ Sin^2\left(\frac{\theta}{2}\right) \tag{1.1}$$

where

$$T_{max} = \frac{4M_1M_2}{(M_1+M_2)^2}\ E_0 \tag{1.2}$$

is the maximum energy transferred during collision. The nuclear scattering cross section can also be written as [51,52]

$$d\sigma(E,T) = C_m\ E^{-m}\ T^{-1-m}\ dT \tag{1.3}$$

where

$$C_m = \frac{\pi}{2}\ \lambda_m u^2 \left(\frac{M_1}{M_2}\right)^m \left(\frac{2Z_0Z_1e^2}{u}\right)^{2m} \tag{1.4}$$

Here,

$$u = 0.885\ a_0(Z_0^{2/3} + Z_1^{2/3})^{-1/2} \tag{1.5}$$

where, a_0 is the Bohr radius, Z_0 and Z_1 is the atomic number of the projectile and target atoms, respectively and λ_m is a function that depends on m. For higher energy, *m* approaches unity while for lower energy, *m*, vanishes. Thus, the nuclear stopping power can be defined as the mean ionic energy loss due to elastic collision per unit length.

$$\left(\frac{dE}{dX}\right)_n = \int T \, d\,\sigma \tag{1.6}$$

using Eqn-1.3

$$\left(\frac{dE}{dX}\right)_n = \frac{1}{1-m} \, C_m \, \gamma^{1-m} \, E^{1-2m} \tag{1.7}$$

where

$$T_{max} = \gamma \, E \tag{1.8}$$

and

$$\gamma = \frac{4M_1M_2}{(M_1+M_2)^2} \tag{1.9}$$

is the reduced mass.

1.2.2 Electronic Energy Loss

The electronic energy loss is due to the resistance that the projectile encounters when it passes through the electron cloud of the target atoms. This causes an inelastic scattering due to the complex nature of energy loss process which results in the ejection of atomic electrons. As the mass of the electron is much less compared to the mass of incident ion, electronic collisions involve negligible energy loss per collision as well as small lattice disorder. During the motion of the projectile inside the target atom, in addition to stopping, the electronic interaction results in a change in the charge state of these ions in matter which is determined by a balance between electronic loss and electron attachment. In the limit of very low energy, the projectile becomes neutral and its electrons interact with the electrons of the target. At higher energy, $v \geq v_0 \, Z_0^{2/3}$, where v is the velocity of heavy ions and v_0 is the Bohr's velocity, the projectile loses all its electrons. At this velocity, the projectile can be considered as a positive point particle with effective charge, $Z^{eff} = Z_0$, moving with velocity greater than the mean orbital velocity of the atomic electrons in the target. The influence of these incident ions can be considered as a small perturbation due to their very high energy. Thus, using Bohr theory of stopping power, the effective charge of the incident ion can be approximated as [50]

$$Z_0^{eff} = Z_0\left[1 - exp\left(- \frac{v}{v_0} Z_0^{-2/3}\right)\right] \tag{1.10}$$

where the upper limit of velocity can be considered as $Z^{eff} = Z_0$. When the velocity of the incident ion $v < v_0\ Z_0^{2/3}$, the electronic stopping power can be calculated using Lindhard and Scharff approximation [53,54]

$$\left(\frac{dE}{dx}\right)_e = \frac{3.83\ Z_0^{7/6}\ Z_1}{(Z_0^{2/3} + Z_1^{2/3})^{3/2}}\left(\frac{E}{M_1}\right)^{1/2} = K_L\ E^{1/2} \tag{1.11}$$

or

$$\left(\frac{dE}{dx}\right)_e \propto v_{ion} \tag{1.12}$$

Here, stopping power is directly related to the incident projectile velocity. For incident ion energies $v \geq v_0\ Z_0^{2/3}$, the electronic stopping cross section can be estimated using Bethe and Bloch approximation in non-relativistic regime [55,56]. The electronic energy loss in this regime is given by

$$\left(\frac{dE}{dx}\right)_e = \frac{2\ Z_0^2\ e^4}{E}\ N\ Z_1\left(\frac{M_1}{m_e}\right) ln\left(\frac{2\ m_e\ v_{ion}^2}{I}\right) \tag{1.13}$$

where m_e is the mass of the electrons.

In the present work, 200 keV cobalt ions have been implanted in rutile TiO_2 and 3 keV Ar^+ ions have been utilized for the irradiation of Tantalum foils. For 3 keV Ar irradiation on Ta foil, the nuclear and electronic energy losses are calculated to be $\left(\frac{dE}{dx}\right)_e = 9.122\ eV/A^\circ$ and $\left(\frac{dE}{dx}\right)_n = 43.73\ eV/A^\circ$, respectively. For 200 keV Co ion implantation of TiO_2, the values are $\left(\frac{dE}{dx}\right)_e = 36.89\ eV/A^\circ$ and $\left(\frac{dE}{dx}\right)_n = 131.1\ eV/A^\circ$, respectively. So, here at this energy range nuclear loss is dominant, hence electronic loss has been neglected.

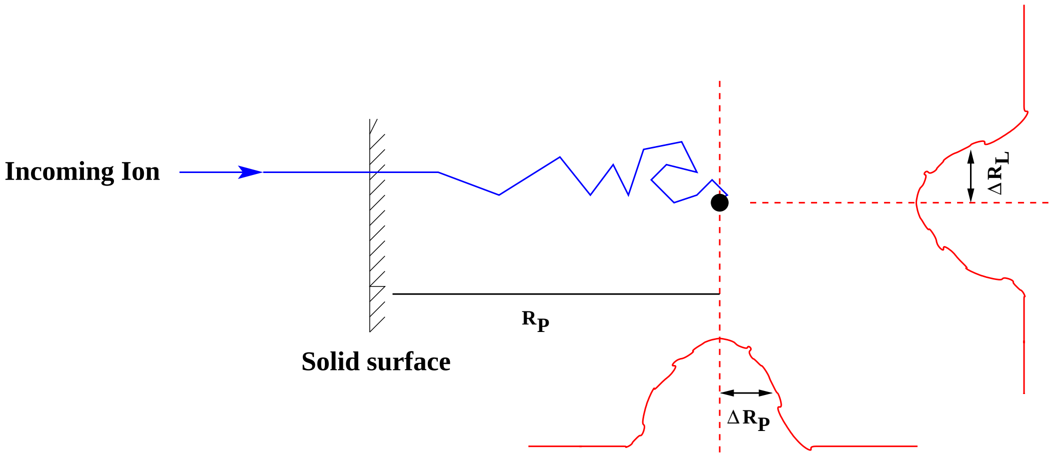

Figure 1.4: Schematic illustration to represent ion beam parameters which is being used to characterize the ion implanted distributions.

1.2.3 Ion Range

It can be defined as the integrated distance that an ion travels while moving in a solid and is inversely related to its stopping power. This can be written as

$$R_T = \int_0^{E_0} \left(\frac{dE}{dx} \right)^{-1} dE \tag{1.14}$$

where, E_0, is the incident ion energy and $\frac{dE}{dx}$ is the energy loss (nuclear and electronic) of the projectile at depth x.

The above equation describes the projected range for single projectile ion, but ion irradiation process requires the collective effect of large number of ions. The probability function describing the implantation depth is a Gaussian for low implantation dose, in the absence of crystallographic channeling effects. The mean of this distribution is the projected range, R_p, and the standard deviation is the straggling ΔR_p. For high implantation doses or crystallographic orientation effect, these distributions do deviate from Gaussian profile. Ion channeling causes the depth distribution to be skewed because penetration depth of channeled ions are several times greater than R_p.

1.3 Damage Distribution

When an energetic ion strikes the target atom during implantation, it can provide enough energy to displace an atom, thereby creating a collision cascade which leads to creation of vacancies, interstitials and several other lattice disorders. An accurate information of damage distribution created by ion implantation helps in the detailed investigation of the changes in the surface layer, post irradiation. The knowledge of depth dependent lattice disorder provides information about the substitution fraction of the incident ion in the host lattice which plays a crucial role in device fabrication [57, 58]. In addition, the implantation induced annealing, which depends on nature and density of damage leads to defect annihilation, thus modifying the properties of the substrate.

1.3.1 Dechanneling due to lattice disorder

Channeling of incident beam using Rutherford Backscattering Spectrometry (RBS) technique is a useful technique to extract information about ion induced lattice disorder in the solid. RBS/C spectrum contains full information about the lattice disorder as a function of depth of host lattice. During Channeling measurements, the He ion beam encounters different zones inside the host lattice. In a defect free zone, these probing particles undergo very small scattering events with electrons. The angle with which the channeled particles cross the center of the channel slowly increases because of multiple scattering and thus an increasing number of particles come closer to the rows and planes. Such particles can then collide with lattice atoms displaced out from their static rest positions because of thermal vibrations. The combination of multiple scattering by electrons and thermally displaced atoms at the channel walls leads to an increase in the number of non channeled particles as a function of depth. For disordered zone, the probing particle not only gets deflected from the normal lattice sites but also backscatters from the defects within the host lattice. The interaction of probing ion beam with defects results in small angle scattering that deflect particle out of channel and gradually increase the dechanneling component. The disordered region in the host lattice, however, provides large angle scattering events due to random position of the atoms. Thus in a crystal with defects, an increase in scattering yield over defect free crystal can occur due to [47] :

- Direct scattering of the incident beam with interstitial ions (defects) along their path.
- The gradual increase with depth in the non-channeled component of the beam due to defect channeling mechanism.

Thus, depth dependent damage density can be evaluated using the dechanneling contribution of incident ion beam due to lattice disorder from RBS/C spectra. The formalism is given below.

(A.) Energy to Depth Conversion

During RBS/C measurements, the stopping power is different for channeled and random beam respectively. The energy scales of both random and aligned spectra taken using RBS/C can be converted into depth scale on the basis of one to one relationship [59]. The energy dependence of stopping power must be taken into account during depth scale conversion. This can be calculated as follows

$$\Delta x_i = \frac{(K\ E_{i(in)} - E_{i(out)})}{[S]} \tag{1.15}$$

where, Δx_i = width of each channel in the spectrum and

$$[S] = \alpha\ K\ \frac{dE}{dx}\bigg|_{E\ C_{i(in)}} + \frac{1}{Cos\theta}\frac{dE}{dx}\bigg|_{E_{i(out)}} \tag{1.16}$$

$$E\ C_{i(in)} = E\ C_{i-1(in)} - \Delta\ x_i\ \alpha\frac{dE}{dx}\bigg|_{E\ C_{i-1(in)}} \tag{1.17}$$

$$E\ R_{i(in)} = E\ R_{i-1(in)} - \Delta\ x_i\frac{dE}{dx}\bigg|_{E\ R_{i-1(in)}} \tag{1.18}$$

$$E_{i(out)} = E_{i-1(out)} + \Delta\ x_i\frac{1}{Cos\theta}\frac{dE}{dx}\bigg|_{E_{i-1(out)}} \tag{1.19}$$

$$Cor_i = \left(\frac{E\ C_{i(in)}}{E\ R_{i(in)}}\right)^2 \tag{1.20}$$

Here, K is the kinematic factor and α is the stopping power ratio of the incident ion during channeling and random direction. In this thesis channeling studies and damage distributions have been investigated in cobalt implanted TiO_2, a stopping power of 0.7 has been considered [59]. For a thin strip of width Δx_i, $E\ C_{i(in)}$ is the channeled He^+ ion energy before scattering whereas, $E_{i(out)}$ is the energy of backscattered ions after penetration. The stopping power $\frac{dE}{dx}$ can be extracted from TRIM simulation code [60]. $E\ R_{i(in)}$ is the energy of the random particle just before Δx_i. The difference between $E\ R_{i(in)}$ and $E\ C_{i(in)}$ is termed as the energy spreading which gets larger *wrt.* penetration depth. The influence of energy spreading on scattering cross section must be taken into account as the scattering cross section is inversely proportional to the energy [61]. The yield of the RBS/C spectra can be written as [62]

$$Y(E_1) = Q\ \sigma(E)\Omega \frac{\Delta E}{[\epsilon(E)]} \frac{\epsilon(K\ E)}{\epsilon(E_1)} \tag{1.21}$$

where Q is the total incident ions hitting the target, σ is the scattering cross section, Ω is the solid angle of the solid state detector, ϵ is the stopping cross section and $\Delta\ E$ is the width of each channeled spectrum. E is the energy of the incident ion beam while E_1 is the scattered beam energy. So, using Eqn-1.21, the channeled yield $Y(E\ C_{i(in)})$ can be corrected as $Y'(E\ C_{i(in)})$, by considering the influence of energy spreading which provides one to one mapping for depth conversion *wrt.* energy spectra.

$$Y'(E\ C_{i(in)}) = Y(E\ C_{i(in)}) \times\ Cor_i \frac{[\epsilon(E\ R_{i(in)})]}{[\epsilon(E\ C_{i(in)})]} \frac{\epsilon(K\ E\ C_{i(in)})}{\epsilon(K\ E\ R_{i(in)})} \tag{1.22}$$

Therefore, one to one mapping can be done for depth conversion *wrt.* energy spectra.

(B.) Dechanneling Analysis

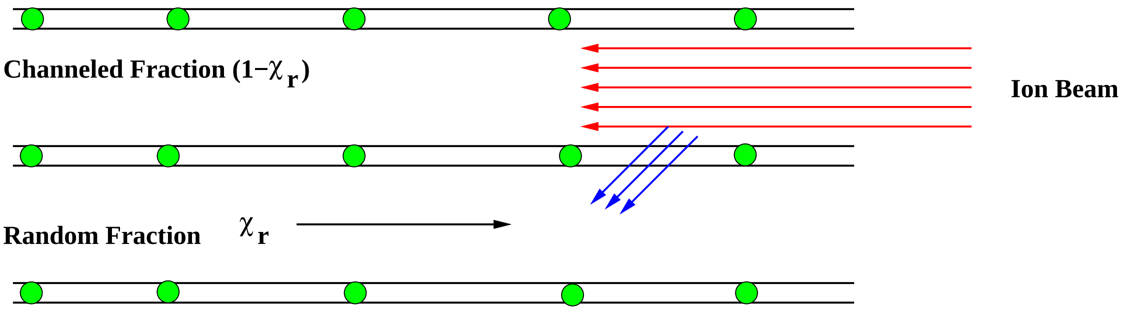

Figure 1.5: Schematic illustration of channeled (1-χ_r) and random (χ_r) fractions, respectively of He$^+$ beam inside the crystal.

For dechanneling, the interaction of incident beam can be composed of two components, the channeled fraction or the interaction with the defect-free region and the random fraction from defect region. The random fraction χ_r is the component of beam that is interacting with disordered or randomly located atoms in the host lattice. The random component at a depth *x* consists of those particles that are initially non channeled and those that are initially channeled but are dechanneled due to damage.

The lattice disorder, N_d(x) can increase the RBS/C yield due to random arrangement χ_r of atoms. Using this, we compared the back scattering yield during channeling direction as a function of depth *wrt.* a perfect crystal (pristine), whose random fraction can be denoted as χ_v(x). The χ_v(0) = χ_{min}, where χ_v(x) includes the fraction that was initially not channeled. χ_{min} is relatively small fraction of dechanneled component due to finite scattering interactions in the unirradiated crystal.

The quantity χ_v(x) can be taken from experimental RBS/C spectra for unirradiated crystal. This is also called as normalized yield which is the ratio of the aligned yield *wrt.* the random yield at a fixed depth. The channeling yield at the same depth for disordered crystals can be denoted as χ_d(x) and is also taken from experimental data. Thus the relationship between χ_d(x) and the random fraction of the beam χ_r(x) can be written as

$$\chi_d(x) = \chi_r(x) + [1 - \chi_r(x)]\left(\frac{N_d(x)}{N}\right) \tag{1.23}$$

where N_d and N are the number density of the displaced and host atoms, respectively, at position x. It can be clearly seen from Eqn-1.23, that the normalized yield of ion irradiated crystal is the sum of the contribution from scattering of the random component $\chi_r(x)$ with all atoms and the scattering due to channeled components $(1 - \chi_r(x))$, with defects within the host lattice. N_d(x) can be easily calculated from the above equation if $\chi_r(x)$ is known. However, $\chi_r(x)$ is not a directly measurable quantity. This can be evaluated by considering single and multiple scattering events during dechanneling. For single scattering [63]

$$\chi_r(x) = 1 - [1 - \chi_v(x)]exp^{-\gamma(x)} \tag{1.24}$$

and

$$\gamma(x) = \frac{\pi\, Z_1^2 Z_2^2 e^4}{E^2 \psi_c^2(x)} \int_0^x N_d(x)\, dx \tag{1.25}$$

Here Z_1 and Z_2 are the atomic numbers of the incident and target atoms, respectively, e is the electronic charge and E is the energy of the incident ion beam. ψ_c(x) is the critical angle for channeling at depth *x* and can be written as [47]

$$\psi_c(x) = \left(\frac{2\, Z_1 Z_2 e^2}{dE(x)}\right)^{1/2} \left[\frac{1}{2} ln\left(\frac{C\; a}{\rho}\right)^2 + 1\right]^{1/2} \tag{1.26}$$

Here, a is the Thomas-Fermi distance given by, a = $0.8854\; a_0(Z_1^{2/3} + Z_2^{2/3})^{-1/2}$, a_0 being Bohr radius. ρ is the thermal vibration amplitude in TiO_2 (=0.081 A°) [64] and C is a constant (= 1.732) [65]. E(x) is the incident energy at depth *x*, *d* is the lattice spacing for TiO_2 along (110) direction (=4.594 A°) [66].

Studies however, suggests that multiple scattering is dominant over most of the range of defect densities where the dechanneling is important. Hence, we have used Feldman and Rodgers approximation for multiple scattering in our analysis [65]. According to this :

$$\chi_r(x) = \chi_v(x) + (1 - \chi_v(x)) exp\left(\frac{-\psi_c^2}{\Omega^2(x)}\right) \tag{1.27}$$

where

$$\Omega^2(x) = \frac{\pi}{2}\left(\frac{2\; Z_1\; Z_2\; e^2}{dE(x)}\right)^2 d^2\; ln\left(\frac{1.29\; a\; E(x)}{Z_1\; Z_2\; e^2}\; \frac{M_2}{M_1 + M_2}\right) \int_0^x N_d(x)\; dx \tag{1.28}$$

where, M_1 and M_2 are the atomic masses while Z_1, Z_2 are atomic numbers for projectile and host atoms, respectively.

Thus, the defect density N_d(x) as a function of depth can be estimated using an iterative procedure. Assuming, at surface, $\Omega^2(0)$ = 0, and N_d(0) is defect density at the surface, gives

$$\frac{N_d(0)}{N} = \frac{[\chi_d(0) - \chi_v(0)]}{[1 - \chi_v(0)]} \tag{1.29}$$

The quantity $\frac{N_d(x)}{N}$ is calculated for each subsequent depth interval. The critical angle ψ_c can be tailored to make damage density zero at deep layers. Using the above formalism, the damage distributions after 200 keV Cobalt ion implantation in rutile TiO_2 (110) have been investigated using RBS/C data.

1.4 Ion Beam Sputtering

Sputtering is the removal of surface atoms by energetic ions and is caused by collisions between the incoming particles with the atoms at or near surface layers of a solid [67]. If the energy transferred is greater than the binding energy of the lattice site, a primary recoil atom is created. This primary recoil atom will collide with another target atom to distribute the energy via collision cascade. A surface atom is then knocked-off if the energy transferred to its component normal to the surface is larger than the surface binding energy. Sputtering is measured by the sputtering yield, Y, defined as the mean number of atoms removed per incident particle. The incident particles may be ions, neutral atoms, neutrons, electrons or energetic photons. Mostly sputtering mechanisms have been investigated on mono atomic targets [68, 69]. For crystalline materials, the sputtering yield are influenced by various parameters like lattice structure, crystallographic orientation, etc. [70, 71]

1.4.1 Self Organized Pattern formation by Ion Beam Sputtering

The removal of atoms, due to elastic collision between the incident ion and target atom, can lead to the development of wide variety of patterns on surfaces. Navez et.al [72] for the first time in 1956, have observed the formation of ripple patterns on SiO_2 substrates. The pattern formation due to ion beam sputtering arises due to the competition between erosive process and the surface relaxation by various diffusive mechanisms. The angle of incidence of ion beam also plays a crucial role in obtaining wide variety of nanostructures [38]. For normal incidence, one observes isotropic nanodots on the surface, whose sizes can be tailored by varying ion energy and fluence. For off normal incidence, formation of quasi periodic ripple patterns have been observed. The ripple wave vector is, however, aligned along the direction of ion beam if the angle is less than the critical angle (θ_c). Anisotropic surface diffusion and Ehrlich-Schwoebel barrier also play key role in pattern formation [40, 73, 74].

Several researchers have contributed, both theoretically and experimentally, to understand the complexity behind the pattern formation on various surfaces like metals, insulators or semiconductors [33–35, 37–40, 69]. The first theoretical explanation had been given by Sigmund who studied the surface erosion rate for different surface topographies and addressed the existence of surface instability during ion beam sputtering [75]. Bradley and Harper, however, considered the effect of surface curvature on sputtering yield. B-H model also incorporated surface relaxation due to surface diffusion in their model, and it is the most successful theoretical approach for explaining ripple patterns on surfaces. Makeev, Cuerno and Barabasi [48] have included non linear terms to predict the behavior of surface evolution of ion sputtered surfaces in long time scale. The brief description about their work has been discussed below.

Sigmund Sputtering Approach

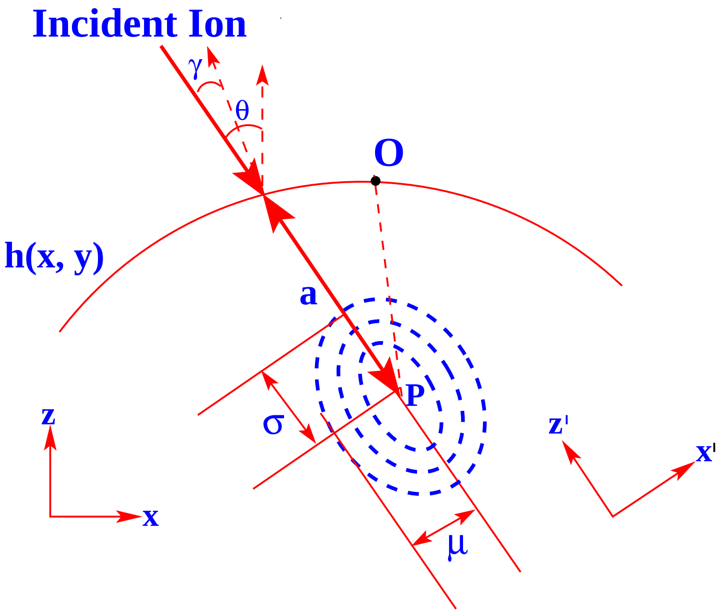

Figure 1.6: Schematic diagram of energy distribution process during ion beam sputtering. θ and γ are global and local angle of incidence, respectively.

The Ion Beam Sputtering (IBS) on various surfaces leads to the generation of patterns. Incident ions can be implanted and reflected from the host lattice or they can result in the emission of electrons, atoms or photons due to recoiling. Moreover, an ion penetrating into solid undergoes multiple collisions by transferring kinetic energy and momentum during each collision and forms collision cascade [76–78]. If we assume that the collision density is isotropically distributed for small number of atoms in motion, this process can be termed as linear collision cascade which can be described in terms of binary collision between moving ions and stationary atoms. Due to the momentum reversal, target atoms traveling towards the surface by gaining enough energy, can overcome the surface binding energy and be emitted in vacuum. This process will lead to material erosion and development of lattice defects like vacancies and interstitials.

Incident ions can loose their energy in both elastic and inelastic processes via nuclear and electronic collisions, respectively. However, for low energy incident ions, the energy loss is mainly due to the nuclear collision phenomenon. The amount of energy deposited by incident ion during IBS depends upon intrinsic material properties, ion mass and energy. Prolonged irradiation may lead to additional defects in the crystalline structure which can produce surface amorphization via overlapping of large lattice disordered areas. The erosion rate of the material can be determined by sputtering yield *(Y)*, defined as the average number of ions removed from the surface per incident ion [75, 77, 79]. The scattering phenomenon between target atom and incident ion forms collision cascade and takes place within a certain layer of average depth *d*, called the penetration depth of the incident ion. A well established formulation of ion beam sputtering has been developed by Sigmund [75, 79].

For amorphous targets, a set of transport equations describing the energy transfer during the sputtering, have been formulated. In Sigmund theory, the rate of sputtering from a surface to any arbitrary point z(x,y) is proportional to the energy deposited there by incident ions. The average energy deposited at point **r** in the target lattice by the incident ion which travels along z-axis has the following Gaussian distribution

$$E(\mathbf{r}) = \frac{\epsilon}{(2\pi)^{3/2}\,\sigma\,\mu^2} exp\left[-\frac{(z-h(0,0)+a)^2}{2\sigma^2} - \frac{x^2+y^2}{2\mu^2}\right] \tag{1.30}$$

where ϵ is the energy of the incident ion. The terms σ and μ in Eqn-1.30 represent the width of the Gaussian distribution in the direction parallel and perpendicular to the incoming ion beam, respectively. A schematic diagram has been shown in fig. 1.6.

Several theoretical works have predicted that the energy distribution during ion beam irradiation process can be well approximated by a Gaussian distribution function [50]. Thus, the mean energy deposition depth of the incident ion traveling inside the host lattice is usually comparable to the penetration depth, and is proportional to the ion energy, according to the relation

$$a(\epsilon) = \frac{1-m}{2m}\gamma^{m-1}\frac{\epsilon^{2m}}{N\,C_m} \tag{1.31}$$

where N is the atomic density of the target and

$$\gamma = \frac{4M_1M_2}{(M_1+M_2)^2} \tag{1.32}$$

is the reduced mass, where, M_1 and M_2 are being the mass of the incident ion and target atom, respectively. C_m is a constant which depends upon the inter atomic potential and $m = m(\epsilon)$, varies between 0 and 1 for very low and high energy, respectively. For intermediate energies (10-100 keV), $m \sim 1/2$ and the penetration depth becomes directly proportional to energy.

Eqn-1.30 describes the event for single ion hitting on the target, but the sample is being irradiated with a uniform flux *f* of incident ions, which penetrates the host lattice at different points simultaneously. Therefore, the rate of erosion at an arbitrary point O depends on the energy deposition of all the ions entering within the range of distribution. The normal erosion velocity at a point O is calculated as [79]

$$v(O) = \Lambda \int_Q \Phi(\mathbf{r})\; E(\mathbf{r})\; d\mathbf{r} \tag{1.33}$$

The integral is taken over whole range in which the deposited energy contributes to the erosion. $\Phi(\mathbf{r})$ is a local correction to the uniform flux *f* due to the curvature dependent sputtering, and Λ is a constant which depends on the material properties according to the binding energy and scattering cross section and can be written as

$$\Lambda = \frac{3}{4\pi^2}\frac{1}{N\,U_0\,C_0} \tag{1.34}$$

Here, U_0 is the surface binding energy and C_0 is a constant proportional to the square of the effective radius of the inter atomic potential. Shadowing effects and material re-deposition were not taken into account during Sigmund formalism. Sigmund theory provides a better insightful description about ion bombardment but is unable to provide direct information about the morphology of the ion irradiated surfaces. The equation in the prescribed form can not be used to provide information about surface evolution of ion irradiated surfaces.

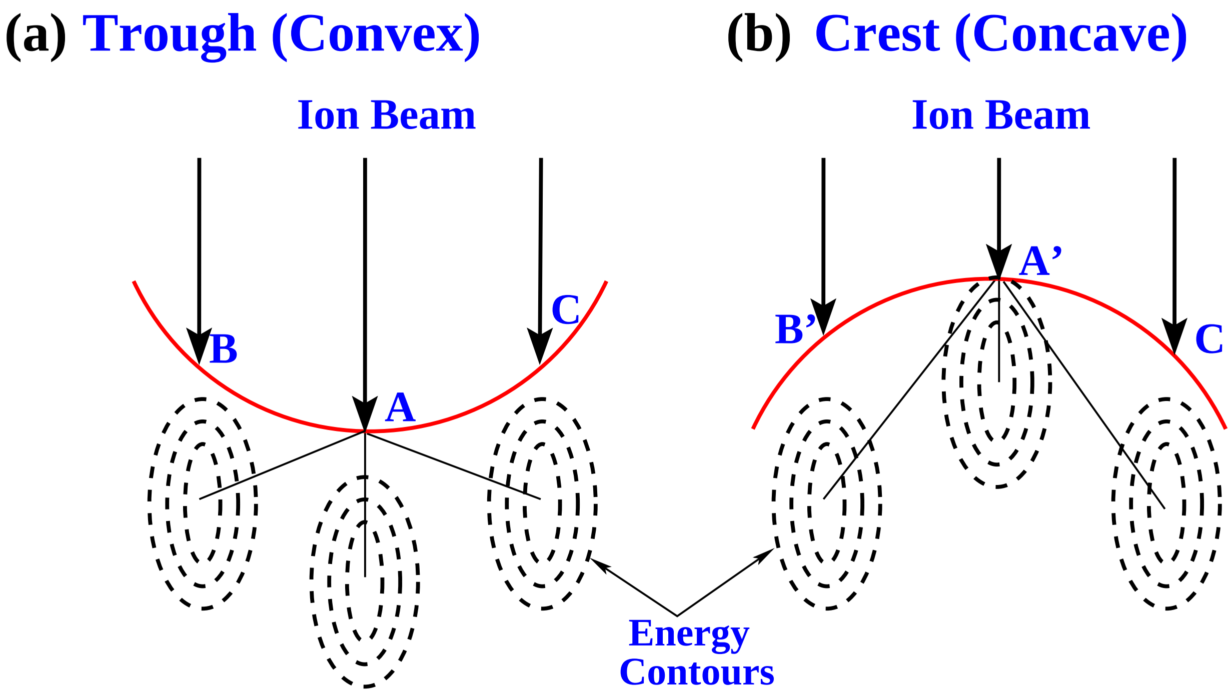

Figure 1.7: Schematic diagram of the physical origin of instability during ion beam sputtering phenomenon displays (a) convex geometry is eroded faster than concave surfaces (b) due to the larger energy deposition at A than at A′.

Bradley Harper Model

In 1988, Bradley and Harper [38] proposed a theory to explain the surface evolution due to ion irradiation. In contrary to Sigmund theory, they proposed a curvature dependent sputtering yield which induces a instability on the ion sputtered surfaces. This instability plays a major role in the formation of quasi periodic ripple like pattern on the sputtered surfaces. To determine the curvature dependent sputtering yield, they have calculated the normal component of the surface velocity $v(\phi, R)$, using Eqn-1.33, at point O, by taking uniform flux *f* of incoming ions at an angle ϕ.

The direction of incoming ion beam has been chosen as z-axis, while x and y axis are chosen parallel and perpendicular to the projection of ion beam, respectively. Moreover, they also assumed that the surface height h(x) varies slowly enough so that R, the radius of curvature at point O, is much larger than the penetration depth. Thus, the normal velocity component has the form

$$v(\phi, R) \approx \frac{\Lambda\epsilon\ f\ a}{\sqrt{2\pi}\sigma\mu} B_1^{-1/2}\ exp\Bigg(- \frac{a^2}{2\sigma^2} + \frac{A^2}{2B_1}\Bigg)\Bigg[Cos\phi + \Gamma_1(\phi)\frac{a}{R}\Bigg] \tag{1.35}$$

where, Λ is a constant which is related to the energy deposited at point O and the coefficients A, B$_1$, B$_2$ and C depend on σ, μ and ϕ [38]. $\Gamma_1(\phi)$ can be described as :

$$\Gamma_1(\phi) = \frac{A}{B_1} Sin\phi - \frac{B_2}{2B_1}\Bigg(1 + \frac{A^2}{B_1}\Bigg)Cos\phi - \frac{A\ C}{B_1^2}\Bigg(3 + \frac{A^2}{B_1}\Bigg)Cos\phi \tag{1.36}$$

This equation contains the information about curvature dependent sputtering of ion irradiated surfaces. For ϕ=0, the coefficient $\Gamma_1(\phi)$ will be negative. This means that when the incident beam is perpendicular to the target, the trough will be eroded more than the crest. This is due to the radius of curvature, R, which is negative at the valley, This results in the enhancement of sputtering in that region, thus leading to instability and roughening of the surface. This process is well described in fig. 1.7.

For a flat surface, i.e., R= ∞ and $Y_0(\phi) = N\ v(\phi, R = \infty)/f\ Cos\phi$, the sputtering yield can be estimated as

$$Y_0(\phi) \approx \frac{\Lambda\epsilon\ N\ a}{\sqrt{2\pi}\sigma\mu} B_1^{-1/2}(\phi) exp\Bigg(- \frac{a^2}{2\sigma^2} + \frac{A^2(\phi)}{2B_1(\phi)}\Bigg) \tag{1.37}$$

where

$$B_1^{-1}(\phi) = \Bigg(\frac{\sigma}{a}\Bigg)^2 \Bigg[1 + \Bigg[\Bigg(\frac{\sigma}{\mu}\Bigg)^2 - 1\Bigg]Cos^2\phi\Bigg]^{-1} \tag{1.38}$$

where, $\sigma > \mu$ and N is the atomic density in amorphous region. This equation reveals the angular dependence of sputtering yield, which increases with increase in ϕ. For grazing incidence, the above equation is not valid anymore. The energy deposited at point A will be same as A'. But the average energy deposited at A by the incoming ions will be larger than at A', which leads to higher rate of sputtering at A. Now considering smoothening mechanism due to thermally activated surface diffusion along with the erosion, Bradley and Harper formulated a linear equation to describe the surface evolution of ion sputtered surfaces [38].

$$\frac{\partial h}{\partial t} = -v_0(\phi) + v_0'(\phi)\partial_x h + S_x(\phi)\partial_x^2 h + S_y(\phi)\partial_y^2 h - K\nabla^4 h \tag{1.39}$$

Here, K is thermally activated surface diffusion and S$_x$, S$_y$ are the coefficients which depend on experimental condition. This equation describes the surface evolution of ion sputtered surface h(x,y,t), due to competition between erosion and diffusion at an incident angle ϕ *wrt.* surface normal. The first term on the right hand side represents the angle dependent erosion velocity of a flat surface while the second term is due to the lateral movement of the structures on the surface. These terms do not have any effect on the characteristic properties like wavelength and amplitude of quasi periodic pattern. The third and fourth term of Eqn-1.39,contribute to the curvature dependent erosion while the last term contributes to the surface relaxation due to material transport on the surface. The two coefficients S_x, and S_y depends on ion energy, incidence angle and material properties.

$$S_{x,y} = \frac{f\,a}{N} Y_0(\phi)\Gamma_{1,2}(\phi) \tag{1.40}$$

The two coefficients $\Gamma_1(\phi)$ and $\Gamma_2(\phi)$ is responsible for the local variations of sputtering yield and are given by [50]

$$\Gamma_1(\phi) = \frac{A}{B_1} Sin\phi - \frac{B_2}{2B_1}\left(1 + \frac{A^2}{B_1}\right)Cos\phi - \frac{A\,C}{B_1^2}\left(3 + \frac{A^2}{B_1}\right)Cos\phi \tag{1.41}$$

$$\Gamma_2(\phi) = -\frac{\mu^2}{a^2}\left(\frac{1}{2}B^2 + \frac{A\,C}{B_1}\right)Cos\phi \tag{1.42}$$

The coefficient K accounts for the thermally activated surface diffusion on the surface.

$$K = \frac{D_s \gamma \Omega^2 N}{K_B T} exp\left(-\frac{\Delta E}{K_B T}\right) \tag{1.43}$$

Here, D_s is the surface diffusion constant, γ is the surface energy per unit area, Ω is the atomic density of the target and N is the number density of the surface atoms. ΔE accounts for activation energy barrier for surface diffusion, K$_B$ is the Boltzmann constant and T is the surface temperature. So, the incorporation of diffusion term was really necessary to obtain periodic structures on ion irradiated surfaces. Only roughening term alone will not produce quasi periodic structures. For investigating the periodic solutions for ripple patterns, it is useful to take a Fourier transform of Eqn-1.39 with **q** = (q_x, q_y) as a wave vector. The Eqn-1.39 can be rewritten in fourier space as

$$\frac{\partial h(q_x, q_y)}{\partial t} = [-S_x\, q_x^2 - S_y\, q_y^2 - K(q_x^4 + q_x^4)]\; h(q_x, q_y, t) \tag{1.44}$$

The solution of the above equation can be described as

$$h(q_x, q_y, t) = h(q_x, q_y, 0)\ exp[r(q)\ t] \tag{1.45}$$

where $h(q_x, q_y, 0)$ is the initial amplitude of the surface height with growth factor

$$r(q_x, q_y) = -S_x\ q_x^2 - S_y\ q_y^2 - K(q_x^4 + q_y^4) \tag{1.46}$$

Eqn-1.45 describes the time evolution of the amplitude of the Fourier component and it increases or decreases experimentally with the nature of r(**q**). The nature of r(**q**) plays a crucial role in roughening or smoothening of the surface. The function r(**q**) has a maximum at $q^* = \left(\frac{max|S_{x,y}|}{2K}\right)^{1/2}$, where $|S_{x,y}|$ is the largest absolute value between -S_x and -S_y. The amplitude with wave number q^* will grows faster than the others, resulting in a periodicity with wave numbers q^* which will dominate the surface topography. Thus, the wavelength of the quasi periodic pattern can be estimated using

$$\lambda = \frac{2\pi}{q^*} = 2\pi\left(\frac{2K}{max|S_{x,y}|}\right)^{1/2} \tag{1.47}$$

The direction of ripple wave vector will depend on the value of S_x and S_y. The model can actually predict the dependence of wavelength λ_x, λ_y on the ion incidence angle.

B-H model does not take any possible diffusion mechanism except thermally activated diffusion mechanism. This mechanism is highly active only at high temperature. For low temperature ion irradiation experiments, it is necessary to include other smoothening effects. Makeev et.al [80], have introduced Effective Surface Diffusion (ESD) as the main relaxation mechanism at low temperature. The diffusion here does not imply a real mass transport along the surface, but occurs due to local variation of erosion of the target during ion beam irradiation. Thus, Eqn-1.39 can be modified as

$$\partial_t(h) = -v_0 + v_0\partial_x h + S_x\ \partial_x^2 h + S_y\ \partial_y^2 h - D_{xx}\ \partial_x^4 h - D_{yy}\ \partial_y^4 h - D_{xy}\ \partial_x^2\partial_y^2 h \tag{1.48}$$

The term with coefficients D_{xx}, D_{yy}, D_{xy} is proportional to the fourth derivative of height function, thus leading to additional anisotropic smoothening on the surface. However, it is important to note that ESD results from preferential sputtering during ion irradiation process which appears as reorganization of the surface and does not involve any mass transport on the surface. If ESD is considered as relaxation mechanism, the ripple wavelength can be rewritten as

$$\lambda_{x,y} = \frac{2\pi}{q^*} = 2\pi \left(\frac{2D_{xx,yy}}{max|S_{x,y}|} \right)^{1/2} \tag{1.49}$$

In this case the wavelength of ripple pattern is independent of ion flux and fluence but increases with increase in ion energy.

Anisotropic Kuramoto Sivashinsky Equation

The B-H model was indeed a very successful one to explain the formation of quasi periodic ripple wave patterns on various surfaces. But it was unable to explain the long time behavior of the surface evolution or the stochastic nature of the sputtering process [81]. According to linear theory, the amplitude of the ripple pattern, during ion beam irradiation, increases exponentially with time, but experimentally one always observes a saturation of the amplitude of these ripple patterns [82]. The addition of non linear terms, which depend on higher order derivatives of surface height, play vital role in the long term behavior of surface evolution. Cuerno et.al [83, 84], have incorporated the non-linear term in B-H model to include higher order perturbation. Using normal velocity of erosion at any point O on the surface, the equation of motion of height profile can be written as

$$\partial_t h(x,y,t) \approxeq -v(\phi, R_x, R_y)\sqrt{1 + (\bigtriangledown h)^2} \tag{1.50}$$

where ϕ is the angle of ion beam *wrt.* the local normal to the surface h(x,y) and R_x, R_y are the radius of curvature at point O. A Gaussian white noise η(x,y,t) has to be incorporated to take account of the stochastic arrival of ions on the surface. Thus by expanding Eqn-1.50, we obtain a anisotropic noisy K-S equation.

$$\partial_t(h) = -v_0 + v_0'\partial_x h + S_x\, \partial_x^2 h + S_y\, \partial_y^2 h + \frac{l_x}{2}(\partial_x h)^2 + \frac{l_y}{2}(\partial_y h)^2 - D \bigtriangledown^4 h + \eta(x,y,t) \tag{1.51}$$

The coefficients l_x and l_y depend on the ion beam parameters and energy distribution parameters a, σ and μ. Unlike linear model, Eqn-1.51 is not possible to be solved analytically [85]. It has been shown that for very small irradiation time, the effect of non linear contribution is negligible and hence surface evolution can be well described by linear stability mechanism [85]. However, after a cross over time, which depends on the coefficients of Eqn-1.51, the morphological evolution is completely dominated by non linear terms. The cross over time τ can be written as

$$\tau \backsimeq \frac{D}{S_{max}^2} ln\left(\frac{S_{max}}{l_{max}}\right) \tag{1.52}$$

l_{max} will be along the direction of S_{max} for crossover time τ. The amplitude during crossover time can be proportional to the ratio $\frac{S_{max}}{l_{max}}$ [85]. Depending on the sign of l_x and l_y, two cases may be distinguished. For $l_x \times l_y > 0$, the non linear term destroys the ripple morphology and leads to kinetic roughening. In case of $l_x \times l_y < 0$, ripple pattern formation is followed by a long transient rough regime which ends in the new morphology due to rotation of ripple wave vectors. The ripple wavelength and orientation are also correctly described by the linear theory. Beyond the crossover time the non linear terms become effective and surface width saturates [85].

1.5 Scaling Theory

The formation of surfaces and interfaces due to ion irradiation is influenced by competition between roughening, diffusion and material transport [86]. Scaling theory presents a unique framework to characterize the non-equilibrium pattern formation [87–89]. In many cases, the surface morphology is found to exhibit spatial and temporal fluctuations which obey scaling laws similar to that of several others non-equilibrium critical phenomenon [87–89]. As in the case of these phenomenon, scaling exponents can be determined which characterize the fluctuations of the surface and do not depend upon the microscopic details of the system under investigation. Based on these scaling exponents, a particular growing surface can be assigned to a certain universality class and, therefore, to a certain continuum model which can describe the evolution of the system. Consider a two dimensional surface which is characterized by the height function $h(i, j)$. To describe the growth qualitatively we introduce following functions

- The mean height of the surface, $\overline{h}$, can be defined as

$$\overline{h}(t) = \frac{1}{L^2}\Sigma[h(i,j,t)] \tag{1.53}$$

where $h(i,j)$ is the height of each column *i* for a fixed row *j*, at time *t* and $i \neq j$. If the erosion rate is uniform, the mean height increases linearly with time.

$$\overline{h}(t) \sim t \tag{1.54}$$

- The interface width provides the information about the surface roughness and is defined by rms fluctuations in the height :

$$\sigma(L,t) = \sqrt{\frac{1}{L^2}\Sigma[h(i,j,t) - \overline{h}(t)]^2} \tag{1.55}$$

The width of the interface can be evaluated as a function of time to monitor the roughening process. Generally for measuring surface roughness over the whole sample size $L \times L$, one chooses a window size of $l \times l$ where, $l < L$ and measures the local width σ(l). A typical plot, as shown in fig. 1.8, of time evolution of the surface width has two regions separated by crossover time t_x.

(a) Initially the width increase as a power of time [88].

$$\sigma(L,t) \sim t^{\beta}[t \ll t_x] \tag{1.56}$$

The exponent β is termed as growth exponent which characterizes the time dependent dynamics of roughening process.

(b) The power law increases and gets saturated for $t \gg t_x$. As L increases, the saturation width σ_{sat}, increases as well, and the dependence also follows the power law

$$\sigma_{sat}(L) \sim L^{\alpha} \tag{1.57}$$

The exponent α is termed as roughness exponent and is a second critical exponent that characterizes the roughness of the saturated interface.

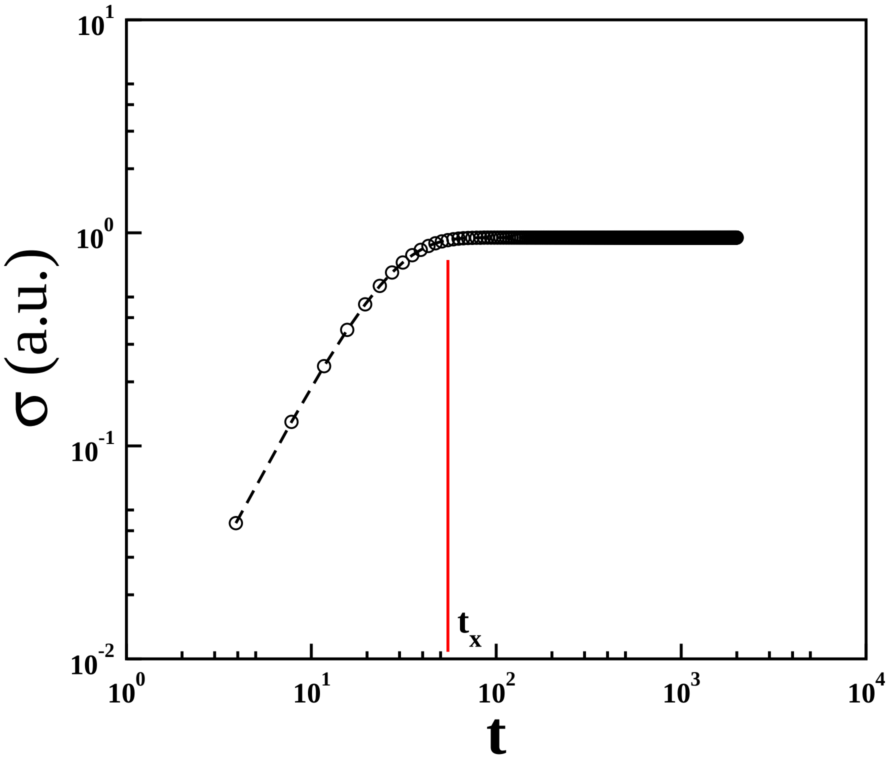

Figure 1.8: Variation in rms roughness with ion fluence

(c) The crossover time t_x at which the interface crosses over from the behavior of Eqn-1.56 to Eq-1.57, depends upon the system size.

$$t_x \sim L^z \tag{1.58}$$

where z is called the dynamic exponent.

Thus the exponents α, β and z describe the universality class of the surface evolution of surfaces and are independent of the many microscopic details of the system [87–90]. The ion beam irradiated surfaces, in general display rough interfaces, with height fluctuations displaying kinetic roughening behavior similar to those observed during film growth [87]. All the interfaces have a common frame work defined by non equilibrium growth models [88]. Dynamical scaling models, discussed above have been utilized to investigate the ion beam irradiated systems [89]. The beauty and importance of scaling theories lies in the fact that though the phenomenon producing the interfaces may be widely different, e.g, fronts created by fire, film grown by MBE, wave pattern on sand dune etc., but their underlying formation can be described by theories which belong to a few specific “classes” only and do not depend on the microscopic details of the system. In this thesis, pattern formation, after ion beam irradiation, have been investigated in detail both on TiO_2 and Ta surfaces using scaling studies. Although TiO_2 is a semiconductor and Tantalum is metallic, yet both the surfaces display self affine scaling with the widths of the interface following the relation Eqn-1.56 to 1.58. These studies and the derived exponents have been utilized in determining the general ”classes” to which these patterned surfaces belong.

1.6 Photo absorption Response

In a semiconductor, excitation of electrons from the valence band to conduction band is accomplished by absorption of photon of energy equal to or higher than the band gap of semiconductor. This light induced generation of electron hole pair is a prerequisite step in all semiconductor mediated photo catalytic processes. Photo generated species tend to recombine and dissipate energy as heat. This is because the kinetic barrier for the electron hole recombination process is low. However, conduction band electrons and valence band holes can be separated efficiently via generation of oxygen vacancies on semiconductor surfaces [6, 7]. These oxygen vacancies play a pivotal role by becoming the potential centers for the capture of photo induced electrons which effectively inhibit the recombination of photo induced charge carriers hence, promoting photo catalysis as well as photo absorbance [6, 7]. Photo catalysis can be defined as a process in which light is used to activate a substance, to modify the rate of chemical reaction without being involved itself in the chemical transformation. Photo catalytic reactions may occur homogeneously or heterogeneously, but heterogeneous photo catalysts have been far more intensively studied in recent years because of their potential use in a variety of environmental and energy related applications [57, 58]. Heterogeneous photo catalysis is mainly used in cases where a light absorbing semiconductor photo catalyst is utilized, which in contact with either liquid or gas, performs a photo catalytic activity.

Nanostructured metal oxide semiconductors have shown potential applications in the field of photo voltaics and photo catalysis [91]. TiO_2, a part of this family, has also been extensively studied for its unique physical and chemical properties which have useful applications in photo catalysis, solar cells, gas sensors, environmental remediation and self cleaning. However, due to its wide band gap, it has been nearly ineffective for visible light photo catalysis. Thus tuning the optical property of TiO_2 is an active area of research. Numerous techniques such as dye sensitization, synthesis as thin films, formation of nano crystals, incorporation of dopants by chemical methods have been employed to increase the visible light absorption. In this direction, several dopnats like N [92], C [93], S [91], Ni [94], Pt [95], Cu [96], Ag [97], etc., have been used in TiO_2 thin films to shift the optical absorption of TiO_2 towards visible wavelength.

1.7 Magnetic Behavior

Dilute magnetic semiconductors are a class of magnetic semiconductors in which a fraction of the cations are substitutionally replaced by magnetic ions. The search for novel DMS candidates has been driven by two major requirements : a material system with well developed growth technology and a high curie temperature. Therefore, with focus for achieving high curie temperature, several compounds have been investigated. At initial stage, the work was mainly concentrated on transition metal doped Group II-VI compound semiconductors whereas later it was also on group III-V etc. [98–107]. Ferromagnetism is observed but curie temperature lies way below the room temperature which shows only limited technological applications [103]. The theoretical prediction by Deith et.al [104] with possibility of achieving high curie temperature ferromagnetism in wide band gap semiconductors has led to many efforts to prepare oxide based DMS by doping a variety of transition metal or rare earth ions. Several experimental reports on ZnO doped with Ni [108, 109], V [110], Mn [109, 111, 112], Cr [109], Fe [113] and also Co [109, 114], discuss the existence of room temperature ferromagnetism. Since the discovery of room temperature ferromagnetism in Co doped TiO_2 thin films [115], much effort has been devoted to explain the mechanism behind the nature of ferromagnetism. In fact, different controversial magnetic properties such as paramagnetism, ferromagnetism, anti ferromagnetism, superparamagnetism and also spin glass behavior have been observed [116–119]. Several mechanisms have been proposed to explain the source of magnetism in these materials but a unique model is still not available for understanding and explaining the theoretical and experimental observations.

Magnetic properties of TM-doped oxides are found to largely depend on the sample preparation conditions and, thus, the reproducibility of measurements becomes very difficult. There are reports which initially reported room temperature ferromagnetism but later, only paramagnetism due to substituted transition metal ions by x-ray magnetic circular dichroism (XMCD) studies [120, 121]. This indicates that transition metal 3d electrons may not be responsible for the origin of ferromagnetism in such oxides. In most of the cases, small amount of TM impurity as secondary phases or defects may lead to the origin of observed ferromagnetism [122]. Therefore, in order to overcome the existing controversies on oxide DMS, a systematic study accompanied by careful identification of the phases and micro structures is very essential.

1.8 Kinetic Monte Carlo Simulation

Theoretically pattern formation via ion beam irradiation has been studied using atomistic simulations, kinetic theory, kinetic monte carlo, continuum theory, etc., at various time, energy and length scales. In Kinetic Monte Carlo (KMC), one uses a simple functional form of the average energy deposited by a collision cascade for single ion impact to determine the erosion probability of surface atoms. Diffusion process can be added easily in this approach. In KMC approach, surface evolution can be modeled by first assigning rates to different processes like erosion, surface diffusion due to defects and then executing these events on the surface with a probability proportional to their relative rates. The surface is modeled as a 1-d lattice and uses a Solid on Solid (SOS) model [123] so that there is only one surface site associated with each lattice site (no overhangs are allowed). The surface processes that are generally included are based on the physical mechanisms that have been previously proposed in the continuum theory of ripple formation, i.e., ion induced sputtering and surface diffusion of surface defects [38, 83]. Several groups have modeled the ion sputtered surface via KMC approach which are based on the results form the kinetic theory of roughening by taking erosion and surface relaxation processes [83, 84, 124–126]. In the following, we describe some details of the model that was developed by Cuerno et.al [84], and has been modified in the present thesis to include Schwoebel barrier effects in order to tailor the morphology and other scaling properties of metallic Tantalum after ion beam irradiation.

Consider a system of 1 dimensional lattice of length L, with a periodic boundary condition. Each lattice point consists of a inter valued time dependent height function h(x,t) which is initially flat, i.e. h(x,0)=0. A random site i, is then selected at the interface, where i= 1,...,L. The chosen site is subjected to erode with probability p or diffuse to its nearest neighboring sites with probability 1-p. The details of erosion and diffusion trials is as follows.

- **Erosion** : The rule for erosion incorporates the unstable behavior due to higher rate of protrusion of trough than crests. This also considers the phenomenological dependence of sputtering yield Y on the angle of incident ion beam *wrt.* the local surface normal. The particle at i is eroded with probability $P_e Y_i$ [84]. The quantity P_e is computed as $\frac{1}{7}$ times the number of occupied sites in a box of size 3×3 centered at the chosen site. The definition of P_e accounts for the unstable erosion mechanism which exists in the physical systems due to the finite penetration depth of the bombarding ions into the eroded substrate [79, 83]. The efficiency of the sputtering process is measured by the following sputtering yield [77].

  $$Y_i = Y(\phi_i) = y_0 + y_1\phi_i^2 + y_2\phi_i^4 \tag{1.59}$$

  where, the local slope ϕ_i is

  $$\phi_i = tan^{-1}\left[\frac{h_{i+1} - h_{i-1}}{2\ a}\right] \tag{1.60}$$

  where a is the lattice constant. The parameters y_0, y_1, y_2 can be chosen such that $y_i(0) = 0.5$ and $y_i(\frac{\pi}{2}) = 0$. In general, one would merely require that $y_0 > 0, y_1 > 0, y_2 < 0$.

- **Surface Diffusion** : For surface diffusion we have used a thermal diffusion model which is based on Hamiltonian H, which controls the thermal roughening of the facets [87, 88, 123]. A diffusive move of particle i, to its nearest neighbor is accepted with probability $(p_{i \longrightarrow f})$

  $$P(i \longrightarrow f) = \frac{1}{\left[1 + exp\left(\frac{\Delta H}{K_B\ T}\right)\right]} \tag{1.61}$$

where ΔH is the change in the Hamiltonian due to hopping. The following Hamiltonian has been utilized to study the diffusion phenomenon [123] in an MBE system. The non- linearity term (second term) was included to incorporate diffusion related to Schwoebel barrier.

$$H = \frac{J}{2} \sum_{\langle i,j \rangle} |h_i - h_j|^2 + \epsilon |h_i - h_j|^4. \tag{1.62}$$

Here $0 < \epsilon < 1$ is a non linearity parameter which controls the intensity of Schwoebel effect.

This thesis has been collocated as follows. A brief discussion about ion-solid interaction, characteristics and application of keV ion implantation in semiconductors etc. have been discussed in Chapter 1. Chapter 2 discusses the different experimental techniques that have been employed in present thesis. Chapter 3 discusses with the effect of Cobalt ion implantation on the surface evolution, structural modification, electronic properties and optical properties of rutile TiO_2 (110). Magnetic properties of TiO_2 after cobalt implantation have been investigated in Chapter 4. Chapter 5 presents the range parameters and damage distribution, investigated using RBS/C, in rutile TiO_2 due to 200 keV Co implantation. In Chapter 6, scaling behavior of implanted TiO_2 surfaces has been investigated to extract several scaling exponents which can provide insightful description regarding pattern formation. We have also developed a KMC simulation model to investigate the mechanism behind pattern formation on metallic Tantalum surfaces, and has been discussed in Chapter 7. The summary and the conclusion of the present work have been described in Chapter 8.

Bibliography

[1] A. D. Maynard, R. J. Aitken, T. Butz, V. Colvin, K. Donaldson, G. Oberdorster, M. A. Philbert, J. Ryan, A. Seaton, V. Stone, S. S. Tinkle, L. Tran, N. J. Walker, and D. Warheit, Nature **444**, 267 (2006).

[2] D. Caruntu, G. Caruntu, and C. J. OConnor, J. Phys. D: Appl. Phys. **40**, 5801 (2007).

[3] G. M. Whitesides, and B. Grzybowski, Science **295**, 2418 (2002).

[4] K. K. Nanda, and S. N. Sahu, Appl. Phys. Lett. **79**, 2743 (2001).

[5] F. Frost, A. Schindler, and F. Bigl, Phys. Rev. Lett. **85**, 4116 (2000).

[6] S. Majumder, D. Paramanik, V. Solanki, B. P. Bag, and S. Varma, Appl. Phys. Lett. **98**, 053105 (2011).

[7] V. Solanki, S. Majumder, I. Mishra, P. Dash, C. Singh, D. Kanjilal, and S. Varma, J. Appl. Phys. **115**, 124306 (2014).

[8] D. J. Eichelsdoerfer, X. Liao, M. D. Cabezas, W. Morris, B. Radha, K. A. Brown, L. R. Giam, A. B. Braunschweig, and C. A. Mirkin, Nature **8**, 2548 (2013).

[9] J. Saghaei, A. Fallahzadeh, and T. Saghaei, Sensors and Actuators A: Physical **247**, 150 (2016).

[10] A. Fujishima, and K. Honda, Nature **238**, 37 (1972).

[11] Y. Matsumoto, M. Murakami, T. Shono, T. Hasegawa, T. Fukumura, M. Kawasaki, P. Ahmet, T. Chikyow, S. Koshihara, and H. Koinuma, Science **291**, 854 (2001).

[12] Z. L. Wang, J. Phys.: Cond. Mat. **16**, R829 (2004).

[13] P. V. Kamat, R. Huehn, and R. Nicolaescu, J. Phys. Chem. B **106**, 788794 (2002).

[14] K. Jung, J. Choi, Y. Kim, H. Im, S. Seo, R. Jung, D. Kim, J. S. Kim, B. H. Park, and J. P. Hong, J. Appl. Phys. **103**, 034504 (2008).

[15] F. Nardi, D. Deleruyelle, S. Spiga, C. Muller, B. Bouteille, and D. Ielmini, J. Appl. Phys. **112**, 064310 (2012).

[16] D. S. Jeong, R. Thomas, R. S. Katiyar, J. F. Scott, H. Kohlstedt, A. Petraru, and C. S. Hwang, Rep. Prog. in Phys. **75**, 076502 (2012).

[17] X. Chen, and S. S. Mao, Chem. Rev. **107**, 2891 (2007).

[18] D. Li, and H. Haneda, Chemosphere **51**, 129 (2003).

[19] M. Qamar, and M. Muneer, Desalination **249**, 535 (2009).

[20] K. S. Ahn, Y. Yan, S. Shet, K. Jones, T. Deutsch, J. Turner, and M. Al-Jassim, Appl. Phys. Lett. **93**, 163117 (2008).

[21] Q. Yu, and C. Cao, J. Nanosci. Nanotech. **12**, (5):3984 2012.

[22] F. Decker, J. F. Juli, and M. Abramovich, Appl. Phys. Lett. **35**, 397 (1979).

[23] B. Karunagaran, P. Uthirakumar, S.J. Chung, S. Velumani, and E.K. Suh, Materials Characterization **58**, 680 (2007).

[24] Q. Qi, T. Zhang, Q. Yu, R. Wang, Y. Zeng, L. Liu, and H. Yang, Sens. and Actu. B **133**, 638 (2008).

[25] P. Kofstad, J. Electrochem. Soc. 109 (1962) 776.

[26] G.M. Choi, H.L. Tuller, J.S. Haggerty, J. Electrochem. Soc. 136 (1989) 835.

[27] S. Maeng, L. Axe, T.A. Tyson, L. Gladczuk, M. Sosnowski, Corros. Sci. 48 (2006) 2154 ;S. Maeng, L. Axe, T.A. Tyson, L. Gladczuk, M. Sosnowski, Surf. Coat. Technol. 200 (2006) 5717.

[28] S. Kimura, Y. Nishioka, A. Shintani, K. Mukai, J. Electrochem. Soc. 130 (1983) 2414; Y. Nishioka, H. Shnriki, K. Mukai, J. Electrochem. Soc. 134 (1987) 410

[29] D.S. Wuu, C.C. Chan, R.H. Horng, W.C. Lin, S.L. Chiu, Y.Y. Wu, Appl. Sci. Lett. 144145 (1999) 315.

[30] H. Kato, A. Kudo, Catal. Lett. 58 (1999) 153.

[31] D.W. Matson, E.D. McClanahan, J.P. Rice, S.L. Lee, D. Windover, Surf. Coat. Technol. 133134 (2000) 411.

[32] S. Facsko, T. Dekorsy, C. Koerdt, C. Trappe, H. Kurz, A. Vogt, and H.L. Hartnagel, Science **285**, 1551 (1999).

[33] A. Keller, S. Rossbach, S. Facsko, and W. Mller, Nanotechnology **19**, 135303 (2008).

[34] F. Frost, and R. Rauschenbach, Appl. Phys. A **77**, 1 (2003).

[35] R. Gago, L. Vzquez, R. Cuerno, M. Varela, C. Ballesteros, and J. Albella, Nanotechnology **13**, 304 (2002).

[36] B. Ziberi, F. Frost, T. Hoche, and B. Rauschenbach, Vacuum **81**, 155 (2006).

[37] T. Basu, J. R. Mohanty, and T. Som, Appl. Surf. Sci. **258**, 9944 (2012).

[38] R. M. Bradley, and J. M. E. Harper, J. Vac. Sci. Technol. A **6**, 2390 (1988).

[39] A. R. Cubero, R. Gago, F. Palomares, A. Mucklich, M. Vinnichenko, and L. Vazquez, Phys. Rev. B **86**, 085436 (2012).

[40] U. Valbusa, C. Boragno, and F. B.de Mongeot, J. Phys.: Cond. Matt. **14**, 8153 (2002).

[41] V. J. Solanki, Thesis, (2016).

[42] G. Carter, J. Phys. D **34**, R1 (2001), C. Teichert, Appl. Phys. A : Mater. Sci. Process. **76**, 653 (2003).

[43] J. S. Williams, Rep. Prog. Phys. **49**, 491-587 (1986).

[44] M. Chicoine, S. Roorda, L. Cliche, and R. A. Masut, Phys. Rev. B **56**, 1551 (1997).

[45] G. Tempel, N. Schwarz, F. Muller, F. Koch, H. P. Zeindl, and I. Eisele, Thin Solid Films **174**, 171 (1990).

[46] M. Tamura and T. Suzuki, Nucl. Instr. and Meth. B **39**, 318 (1989).

[47] L. C. Feldman, J. W. Mayer, and S. T. Picraux, Material Analysis by Ion Channeling, Academic Press, New York (1982).

[48] M. A. Makeev, R. Cuerno, and A. L. Barabsi, Nucl. Instr. Meth. Phys. Res. B **197**, 185 (2002).

[49] J. F. Ziegler, Handbook of Stopping Cross sections for Energetic Ions in all Elements, Peragmon Press, (1980).

[50] J. F. Ziegler, J. P. Biersack, and U. Littmark, Stopping Range of Ions in Matter, Volume-1, New York, Peragmon Press, (1985).

[51] E. Rutherford, Phil. Mag. **21**, 212 (1911).

[52] K. B. Winterbon, P. Sigmund, J. B. Sanders, K. Dan, Mat. Fys. Medd. Vidensk. **37**, 14 1970.

[53] J. Lindhard, M. Scharff, and H. E. Schoitt, Range Concepts and Heavy Ion Range (notes on atomic collision II) Mat. Fys. Medd. Vidensk. Selsk. **33**, 3 (1963).

[54] L. D. Landau and E. M. Lifshitz, Electrodynamics of Continuous Media, (1960).

[55] H. A. Bethe, Ann. Phys. **5**, 325 (1930).

[56] R. M. Barnett, etal., Phys. Rev. D **54**, 1 (1996).

[57] S. R. Joshi, B. Padmanabhan, A. Chanda, V. K. Malik, N. C. Mishra, D. Kanjilal, and Shikha Varma, Appl. Phys. A. **122**, 713 (2016).

[58] S. R. Joshi, B. Padmanabhan, A. Chanda, I. Mishra, V. K. Malik, N. C. Mishra, D. Kanjilal, and Shikha Varma, App. Sur. Sci., http://dx.doi.org/doi:10.1016/j.apsusc.2016.07.038

[59] G. S. Sandhu, M. Anjum, S. Cherekdjian, B. K. Patnaik, N. R. Parikh, and M. L. Swanson, Nucl. Instr. Meth. Phys. Res. B **59**, 145 (1991).

[60] J. P. Biersack and L. G. Haggmark, Nucl. Instr. Meth. Phys. Res. B **174**, 257 (1980).

[61] W. K. Chu, J. W. Mayer, and M. A. Nicolet, Backscattering Spectrometry, Academic Press, New York, (1978).

[62] S. U. Campisano, W. K. Chu, G. Foti, J. W. Mayer, M. A. Nicolet, and E. Rimini, Ion Beam Handbook for Material Analysis, Academic Press, New York, (1977).

[63] E. Bogh, Can. J. Phys. **46**, 653 (1968).

[64] E. Yagi, A. Koyama, H. Sakairi and R. R. Hasiguti, J. Phys. Soc. Jap. **42**, 939 (1997).

[65] L. C. Feldman and J. W. Rodgers, J. Appl. Phys. **41**, 3776 (1970).

[66] W. T. Geng and K. S. Kim, Phys. Rev. B **68**, 125203 (2003).

[67] P. Sigmund, Nucl. Instr. Meth. Phys. Res. B **27**, 1 (1987).

[68] W.L. Chan, N. Pavenayotin, and E. Chason, Phys. Rev. B **69**, 245413 (2004).

[69] B. Ziberi, F. Frost, Th. Hoche, and B. Rauschenbach, Phys. Rev. B **72**, 235310 (2005).

[70] Z.L. Liau, J.W. Mayer, W.L. Brown, and J.M. Poate, J. Appl. Phys. **49**, 5295 (1978).

[71] H. H. Andersen, and H. L. Bay, J. Appl. Phys. **46**, 2416 (1975).

[72] M. Navez, C. Sella, and D. Chaperot, C. R. Acad. Sci. Paris **254**, 240 (1962).

[73] H. B. Huntington, and G. A. Sullivan, Phys. Rev. Lett. **14**, 177 (1965).

[74] M. Kolmer, A. A. Zebari, M. Goryl, F. B. de Mongeot, F. Zasada, W. Piskorz, P. Pietrzyk, Z. Sojka, F. Krok, and M. Szymonski, Phys. Rev. B **88**, 195427 (2013).

[75] P. Sigmund, Phys. Rev. B **184**, 383 (1969).

[76] P. Sigmund and A. Oliva, Alloy Sputtering at High Fluence : Preferential Sputtering and Competing Effects, (1992).

[77] R. Behrisch, Sputtering by Particle Bombardment, Springer, Heidelberg (1981).

[78] H. Gnaser, Low Energy Ion Irradiation of Solid Surfaces, Springer, Berlin (1999).

[79] P. Sigmund, J. Mat. Sci. **8**, 1545 (1973).

[80] M. A. Makeev and A. L. Barabasi, Appl. Phys. Lett. **71**, 2800 (1997).

[81] S. Habenicht, W. Bolse, K. Reimann, and U. Geyer, Phys. Rev. B **60**, 2200 (1999).

[82] J. Erlebacher, M. J. Aziz, E. Chason, M. B. Sinclair, and J. A. Floro, Phys. Rev. Lett. **82**, 2330 (1999).

[83] R. Cuerno, and A. L. Barabasi, Phys. Rev. Lett. **74**, 4746 (1995).

[84] R. Cuerno, H. A. Makse, S. Tomassone, S. T. Harrington, and H. E. Stanley, Phys. Rev. Lett. **75**, 4464 (1995).

[85] S. Park, B. Kahng, H. Jeong, and A. L. Barabasi, Phys. Rev. Lett. **83**, 3486 (1999).

[86] E. A. Eklund, E. J. Snyder, and W. R. Stanley, Surf. Sci. **285**, 157 (1993).

[87] A. L. Barabasi and H. E. Stanley, Fractal Concepts in Surface Growth, Cambridge University Press, (1995).

[88] F. Family and T. Vicsek, Dynamics of Fractal Surfaces, World Scientific, Singapore, (1991).

[89] P. Meakin, Phys. Rep. **235**, 189 (1993); T. H. Healey, Y. C. Zhang, Phys. Rep. **254**, 215 (1995).

[90] F. Family and T. Vicsek, J. Phys. A **18**, L15 (1985).

[91] R. Yu, Q. Lin, S. F. Leung, and Z. Fan, Nano Energy **1**, 57 (2012).

[92] R. Asahi, T. Morikawa, T. Ohwaki, K. Aoki, and Y. Taga, Science **293**, 269271 (2001).

[93] S. U. M. Khan, M. A. Shahry, and W. B. Ingler Jr., Science **297**, 22432245 (2002).

[94] G. Akpan and B. H. Hameed, Applied Catalysis A. General **375**, 1 (2010).

[95] D. H. Kim, K. S. Lee, Y. S. Kim, Y. C. Chung, S. J. Kim, J. Am. Ceram. Soc. **89**, 515 (2006).

[96] S. Kim, S. J. Hwang, W. Choi, J. Phys. Chem. B **109**, 24260 (2005).

[97] M. S. Lee, S. S. Hong, M. Moheseni, J. Mol. Catal A **242**, 135 (2005).

[98] J. K. Furdyna, J. Appl. Phys. **64**, R29 (1988).

[99] D. Ferrand et al., Phys. Rev. B **63**, 085201 (2001).

[100] W. Mac et al., Phys. Rev. Lett. **71**, 2327 (1993).

[101] W. Mac et al., Proc Intl. Conf.on Phys. Semicond. (Vancouver 1994); ed. D. J. Lockwood, 2573 (World Scientific, 1995).

[102] L. Zhao, B. Zhang, and Q. Pang et al., Appl. Phys. Lett. **89**, 092111 (2006).

[103] H. Ohno, Science **281**, 951 (1998).

[104] T. Dietl, H. Ohno, F. Matsukura, J. Cibert, and D. Ferrand, Science **287**, 1019 (2000).

[105] T. Story, P. J. T. Eggenkamp, C. H. W. Swuste et al., Phys. Rev. B **45**, 1660 (1992);

[106] T. Story, P. J. T. Eggenkamp, C. H. W. Swuste, et al., Phys. Rev. B **47**, 227 (1993).

[107] W. J. M. de Jonge, T. Story, H. J. M. Swagten, et al., Europhys. lett. **17**, 631 (1992).

[108] T. Wakano, N. Fujimura, Y. Morinaga et al., Physica E **10**, 260 (2001).

[109] K. Ueda, H. Tabata and T. Kawai, Appl. Phys. Lett. **79**, 988 (2001).

[110] H. Saeki, H. Tabata, and T. Kawai, Solid State Commun. **120**, 439 (2001).

[111] T. Fukumura, Z. Jin, A. Ohtomo, and H. Koinuma, Appl. Phys. Lett. **75**, 3366 (1999).

[112] X. M. Cheng and C. L. J. Chien, Appl. Phys. **93**, 7876 (2003).

[113] S. J. Han, J. W. Song, C. H. Yang, S. H. Park, et al., Appl. Phys. Lett. **81**, 4212 (2002).

[114] W. Prellier, A. Fouchet, B. Mercey, et al., Appl. Phys. Lett. **82**, 3490 (2003).

[115] Y. Matsumoto, M. Murakami, T. Shono, T. Hasegawa, T. Fukumura, M. Kawasaki, P. Ahmet, T. Chikyow, S. Y. Koshihara, and H. Koinuma, Science **291**, 854 (2001).

[116] A. P. Guimaraes, Principles of Nanomagnetism, Springer-Verlag, Berlin, (2009).

[117] T. Kaneyoshi, J. Phys. Cond. Mat. **3**, 25 (1991).

[118] C. P. Bean and J. D. Livingston Jour. Appl. Phys **30**, 120 (1959).

[119] K. Binder and A. P. Young Rev. Mod. Phys. **58**, 801 (1986).

[120] A. Barla, G. Schmerber, E. Beaurepaire, et al., Phys. Rev. B **76**, 125201 (2007).

[121] M. Gacic, G. Jakob, C. Herbort, H. Adrian et at., Phys. Rev. B **75**, 205206 (2007).

[122] T. C. Kaspar, S. M. Heald, C. M. Wang, et al., Phys. Rev. Lett. **95**, 217203 (2005).

[123] M. Siegert and M. Plishke, Phys. Rev E, **50**, 917 (1994).

[124] E. Chason, W. L. Chan, and M. Bharathi Phys. Rev B, **74**, 224103 (2006).

[125] A. K. Hartmann, R. Kree, R. Geyer, and M. Kolbel, Phys. Rev. B **65**, 193403 (2002).

[126] E. O. Yewande, A. K. Hartmann, and R. Kree, Phys. Rev. B **73**, 115434 (2006).

Chapter 2

Experimental Techniques

This chapter discusses the experimental techniques that have been used here to fabricate nanostructures as well as the facilities that have been used in their characterization. TiO_2 is a wide band gap (3.0 eV for Rutile and 3.2 eV for Anatase), n- type metal oxide semiconductor. Tantalum is a rare, hard, lustrous transition metal that is highly corrosion resistant. Formation of nanostructures on these surfaces display many exciting properties which can have numerous technological applications. The nanostructures, in this work, were prepared using ion beam irradiation technique. Several characterization techniques like Scanning Probe Microscopy, X-ray Photo electron Spectroscopy (XPS), UV-Vis Spectroscopy (UV-Vis), Raman Spectroscopy, Superconducting Quantum Interference Device (SQUID), Rutherford Back scattering Spectrometry (RBS), Channeling, X-ray Diffraction (XRD), etc., have been used for TiO_2. For Tantalum, Kinetic Monte Carlo (KMC) simulations have been performed to study the dominant mechanism for evolution of the surfaces upon ion irradiation. In this chapter, we discuss the experimental techniques that have been used to develop and characterize nanostructures on both the surfaces.

In Section 2.1, we discuss about the technique of ion irradiation that has been used here to develop nanostructures on surfaces. In Section 2.2, several characterization techniques have been discussed in detail. In Section 2.3, crystal structures of TiO_2 and Ta have been discussed.

2.1 Techniques for Fabrication of Nanostructures

Variety of techniques have been utilized for fabricating low dimensional structures through top down or bottom up approaches. These nanostructures show tremendous technological applications in solar cells, photo catalysis, photo voltaic, etc. Bottom up approach such as electrochemical process, continuous reaction, sol gel method, etc. have been extensively used to produce low dimensional materials. These methods are however limited due to various complicated steps involved during nanostructures fabrication. Though defects are present in these nanostructures, yet these methods provide no control over introducing defects. Ion irradiation is a widely used technique to introduce dopants in a very controlled manner. This is a top down approach which creates self organized nanostructures on various surfaces in a single technological step. In this thesis, the technique of ion irradiation has been utilized to fabricate nanostructures.

2.1.1 200 keV Co Ion Implantation

In the present thesis TiO_2 nanostructures have been fabricated at Room temperature using Negative Ion Implanter at Inter University Accelerator Center (IUAC), New Delhi. In the following, some beam line components are discussed.

Fig. 2.1 displays the schematic diagram of negative ion implanter facility with a new modified MC-SNICS ion Source at IUAC, New Delhi. This facility contains a sputter negative ion source called MC-SNICS (multi cathode source of negative ion by Cesium sputtering). These negative ions can be accelerated to required kinetic energy with applied voltage difference between the high voltage deck and the ground. Electrostatic Quadrupole Triplets and Electrostatic Steerers are the most vital parts of ion implanter. The former is used for focusing charged particles beam by using either a magnetic or electrostatic field while the later contains two orthogonal pairs of longitudinally separated plates for accurate, low power electrostatic steering of charged particle beams. These also accommodate Faraday cups for variety of applications involving the accurate monitoring of ion beam currents, beam profile monitors which provide a continuous scope display of the shape and position of the beam cross section in both x and y co-ordinates. Various controllers,

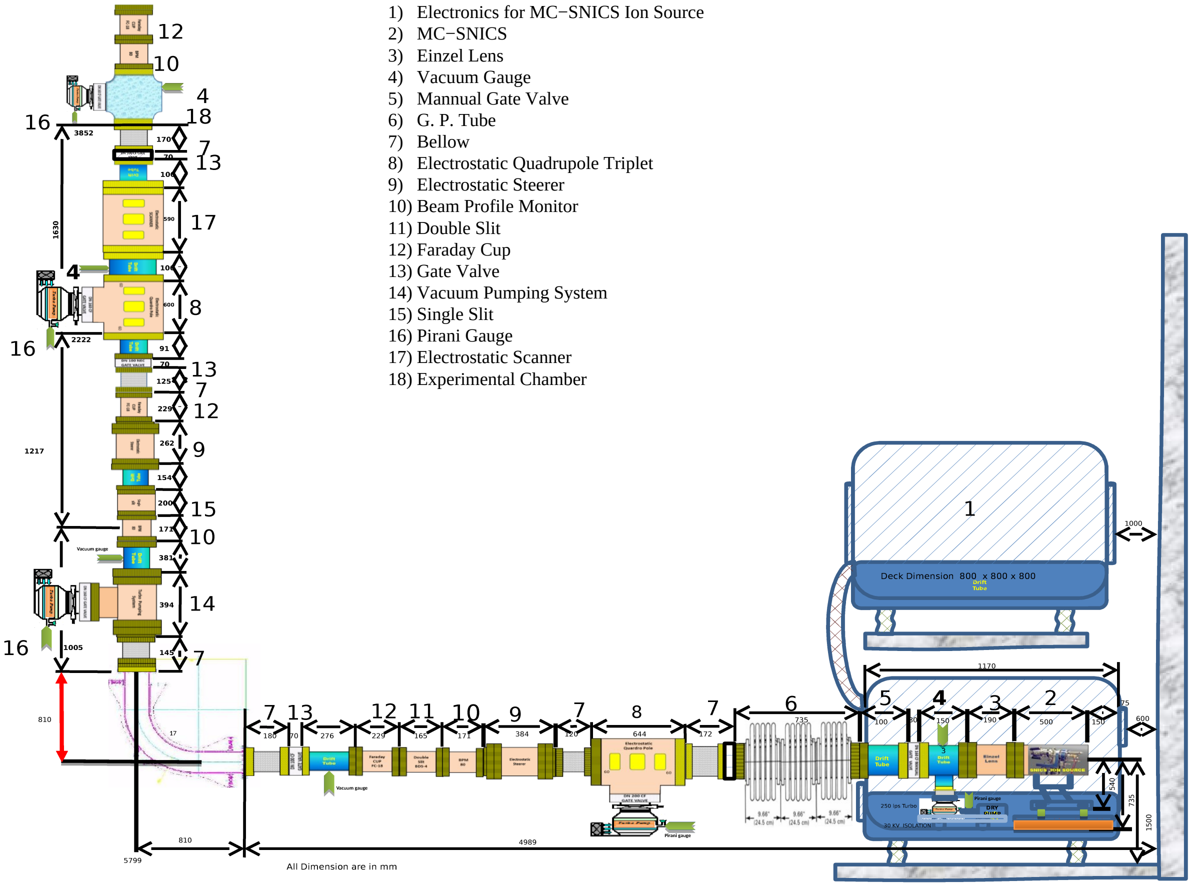

Figure 2.1: Schematic diagram of negative ion implanter facility at IUAC, New Delhi. [with permission]

such as Faraday cup controllers, Beam Line Valve (BLV) controllers, Mixer stage for electrostatic Quadrupole triplets and electrostatic steerers were also a part of this system to achieve a well collimated beam on the sample surface. The control system used for its operation is indigenously developed and named as Indigenous Measurement And Control System (IMACS).

The Negative ion implantation facility, shown in fig. 2.2, has been utilized for implantation on single crystal rutile TiO_2 with 200 keV Co^- ions (flux = 1.6×10^{13} ions/cm^2.sec). Irradiations were done for various ion fluences ranging from 1×10^{16} to 1×10^{17} $ions/cm^2$ at room temperature.

Figure 2.2: Negative Ion Implantation facility at IUAC, New Delhi. [with permission]

2.1.2 3 keV Ar Ion Beam Irradiation

Low energy ion beam irradiation has been performed using Argon ion gun facility in our laboratory. The Ar^+ ion gun is a variable energy source with a maximum energy of 3 keV. High purity Argon gas (99.99%) is introduced into the source region of the gun through an auxiliary gas inlet. A source current is run through a refractory oxide filament to produce electrons for impact ionization of the neutral gas. The source region is connected through a tube to achieve better vacuum. The ions are extracted from the source using electrostatic lenses to focus the beam on the target.

In this work, Tantalum foils were irradiated with Ar^+ ions at 3 keV energy. Irradiation was performed at room temperature and the incident angle was kept at 15° with respect to surface normal. The flux of the ion gun was 6×10^{13} $ions/cm^2sec$. The Tantalum surface were irradiated for 80 minutes to obtain well resolved quasi periodic ripple patterns. During the experiment the beam current was kept at 20μA and was scanned over a circular area of 1.0 cm diameter on the sample surface. The base pressure in the system is maintained at 1×10^{-8} mbar and during ion irradiation it is 4×10^{-6} mbar.

2.2 Characterization Techniques :

2.2.1 X-ray Photoelectron Spectroscopy (XPS)

X-ray Photoelectron Spectroscopy (XPS) is a powerful research tool for the study of chemical and physical phenomenon occurring at the surfaces of a wide range of materials. It was developed by Kai Siegban at the University of Uppsala, Sweden in the 1950-60, for which he was awarded Nobel prize in 1981 [1,2]. It works on the principle of photoelectric effect [3] in which soft X-rays (Mg and Al K x-ray) are used as the exciting photon source. The schematic diagram of XPS process is shown in fig 2.3. The emitted photo electrons have a kinetic energy distribution consisting of discrete peaks related to the binding energies of the photo ionized atom and provide information on the electronic structure of the surface and its chemical composition.

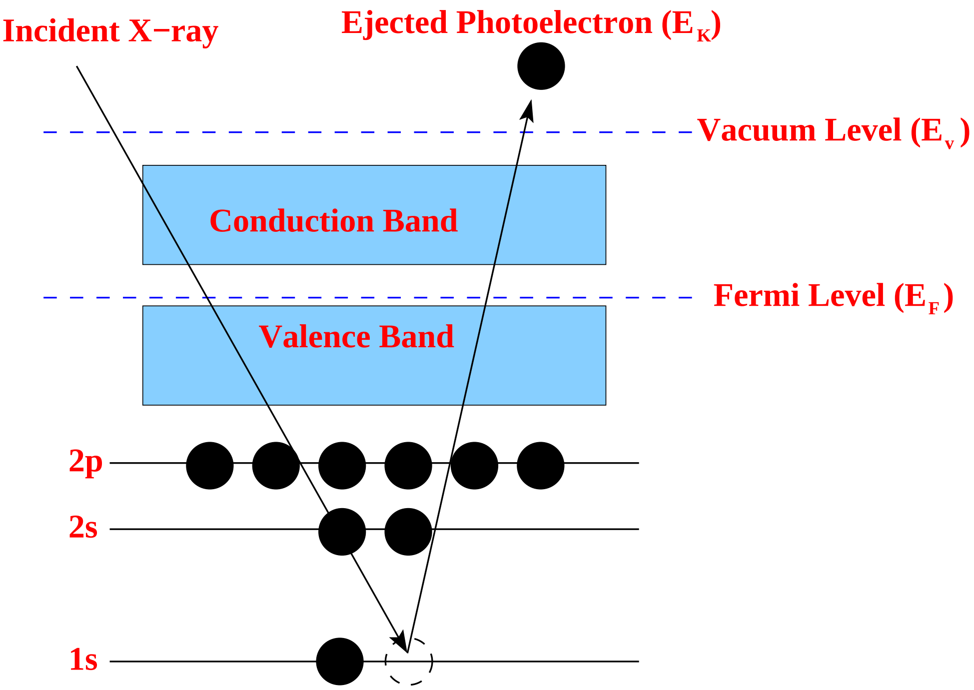

Figure 2.3: Block diagram of core level X-ray photo electron emission process.

Principle of XPS

The principle of the XPS technique is the emission of electrons from atoms by absorption of photons. The sample under investigation is irradiated with mono energetic x-rays, using Mg-K_α (1253.6 eV) or Al-K_α (1486.6 eV). Photoelectron emission occurs when a photon transfers its energy to an electron. A photo electron can be emitted only when the photon energy is larger than the binding energy of the electron. The X-ray photons whose absorption is very fast ($\sim 10^{-10}$ sec), eject electrons from inner shell orbitals of the atoms of the surface material. The kinetic energy of the emitted photo electron is

$$E_B = h\nu - E_k \tag{2.1}$$

Where, E_k is the kinetic energy of the emitted photo electron while E_B is the binding energy of the inner shell emitted electron. The term hν is the incident photon energy from an X-ray source.

As, the binding energy is dependent on the chemical environment of the atoms, hence XPS is a very useful technique to identify the oxidation states and ligands of an atom. Since, the binding energy of the energy levels are measured *wrt.* the Fermi level of the solid rather than the vacuum level, a small correction to the Einstein's photoelectric equation, i.e., work function of the spectrometer (as shown in fig 2.4) is required. So, Eq-2.1 becomes

$$E_B = h\nu - E_k - \Phi \tag{2.2}$$

where, Φ is the spectrometer's work function. As the energy of the photons and the spectrometer work function are known quantities, the electron binding energies can be obtained by measuring the kinetic energies of the photo electrons.

XPS Spectral Features

XPS is a very surface sensitive analyzing method. This is due to the relatively short inelastic mean free paths of the photo electrons and the Auger electrons. Hence, the transportation of emitted electrons, generated in the solid, to the surface can only occur from a few atomic layers. Using XPS it is possible to detect all elements except for H and He. XPS spectrum shows the number of photo electrons as a function of binding energy. The spectrum will be a superposition of photo

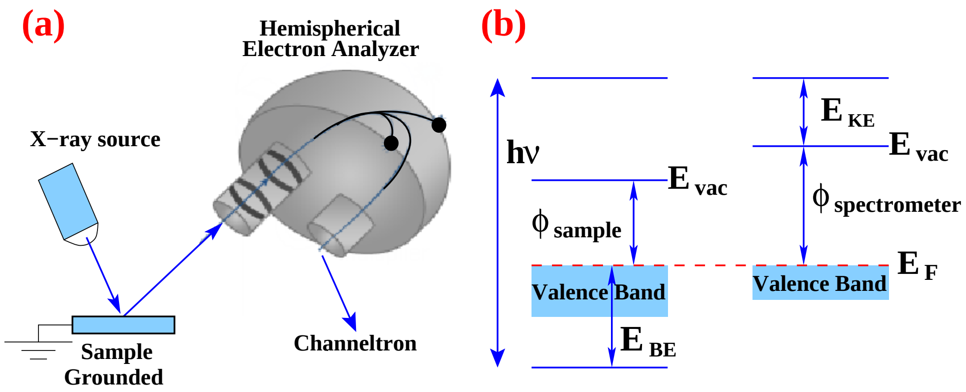

Figure 2.4: (a) Process of the photo electron emission via X-ray-surface interaction and its detection by channeltron, and (b) schematic diagram to evaluate the kinetic energy, E$_K$, of the electron inside the atom.

electron and Auger lines with accompanying satellites, loss peaks and a background due to inelastic scattering in the substrate. Some of the above mentioned features are discussed below.

i). Chemical Shift : The main advantage of using the XPS-technique lies in the fact that the binding energy of a photo electron is sensitive to the chemical surrounding of the atom. Thus a shift in binding energy is generally observed when there is some change in the chemical environment of the material. These shifts are very important since they provide a tool to identify individual chemical states of an element. Unfortunately, it is not always straightforward to interpret these chemical shifts because they depend both on initial and final state effects. In general, the chemical shift increases with increasing positive charge of the element of interest, e.g. the C-1s binding energy is observed to increase monotonically as the number of oxygen atoms bonded to carbon increases $(E_b(C-C) < E_b(C-O) < E_b(C=O) < E_b(O-C=O) < E_b(O-(C=O)-O))$. Thus a proper binding energy correction is extremely crucial for interpreting observed chemical shifts.

ii). Multiplet Splitting : The total angular momentum (**j**) of an electron is found by summing the individual electron orbital (**l**) and spin (**s**) angular momenta, **j=l+s**. For the Au (4f) orbital, the principle quantum number **n** equals 4 and the angular momentum quantum number **l** equals 3. The electron spin quantum number can be +1/2 or -1/2, depending upon whether the spins of the two electrons are parallel or anti parallel. Therefore, **j** can be either 7/2 or 5/2. In this way, the Au (4f) orbital splits as two different energy states $4f_{7/2}$ and $4f_{5/2}$. The separation between the two energy states is about 3.7 eV. In some cases, the separation of the energy states can be so small that the doublet peaks are not resolved if separation energy is less than the binding energy resolution of the system. The intensity of the doublets is determined by the occupation probability of the two different energy states, which can also be expressed as the multiplicity, **M=2j+1**. Therefore the intensity ratio of $4f_{7/2}$ to $4f_{5/2}$ can be calculated as 4/3.

iii). Shake up satellites : Shake up satellites are the extra peaks which result from interaction between photo electron and valance electrons. A photo electron can excite a valence electron to a higher energy level which results in the loss of kinetic energy of photo electrons by a few keV. This will create a peak associated with core level peaks of photo electrons at higher binding energy. For certain transitions and rare earth metals with unpaired electrons in a 3d and 4f shells, the shake up satellite produces strong peaks. Organic materials with aromatic systems also show shake up satellites with intensity approximately 10% of the core level. Thus, shake up transitions are extremely useful for studying aromatic or unsaturated structures or paramagnetic species.

iv). Plasmon Loss : Plasmon loss refers to the energy loss of a photo electron due to the collective vibration of conduction electrons in a metal. These vibrations are characteristics for various elements and cause generation of satellite peaks at higher binding energy with respect to the main peak. Plasmon loss peaks can be seen in XPS spectra of clean metal surfaces.

Quantitative Analysis :

The XPS spectrum of a material contains peaks of various elements present on the surface. The area under these peaks, or the intensities of these peaks, are related to the amount of each element present [4]. So the concentration of each detected element can be determined by measuring the intensity of the peaks. The equation to measure the intensity of peaks is

$$I_{ij} = KT(E)L_{ij}(\gamma)\sigma_{ij} \int_0^d n_i(\mathbf{z})exp(\frac{-\mathbf{z}}{\lambda_{ij}(E)cos\theta})d\mathbf{z} \tag{2.3}$$

where I_{ij} is the area of peak *j* from element *i*, K is an instrumental constant, T(E) is the transmission function of the analyzer, $L_{ij}(\gamma)$ is the angular asymmetry factor for orbital *j* of element *i*, σ_{ij} is the photo ionization cross-section of peak *j* of element *i* , $n_i(\mathbf{z})$ is the concentration of element *i* at a distance **z** below the surface, $\lambda_{ij}(E)$ is the inelastic mean free path length of the photo electron emitted from the orbital *j* of element *i* with a certain kinetic energy, and θ is the take off angle of the photo electrons measured with respect to. the surface normal.

If we assume that the elemental concentrations are homogeneous within the XPS sampling depth (from 0 to d), which means the distance **z** has no effect on the concentration n_i, the Eq-2.3 can be integrated to obtain :

$$I_{ij} = K\ T(E)\ L_{ij}(\gamma)\ \sigma_{ij}\ n_i\ \lambda_{ij}(E)\ cos\theta\ \left[1 - exp\left(\frac{-d}{\lambda_{ij}(E)\ cos\theta}\right)\right] \tag{2.4}$$

XPS measurements are normally performed with a zero degree take off angle, thus cosθ term can be neglected. The XPS sampling depth d is generally $\sim$10 nm, which is usually 3 to 5 times bigger than the λ of most photo electrons with a kinetic energy in the range from 10 to 1000 eV, therefore, the value of exp(-d/λ) is very small and can be neglected. Thus Eq-2.4 can be further simplified as

$$I_{ij} = KT(E)L_{ij}(\gamma)\sigma_{ij}n_i\lambda_{ij}(E) \tag{2.5}$$

Typically, either elemental ratios or atomic percentages are calculated. Thus, it is only necessary to determine the relative relationships, not the absolute values of the quantities as mentioned in Eq-2.5.

The instrumental constant K is assumed not to vary over the time period and under conditions used to acquire the XPS spectra. It cancels when either elemental ratios or atomic percentages are calculated. The angular asymmetry factor $L_{ij}(\gamma)$ accounts for the type of orbital the photo electron is emitted from and γ is the angle between the incident X-rays and the emitted photo electrons. If only **s** orbitals are used for relative quantification, $L_{ij}(\gamma)$ will be the same and therefore cancel.

This makes the calculation much easier, especially for the organic polymeric samples. Even for samples where different types of orbitals are used for quantification, the variation of $L_{ij}(\gamma)$ is very small and is usually neglected. Thus, the atomic percentage can be calculated as [5]

$$\%n_i = 100\left(\frac{n_i}{\Sigma n_i}\right) \tag{2.6}$$

where $\%n_i$ is the atomic percent of element *i*.

Depth Profiling :

While XPS is a surface sensitive technique, a depth profile of the sample in terms of XPS quantities is helpful in compositional analysis. It can be obtained by using either destructive or non destructive technique. Angle Resolved XPS is a method to study the compositional variation in the top few layers of the solid by assuming a possible model of depth profiling using Lambert-Beer's law. By tilting the specimen away or towards the analyzer, the signal can be sensitive to the outermost layers.

Lambert-Beer's law is an empirical relationship between the adsorption of electromagnetic radiation and the properties of the material through which the radiation is traveling. It is usually expressed as follows

$$I_i = I_i^\circ \times exp(-\epsilon cd) \tag{2.7}$$

where I_i is the intensity of the radiation after transmission through the material and I_i° is the intensity of the radiation before the transmission. ϵ is the adsorption constant, c is the concentration, and d is the thickness of the material.

If a thin film is deposited on a substrate, the thickness of the thin film d can be calculated by the attenuation of the signal from the substrate caused by the over layer. In this case, Lambert-Beer's law can also be applied and expressed as

$$I_i = I_i^\circ \times exp[-d/\lambda(E)cos\theta] \tag{2.8}$$

The signal intensity I_i is obtained from the substrate with a thin film deposited on its surface. The signal intensity I_i° is obtained from the substrate without any over layer. d is the thickness of the over layer, $\lambda(E)$ is the inelastic mean free path. To calculate the thickness of the thin film d, Eq-2.8 can be transformed as

$$d = \lambda \times cos\theta \times ln\left(\frac{I_i^\circ}{I_i}\right) \tag{2.9}$$

For the calculation of film thickness, XPS measurements are performed with zero degree take off angle.

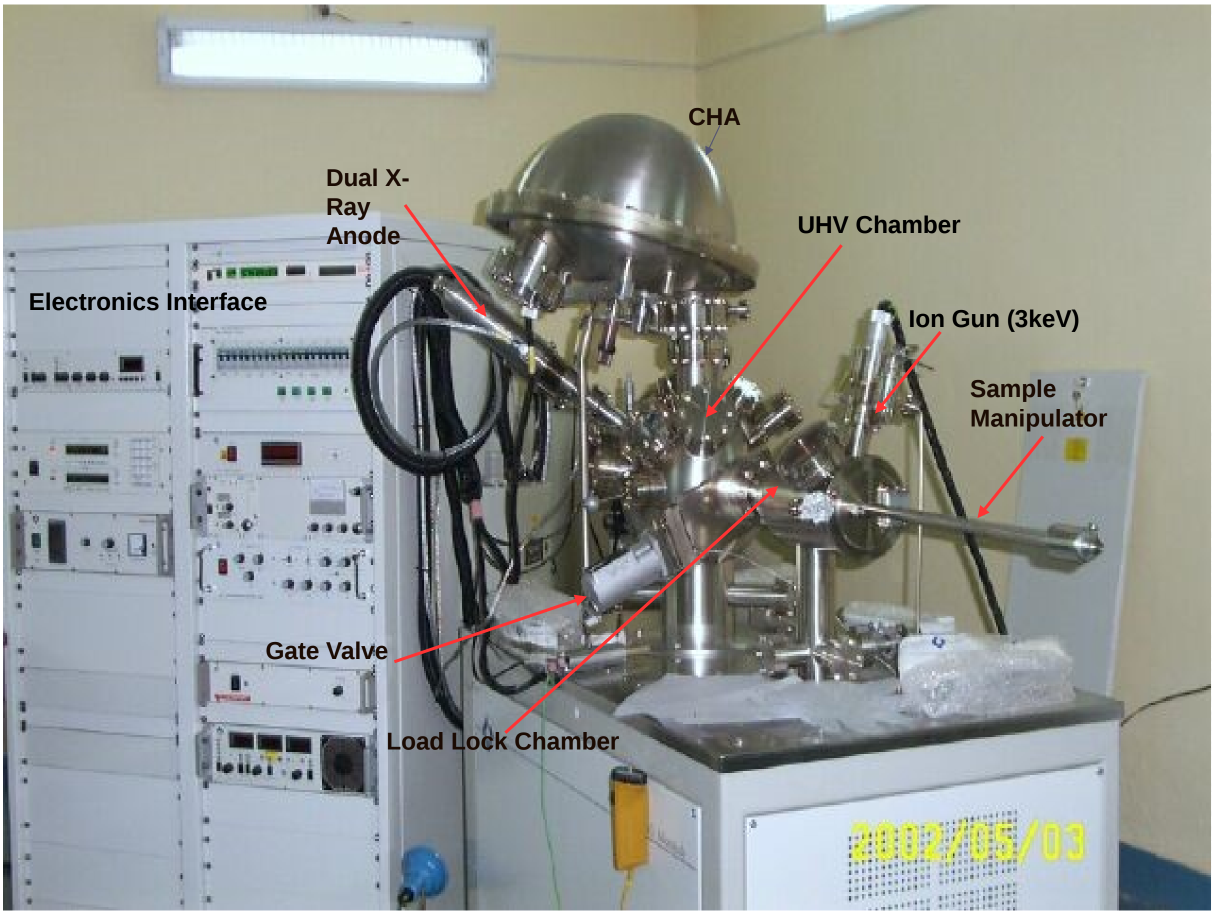

Figure 2.5: XPS system at IOP

In the present thesis, XPS system from VG microteck has been used. The XPS setup is shown in fig. 2.5. This system operates under UHV at base pressure of 1×10^{-11} mbar. The load lock chamber is maintained at a base pressure of 1×10^{-8} mbar and is equipped with an Ar ion gun. For maintaining UHV, system is equipped with an ion pump, turbo molecular pump and rotary pump.

The XPS system consists of a dual anode gun, Mg-K$_\alpha$ (1253.6 eV) and Al-K$_\alpha$ (1486.6 eV), a hemispherical analyzer, and a channeltron unit. For any unknown sample, survey scan from 0-1200 eV (depending upon the x-ray source used) is first acquired by operating the analyzer with pass energy of $\sim$200 eV. High resolution scans with $\sim$20 eV pass energy are obtained for quantitative analysis of XPS spectrum. The resolution of the system is 0.9 eV. Shirley background correction has been used to subtract the background from XPS spectrum. Binding energy referencing have been taken care of using C-1s peak position. For analysis and peak fitting of XPS spectrum, VGX900 software has been used.

2.2.2 Scanning Probe Microscopy

Scanning probe microscopy is one of the powerful modern research technique that allows us to investigate the morphology and the local properties of the solid surface with high spatial resolution. During last 10 years scanning probe microscopy has turned from an exotic technique accessible only to a limited number of research groups, to a widespread research tool for investigating surface properties. Scanning probe microscopy has also formed a basis for the development of new methods in nanotechnology, e.g. the technology of the creation of structures at nanometric scales. The Scanning Tunneling Microscope (STM), was the first member of Scanning probe microscopy family, invented in 1981 by the Swiss scientists Gerd Binning and Heinrich Rohrer [6, 7]. As the tunneling probability was found to be exponentially dependent on the potential barrier width, the experimental observation of tunneling events is measurable only for barriers with small width. In their works they have shown, that this is a quite simple and rather effective way to study a surface with spatial resolution down to single atom. Their technique was fully acknowledged after visualization of the atomic structure of the surface of some materials and, particularly, the reconstructed surface of silicon. In 1986, G.Binning and H.Rohrer were awarded the Nobel Prize for their contribution in physics. STM and may techniques like Atomic Force Microscope (AFM), Magnetic Force Microscope (MFM), Electric Force Microscope (EFM), Scanning Near-field Optical Microscope (SNOM) and many other techniques having similar working principles form the technique of scanning probe microscopy. Now the probe microscopy is a rapidly developing area of technology and applied scientific research.

Working Principle of Scanning Probe Microscope

The analysis of surface structures and their local properties is performed by scanning probe microscopes using specially prepared tips in the form of needles. The size of the working part of such tips (the apex) is less than five nanometers. The usual tip- surface distance in probe microscopes is about 0.1 to 10 nanometers. The interaction of the tip with the surface varies in different types of probe microscopes. For example the tunnel microscope is based on the phenomenon of a tunneling current between a metallic needle and a conducting sample whereas various types of interactive force govern the working mechanism of atomic force, magnetic force and electric force microscopes. We will consider the common features inherent to various probe microscopes. Let the interaction of a tip with a surface be characterized by some parameter P. If there is a sharp enough and unique (single valued) dependence P = P (z) of that parameter on the tip-sample distance, then P can be used in the feedback system (FS) that control the distance between the tip and the sample. A block-diagram of the feedback system in scanning probe microscope is shown in fig 2.6.

The feedback system tries to maintain a constant value of the parameter P (equal to the value Po , set by the operator). During the measurement tip sample distance changes which will change the value of P. The feedback system then tries to amplify the differential signal which goes into the piezo transducer (PT) and try to control the tip sample interaction. Thus it is possible to control the tip- sample distance with high accuracy. In existing probe microscopes the accuracy in the tip- surface distance control reaches the value of $\sim$0.01A°. During tip movement along the sample surface the sample topography induces changes in the interaction parameter P. The feedback system restores the preset value of the tip- sample distance (i.e. of the interaction parameter Po) in real time, so that when the tip is moved to a point x,y over the sample, the signal V(x,y) fed to the transducer is proportional to the local departure of the sample surface from the ideal plane X, Y(z = 0). This makes possible to use the values V(x,y) to map the surface topography, and to obtain an image. During scanning the tip first moves above the sample along a certain line (line scan),

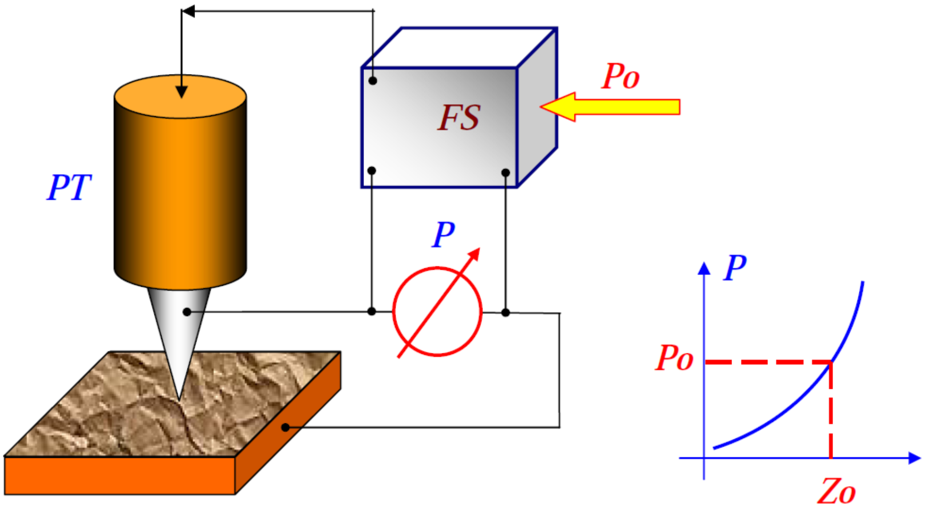

Figure 2.6: Feedback system of Scanning Probe Microscope [8]

thus the value of the signal fed to the transducer, proportional to the height value in the surface topography, is recorded in the computer memory. Then the tip comes back to the initial point and steps to the next scanning line (frame scan), and the process repeats again. The feedback signal recorded during scanning is processed by the computer, and then the surface topographic image Z = f(x,y) is plotted by means of computer graphics. In addition to the investigation of the sample topography, probe microscopes allow to study various properties of a surface: mechanical, electric, magnetic, optical and many others.

Atomic Force Microscope(AFM)

AFM is an amazing technique that allows us to view and measure surface structure with unprecedented resolution and accuracy. Very small images less than 5 nm in size showing only very few individual atoms, can be collected to measure the surface structure of materials. An AFM is rather different from other microscopes, because it does not form an image by focusing light or electrons onto a surface, like an optical or electron microscope. An AFM physically feels the sample surface with a sharp probe, building up a map of the height of the sample surface. This is very different from the imaging microscopes, which measure two dimensional projection of the sample surface. Such a two dimensional object does not have any height information in it. With a traditional microscope, we must infer such information from the image by doing a very complex analysis. Atomic force microscope (AFM) was invented in 1986 by Gerd Binning, Calvin F. Quate and Christopher Herber [9]. The AFM working principle is the measurement of the interactive forces between a tip and the sample surface using special probes made by an elastic cantilever with a sharp tip at the end (as shown in fig 2.6). The force applied to the tip by the surface, results in bending of the cantilever. Measurement of the cantilever deflection allows the evaluation of the tip surface interactive forces. The interactive forces measured by AFM can be qualitatively explained by considering, for example, the Van-der Waals forces [Ref]. The Van-der Waals potential energy of two atoms, located at a distance *r* from each other, is approximated by Lennard-Jones potential :

$$U = U_0\left\{ -2\left(\frac{{r_0}^6}{r}\right) + \left(\frac{{r_0}^{12}}{r}\right)\right\} \tag{2.10}$$

The first term here describes the long-range attraction caused, basically, by a dipole-dipole interaction and the second term takes into account the short range repulsion due to the Pauli exclusion principle. The parameter r_0 signifies the equilibrium position between two atoms where the potential energy is minimum.

AFM Modes

The initial method of AFM imaging relied on the constant force mode where a constant force was applied between the tip and the moving substrate. Though, this method produces quality images, recent investigations have opened up several other modes to produce high resolution images. Some of the modes are described below.

i. Contact mode operation :

Contact mode AFM was the first mode developed for AFM. It is capable of obtaining very high resolution images. It is also the fastest of all the topographic modes, as the deflection of the cantilever leads directly to the topography of the sample, so no summing of oscillation measurements is required which can slow the imaging process. Contact mode AFM always works in repulsive force regime of Force-distance curve (as shown in fig 2.7), i.e, the tip of the probe is always touching the sample. The implication of the probe touching the sample surface are as follows :

- As a result of the repulsive force between the tip and the sample, the sample may be damaged or otherwise changed by scanning process. Conversely, the tip can also get damaged or change by scanning process.
- As the tip and sample are constantly in contact with each other when the tip is moving across the sample, in addition to the normal force they apply to each other, lateral forces are also experienced by both probe and the sample.
- Due to the contact between the tip and the sample, the nature of the sample surface may affect the result obtained. This means that this technique is sensitive to the nature of the sample.

Application of Contact mode AFM :

- The best reason to use contact mode is to obtain high resolution images.
- In case of weakly adsorbed samples, or soft samples, this can lead to sample damage. Because of this it has been suggested that contact mode AFM is not suitable for soft samples.
- Imaging in liquid environment is a strong point of contact mode AFM.
- Contact mode also works well in high speed AFM measurements.

ii. Non-contact mode operation :

One of the great advantages of oscillating modes in AFM is that they can decrease the size of tip sample forces, while maintaining high sensitivity to the sample topography. To achieve non contact AFM, the tip must be close enough to the sample surface to achieve the high sensitivity, without

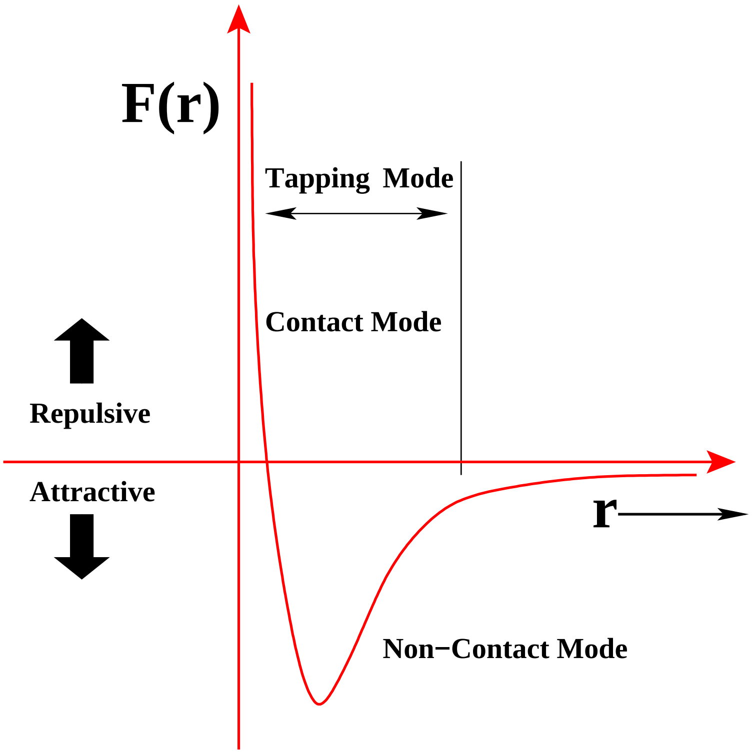

Figure 2.7: Force Displacement curve (F-r) for two atoms

passing into the repulsive regime used for contact mode AFM. Non contact AFM is therefore carried out in attractive regime and in amplitude modulation mode (fig 2.7). The error signal in the non contact mode can be either the amplitude or phase oscillation of the tip. To avoid the possibility of slipping into repulsive regime which will likely damage the tip, a high frequency cantilever is typically used.

Application of Non-Contact mode AFM :

- The best reason to use non contact mode AFM is to do imaging on soft samples. As the tip is not in contact with the sample surface, there will be no change on the sample properties.
- Non-Contact mode also works well in high speed AFM but the image resolution is poor as compared to contact AFM.

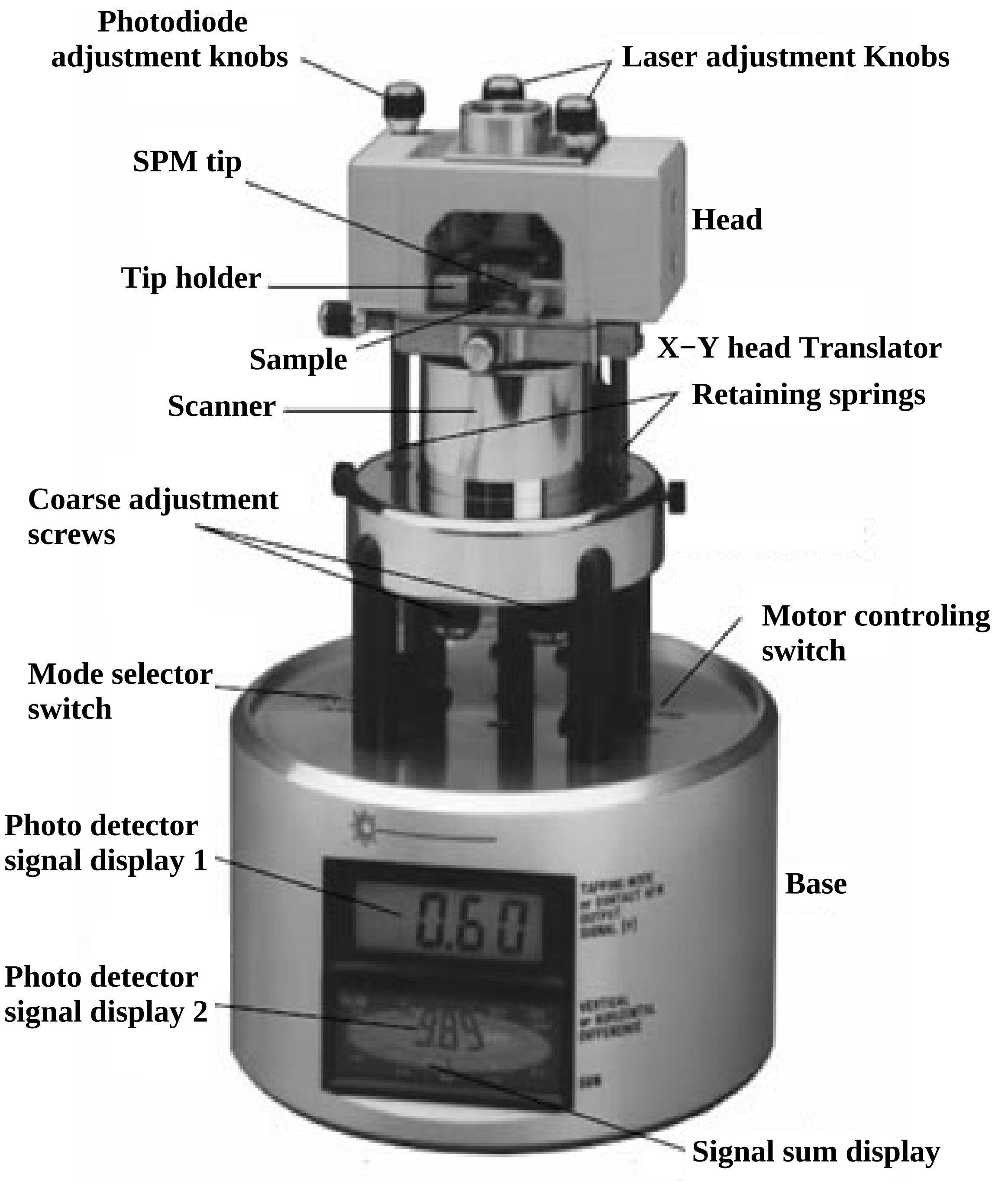

Figure 2.8: AFM system at IOP

iii. Tapping mode operation :

Tapping mode is a key advancement in AFM. This potential technique allows high resolution topographic imaging of sample surfaces that are easily damaged, loosely hold to their substrate, or difficult to image by other AFM techniques. Tapping mode overcomes problems associated with friction, adhesion, electrostatic forces, and other difficulties that conventional AFM scanning methods lags. Tapping mode imaging is implemented in ambient air by oscillating the cantilever assembly at or near the cantilever's resonant frequency using a piezoelectric crystal. The piezo motion causes the cantilever to oscillate with a high amplitude, when the tip is not in contact with the surface. The oscillating tip is then moved toward the surface until it begins to lightly touch, or tap the surface. During scanning, the vertically oscillating tip alternately contacts the surface and lifts off, generally at a frequency of 50,000 to 500,000 cycles per second. As the oscillating cantilever begins to intermittently contact the surface, the cantilever oscillation is necessarily reduced due to energy loss caused by the tip contacting the surface. The reduction in oscillation amplitude is used to identify and measure surface features. During tapping mode operation, the cantilever oscillation amplitude is maintained constant by a feedback loop. Selection of the optimal oscillation frequency is software-assisted and the force on the sample is automatically set and maintained at the lowest possible level. When the tip passes over a bump in the surface, the cantilever has less room to oscillate and the amplitude of oscillation decreases. Conversely, when the tip passes over a depression, the cantilever has more room to oscillate and the amplitude increases (approaching the maximum free air amplitude). The oscillation amplitude of the tip is measured by the detector and input to the AFM electronics. The digital feedback loop then adjusts the tip-sample separation to maintain a constant amplitude and force on the sample. When the tip contacts the surface, the high frequency (50k - 500k Hz) makes the surfaces stiff (viscoelastic), and the tip-sample adhesion forces is greatly reduced. Tapping Mode inherently prevents the tip from sticking to the surface and prevent damage during scanning.

Application of Tapping mode AFM :

- Unlike contact and non-contact modes, when the tip contacts the surface, Tapping mode has sufficient oscillation amplitude to overcome the tip-sample adhesion forces.

- The surface material is not pulled sideways by shear forces since the applied force is always vertical.
- Another advantage of the tapping mode technique is its large, linear operating range. This makes the vertical feedback system highly stable, allowing routine reproducible sample measurements.

In the present work, the morphological evolution of the cobalt implanted rutile TiO_2 surfaces have been investigated using multimode AFM (fig 2.8), with Nanoscope V controllers, from Bruker. All the topographic images have been acquired in tapping mode AFM. Analysis have been carried out using Nanoscope software.

2.2.3 UV-VIS Spectroscopy :

UV-vis spectroscopy is one of the more ubiquitous analytical and characterization technique in science. It measures the attenuation of a beam of light after it passes through a sample or after reflection from the sample surface. These measurements can be at single wavelength or over an extended range. These UV and visible energy photons are energetic enough to promote electrons to higher energy states in molecules and materials. Therefore, UV-Vis spectroscopy is useful for the exploration of the electronic properties of materials and materials precursors in basic research as well as in the development of applied materials. Materials that can be characterized by UV-Vis spectroscopy include semiconductors for electronics, lasers, and detectors; transparent or partially transparent optical components; solid state laser hosts; optical fibers, wave guides, and amplifiers for communications; and materials for solar energy conversion.

When an electromagnetic radiation interacts with matter, diverse processes like scattering, reflection, transmission, etc., can takes place. Interaction of matter with UV-vis radiation provides important information about various properties of materials, especially, the wide band gap materials which exhibit many interesting properties. The total energy possess by a molecule consists of electronic energy, vibrational energy and rotational energy. While interaction with infrared light causes molecules to undergo vibrational transition, high energy radiation in the UV and visible

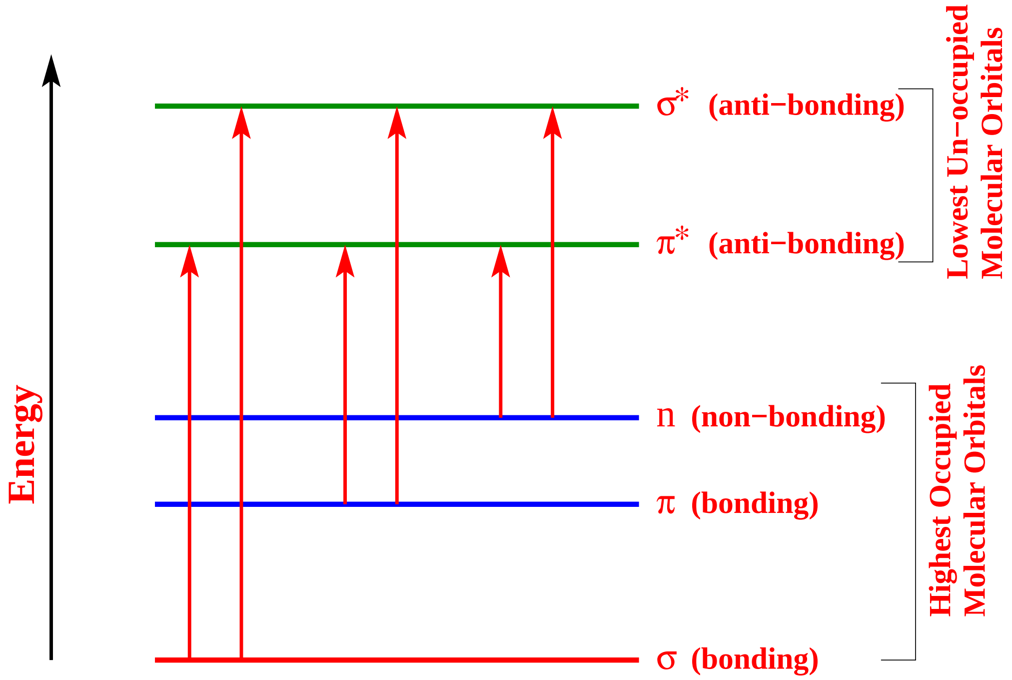

Figure 2.9: Generalized molecular orbital energy level diagram and different possible transitions.

range of the electromagnetic spectrum causes many organic molecules to undergo electronic transition. When the energy from UV or visible light is absorbed by a molecule, electrons from lower energy levels are excited to higher energy levels. The molecular orbital picture for any molecule consists of bonding σ molecular orbital, and a higher energy anti bonding molecular orbital (σ^*). When the molecule is in ground state, both electrons are paired in the lower energy bonding orbitals, which is the Highest Occupied Molecular Orbital (HOMO). The anti bonding σ^* orbital, in turn, is the Lowest Unoccupied Molecular Orbital (LUMO). Different types of allowed transitions, as shown in fig 2.9, can occur between bonding and anti-bonding orbitals :

- σ to σ^* Transition: If the molecule is exposed to light of a wavelength with energy equal to ΔE, the HOMO-LUMO energy gap, the wavelength will be absorbed and the energy used to jump one of the electrons from HOMO to LUMO or in other words, from σ to the σ^* orbital. This is referred to as $\sigma- > \sigma^*$ transition.

- π to π^* Transition: When a double bonded molecule such as ethene absorbs light, it undergoes a $\pi- > \pi$ transition. $\pi- > \pi$ transition energy gaps are narrower than $\sigma- > \sigma$ gaps.

- n to π^* Transition: This is due to the transition of a non-bonding (lone pair electrons) to the π^* anti bonding molecular orbital. The non bonding molecular orbitals are higher in energy than the highest bonding orbitals, so the energy gap for an $n- > \pi^*$ transition and thus the $n- > \pi^*$ peak is at a longer wavelength. In general, $n- > \pi^*$ transition are weaker than these due to $\pi- > \pi^*$ transition.

The UV-Vis spectra helps us to determine the electronic property of the material. There is a linear relationship between absorbance and absorber concentration, which makes this technique extremely attractive for quantitative measurements. This linear relationship is known as the Beer-Lambert Law [10] and allows accurate concentration measurements of absorbing species in a sample. The general Beer-Lambert law is usually written as

$$A = a \times b \times c \tag{2.11}$$

where A is the measured absorbance, a is a wavelength dependent absorptivity constant, b is the path length, and c is the analyte concentration. When concentration is in units of molarity, the Beer-Lambert law can be modified as

$$A = \epsilon \times b \times c \tag{2.12}$$

where, ϵ is the wavelength dependent molar absorptivity coefficient with units of reciprocal molarity per centimeter and *b* has a units of centimeters.

The linear relationship of the Beer-Lambert law depends on several conditions. The incident radiation must be monochromatic and collimated through a sample. Samples, including calibration standards, must be homogeneous without irreproducible losses due to reflection or scattering. For analytes in a matrix, such as a solution or a glass, the absorber concentration must be low enough

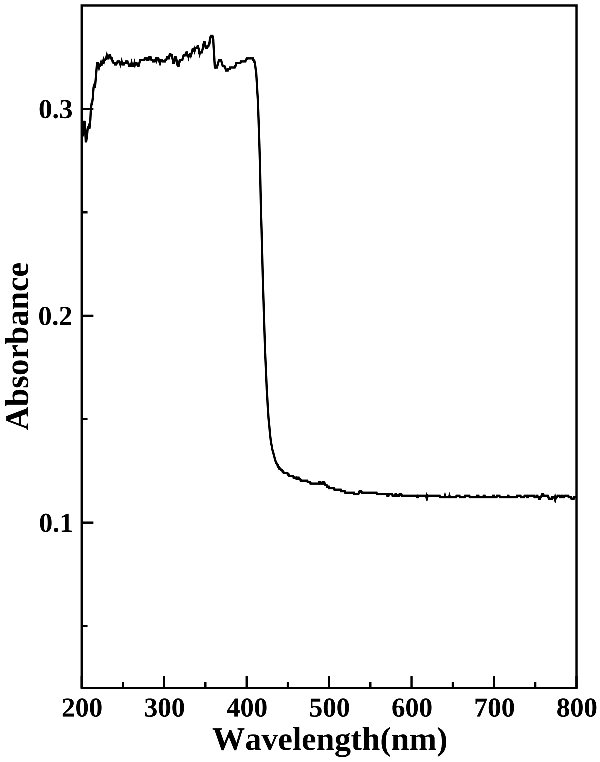

Figure 2.10: A typical UV-Vis absorbance spectra for Single crystal rutile TiO_2 with E_g= 3.25 eV.

so that absorbing species do not interact. Interactions between absorbing species can lead to deviations in the absorptivity coefficient as a function of concentration. The relationship between absorbance A and the experimentally measured transmittance T is

$$A = -logT = -log\left(\frac{P}{P_0}\right) \tag{2.13}$$

where T and A both are dimensionless. The parameter P can de defined as radiant power (radiant energy on unit area in unit time) after is passes through the sample and P_0 is the inital radiant power. Absorption data and spectra will often be presented using A versus wavelength, which is used to extract band gap of various semiconducting materials.

In a semiconductor, the term “Band Gap” refers to the energy difference between the top of the valence band and the bottom of the conduction band. The transition of electrons from valence band to conduction band requires specific amount of energy, called as the band gap energy. The band gap is important as it determines the portion of the solar spectrum which a photo voltaic cell absorbs. Much of the solar radiation reaching earth is comprised of wavelengths whose energies are greater than the band gap of silicon, used extensively in solar cell applications. These higher energies will be absorbed by the solar cell, but the difference in energy is converted into heat rather than into usable electrical energy. Consequently, unless the band gap is controlled, the efficiency of the solar cell will be poor.

Fig 2.10 displays an absorbance spectrum for single crystal rutile TiO_2, which has a band gap of 3.25 eV. The band gap, thus can be evaluated from the absorbance data using Tauc equation :

$$\alpha h\nu = A(h\nu - E_g)^{\frac{n}{2}} \tag{2.14}$$

where, α and A are related to the absorbance of the material while $h\nu$ is the incident photon energy. The term n, in exponent refers to the nature of the transition. The n can take following values

- n=1 for direct allowed transition
- n=3 for direct forbidden transition
- n=4 for indirect allowed transition
- n=6 for indirect forbidden transition

A Tauc plot is the most effective way to extract the band gap of semiconducting materials using Absorbance versus wavelength spectrum [11]. To extract the Tauc plot for direct band gap, the y axis gets modified to $(Ah\nu)^2$ instead of Absorbance and x-axis gets converted to energy. Then the band gap is calculated by taking the slope of the band edge.

Shimadzu UV-vis spectrophotometer has been used in this thesis to investigate the photo absorbance properties of single crystal rutile TiO_2, before and after cobalt ion implantation. The schematic diagram for this system has been shown in fig 2.11. This system contains a double beam splitter which splits the incident radiation coming from the monochromator. These dual beams then passes simultaneously through the reference and the unknown sample. The detector then detects the difference in the signal from the reference and the unknown sample, at all the

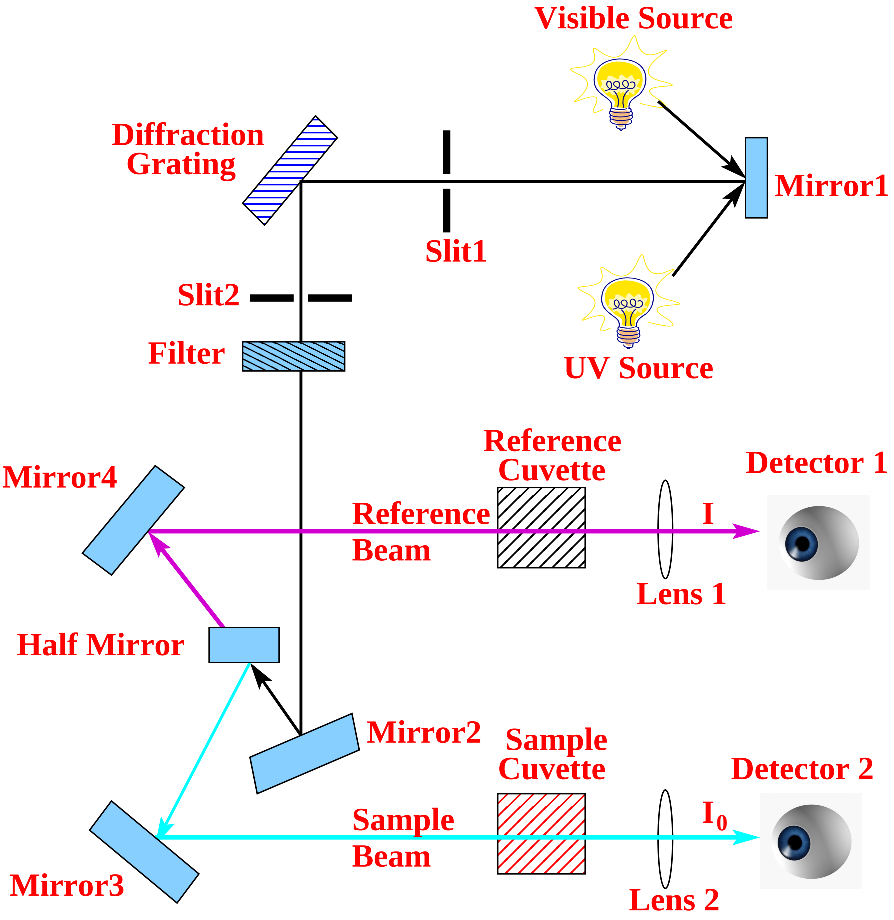

Figure 2.11: UV-Vis spectroscopy setup.

wavelengths. System also contains two light sources to produce photons of different energies. Deuterium arc discharge lamp can generate high intensity radiation in the 190-380nm range while tungsten halogen lamp emits radiation in the range from 320-900nm. The photon source gets automatically changed by the system during the measurement. The wavelengths of the incident source then gets dispersed by a silicon dioxide coated reflecting optical system with holographic grating monochromator. The spectral band bass can be tuned using monochromator slit width or by the array element width in array detector spectrometers. These systems are designed to reject all the stray light coming from the outer environment which can affect the absorbance measurements. The detector used to measure the absorbance of the sample consists of a photo multiplier tube detector. The resolution of the system is 0.1nm.

2.2.4 X-ray Diffraction(XRD)

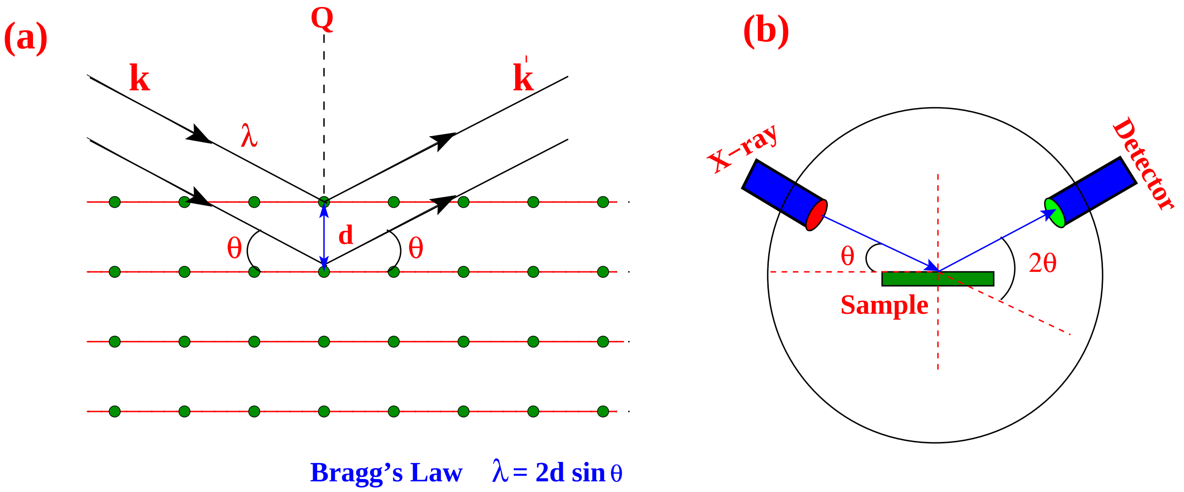

Figure 2.12: (a) Bragg's reflection in single crystal and (b) X-ray diffractometer setup.

When x-rays interact with materials, phenomenon like scattering or absorption of x-rays may occur. The first process is related to the elastic scattering which is used in diffraction measurements and the second process is related to a resonant process [12]. The incident x-ray is an electromagnetic wave with its electric and magnetic field vectors changing sinusoidally with time and space.

This electromagnetic wave exerts a force on electrons in atoms, causing them to vibrate with the same frequency of the x-ray. The re-oscillation of the electrons generates x-ray radiation in all directions again.

Diffraction is due to the constructive phase relation between scattered x-rays from matter. x-rays scattered from a periodic structure interfere constructively to form enhanced signals in certain directions, illustrated in fig 2.12. If all the x-rays originating from the oscillating electrons are summed, the distribution function f(Q) is simply same as a Fourier transformation of the electron density ρ(r), as given in equation:

$$f(Q) = \int \rho(r) e^{iQ.r} dr \tag{2.15}$$

where,

$$Q.r = 2\pi N \tag{2.16}$$

and,

$$n\lambda = 2dsin\theta \tag{2.17}$$

where Q is the momentum transfer, d is the inter planar distance, λ is the wavelength of the X-ray, θ is the incident angle, N and n are integers. The constructive condition applied to the fourier transformation is known as the Laue condition, given in Eq-2.16 (the momentum transfer should be a multiple of a reciprocal lattice vector), which is identical to the Bragg condition in Eq-2.17 (the path difference should be a multiple of the x-ray wavelength). The latter is mostly used by material scientists to represent the conditions for constructive interference in a simple view. Therefore, the scattered electric field (or magnetic field) is the reciprocal space representation of electron density in terms of the wave. The magnetic field is usually neglected since its contribution is much smaller by a factor of approximately 10^{-4} than the electric field [13].

The Bragg peak position is directly related to the atomic spacing, employed for the identification of compounds, or chemical phases. The peak width is related to the coherent volume of a scattering object, which is simply calculated from a fourier transformation, and used to calculate the size of the object (e.g. the grain size for poly crystalline samples). The Scherrer formula can be written as :

$$W(2\theta) = \frac{0.94\lambda}{LCos\theta} \tag{2.18}$$

where, W(2θ) is the full width half maximum of the Bragg peak, λ is the wave length of the x-ray, and L is the size of the object.

In this thesis, X-ray diffraction studies have been pursued using a X-ray diffractometer from Bruker. This system mainly consists of three parts: An X-ray source, a goniometer and a detector. The x-ray source produces a Cu K_α radiation $(\lambda = 1.5406A^\circ)$ which was used for the structure and phase characterization. We have performed XRD measurements in two scan directions:

i). Normal Incidence X-ray Diffraction : In X-ray diffraction, Bragg reflections are of interest because the positions, shapes, and intensities of the measured peaks are related to the micro structure of the material. An instrument which is often used to measure Bragg reflections of a thin film is the θ-2θ diffractometer. Because the scattered intensity depends on the distance from the sample to the detection system, the distance has to be kept constant during the measurement. The movement of the detector is therefore restricted to a sphere of constant radius with the sample positioned in the center of it. Since the wave vectors **k** and **k**$'$, and the surface normal form a common plane, called scattering plane, the geometry is said to be co planar [14].

The symmetric θ-2θ scan is the commonly used technique to acquire diffracted signal. The X-rays impinge the sample at an angle θ while the detector monitors the scattered radiation at the same angle. The angle between elongation of the incoming beam and the exiting beam is thus 2θ. During the scan, the angle is varied to measure intensities from an angle 2θ but the incident and exit angle are kept equal. Therefore, the scattering vector will always be parallel to the surface normal, and Bragg reflections occur only from the planes (hkl) which are parallel to the surface plane of the sample. Because of the finite divergence of the beam, the scattering vector is, however, somewhat tilted from the surface normal for the beams which deviate from the central beam. This causes reflections also from the planes which are not quite parallel to the surface plane [14]. The measurement geometry of the symmetric θ-2θ scan is shown in fig 2.12(b).

2. Grazing Incidence X-ray Diffraction :

In Normal X-ray diffraction, the penetration depth of the x-rays is very high. This causes a large

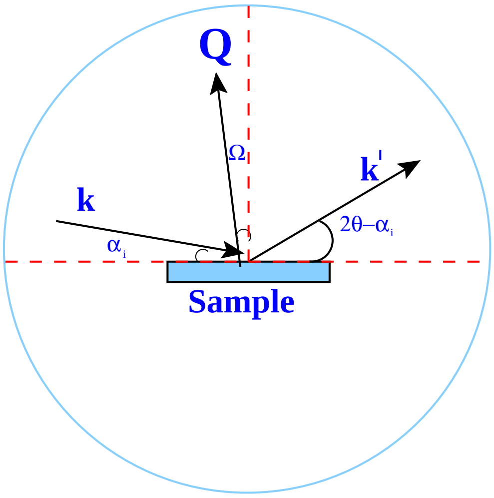

Figure 2.13: Diagram representing Glancing Incidence X-ray Diffraction (GIXRD) scan.

fraction of the signal to reflect from very deep (bulk) rather than from a very few layers, when θ-2θ scan is utilized. The path travelled by X-ray in the sample can be significantly increased by utilizing small incident angles. This technique is known as the grazing incidence X-ray diffraction (GIXRD), and makes it possible to obtain depth-resolved structural information by probing the sample under different angles of incidence [14]. The schematic has been shown in fig 2.13. The incident angle, denoted by α_i, is usually only few degrees or even less. During the measurement, it is kept constant while the detector is moved along the 2θ circle so that the angle between the sample surface and outgoing beam is (2θ - α_i). This distinguishes GIXRD from the symmetric θ-2θ configuration but both are co planar configurations. The intensity is gathered from the angle 2θ and Bragg peaks are found at comparable positions [14]. The difference in the measurement geometry of symmetric and asymmetric scan has a clear impact on the orientation of the scattering vector. In grazing incidence configuration, the orientation of the scattering vector changes in the course of the measurement, and it is not parallel to the surface normal. Since the orientation of the scattering vector is constantly changed, the measurement probes planes which are tilted with respect to the sample surface and which are not parallel to each other. The change in the orientation of the scattering vector with respect to the surface normal is

$$\Omega = \alpha_i - \frac{\mathbf{2}\theta}{2} \tag{2.19}$$

where α_i is the incident angle and $\mathbf{2}\theta$ is the angle between elongation of the incident beam and the exit beam [14]. The measurement geometry of GIXRD method is shown in fig 2.13.

2.2.5 Raman Spectroscopy :

Raman scattering is a spectroscopic technique that is used to study vibrational modes of molecules, much like the commonly used infrared (IR) absorption spectroscopy. Raman scattering gets its name from Sir C. V. Raman, who discovered the process in 1928, and subsequently won the Nobel Prize in Physics for his discovery in 1930. Unlike IR spectroscopy, which measures the absorption of infrared light used to directly excite molecular vibrations, Raman spectroscopy irradiates a sample with visible light to indirectly excite vibrations via virtual electronic excitations. The energy difference between the incident and resulting scattered light corresponds to the vibrational excitation. The fundamental differences between these two vibrational excitations give rise to different selection rules. Thus, IR and Raman spectroscopy are often used together to give complementary information about a molecule.

When a molecule is irradiated with intense light from a laser, it can be excited from its ground electronic state to a virtual state that is lower in energy than the first excited state. The majority of the time, this light is elastically scattered and the molecule returns to its initial state. This effect is known as Rayleigh scattering. Some light can be inelastically scattered, however, and the molecule can end up in a vibrational state that is different from where it originated. The light that is scattered from the sample after this process will be shifted in frequency by an amount equal to the energy spacing between the vibrational states. Transitions to a higher vibrational state ($\Delta\nu$ = +1) give rise to Stokes scattering, while ($\Delta\nu$ = -1) transitions to lower states result in anti-Stokes scattering, as shown in fig 2.14. Since the vibrational ground state is generally more populated than the excited states, which is expected by the Maxwell-Boltzmann distribution, Stokes scattering intensities are generally higher than those of anti-Stokes.

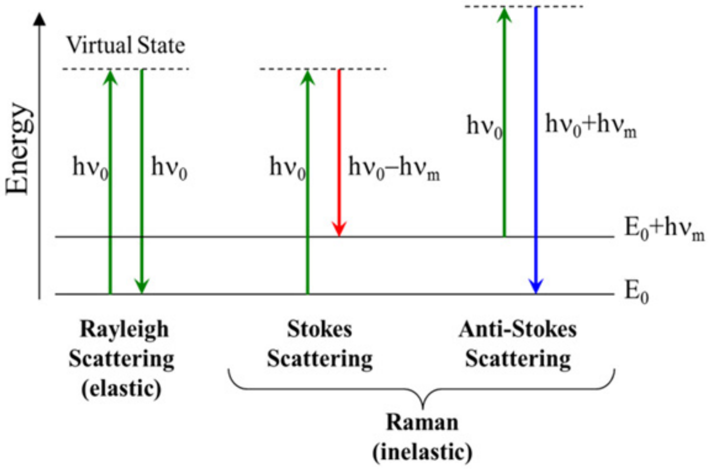

Figure 2.14: Diagram of vibrational transitions giving rise to three types of scattering possible during Raman spectroscopy,i.e., Rayleigh, Stokes and Anti-Stokes scattering.

The selection rules for Raman scattering can by found by considering the electric field (E) of the laser light used to excite the sample. The electric field varies with time (t) as shown by the equation [15]

$$E = E_0 Cos 2\pi\nu_0 t \tag{2.20}$$

where E_0 is the amplitude and ν_0 is the frequency of the incident light.

For a molecule vibrating at a frequency of ν_m, the nuclear displacement (q) can be written as

$$q = q_0 Cos 2\pi\nu_m t \tag{2.21}$$

where q_0 is the amplitude of the vibration of the molecule.

When this molecule is placed within the electric field of the laser, an electric dipole moment (P) is induced, given by the equation

$$P = \alpha E \tag{2.22}$$

where α is the polarizability of the molecule, or the measure of the response of the electronic charge distribution to the electric field (E). The polarizability (P) can be written as a Taylor series expansion, as follows:

$$\alpha = \alpha_0 + \left(\frac{\partial\alpha}{\partial\, q}_0\right) q + ... \tag{2.23}$$

In this expression, α_0 is the polarizability at the equilibrium position, and $\partial\alpha/\partial q_0$ is the rate of change of α with respect to q, evaluated at equilibrium. For small amplitude vibrations α can be considered to be a linear function of the displacement, so only the linear term needs to be considered.

Combining Eq-2.20-2.23, gives the following expression for the induced dipole moment:

$$P = \alpha_0 E_0 Cos 2\pi\nu_0 t + \left(\frac{\partial\alpha}{\partial q}_0\right) q_0 E_0 Cos 2\pi\nu_0 t Cos 2\pi\nu_m t \tag{2.24}$$

The cosine terms can be combined to better reveal the physics of Raman scattering:

$$P = \alpha_0 E_0 Cos 2\pi\nu_0 t + \frac{1}{2}\left(\frac{\partial\alpha}{\partial q}_0\right) q_0 E_0 [Cos 2\pi(\nu_0 - \nu_m)t + Cos 2\pi(\nu_0 + \nu_m)t] \tag{2.25}$$

The first term corresponds to Rayleigh scattered light, while the second represents both Stokes $(\nu_0 - \nu_m)$ and anti-Stokes $(\nu_0 + \nu_m)$ scattering. From here it can be seen that if the polarizability does not change with the displacement then the second term is zero, and that particular vibration is Raman inactive. Although usually the energy of the exciting laser is below that of any electronic excited states, it can also be tuned to be resonant with a particular electronic transition in the sample.

In this work, micro raman scattering studies were carried out in back scattering geometry with Horiba Jobin Yvon T64000 triple monochromator system with a liquid nitrogen cooled Charged Coupled Device (CCD) detector, as shown in fig 2.15. 100x objective was used to acquire raman spectra which provides $\sim 1\mu m^2$ laser spot on the sample surface. A Green line (514 nm) from Argon ion laser was used with very low power to avoid any damage to the sample due to laser heating.

Figure 2.15: Micro Raman setup at CMPF Lab, IOP.

2.2.6 Superconducting quantum interference device (SQUID) :

The Superconducting Quantum Interference Device (SQUID) is the most sensitive magnetometer to investigate the magnetic properties . In many cases, SQUID instrumentation offers the ability to make measurements where no other methodology is possible. Generally, SQUID has a superconducting loops containing one or more Josephson junction. Superconductor, invented in 1911, is an element that loses its electrical resistance below a Curie temperature T_c. In superconductors, the current is not carried by single electrons but by pairs of electrons with opposite spins called cooper pairs. Their binding energy is large compared to the thermal scattering and as a result cooper pairs propagate through the material without any resistance. Cooper paired electrons have lower energy than fermi energy. If two superconducting regions are kept isolated from each other by a very thin non-superconducting material, there will be a tunneling across the gap. The tunneling of the electron-pairs across the gap carrying a superconducting current was predicted by 'Josephson Junction' [16].

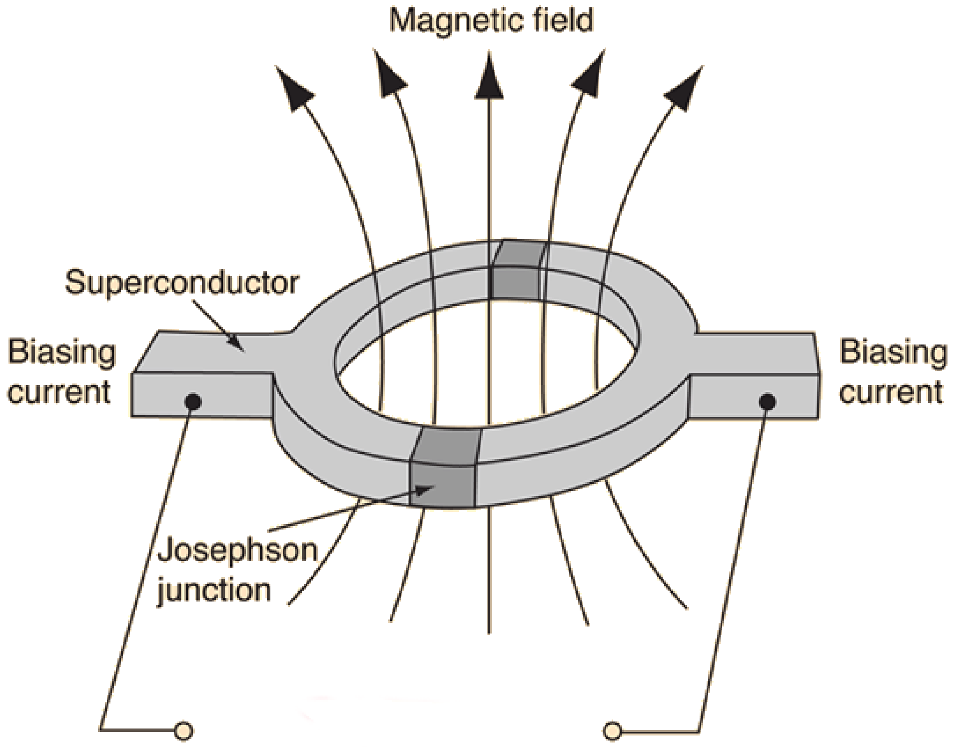

Figure 2.16: Schematic diagram for Josephson junction.

SQUID uses Josephson effect to measure extremely small variations in magnetic flux. The schematics of Josephson junction is shown in fig 2.16. The Josephson junction contains two weakly coupled superconductors which are separated by a thin layer of insulator. The electron-pairs in superconductors can tunnel across the insulating barrier at zero voltage bias. The tunneling current i relates to the phase difference ($\Delta\phi_j$) between electron-pair wave in each superconductor as :

$$i = i_c sin\Delta\phi_j \tag{2.26}$$

where i_c is the critical current of a Josephson junction.

A simple SQUID consists of a closed loop of superconductors with two Josephson junctions. When a magnetic field (B) is applied perpendicular to the plane of the loop, a phase difference

$\Delta\phi_B$=$4\pi\Phi\frac{h}{e}$, is produced in the electron-pair wave in the superconducting regime, where Φ is the flux across the loop, h is the Planck's constant and e is the electronic charge. A small current i is also induced to flow around the loop, producing a phase difference ($\Delta\phi(j)$) across each Josephson junction. Thereby, the total phase difference is :

$$\Delta\phi_{tot} = \Delta\phi_B + 2\Delta\phi(j) \tag{2.27}$$

The total phase difference must be equal to $2n\pi$. Integrating this equation, gives

$$i = i_c sin\Delta\phi_j = i_c sin\left(\frac{\Delta\phi_{tot} - \Delta\phi_B}{2}\right) = i_c sin\left(2\pi\frac{h}{e}\right) = i_c sin(\pi\Phi/\Phi_0) \tag{2.28}$$

where Φ_0=$\frac{2e}{h}$=2.07×10^{-15}. Thus, the current has a periodic dependence on the magnitude of magnetic fluc Φ.

For the direct current (DC) magnetization measurements performed in this thesis, SQUID sensor has been used to measure the global magnetic moment of the sample. The sample is magnetized by an external magnetic field and this magnetized sample with a magnetization of M can generate magnetic flux Φ through the SQUID coils and hence causes an electrical output (i). The magnetization (M) of a sample is computed by this electrical output. Since the period of variation Φ_0 is very small, SQUID sensor can detect very weak magnetic moment of a sample (as low as $\sim10^{-8}$ emu). The schematics of SQUID detection has been shown in fig 2.17. In this setup the sample could be cooled down to below 2K using liquid Helium. The upper temperature limit was about 400K. The Helium cooled magnet could operate in the range of -90 to 90kOe.

All ferromagnetic materials exhibit magnetic hysteresis, when subjected to an external magnetic field. Fig 2.18 shows the typical hysteresis loop for a ferromagnet. As the external field is increased, the magnetization of the sample also increases till its magnetization reaches a saturation value, given by M$_s$. Thereafter, even if the field is completely removed, the sample still retains some of its magnetization, known as remanence or M$_R$. If the external field is now reversed, the magnetization slowly drops, until it is completely demagnetized, at a value for the external field corresponding to the coercive field H$_C$. Thus, the sample absorbs energy from an external applied magnetic field.

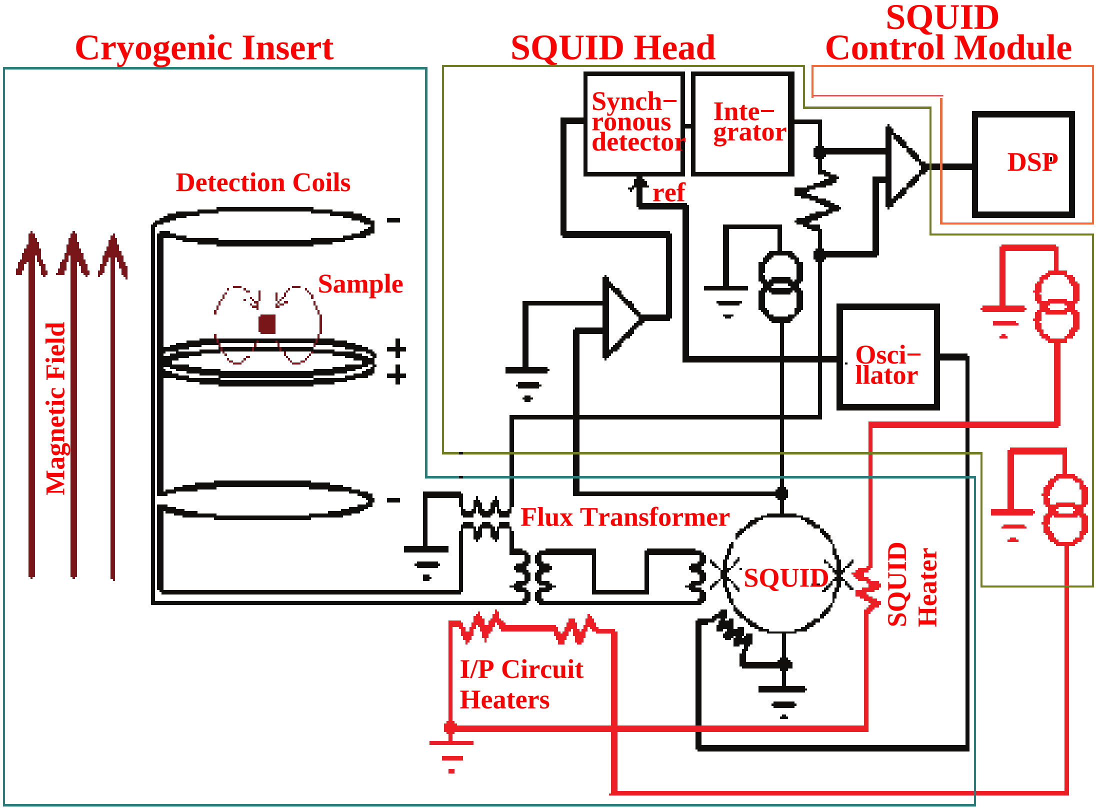

Figure 2.17: Example of SQUID detection diagram [17].

The shape of the hysteresis curve is also indicative of whether the sample is magnetized along its easy or hard axis. The difference between these two axes is that the magnetization of a sample can be saturated along its easy axis with a much lower external applied field, than required to saturate the sample along its hard axis. The anisotropy of a sample is the energy required to flip its magnetization from the easy to the hard axis. The reason for anisotropy is the coupling between the spin magnetic moment and the crystal lattice. Anisotropy can also be caused due to various other reasons such as shape of the sample, or crystalline orientation, stress etc.

In this thesis, the magnetic measurements have been carried out using SQUID system from Quantum design [17] at IGCAR, Kalpakkam. A non-magnetic plastic straw provided by Quantum Design was used for the sample holder. The instrument was operated between 2K to 300K at a low

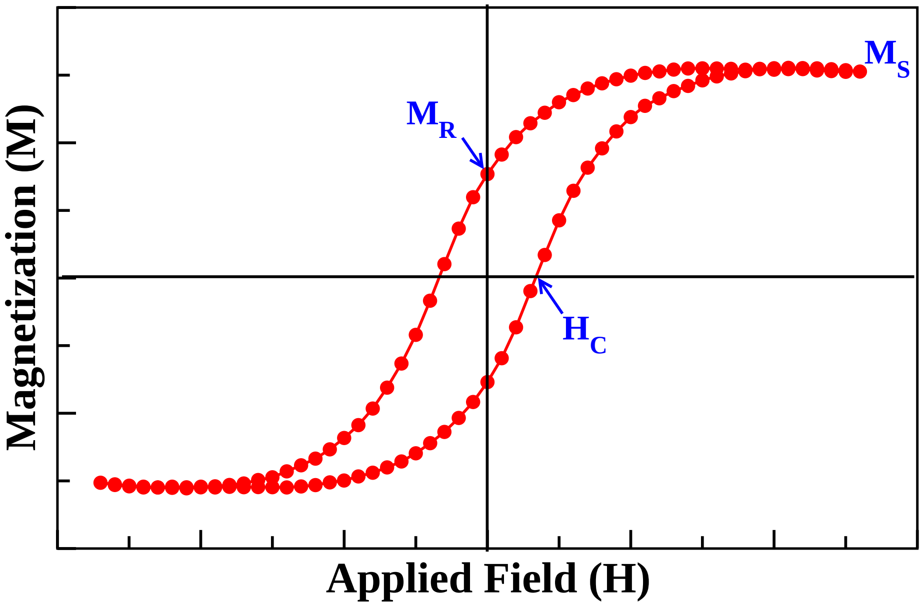

Figure 2.18: Example magnetization loop for ferromagnetic material.

field for ZFC-FC measurements. During isothermal measurements, field of the order of 1 Tesla was used. The sensitivity of the instrument was 10^{-8} emu.

2.2.7 Rutherford Back scattering Spectrometry (RBS) :

RBS is a widely used nuclear method for depth dependent elemental identification in solids. The discovery of this technique dates back to 1911 by Rutherford, when he used the back scattering of alpha particles from a gold film to determine the fine structure of the atoms which resulted in the discovery of the nucleus. RBS as a method for material analysis was first described in 1957 by Rubin et.al [18]. A target is bombarded with ions at an energy in the MeV range (typically 0.5-4 MeV). The energy of the back scattered projectile is recorded with an energy sensitive detector, typically a solid state detector. The schematic diagram for RBS has been shown in fig 2.19. It allows a quantitative determination of the composition of material as well as depth dependent quantitative information on elements. RBS is a quantitative technique with a good depth resolution of the order of several nm with a very good sensitivity for heavier elements of the order of ppm

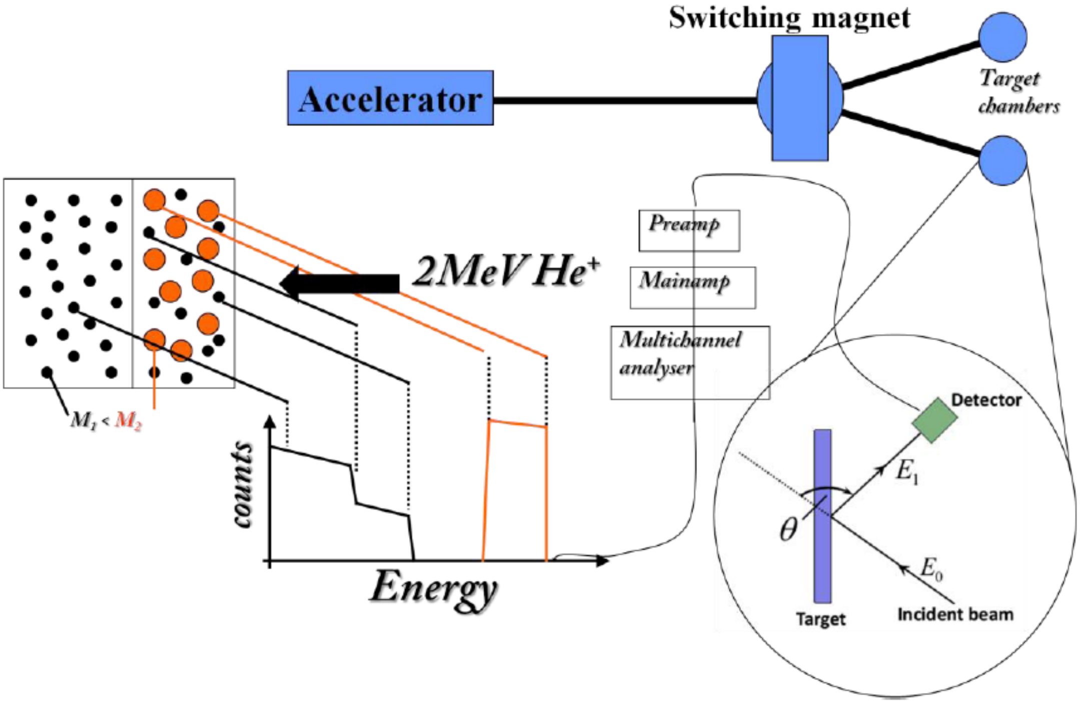

Figure 2.19: Example of RBS/C measurement technique [19].

levels. It is a non destructive technique, not requiring any reference samples. The analysis depth is typically about 2μm for incident He ions and about 20μm for incident protons. The drawback of RBS is low sensitivity for light elements, which often requires the combination of other nuclear based methods like Nuclear Reaction Analysis (NRA) or Elastic Recoil Detection Analysis (ERDA).

When a sample is irradiated with energetic ions, the interaction between ions and the target atoms can be modeled accurately as an elastic collision using classical mechanics. The main process that needs to be addressed to study the dynamics of these collision process is as follows [19]

i. Kinematic Factor

For scattering at the sample surface, the only energy loss mechanism is the momentum transfer to the target atom. The ratio of the projectile energy after a collision to the projectile energy before a collision is defined as the kinematic factor.

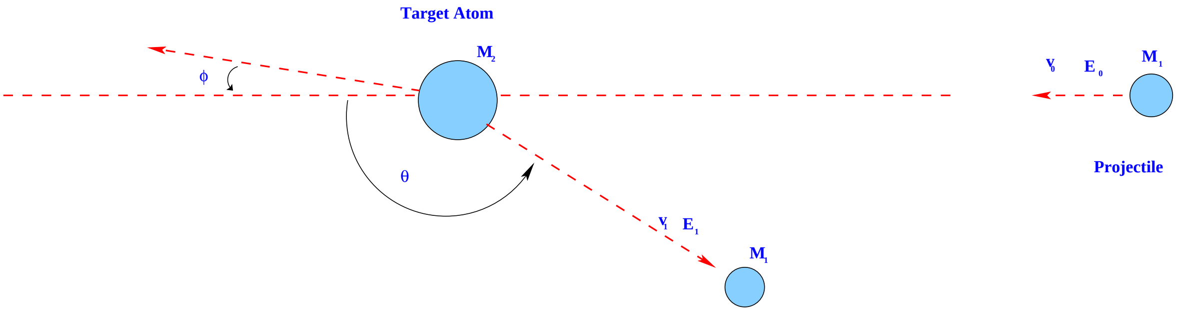

Figure 2.20: Schematic diagram for elastic collision between a projectile and a target atom having masses M_1 and M_2, respectively. E_0 is the initial energy of the projectile atom while the target is at rest.

Let us assume a particle of mass M_1 moving with constant velocity undergoes an elastic collision with a stationary particle of mass M_2. Thus, the total energy will be transferred from the moving object to the stationary particle. In RBS measurement, with M_1 being the mass of the projectile and M_2 being the mass of the target atom, the following two necessary conditions need to be fulfilled :

- The incident energy of the projectile ion (E_0) must be larger than the binding energy of the atoms in the target atoms. Generally, it should be larger than 10 eV as the energy of the chemical bonds is generally of that order.
- Nuclear reactions and resonances must be forbidden which enforce an upper limit to the projectile energy. The upper limit depends on choice of the projectile and the target atoms. For example, If we choose H^+ beam as a projectile, nuclear effects can appear even below 1 MeV while for He^+, they begin to appear at 2 to 3 MeV.

So, the problem of elastic collision of two masses M_1 and M_2 can be solved by applying law of conservation of energy and momentum. Assume, $\mathbf{v}_0$ and E_0 are the velocity and the energy of a projectile atom of mass M_1 before the collision, while the target atom M_2 is at rest. After the collision, let $\mathbf{v}_1$ and $\mathbf{v}_2$ be the velocities and E_1 and E_2 be the energies of projectile and target atoms, respectively. So, the kinematic factor, K, for a target mass, M$_2$, can be written as

$$K = \frac{E_1}{E_0} \tag{2.29}$$

By applying the energy and the momentum conservation, using lab co-ordinates, the kinematical factor can be obtained as [19]

$$K = \left\{ \frac{[1 - (M_1/M_2)^2 Sin^2\theta]^{1/2} + (M_1/M_2) Cos\theta}{1 + (M_1/M_2)} \right\}^2 \tag{2.30}$$

where θ is the scattering angle of the projectile atoms in the lab reference frame. In the Center of mass frame, the above equation can be simplified as follows

$$K = 1 - \left\{ \frac{2M_1M_2}{(M_1 + M_2)^2} \right\} (1 - Cos\theta_c) \tag{2.31}$$

where, θ_c is the scattering angle in the center of mass reference frame.

During RBS measurements, angle near 180° is of great interest. To analyze the behavior of kinematic factor, near this angle, we introduce a term, δ as

$$\delta = \pi - \theta \tag{2.32}$$

where, δ measures the deviation of θ from π in units of arc. The kinematic factor can be estimated by taking first order expansion in δ [19]

$$K = \left\{ \frac{1 - x}{1 + x} \right\}^2 (1 + x\delta^2) \tag{2.33}$$

where, x is the ratio of the mass of the projectile and the target atom.

If the target atom has two type of atoms that differ in their masses by a very small amount ΔM, the difference ΔE in the energy of the projectile after collision is given by [19]

$$\Delta E = E_0 \left(\frac{dK}{dM} \right) \Delta M \tag{2.34}$$

For special case, i.e., $\theta = 180°$ and $M_2 \gg M_1$, which is most often the case, this reduces further to

$$\Delta E = E_0 (4 - \delta^2)(M_1/M_2^2) \Delta M \tag{2.35}$$

Detectors used in the experiments generally have a finite resolution. If ΔE falls below this limit, the distinction between two masses is lost. So, to achieve a good mass resolution, the coefficient of ΔM should be as large as possible. This can be attained through

- Increasing the incident energy of the projectile ions.
- Using heavier projectile (however, the mass of the projectile must be smaller than the target atom, otherwise back scattering signal will not produce.)
- Measuring the incident particles at a very large scattering angle (i.e. small δ).

ii. Scattering Cross Section (σ) :

In RBS measurements, the particles get scattered by an angle θ, and are collected by a solid state detector having a small solid angle (less than 10^{-2} sr). The number of projectiles hitting the detector after scattering is

$$Y = QNt\frac{d\sigma}{d\Omega}\Omega \tag{2.36}$$

where Q is the number of projectile striking the target, N is the volume density of the target atoms, t is the thickness of the sample and $\frac{d\sigma}{d\Omega}$ is the differential scattering cross section for scattering into a solid angle Ω at a scattering angle θ. For a very small detector angles Ω, $\sigma \rightarrow \frac{d\sigma}{d\Omega}$. This is the value that is generally used in back scattering geometry. Thus, the yield can be written as

$$Y = QNt\sigma\Omega \tag{2.37}$$

If the number of projectile striking the target and the detector is known, then the number of atoms per unit area of the target (Nt), can be determined from RBS measurements. If we consider an elastic collision between two atoms which have coulombic interaction between them, the differential scattering cross section for these two atoms in laboratory frame of reference, can be written as [19]

$$\frac{d\sigma}{d\Omega} = \left(\frac{Z_1 Z_2 e^2}{4E}\right)^2 \frac{4}{Sin^4\theta} \frac{([1-((M_1/M_2)Sin\theta)^2]^{1/2} + Cos\theta)^2}{(1-((M_1/M_2)Sin\theta)^2)^{1/2}} \tag{2.38}$$

where E is the energy of the projectile just before the scattering and Z_1 and Z_2 are the atomic numbers of the projectile and target atoms respectively.

- For M$_1$ $<< M_2$, the above expression can be written in a very simplified form as :

$$\frac{d\sigma}{d\Omega} = \left(\frac{Z_1 Z_2 e^2}{4E}\right)^2 \frac{1}{Sin^4(\frac{\theta}{2})} \tag{2.39}$$

The magnitude of differential scattering cross section is strongly influence by the term $\left(\frac{Z_1 Z_2 e^2}{4E}\right)^2$. Thus the scattering cross section is highly sensitive for heavier elements. For example, for a beam of 1 MeV He$^+$ and scattering angle (θ)= 170°, the scattering cross section (σ) for Si is 1 barn while the same for Au is 32.8 barn. It can also be seen from the above equation that the scattering cross section is inversely proportional to the square of the projectile energy.

The Rutherford scattering cross section assumes coulomb interaction potential V(r), between the projectile and the target atoms with atomic numbers Z$_1$ and Z$_2$, respectively. It also assumes that the energy of the projectile is high enough to penetrate the deep levels of the target atoms. Thus, the scattering is due to the repulsion between two positively charged nuclei of the projectile and the target atoms. Assuming coulomb interaction to be valid for back scattering, the impact parameter (distance of closest approach, d) is given by

$$d = \frac{Z_1 Z_2 e^2}{E} \tag{2.40}$$

where e is the electronic charge. For 2MeV He$^+$ ions, the impact parameter will be $6.8\times10^{-4}A°$, which is smaller than the Bohr's radius ($a_0 = 0.53\ A°$) and the K shell radius of silver atom ($10^{-2}A°$). Thus, the ion penetrates the K shell. Therefore, the use of unscreened coulomb potential for the calculation of cross section is justified.

During small angle scattering of projectile atoms, the differential scattering cross section deviates from the Rutherford's formula. In this case, the projectile does not completely penetrate the electron shells of the target atoms and hence the innermost electrons screen the charge of the atom. In this scenario, the electrostatic interaction is absent between the two particles. For the coulomb potential to be valid for back scattering, the impact parameter must be smaller than the K-shell electron radius. Thus, this requirement sets the lower limit on the energy of the analysis beam, i.e.

$$E > \frac{Z_1 Z_2 e^2}{a_0} \tag{2.41}$$

Given this relation, for RBS with helium ions, the value of E required will be 10keV for Si and 340keV for Au. However, the deviations from the Rutherford cross section occurs at high energies, greater than the screening limit estimate given above, since a part of the trajectory is always outside the electron cloud.

For RBS analysis of solids, the influence of screening can be incorporated by using screened coulomb cross section, σ_{sc}. This can be obtained by multiplying the scattering cross section $\sigma(\theta)$ by a correction factor F

$$\sigma_{sc} = \sigma(\theta)F \tag{2.42}$$

where F = (1- $0.049 Z_1 Z_2^{4/3}$/E). For most of the target elements this correction factor corresponds to a very small value. Hence it can be neglected. At lower analysis energies or with heavier projectiles, however, screening effects can play a vital role. At MeV energy, for a low Z projectile, there will be no charge transfer to the electron cloud of the target and the coulomb interaction of the nuclei is valid. However, for high energy incident ions and small impact parameter, it can deviates from the Rutherford scattering cross section due to the interaction of the projectile with the nucleus of the target atom. This deviation will be very vital when the impact parameter of the projectile and target nucleus system is comparable to the nuclear radius, R of the target atom. Although, the size of the nucleus is not a uniquely defined quantity, early experiments with alpha particles scattering indicated that the nuclear radius can be expressed as

$$R = R_0 A^{1/3} \tag{2.43}$$

where $R_0 \sim 1.4 \times 10^{-13}$cm and A is the mass number. So, when d becomes comparable to the nuclear radius, the Eqn-2.40 becomes

$$E = \frac{Z_1 Z_2 e^2}{R_0 A^{1/3}} \tag{2.44}$$

For He ions as projectile, this energy is about 9.5 MeV and 41 MeV for Si and Li target atoms, respectively. Thus, nuclear reactions and strong deviations from Rutherford scattering should not play a role in back scattering analysis at energies of a few MeV.

iii. Stopping Cross Section (ϵ) :

When an energetic particle interacts with the electrons and nuclei of the target atoms, there is an energy loss. The total stopping cross section for low Z projectiles having energy in MeV range, the nuclear energy loss is negligible. The rate of energy loss in the target atom, dE/dx, is typically 10-1000 eV$A^{\circ^{-1}}$ when we consider He ion as incident beam. The energy, E of the projectile at a depth *x* will be given by

$$E = E_0 - \int_0^x \frac{dE}{dx} dx \tag{2.45}$$

When a particle traverses a very small distance through the surface layer of the target, the rate of energy loss can be considered to be constant and is, $\frac{dE}{dX}|_{E_0}$. Integrating the above equation, using surface energy approximation,we get

$$E = E_0 - \left(\frac{dE}{dx} \right) \Bigg|_{E_0} x \tag{2.46}$$

The stopping cross section (ϵ), thus, can be defined as

$$\epsilon = \frac{1}{N} \frac{dE}{dx} \tag{2.47}$$

where N is the atomic density of the target.

(a) Superposition of Stopping Cross section (Bragg's Rule)

Considering a process by which a particle is loosing energy while passing through a medium having random sequence of independent encounters between the moving projectile and electron attached to an atom (in the case of electronic energy loss), or with an atomic core (nuclear energy loss). For a target that contains more than one element the scenario differs only with respect to. the type of atoms which projectile encounters. The energy loss to the electrons or to the atomic nucleus in each encounter should be same at a given projectile velocity, regardless of the surrounding target atoms. This is because the interaction is considered to take place with only one atom at a time. This is termed as Principle of additivity of stopping cross section. This states that energy loss in a medium, composed of various atomic species, is the superposition of the losses in the constituent elements, weighted proportionally to their abundance in the compound. This was first used by Bragg and Kleeman in 1905, to study the energy loss behavior in molecules. This postulate is now known as Bragg's rule. It states that the stopping cross section $\epsilon^{A_mB_n}$ of a compound A_mB_n or a mixture with an equivalent composition of A_mB_n is

$$\epsilon^{A_mB_n} = m\epsilon^A + n\epsilon^B \tag{2.48}$$

ϵ^A and ϵ^B are the stopping cross sections of elements A and B. Assuming volume density of the molecular units A_mB_n in a compound be $N^{A_mB_n}$, the specific energy loss of the material is

$$\frac{dE^{A_mB_n}}{dx} = N^{A_mB_n}\epsilon^{A_mB_n} \tag{2.49}$$

This formula is equivalent to Equation for an element in which the energy loss over a distance dx is proportional to the number of molecular units A_mB_n traversed over this distance, with a proportionality constant $\epsilon^{A_mB_n}$. For example, In case of SiO_2, the stopping cross section can be calculated as

$$\epsilon^{SiO_2} = \epsilon^{Si} + 2\epsilon^O \tag{2.50}$$

For high velocity projectiles ($\nu >> \nu_0$), ν_0 being the Bohr's velocity, this rule is valid within 1%. However, for He ions in 1-2 MeV range, this is in good agreement with stopping cross sections observed in alloys and compounds. Sometimes deviations are observed when one considers gaseous organic compounds and oxides, nitrides, or other compounds where one element is a gas in elemental form. Generally, the departure is less than 10%.

b. Energy Loss Factor [S] and stopping cross section factor [ϵ]

Now we will now relate the energy of the detected particle from depth x, where the back scattering event occurred in an elemental sample. The schematics has been shown in fig 2.21. The energy of the incident particle is E_0, and the energy immediately before scattering at a depth x is E. The energy of the particle after scattering at the surface is KE_0 and that from depth x is E_1. If the incident particle, the scattered particle and normal to the sample surface are line in the same plane, then scattering angle θ in laboratory frame of reference is

$$\theta = 180^\circ - (\theta_1 + \theta_2) \tag{2.51}$$

where θ_1 and θ_2 is the angle between the surface normal and the direction of incident projectile and the scattered atom. If we assume a constant value of dE/dx along inward and outward paths,

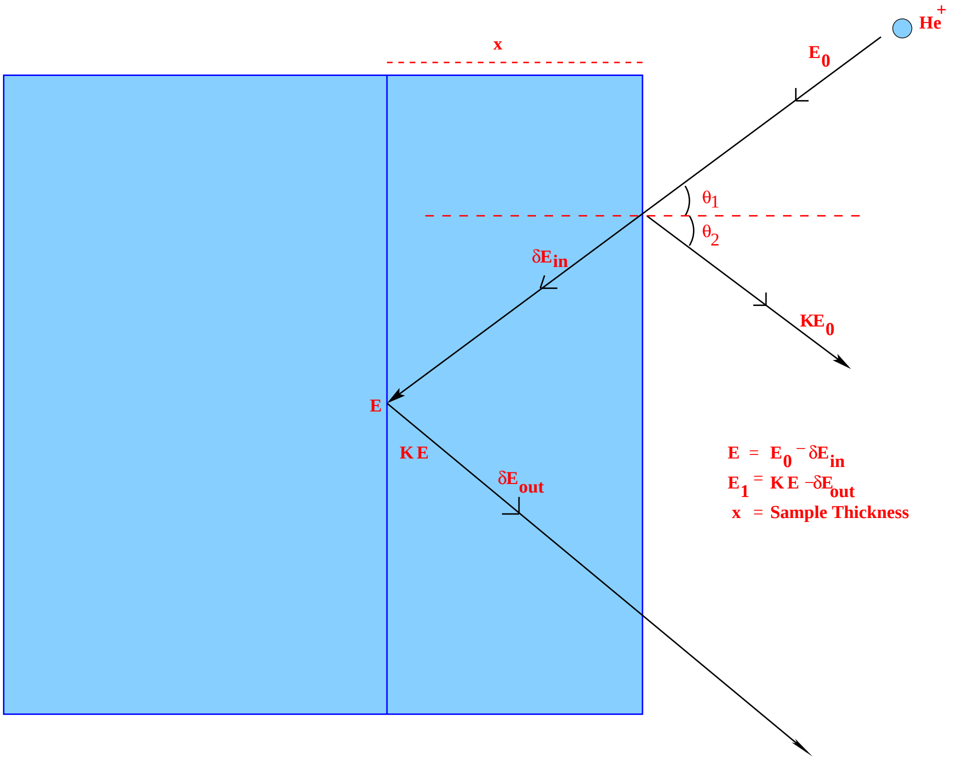

Figure 2.21: Schematic representation of back scattering depth profiling geometry.

the energy E of the particle at depth x, just before the scattering can be written as

$$E = E_0 - \frac{x}{Cos\theta_1}\left(\frac{dE}{dx}\right)\Bigg|_{in} \tag{2.52}$$

Similarly, the particle coming out with as energy E_1 is given by

$$E_1 = KE - \frac{x}{Cos\theta_2}\left(\frac{dE}{dx}\right)\Bigg|_{out} \tag{2.53}$$

Solving these two equation, we get

$$KE_0 - E_1 = \left[\frac{K}{Cos\theta_1}\left(\frac{dE}{dx}\right)\Bigg|_{in} + \frac{1}{Cos\theta_2}\left(\frac{dE}{dx}\right)\Bigg|_{out}\right]x \tag{2.54}$$

The energy KE_0 is the edge of the back scattering spectrum and provides the energy of the particles that are scattered from the surface of the target atoms. E_1 is the energy of particles that are scattered at depth x. Considering ΔE as the energy difference between the particles scattered at the surface and at depth x. It can be written as :

$$\Delta E = KE_0 - E_1 = [S]x \tag{2.55}$$

where,

$$[S] = \left[\frac{K}{Cos\theta_1} \left(\frac{dE}{dx} \right) \Bigg|_{in} + \frac{1}{Cos\theta_2} \left(\frac{dE}{dx} \right) \Bigg|_{out} \right] \tag{2.56}$$

is called the energy loss factor or [S] factor. This equation can also be written in terms of stopping cross section rather than dE/dx

$$\Delta E = [\epsilon] N x \tag{2.57}$$

where,

$$[\epsilon] = \left[\frac{K}{Cos\theta_1} \epsilon_{in} + \frac{1}{Cos\theta_2} \epsilon_{out} \right] \tag{2.58}$$

is called the stopping cross section factor.

iv. Energy Straggling

When a particle moves through a medium it undergoes a series of collisions. As a result, there will be a loss in energy of the incident projectile after passing through a thickness of Δx in a homogeneous medium. This energy loss, ΔE, is termed as the energy straggling and is subjected to a statistical fluctuation. It places a finite limit of precision with which the energy loss can be evaluated, and hence, a precision with which the depth can be resolved by back scattering spectrometry. The ability to identify masses is also impaired, except for atoms located at the surface of the target, because the energy after a collision within the target is no more a constant. Thus, it is really necessary to have the information about the magnitude of the energy straggling for any given combination of energy, target material, target thickness, and projectile.

Light projectile having energy in MeV range loose energy during collision mainly due to interaction with the electrons in the target. In this case, the dominant contribution to the energy straggling will be electronic interaction. However, Bohr's theory predicts that the energy straggling is independent of the energy of the projectile. The root mean square value of the energy variation increases with the square root of the electron density per unit area in the target. For a layer of thickness t, Bohr straggling has a variance

$$\Omega_B^2 = 4\pi (Z_1 e^2)^2 N Z_2 t \tag{2.59}$$

This equation reveals that Ω_B^2 increases with the number of electrons per atom (Z_2), but the plot of Ω_B^2 as a function of Z_2 shows that the pronounced structure in the plot is due to the difference in the density, N, of the elements. This variation can be removed if we take energy straggling per unit density of the target, i.e., Ω_B^2/Nt. These facts can be remembered for quick determination of energy straggling.

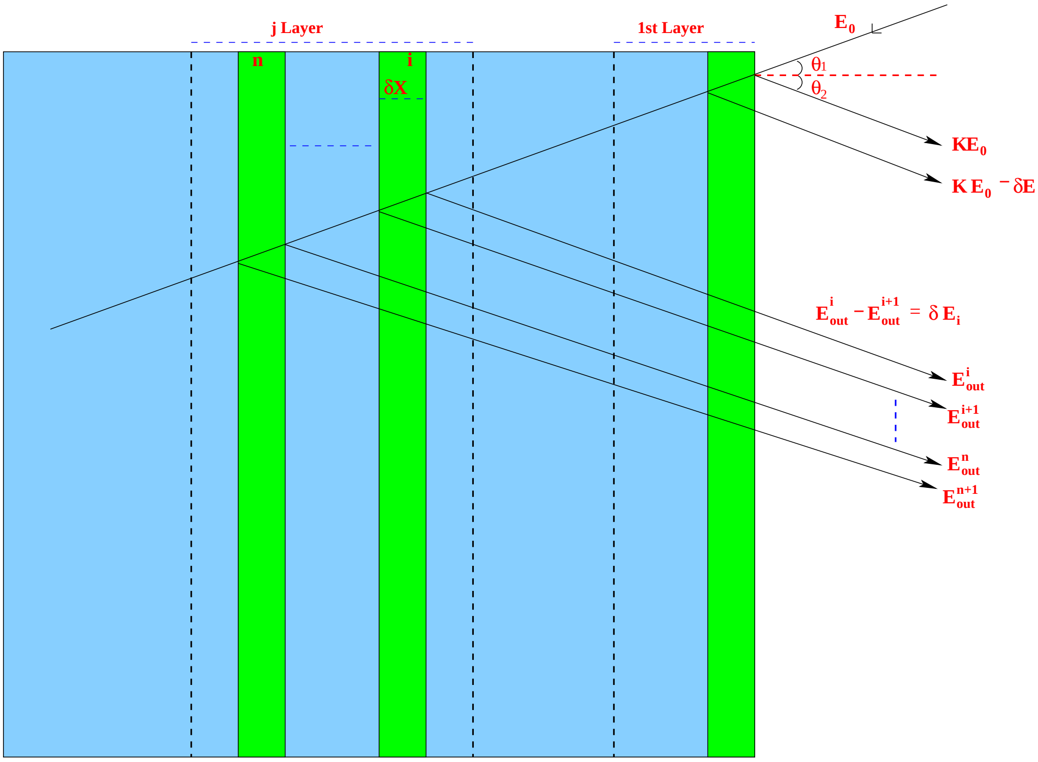

Figure 2.22: Schematic diagram for depth profiling using RBS/C technique. E_0 is the initial energy of the incident ions while E^i_{out} is the energy of the incident ions scattered from the i^{th} strip of thickness δx.

The above mentioned concepts are vital for analyzing the RBS data. The RBS data directly does not provide any information about the depth dependent composition of the system under investigation. Thus, simulation of RBS data is essential for the interpretation of experimental results. Many algorithms developed till date, follow the same procedure to estimate ion energy prior to and post scattering, at various depth. The target is divided into several thin strips of uniform density (as shown in fig 2.22). In the present work, we have used SIMNRA and RUMP softwares which have proved to be very useful for back scattering data analysis including diffusion and implantation profile investigation. These programs can handle RBS spectra for most projectile ions at all significant energies and all target materials.

Channeling

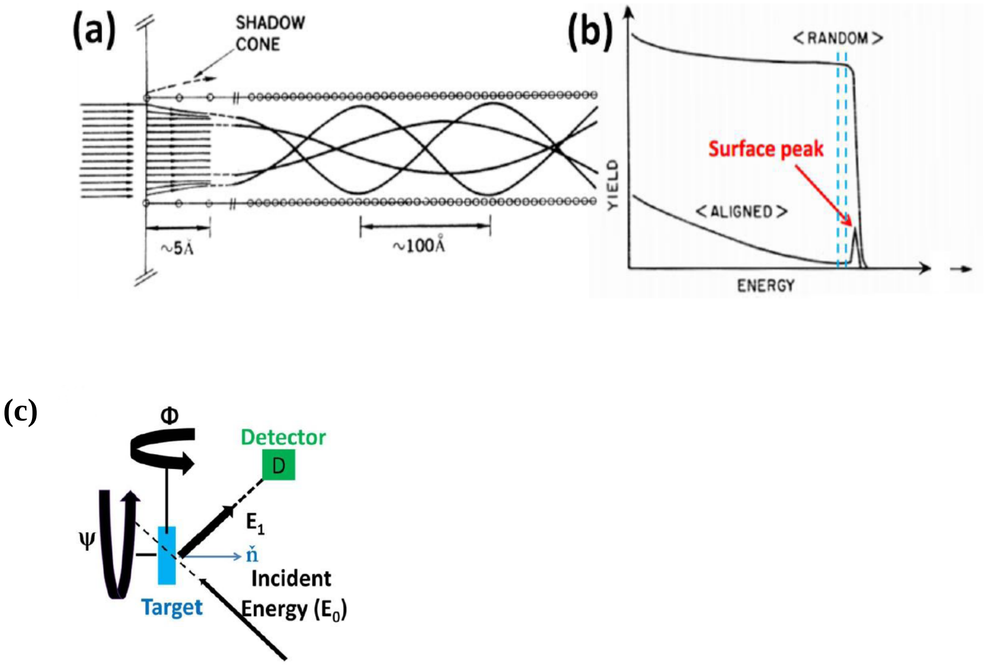

Figure 2.23: Schematic diagram showing (a) trajectory of incident atoms undergoing scattering at the surface and channeling within the crystal, (b) Random and Channeled spectra for random and aligned lattice along the direction of incident beam and (c) channeling geometry.

Channeling is a process that restricts the path of a charged particle in a crystalline solid. The channeling effect was first discovered in a binary collision approximation simulation in 1963 to explain the exponential tails in experimentally observed ion range distributions that did not follow the standard theories of ion penetration. The simulated prediction was confirmed experimentally in the following years by measurements of ion penetration depth in single crystalline Tungsten.

When the direction of the incident beam is along the crystallographic direction of a single crystal, majority of ions penetrate into the crystal. Channeled particles do not go close enough to the atomic nuclei due to the alignment of the incident beam wrt. the target which forbids large angle Rutherford scattering and hence the yield gets significantly reduced. However, there will always be full interaction at the surface of the crystal. The channeling phenomenon and the RBS spectra under random and channeling conditions has been shown in fig 2.23

The trajectory of the incident projectile is such that the ion makes a grazing impact with the axis (axial channeling) or planes (Planar channeling) of the crystal and is steered by small angle scattering collisions at distance greater than $0.01A^{\circ}$ from the atomic nuclei. The channeling effect is always observed within an angular range which depends on the type of ion, the incident energy of the projectile, single crystal target and its specific crystallographic direction along which the beam is incident. It also depends on the thermal vibrational amplitude of the constituent atoms in the sample crystal.

1. Axial Channeling

When the direction of the incident beam is aligned along the crystallographic axis of the crystalline target, axial channeling occurs. This occurs within a very small angular range, which is expressed in terms of critical angle ($\psi_{1/2}$), and is given by

$$\psi_{1/2} = 0.8F_{RS}(\zeta)\psi_1 \tag{2.60}$$

where

$$\psi_1 = 0.307\left(\frac{Z_1Z_2}{Ed}\right)^{1/2} \tag{2.61}$$

where E is expressed in MeV, d is the inter atomic distance and F_{RS} is the continuum Moliere potential, evaluated at ζ. For a compound target, Z_2 is replaced by the average Z_2. ζ = $1.2u_1/a$, where a is the Thomas-Fermi screening radius and is written as

$$a = \frac{0.4685}{(Z_1^{1/2} + Z_2^{1/2})^{2/3}} \tag{2.62}$$

and u_1 is thermal vibration amplitude which can be evaluated form the Debye theory of thermal vibrations.

The ratio of the back scattering yield for the aligned direction with respect to the random direction is called as minimum yield (χ_{min}). It is a measure of the degree of crystallinity of the sample.

$$\chi_{min} = N_a d\pi(2u_1^2 + a^2) \tag{2.63}$$

where N_a is the atomic density of the target. For a good crystal, χ_{min} is very small at room temperature. From an analytical view point, the channeled component of the incident beam act as a probe to detect atoms which can be in substitutional or interstitial sites within the channel . In addition, the drastic reduction in the back scattering yield under the channeling condition improves the ion scattering sensitivity to light impurities on the surface.

ii. Planar Channeling

In comparison to axial channeling, planar channeling can be characterized by narrower critical angles and higher minimum yields. Planar channels have not been used extensively to determine the lattice location of impurities. Generally, planar channeling are used in alignment procedures to determine the axial directions. The planar half angle $\psi_{1/2}$ can be estimated from

$$\psi_{1/2} = kF_{PS}(\zeta, \eta)\psi_a \tag{2.64}$$

where the best fit to the energy dependent values of $\psi_{1/2}$ were found with

$$k = 0.72 \tag{2.65}$$

$$\zeta = \frac{1.6u_1}{a} \tag{2.66}$$

$$\eta = \frac{d_p}{a} \tag{2.67}$$

where d_p is the planar spacing and F_{PS} is the square root of the planar potential using Moliere's screening function and

$$\psi_a = 0.545\left(\frac{Z_1 Z_2 N d a}{E}\right)^{1/2} \tag{2.68}$$

An estimation of the planar minimum yield can be calculated from the continuum approximation

$$\chi = \frac{2a}{d_p} \tag{2.69}$$

RBS/C can be used to the characterize the layered epitaxial materials, single crystals, etc. This technique can also be used to study the crystalline quality, development of strain due to implantation, orientation of epilayers, and lattice location of impurities.

Figure 2.24: Pelletron Accelerator RBS - AMS System (PARAS) setup at IUAC [with permission]

In this thesis the RBS/C analysis was performed using a incident beam of 2 MeV He^+ ions using 1.7MV 5SDH-2 Pelletron Accelerator, at IUAC, as shown in fig 2.24. The beam divergence was less than $0.02°$, the spot diameter was 1mm, the scattering angle was 165° (laboratory coordinates) and the silicon surface barrier detector resolution was 20keV (Full Width at Half Maximum). Typically the beam current was 10nA, the charge was collected at 20μC and the chamber pressure was 1×10^{-6}Torr. The samples were mounted on a four axis goniometer which was used to obtain back scattering from random and channeling orientations, respectively. The energy calibration (0.988keV/channel) of the 2K channel analyzer was achieved with a standard reference siliocn sample coated with a very thin film of gold on the surface.

2.3 Metal Oxides: Crystal structure and properties

The metal oxides constitute a diverse and fascinating class of materials whose properties cover the entire range from metals to semiconductors and insulators. Their surfaces play crucial roles in an extremely wide range of phenomena. Metal oxides act as catalysts for a variety of commercially important reactions. Sometimes a metal oxide is used in its pure form, while in other cases the oxide is supported on another oxide, and the catalytic activity results from the interaction between the two oxides. All these catalytic reactions proceed by complex mechanisms that involve a range of different chemical interactions; these include acid/base reactions as well as oxidation and reduction steps where lattice oxygen are lost and gained by the substrate. A major landmark of transition metal oxide surfaces occurred in 1972 with the report by Fujishima and Honda [20] that TiO_2 could be used as a catalytic electrode in a photo electrolysis cell to decompose water into H_2 and O_2, without the application of external voltage. The crystal structure of metal oxide semiconductors is highly sensitive to the chemical environment around them, like presence of defects, incorporation of dopants, etc. which give rise to the changes in the surface as well as its bulk properties [21–23]. In the present thesis, rutile TiO_2 (110) single crystals, commercially purchased from MaTeck have been investigated. Studies of surface evolution of Tantalum surface using Kinetic Monte Carlo simulation technique have also been discussed in detail.

2.3.1 Titania (TiO_2)

TiO_2 was first discovered in 1791, when a chemist William Gregor examined sand from the local river. He used magnet to extract ilmenite ($FeTiO_3$), from which he removed iron by treatment with HCl. The residue was the impure oxide of a new element. A German scientist M. H. Klaproth independently discovered TiO_2 in 1795. There is a small percentage of titanium in many silicates and oxide minerals as Ti is the 9^{th} most abundant element in the earth crust. Bulk rutile TiO_2 is not found in nature [24]. TiO_2 is a widely used material in many areas like heterogeneous catalysts [25–28], waste water treatment [30], photo catalysis [29], bio compatible implants [31,32], in solar cells for the production of hydrogen and electric energy [29, 33], gas sensor [26, 34], and optical coating [35]. When bombarded with UV light, it becomes a sterile surface and for a long period of time afterwards, will kill any germs that come in contact with it [30, 36].

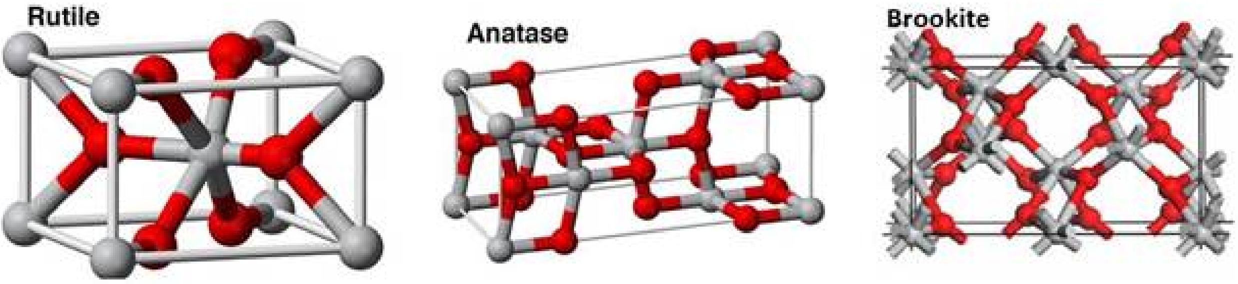

Figure 2.25: Crystal structure of TiO_2: (a) rutile, (b) anatase and (c) brookite. Red spheres represent the oxygen atoms in TiO_2 lattice (from ref [38]).

TiO_2 exists in three different forms which are Rutile (tetragonal structure), Anatase (tetragonal structure) and Brookite (Orthorhombic structure) [37], as shown in fig 2.25. Out of these three phases, anatase phase (lattice parameter $c/a > 1$) has been extensively studied due to its excellent photo catalytic properties [25–29, 37]. Variations in their phases can be understood in terms of octahedral (TiO_6^{2-}) differing by the distortion and connectivity of the octahedral chains. Rutile TiO_2 has a flat tetragonal cell with two Ti atoms and four O atoms. The Ti atoms are surrounded by six O atoms as in many ionic crystals the geometric structure is determined by the relative size of the ions and the coordination. The octahedral coordination of O atoms around the Ti atom is slightly distorted to accommodate all the ions. Bond length between Ti and O atoms are 1.946A° and 1.983A° for the four fold symmetric and two fold symmetric bonds respectively. The stability of the different TiO_2 crystal structures is in the following order: rutile $>$ brookite (+0.7 $kJmol^{-1}$) [39] $>$ anatase (+2.6 $kJmol^{-1}$) [40] with an error of $\pm$ 0.4 k J mol^{-1}, as reported by Navrotsky et.al [41].

The crystal structures for all the three phases of TiO_2 are shown in fig. 2.25. Their respective crystal parameters and physical characteristic are presented in table 2.1.

Table 2.1: Lattice parameters of TiO_2

	Rutile ([42,43])	Anatase ([43–45])	Brookite ([43–45])
Z^a	2	4	8
a($\mathring{A}$)	4.587	3.781	9.174
b($\mathring{A}$)	4.587	3.781	5.449
c($\mathring{A}$)	2.954	9.515	5.138
Volume^b	31.21	33.98	32.17
Formula Wt.	79.89	79.89	79.89
Crys. System	Tetragonal	Tetragonal	Orthorhombic
Point Group	4/mmm	4/mmm	mmm
Space Group	$P4_2/mnm$	$I4_1/amd$	Pbca
Band gap (eV)	3.2	3	2.96

a, b, c are the lattice parameters of the unit cell

[a] Z is the number of asymmetric units in the unit cell

[b] Volume is in $\mathring{A}^3$ per TiO_2 formula unit.

2.3.2 Tantalum (Ta)

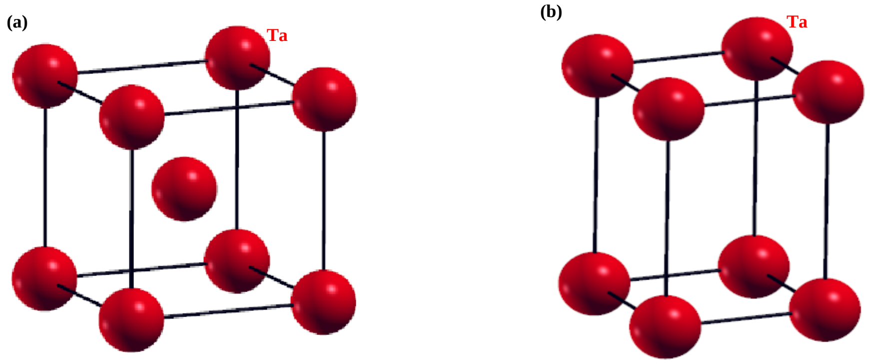

Figure 2.26: Crystal structure of Tantalum: (a) alpha and (b) beta. Red spheres represent the Tantalum atoms.

Tantalum is a chemical element having density 7.935g/cm^3 and atomic number 73. It was discovered in 1802 by Anders Ekeberg. Tantalum is widely used in the production of electronic components mainly capacitors and high power resistors [47]. The high melting point and oxidation resistance leads to the use of this metal in the production of vacuum furnace parts. Tantalum exists in two crystalline phases, alpha and beta. The alpha phase (as shown in fig 2.26(a)) has a Body Centered Cubic structure (space group lm3m, lattice constant, a = 0.33058 nm) [48]. It is soft and ductile. The beta phase (as shown in fig 2.26(b)), however, is hard and brittle. It has a tetragonal crystal symmetry (space group $p42/mnm$ and lattice parameters, a = 1.0194 nm, c= 0.5313 nm) [48]. The beta phase is the meta stable phase and converts to the alpha phase upon heating to $750°$ to $800°$. Therefore, bulk Tantalum is almost entirely alpha phase and the beta phase usually exists in thin films obtained by magnetorn sputtering, chemical vapor deposition [49].

Bibliography

[1] K. Siegbahn, and K. I. Edvarson, Al, Nuclear Physics **1**, 137 (1956).

[2] K. Siegbahn, Electron Spectroscopy for Atoms, Molecules and Condensed Matter, Nobel Lecture, December 8 (1981).

[3] A. Einstein, Ann. Phys. **31**, 132 (1905).

[4] D. Briggs and M. P. Seah, Practical surface analysis: by auger and x-ray photo-electron spectroscopy.

[5] R. W. Paynter, Surf. Inte. anal. **3**, 186 (1981).

[6] G. Binning, and H. Rohrer, Helv. Phys. Acta **55**, 726 (1982).

[7] G. Binning, H. Rohrer, C. Gerber, and E.Weibel, Phys. Rev. Lett. **50**, 120 (1983).

[8] Nikodem Tomczak, Kuan Eng Johnson Goh, Scanning Probe Microscopy, World Scietific Publishing.

[9] G. Binnig, C. F. Quate, and C. Gerber, Phys. Rev. Lett. **56**, 930 (1986).

[10] B. Lambart, Annalen der Physik und Chemie **86**, 78 (1852).

[11] J. Tauc, Materials Research Bulletin **3**, 37 (1968).

[12] X-ray scattering lecture note, D.Y. Noh from GIST.

[13] J. Als-Nielsen, and D. McMorrow, Elements of Modern X-ray physics, John Wiley and Sons, Ltd. (2001).

[14] Birkholz M. (2006) Thin Film Analysis by X-Ray Scattering. Wiley, Weinheim, 378 p.

[15] Introductory Raman Spectroscopy, By John R. Ferraro, Kazuo Nakamoto, Academic Press, 2012.

[16] Josephson, B. D., ”Possible new effects in superconductive tunnelling,” Physics Letters 1, 251 (1962)

[17] Magnetic Property Measurement System SQUID VSM Users Manual, Part Number 1500-100, C0

[18] S. Rubin, T.O. Passell and E. Bailey, Analytical Chemistry 29 (1957) 736.

[19] W. K. Chu, J. W. mayer and M. A. Nicolet, Backscattering Spectrometry, Academic Press, New York, (1978).

[20] A. Fujishima, and K. Honda, Nature **238**, 37 (1972).

[21] X. Chen, and S. S. Mao, Chem. Rev. **107**, 2891 (2007).

[22] S. Majumder, D. Paramanik, V. Solanki, B. P. Bag, and S. Varma, Appl. Phys. Lett. **98**, 053105 (2011).

[23] V. Solanki, S. Majumder, I. Mishra, P. Dash, C. Singh, D. Kanjilal, and S. Varma, J. Appl. Phys. **115**, 124306 (2014).

[24] D. C. Cronemeyer, Phys. Rev. **113**, 1222 (1956).

[25] M. Haruta, N. Yamada, T. Kobayashi, and S. Iijima, J. Catal. **115**, 301 (1989).

[26] C. R. Henry, Surf. Sci. Rep. **31**, 235 (1998).

[27] M. Haruta, CATTECH **6**, 102 (2002).

[28] C. C. Chusuei, X. Lai, K. Luo, and D. Goodman, Topics Catal. **14**, 71 (2001).

[29] M. Gratzel, Nature **414**, 338 (2001).

[30] N. Serpone, and E. Pelizzetti, Photocatalysis - Fundamentals and Applications, (John Wiley Sons, New York (1989).

[31] B. Kasemo, and J. Gold, Adv. Dent. Res. **13**, 8 (1999).

[32] S. Majumder, I. Mishra, U. Subudhi, and S. Varma, Appl. Phys. Lett. **103**, 063103 (2013).

[33] A. Fujishima, T. N. Rao, and A. D. Tryk, J. Photochem. Photobiol. C: Photochem. Rev. **1**, 1 (2000).

[34] W. Gopel, G. Rocker, and R. Feierabend, Phys. Rev. B **28**, 3427 (1983).

[35] H. K. Pulker, G. Paesold, and E. Ritter, Appl. Opt. **15**, 2986 (1976).

[36] A. Heller, Acc. Chem. Res. **28**, 503 (1995).

[37] M. Addamo, M. Bellardita, A. Di Paola, and L. Palmisano, Chem. Commun. 4943 (2006).

[38] http://www.geocities.jp/ohba_lab_ob_page/structure6.html.

[39] S. Chen, and A. Navrotsky, Am. Mineral. **95**, 112 (2010).

[40] A. A. Levchenko, G. Li, J. Boerio-Goates, B. F. Woodfield, and A. Navrotsky, Chem. Mater. **18**, 6324 (2006).

[41] A. Navrotsky, Chem. Phys. Chem. **12**, 2207 (2011).

[42] R. J. Swope, J. R. Smyth, and A. C Larson, Am. Mineral. **80**, 448 (1995).

[43] V. Swamy, J. D. Gale, L. S. Dubrovinsky, J. Phy. Chem. Sol. **62**, 887 (2001).

[44] M. Horn, C. F. Schwerdtfeger, and E. P. Meagher, Z.Kristallogr. **136**, 273 (1972).

[45] E. P. Meagher, and G. A Lager, Can. Mineral. **17**, 77 (1979).

[46] P. Kofstad, J. Electrochem. Soc. 109 (1962) 776.

[47] S. Maeng, L. Axe, T.A. Tyson, L. Gladczuk, M. Sosnowski, Corros. Sci. 48 (2006) 2154

[48] P. T. Moseley, C. J. Seabrook, Acta Crystallographica Section B Structural Crystallography and Crystal Chemistry 29 (5): 11701171 (1963).

[49] S. Lee, M. Doxbeck, J. Mueller, M. Cipollo, P. Cote, Surface and Coatings Technology. 177178: 44 (2004).

Chapter 3

Effect of Cobalt Implantation on Structural and Optical Properties of Rutile TiO_2(110)

3.1 Introduction :

Titanium dioxide (TiO_2) is a wide band gap semiconductor and has recently received immense attention due to its many exciting applications in photocatalysis, solar cells, gas sensors, white pigment, environmental remediation and self cleaning [1, 2]. TiO_2 has demonstrated to be a very effective photocatalyst, but due to the large band gap (3.2 eV for anatase and 3.0 eV for rutile) its excellent photo-absorption characteristics are primarily restricted to UV regime. Consequently, it absorbs visible light poorly and is ineffective in utilizing solar spectrum. Visible- light photo-absorption (PA) in TiO_2 has recently received enormous attention due to its overwhelming importance in photo-catalysis [3]. Bandgap engineering with dopants is considered an important route for enhancing the PA properties [4–7]. Numerous methods have been utilized to increase PA in TiO_2, e.g through dye sensitization, synthesis as thin films, formation of nanocrystals, incorporation of dopants by chemical methods, etc. [8]. However, organic dye can often become unstable at high temperatures which limits its application in device fabrication [8, 9]. On the other hand, preparation by chemical methods usually involve several complex steps for achieving desired band gap tailoring [8, 9]. PA properties in TiO_2 have mostly been investigated on anatase phase which is a metastable phase. Though it forms easily, it gets transformed to rutile phase at high temperatures [8]. Rutile, on the other hand, is the less explored phase but its high stability makes it an attractive candidate for developing devices for photo-catalytic applications [8, 10]. This high temperature stability in tailored rutile TiO_2 photo-catalysts plays vital role in many applications such as anti bacterial self cleaning coatings on ceramic materials like tiles, glass, sanitary wares, etc., which require high processing temperatures [11–13].

Tuning optical properties of TiO_2 is an active area of research. In this direction, doping of several non-metals like N, C, S [4–6, 14] and metals such as Ni, Pt, Cu, Ag [3, 15–17] in TiO_2 thin films have been undertaken via normal doping methods [15–17] and by implantation techniques [18–21]. Incorporation of transition metal like Co in TiO_2 has generated immense interest due to its attractive properties of optical absorption characteristics [20, 22] compounded with room temperature ferromagnetic behavior [18, 19]. Though such studies on single crystals can provide more reliable and specific results without any controversies surrounding the preparation methods as observed in many magnetic studies after Co implantation in TiO_2 single crystals [23, 24], such investigations on photo-absorption properties are not reported in literature.

Implantation with ions is an immensely attractive technique for achieving controlled introduction of dopants in any lattice [25]. Moreover, this usually requires only a single step processing. Theoretically also, the technique is based on well-established understanding that provides good control on physical parameters. Non equilibrium conditions during implantation can generate many vacancy states as well as self organized nano- patterns on the surface [26–28], both of which have demonstrated to play crucial role in photo-catalysis [25]. On oxide surfaces, like TiO_2, surface- vacancies hold promise for becoming photoactive sites [25, 26]. Optically active nature of Cobalt atoms demonstrate many interesting properties [8, 25] and is expected to promote PA properties.

The present study investigates the enhanced photo-absorption characteristics of rutile TiO_2 (110) after it is implanted with Cobalt ions. Implantation results in the development of Ti-rich nanostructures as well as oxygen vacancy states on the surfaces. Development of $Ti_{1-x}Co_xO_2$ phase at low fluences as well as formation of hcp- Cobalt clusters and $CoTiO_3$ at high fluences is observed. Interestingly, enhanced photo-absorption is noticed in both UV and Visible regimes. Though the increase in UV regime is $\sim$1.7 times compared to the pristine TiO_2, surprisingly, the visible light absorption increases by almost 5 times. Creation of self organized nanostructures and Ti^{3+} oxygen vacancy states as well as development of Cobalt nano-clusters after implantation play concerted role in enhancing the photo-absorption characteristics. Such high visible light photo-absorption as observed here, with Cobalt implantation, has never been reported earlier and can be very significant for photo-catalytic applications.

3.2 Experimental :

Untreated Single crystals $5mm \times 5mm \times 1mm$ of rutile TiO_2 (110) (from MaTeck) were implanted with 200 keV Cobalt ions with fluences of 1×10^{16}, 5×10^{16} and 1×10^{17} ions/cm^2, at room temperature. Ions were incident normal to TiO_2 surface with a flux of 1.6×10^{13} ions/cm^2.sec. The projected range and the longitudinal straggling of Co ions in TiO_2 lattice have been estimated using SRIM code to be 98 and 10 nm, respectively [29]. Scanning Probe Microscope (SPM) from Bruker (Nanoscope V) was used in tapping mode for studying surface morphology. High resolution X-ray Diffraction (XRD) measurements were performed on a Bruker system (CuK$_\alpha$ source). Core level studies were undertaken on a VG X-ray Photoelectron Spectroscopy (XPS) system (Mg-K$_\alpha$ source) at 20 eV pass energy with a take off angle of 30° w.r.t. surface normal. For UV-Vis absorption studies, Shimadzu spectrophotometer was utilized. Micro Raman scattering studies were carried out with 514 nm Laser in backscattering geometry on a T64000 triple monochromator Horiba Jobin Yvon system having a liquid nitrogen cooled CCD detector.

3.3 Results and Discussions :

Fig. 3.1 shows morphology from TiO_2(110) surfaces both prior to and after Co ion implantation. Pristine (un-irradiated) surface displays presence of steps (fig. 3.1(a)) as expected on TiO_2(110) [30]. After implantation of 1×10^{16} ions/cm^2, surfaces are observed to be decorated with nanostructures (one marked by a circle in fig. 3.1(b)). Such spontaneous formation of nanostructures (NS) takes place due to many competing processes during irradiation, e.g. differential erosion mechanisms which are weaker at surface- crests than troughs, diffusion gradient of surface atoms

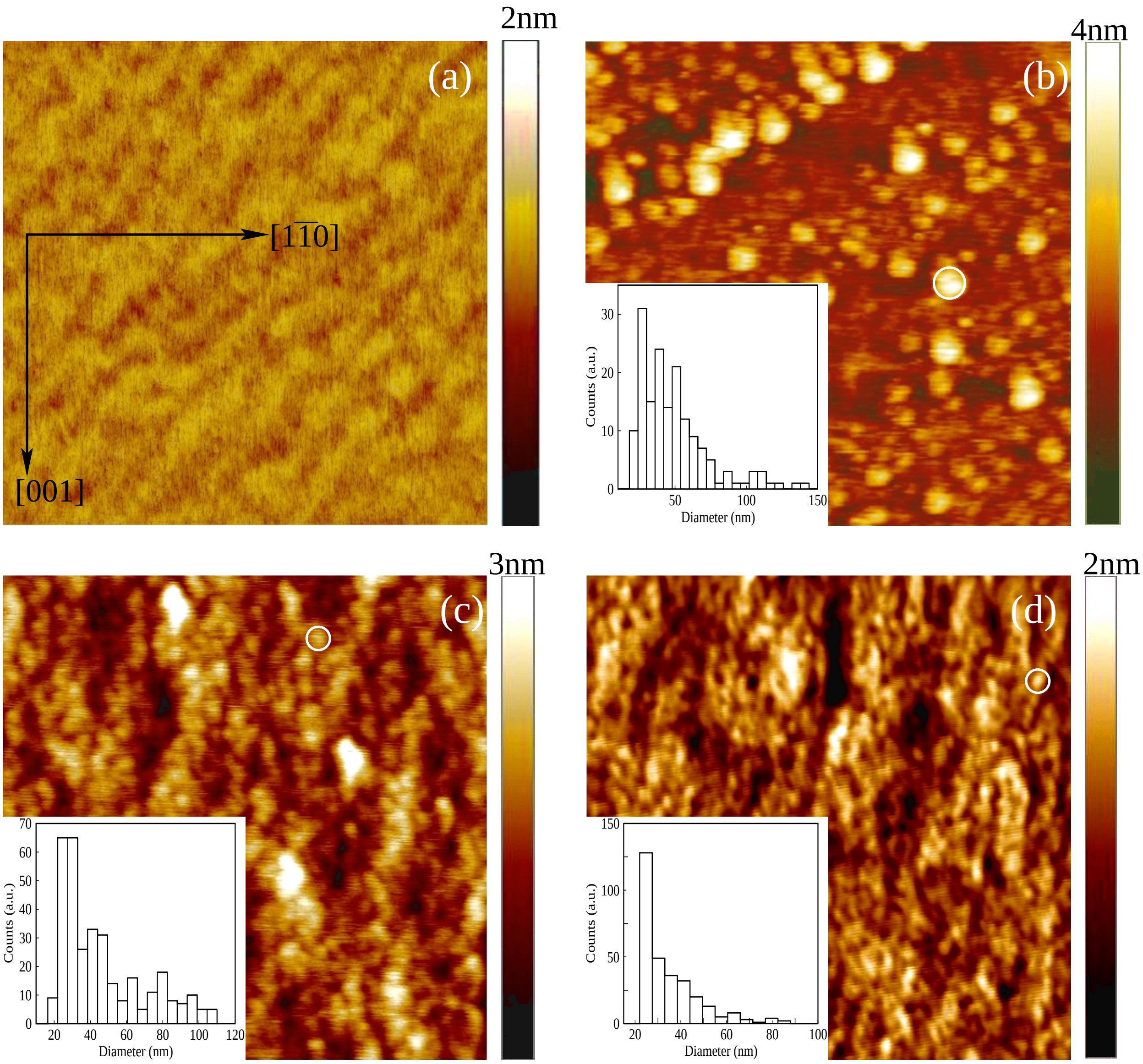

Figure 3.1: AFM images ($1\mu m \times 1\mu m$) of (a) Pristine rutile TiO_2 (110) and after Cobalt ion implantation with fluences of (b) $1{\times}10^{16}$, (c) $5{\times}10^{16}$, and (d) $1{\times}10^{17}$ ions/cm^2. Crystallographic directions are shown on the Pristine surface and were kept same for all the implanted samples. A representative nanostructure is marked by a solid circle at all fluences. Size distribution of nanostructures is shown in the inset.

along crystallographic axes, solid mass flow etc. [31, 32]. In addition, some defect sites may also develop that promote the nucleation of nanostructures [27]. Interestingly, NS (in fig. 3.1(b)) appear to be decorating the step edges of the terraces observed (in fig. 3.1(a)) on the pristine TiO_2. This may be related to the preferential nucleation sites at the step edges, due to the presence of kink sites, as observed in MBE grown InP/InGaP [33]. The size (diameter) distribution for NS (inset fig. 3.1(b)) shows that about 25% are smaller than 30 nm and largest are about 150 nm. After implantation with 5×10^{16} ions/cm^2, more smaller NS which are, surprisingly, mostly arranged along the [001] surface crystallographic direction (fig. 3.1(c)), instead of at steps edges (like in fig. 3.1(b)) are observed. Here, largest NS are about 110 nm in size and nearly 43% are smaller than 30 nm (inset fig. 3.1(c)). NS remain arranged along [001] surface axis but reduce further in size after the fluence of 1×10^{17} ions/cm^2 with largest NS being only 90 nm and almost 59% being smaller than 30 nm (fig. 3.1(d)). This scenario of observing smaller sized NS with increasing fluence can be explained by the systematic fragmentation of existing NS, created at lower fluences, along with the predominant generation of smaller NS at latter stages. Ion beams can be responsible for the fragmentation of NS through erosion. Anisotropic surface diffusion manifests in the systematic assembling of NS along [001] [34]. With varying fluences, the heights of NS remain nearly same and are found to be 1.5, 1.1 and 1.6±0.2 nm for 1×10^{16}, 5×10^{16} and 1×10^{17} ions/cm^2, respectively, whereas the corresponding rms surface roughness is 0.36 nm, 0.43 nm and 0.52 nm (0.089 nm for pristine).

Ti(2p) XPS spectra are presented in fig. 3.2. For pristine TiO_2 two main features, $2p_{3/2}$ and $2p_{1/2}$ (at 458.6 and 464.3 eV) corresponding to Ti^{4+} co-ordination sites on the surface are observed [26]. Due to shakeup effects, each of these features have an additional component, *sat*, on the high binding energy (BE) side [35]. No signs of any impurity or vacancy were noticed. After Co ion implantation with 1×10^{16} ions/cm^2 both the main features, $2p_{3/2}$ (458.3 eV) and $2p_{1/2}$ (464.1 eV), show a *new feature* at the lower BE side (fig. 3.2(b)) reflecting the development of Ti^{3+} oxygen vacancy sites [36]. Ion implantation of oxides, like TiO_2, can produce preferential sputtering of oxygen atoms with the associated 2p-electrons getting transferred to the empty 3d orbitals of the neighboring Ti atoms on the surface leading to the development of two Ti^{3+} oxygen vacancy sites. Presence of oxygen vacancies also leads to the formation of Ti-rich zones which become the nucleation centers for the nanostructure formation [37]. Formation of Ti^{3+} oxygen vacancy states

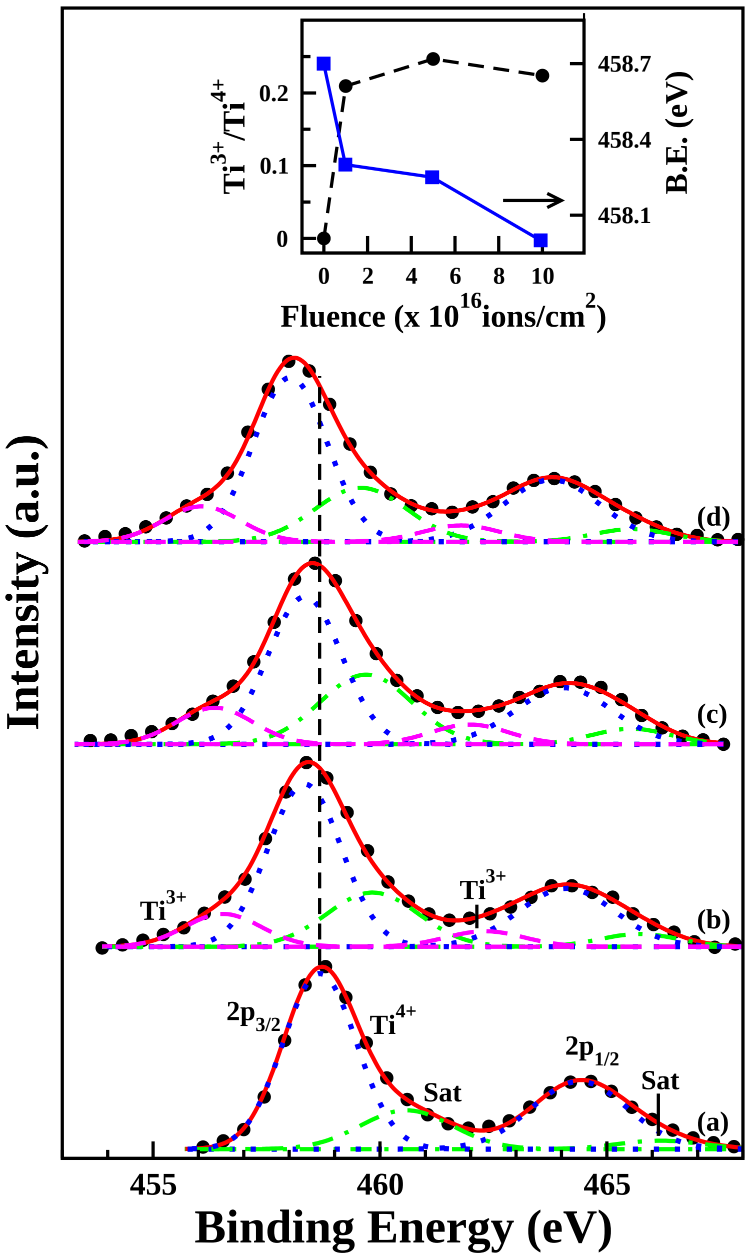

Figure 3.2: Ti(2p) XPS core level spectra for (a) Pristine TiO$_2$ and after Cobalt ion implantation with fluences of (b) 1×10^{16}, (c) 5×10^{16}, and (d) 1×10^{17} ions/cm^2. Inset shows the ratio (- - - -) of Ti^{3+}/Ti^{4+} and variation in BE of 2p$_{3/2}$ (——) as a function of fluence. •: experimental data, ——: full fitting, - - - - : Ti^{3+}, –·–·– : sat, ········: Ti^{4+}

have been observed in earlier studies also [38, 39].

XPS is a very surface sensitive technique with photoelectron intensity displaying an exponentially decaying characteristics with depth. For the energies of interest, here, the mean free path of the electron or the probe depth is about 1 nm. With the NS height being about 1-1.6 nm, XPS results here can be attributed to be from them. Ti^{3+} vacancy states have been observed at all the implantation fluences (fig. 3.2) and their ratio w.r.t. Ti^{4+} state is shown (in inset). After implantation, the Ti^{4+} component of $2p_{3/2}$ state demonstrates a slight shift towards the lower BE which increases with fluence (inset fig. 3.2) suggesting an increased electron density for Ti atoms. This is confirmed by the results presented below from XRD, UV-Vis and Raman scattering where development of $Ti_{1-x}Co_xO_2$ is noticed upon implantation, thus leading to electron transfer from Co to Ti^{4+} sites [40].

Fig. 3.3(a-d) displays the oxygen XPS spectra for pristine and cobalt implanted TiO_2. The O(1s) feature of pristine TiO_2 has been deconvoluted into three peaks. The feature at lowest binding energy can be attributed to oxygen attached to Ti^{4+} sites, while the peak around 531.8 eV is coming due to some hydroxyl group (Ti-OH) attached to the surface [41]. The highest binding energy component at 533.1 eV is assigned to chemisorbed oxygen species which got adsorbed on the surface [41]. The presence of adsorbed hydroxyl species (OH) generally takes place on coordinatively unsaturated Ti sites. This is a thermodynamic energetic requirement to stabilize such sites and is known to occur on the surface of metal oxides. After being irradiated, there is an overall shift towards lower binding energy in the spectrum which is due to charge transfer from ligand to metal and a new feature at 531.2 eV has come up which was absent in unirradiated surface. This feature is due to Oxygen vacancies which have come up due to ion implantation. The presence of O-Ti3+ at higher binding energy component compared to O-Ti^{4+} is also confirmed with correlated studies [41]. This is due to the high polarizability of octahedral site as compared to tetrahedral site. This is in agreement with the structure of Ti_2O_3 which is a trigonal lattice where the Ti^{3+} ions occupy octahedral sites.

The XRD results from the pristine and Co implanted TiO_2 are presented in fig. 3.4. These display prominent features at 27.5° and 56.7° corresponding to the (110) and (220) crystalline

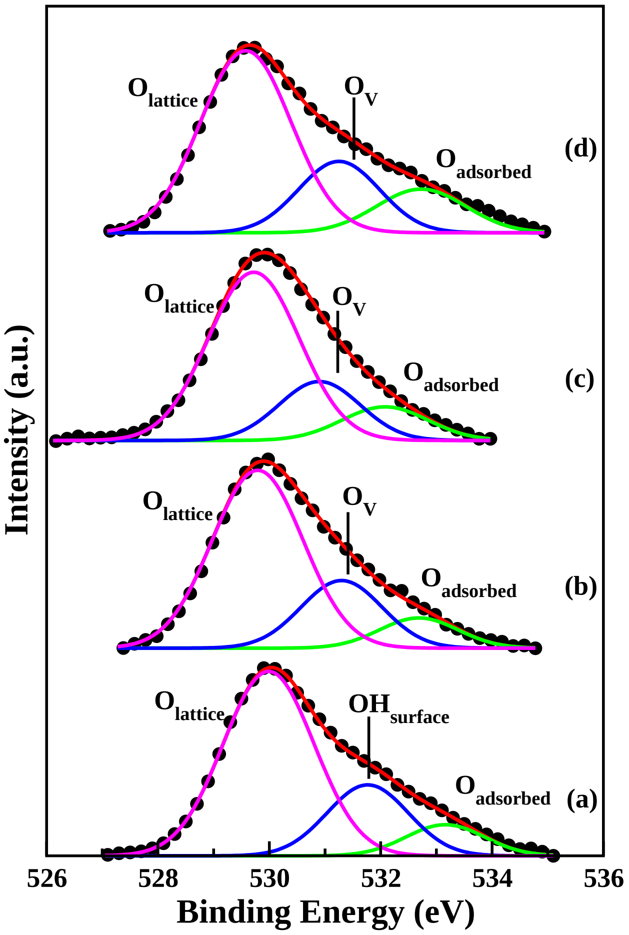

Figure 3.3: O(1s) XPS core level spectra for (a) Pristine TiO_2 and after Cobalt ion implantation with fluences of (b) 1×10^{16}, (c) 5×10^{16}, and (d) 1×10^{17} ions/cm^2.

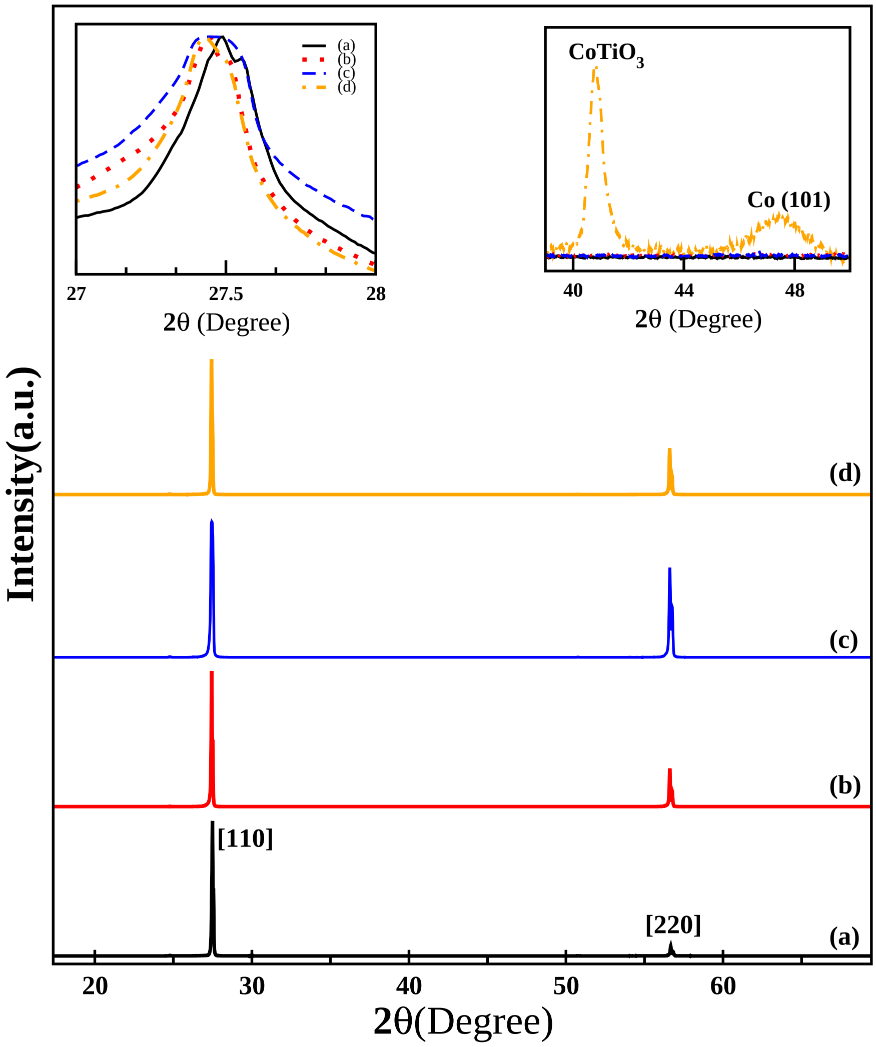

Figure 3.4: XRD spectra for (a) Pristine rutile TiO_2 and after Cobalt ion implantation with fluences of (b) 1×10^{16}, (c) 5×10^{16}, and (d) 1×10^{17} ions/cm^2. All the spectra are normalized wrt (110) Bragg reflection peak of pristine. Left inset shows HRXRD of (110) feature at all fluences and right inset shows HRXRD of $2\theta \sim$ 40- 50° region for all fluences.

planes in rutile TiO_2 [42]. After Co implantation, (110) feature systematically shifts towards lower diffraction angles and its FWHM also increases with fluence (left inset). The former is a signature of the increased inter-planar spacing (d) whereas the latter indicates reduction in the long ranged lattice ordering upon implantation. Both these observation indicate formation of $Ti_{1-x}Co_xO_2$ phase via the substitutional incorporation of Co ions in the TiO_2 lattice as their ionic radii are similar (Co:79.0 pm and Ti:74.5 pm) [43]. Formation of Ti^{3+} oxygen vacancies, as exhibited by XPS (fig. 3.2), after implantation can also generate strain in the host lattice causing modifications in the d-spacing [44].

High Resolution XRD from region $2\theta \sim$ 40- 50° is also presented and displays development of Co clusters at the highest fluence of 1×10^{17} ions/cm^2 only, and not for lower fluences (right inset, fig. 3.4). Two distinct features at 40.7° and 47.3° denote the formation of $CoTiO_3$(210) phase and hcp Co(101) nano-clusters within the TiO_2 lattice. Formation of hcp Co clusters agrees with earlier results [18, 19]. Absence of Co related diffraction features at lower fluences can be due to low Co content which gets incorporated into TiO_2 lattice to form $Ti_{1-x}Co_xO_2$ phase [43]. On the other hand, development of hcp Co(101) clusters and $CoTiO_3$(210) at the highest fluence can be attributed to Co ions reaching solubility limit at this stage.

Rutile TiO_2 is tetragonal and belongs to the point group D_{4h}^{14} with two TiO_2 molecules per unit cell [45]. Raman spectrum (fig. 3.5) from the pristine displays two prominent rutile TiO_2 features at 447 and 610 cm^{-1}. The former is attributed to E_g mode from inharmonious vibrations of oxygen atoms along the c-axis, which is two fold degenerate and non polar [45]. The latter is the polar A_{1g} mode which is due to the out of phase vibration of apical and equatorial oxygen ions along the unit dipole vector i.e. [110] crystallographic direction [45]. Intensity of A_{1g} mode decreases upon implantation due to the substitutional incorporation of Co atoms in the host lattice which in turn generates defects in the lattice. E_g mode being very sensitive to Ti^{3+} oxygen vacancies, decrease in its intensity with implantation reflects reduction in TiO_2 lattice stoichiometry after the formation of these vacancy states. Raman spectrum at the highest fluence shows a new feature at 675 cm^{-1} (fig. 3.5(d)), not observed for pristine or after implantation at lower fluences. This is attributed to the formation of $CoTiO_3$ [46]. Absence of this Raman feature (675 cm^{-1}) after implantation with

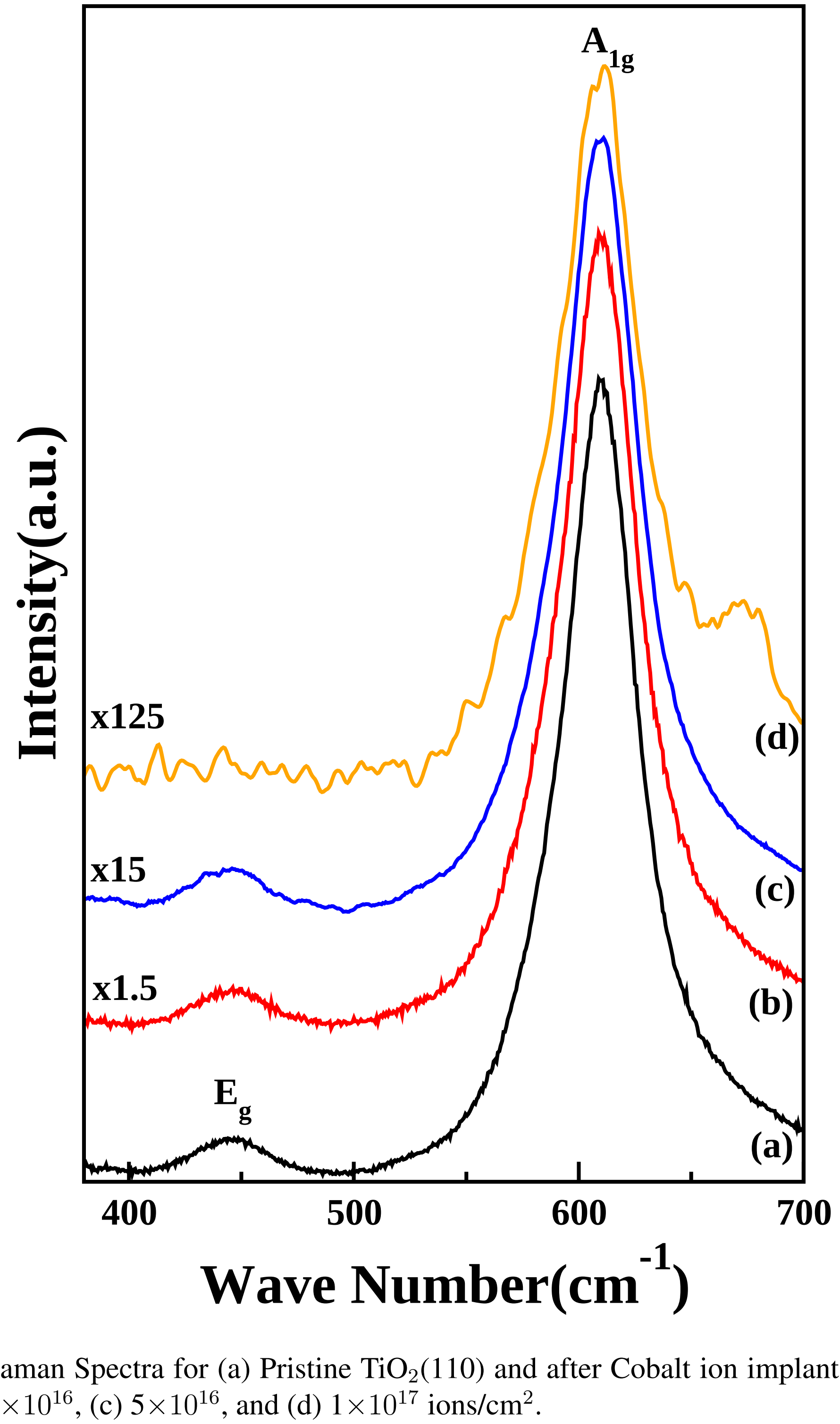

Figure 3.5: Raman Spectra for (a) Pristine TiO_2(110) and after Cobalt ion implantation with fluences of (b) 1×10^{16}, (c) 5×10^{16}, and (d) 1×10^{17} ions/cm^2.

1×10^{16} and 5×10^{16} ions/cm^2 is due to small concentration of Co at these fluences. However, at these low fluences decrease in intensity of the main A1g feature, compared to pristine, indicates formation of secondary phase like $Ti_{1-x}Co_xO_2$ through substitutional incorporation of Co in the TiO$_2$ lattice. Absence of any distinct shifts in Raman features is also due to small concentration and substitutional incorporation [47]. XRD results presented earlier (fig. 3.4) have also indicated formation of $Ti_{1-x}Co_xO_2$ phase.

Photo absorbance measurements are presented in fig. 3.6 where pristine TiO$_2$ displays a band gap, E1, at 3.25 eV due to optical transitions [48] from O(2p) valance band to Ti(3d) conduction band. After implantation with Co ions, a distinct reduction in E1 with fluence, is also noticed (inset). This reduction in band gap can be explained by sp-d exchange interactions between the band electrons and the localized d electrons of Co^{2+} ions from Ti$_{1-x}$Co$_x$O$_2$ and CoTiO$_3$ at low and high fluences, respectively. Exchange interactions promote narrowing of E1 through the lowering of conduction band energy combined with upward shifting of valance band edge [49]. Similar reductions have also been observed in thin films doped with Co atoms [50]. The band edge tail in the region 400-450 nm, in pristine and other fluences, corresponds to the optical absorption due to the surface states. Smearing of this tailing edge at the highest fluence can be attributed to the high absorbance from substituted Co ions in this region [51]. Instead however at the highest fluence two new features, not present in pristine, are observed at 305 and 535 nm (fig. 3.6(d)). The former feature can be explained by quantum confinement effects [52], which according to thermodynamic studies are pronounced for TiO$_2$ nanostructures of sizes smaller than $\sim 27nm$ [53, 54] and in the present study at the highest fluence about 60% NS on the surface are smaller than 30 nm (fig. 3.1). The feature at 535 nm (marked by arrow), due to the octahedral Co^{2+} $\rightarrow Ti^{4+}$ inter valance charge transfer, corresponds to the substitutional incorporation of Co in TiO$_2$ lattice [55] and formation of CoTiO$_3$, thus confirming the XRD and Raman Scattering results. Similar edge is also delineated at lower fluences (fig. 3.6(b, c)) due to the presence of Ti$_{1-x}$Co$_x$O$_2$, but the intensity is very weak for 1×10^{16} ions/cm^2 (fig. 3.6(b)).

Distinct increase in both UV and Visible photo- absorbance (PA), compared to pristine TiO$_2$, is observed in fig. 3.6 after Co implantation. In addition, visible absorption delineates systematic

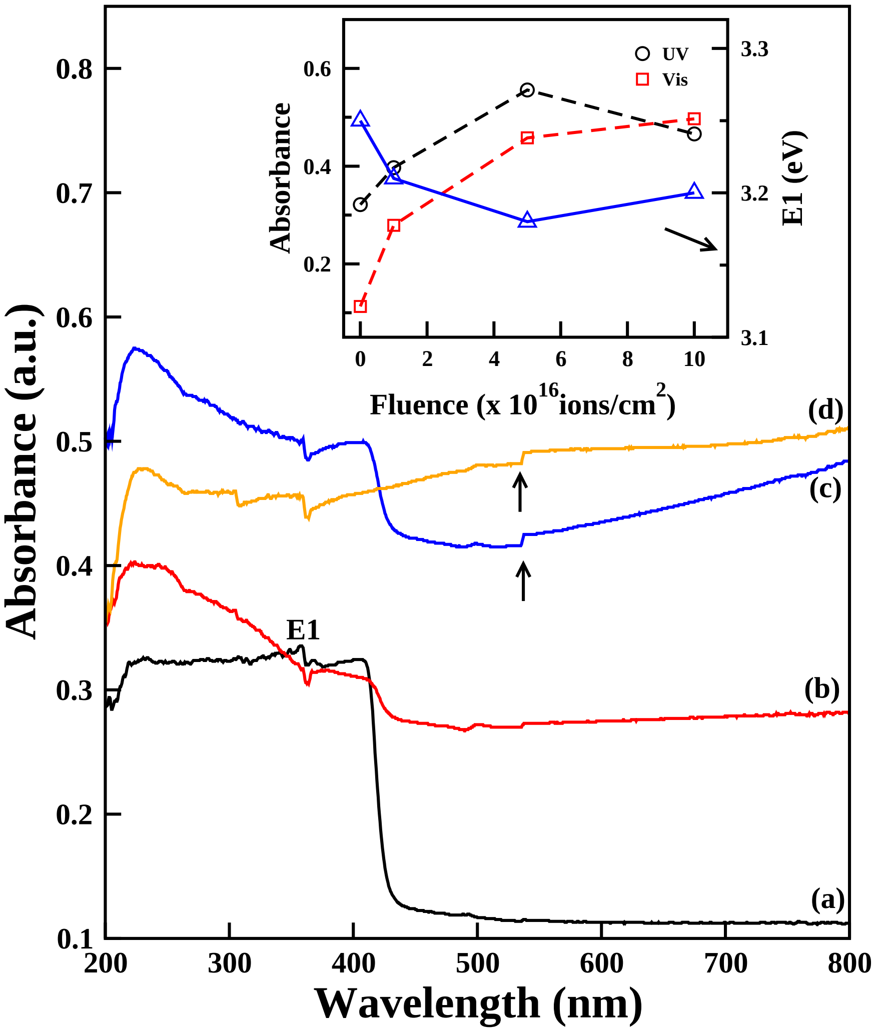

Figure 3.6: UV-Vis absorbance spectra from (a) Pristine TiO_2 and after Cobalt ion implantation with fluences of (b) 1×10^{16}, (c) 5×10^{16}, and (d) 1×10^{17} ions/cm^2. Inset shows variation in bandgap E1 (——) as a function of ion fluence. Inset also shows Photo-Absorbance (- - - -) measured at two wavelengths of 200 nm (UV) and 700 nm (Vis) as a function of ion fluence.

increase as a function of fluence. This is a compelling result demonstrating control of Visible photo-absorption with implantation. Photo absorption at two representative wavelengths, 200 nm (UV) and 700 nm (Visible) are shown in the inset. Though PA in UV region increases by about 1.7 times at the highest fluence, compared to pristine, the enhancement in the visible region is surprisingly 5 times. Photo-absorption studies of 40 keV Co ion implantation in nano-crystalline TiO2 thin films, synthesized by solgel and spin-coating techniques on glass substrates, also demonstrated shift of absorption range to higher wavelength which was ascribed to development of Co energy level in the bandgap [20]. For their highest fluence, an increase in absorption by about 1.4 and 2.5 times is observed in UV and visible ranges, respectively [20]. Formation of d bands arising from the substituted Co atoms, that form $\mathrm{Ti}_{1-x}\mathrm{Co}_x\mathrm{O}_2$ and CoTiO_3 compounds respectively at low and high fluences, as observed here, can be responsible for these observations. In ligand field theory, the ground state of Co^{2+} (d^7) is $^4T_{1g}(^4F)$ and the first excited state is $^4T_{1g}(^4P)$. The absorption band in visible region are due to ligand field transitions, $^4T_{1g}(^4F) \rightarrow ^4 T_{1g}(^4P)$ in the octahedral coordination [56]. In addition to the formation of Co clusters, development of Ti-rich nanostructures and Ti^{3+} vacancy states during implantation also play very crucial role in significantly enhancing the PA. Oxygen vacancies can act as trapping center for electrons [10,26,37]. The mean free path of electrons gets significantly reduced inhibiting the electron-hole recombination process which promotes photo- absorption and photocatalysis.

3.4 Conclusion :

In conclusion, we have investigated the structural, optical and photo-absorption properties of Cobalt implanted rutile TiO_2(110). The presented results show a remarkable increase in UV and Visible light photo-absorption characteristics. At the highest fluence, the increase is UV regime is about 1.7 times, but in Visible it is surprisingly large, 5 times. Creation of CoTiO_3 phase, suggested by XRD, Raman and photo-absorbance results, seems to be the dominant factor controlling the enhanced visible light photo-absorption observed here. Development of nanostructures as well as Oxygen vacancies, as confirmed by AFM and XPS, limit the electron mean free path and decrease the e-h recombination.These results are crucial for enhancing the photo-absorption properties which can have wide applications in photo-catalysis.

Bibliography

[1] H. Li, Y. Zhang, S. Wang, Q. Wu, and C. Liu, J. Hazard. Mater. **169**, 1045 (2009).

[2] U. Diebold, Surf. Sci. Rep. **48**, 53 (2003).

[3] G. Akpan and B. H. Hameed, Applied Catalysis A. General **375**, 1 (2010).

[4] R. Asahi, T. Morikawa, T. Ohwaki, K. Aoki, and Y. Taga, Science **293**, 269271 (2001).

[5] S. U. M. Khan, M. A. Shahry, and W. B. Ingler Jr., Science **297**, 22432245 (2002).

[6] X. H. Tang and D. Y. Li, Journal of Physical Chemistry C **112**, 54055409 (2008).

[7] Y. F. Li, D. H. Xu, J. I. Oh, W. Z. Shen, X. Li, and Y. Yu, ACS Catalysis **2**, 391398 (2012).

[8] J. Choi, H. Park, and M. R. Hoffmann, J. Phys. Chem. C **114**, 783-792 (2010).

[9] F. Dong, W. Zhao, and Z. Wu, Nanotechnology **19**, 365607 (2008).

[10] X. Pan, M. Q. Yang, X. Fu, N. Zhang, and Y. J. Xu, Nanoscale **5**, 3601 (2013).

[11] A. Fujishima, T. N. Rao, D. A. Tryk, J. Photochem. Photobiol. C: Photochem. Rev. **1**, 121 (2001).

[12] O. Carp, C. L. Huisman, A. Reller, Prog. Solid State Chem. **32**, 33177 (2004).

[13] P. Periyat, K. V. Baiju, P. Mukundan, P. K. Pillai, K. G. K. Warrier, Applied Catalysis A: General **349**, 1319 (2008).

[14] J. G. Yu, G. P. Dai, Q. J. Xiang, and M. Jaroniec, Journal of Materials Chemistry **21**, 10491057 (2011).

[15] D. H. Kim, K. S. Lee, Y. S. Kim, Y. C. Chung, S. J. Kim, J. Am. Ceram. Soc. **89**, 515 (2006).

[16] S. Kim, S. J. Hwang, W. Choi, J. Phys. Chem. B **109**, 24260 (2005).

[17] M. S. Lee, S. S. Hong, M. Moheseni, J. Mol. Catal A **242**, 135 (2005).

[18] O. Yildirim, S. Cornelius, A. Smekhova, G. Zykov, E. A. Ganshina, A. B. Granovsky, R. Hbner, C. Bhtz, and K. Potzger, J. Appl. Phys. **117**, 183901 (2015).

[19] N. Akdogan, A. Nefedov, H. Zabel, K. Westerholt, H. W. Becker, C. Somsen, S. Gok, A. Bashir, R. Khaibullin, and L. Tagirov, J. Phys. D. Appl. Phys. **42**, 115005 (2009).

[20] Y. N. Shieh, Y. Y. Chang, Thin Solid Films **518**, 7464 (2010).

[21] L. Z. Qin, H. Liang, B. Liao, A. D. Liub, X. Y. Wub, J. Sun, NIMB **307**, 385-390 (2013).

[22] R. Amadelli, L. Samiolo, A. Maldotti, A. Molinari, M. Valigi, D. Gazzoli, Int. J. Photoenergy **2008**, 853753 (2008).

[23] R. I. Khaibullin, L. R. Tagirov, B. Z. Rameev, S. Z. Ibragimov, F. Yildiz, and B. Aktas, J. Phys. : Condens. Matter **16**, L443-L449 (2004).

[24] C. Silva, A. R. G. Costa, R. C. D. Silva, L. C. Alves, L. P. Ferreira, M. D. Carvalho, N. Franco, M. Godinho, and M. M. Cruz, Jour. Mag. and Mater. **364**, 106-116 (2014).

[25] A. L. Stepanov, Rev. Adv. Mater. Sci. **30**, 150-165 (2012).

[26] V. Solanki, S. Majumder, I. Mishra, P. Dash, C. Singh, D. Kanjilal and S. Varma, J. Appl. Phys. **115**, 124306 (2014).

[27] D. Paramanik, S. R. Sahoo, S. Majumder, P. S. Raman, and S. Varma, Vacuum **84**, 602 (2010);D. Paramanik, S. N. Sahu, and S. Varma, J. Phys. D: Appl. Phys. **41**, 125308 (2008).

[28] S. R. Joshi, T. Bagarti, S. Varma, Surf. Sci. **641** 170 (2015).

[29] J. F. Ziegler, M. D. Ziegler, and J. P. Biersack, Nucl. Instru. Meth. B **268**, 1818 (2010).

[30] S. Fischer, A. W. Munz, K. D. Schierbaum, and W. Gopel, J. Vac. Sci. Tech. B **14**, 961 (1996).

[31] R. M. Bradley and J. M. E. Harper, J. Vac. Sci. Technol. A **6**, 2390 (1988).

[32] T. Kumar, A. Kumar, D. C. Agarwal, N. P. Lalla and D. Kanjilal, Nanoscale Res. Lett. **8**, 336 (2013),T. Kumar, A. Kumar, N. P. Lalla, S. Hooda, S. Ojha, S. Verma and D. Kanjilal, Appl. Surf. Sci. **283**, 417 (2013).

[33] S. Varma, C. M. Reaves, V. B. Hill, S. P. DenBaars and W. H. Weinberg, Surface Science **393** 24 (1997).

[34] M. Kolmer, A. A. Zebari, M. Goryl, F. Buatier de Mongeot, F. Zasada, W. Piskorz, P. Pietrzyk, Z. Sojka, F. Kork and M. Szymonski, Phys. Rev. B **88**, 195427 (2013).

[35] M. A. Khan, A. Kotani, and J. C. Parlebas, J. Phys. Condens. Matter. **3**, 1763-1772 (1991).

[36] H. Y. Jeong, J. Y. Lee, S. Y. Choi and J. W. Kim, Appl. Phys. Lett. **95**, 162108 (2009).

[37] S. Majumder, I. Mishra, U. Subudhi and Shikha Varma, Appl. Phy. Lett. **103**, 063103 (2013), S. Majumder, D. Paramanik, V. Solanki, B. P. Bag, and Shikha Varma, Appl. Phys. Lett. **98**, 053105 (2011).

[38] Z. Zhao, X. Zhang, G. Zhang, Z. Liu, D. Qu, X. Miao, P. Feng, and Z. Sun, Nano Research, doi:10.1007/s12274-015-0917-5.

[39] O. Yldirim, S. Cornelius, M. Butterling, W. Anwand, A. Wagner, A. Smekhova, J. Fiedler, R. Bttger, C. Bhtz, and K. Potzger, Appl. Phys. Lett., **107** 242405 (2015).

[40] Y. Liu, J. H. Wei, R. Xiong, C. X. Pan, and J. Shi, Appl. Surf. Sci. **257**, 8121 (2011).

[41] J. Fang, X. Bi, D. Si, Z. Jiang, and W. Huang, Appl. Surf. Sci. **253**, 8952 (2007).

[42] S. Zhou, G. Talut, K. Potzger, A. Shalimov, J. Grenzer, W. Skorupa, M. Helm, J. Fassbender, E. izmar, S. A. Zvyagin, and J. Wosnitza, J. Appl. Phys. **103**, 083907 (2008).

[43] Y. Matsumoto, M. Murakami, T. Shono, T. Hasagawa, T. Fukumura, M. Kawasaki, P. Ahmet, T. Chikyow, S. Koshihara and H. Koinuma, Science **291** 854 (2001).

[44] D. Ma, Z. Lu, Y. Tang, T. Li, Z. Tang, and Z. Yang, Physics Letters A **378**, 2570-2575 (2014).

[45] S. P. S. Porto, P. A. Fleury, and T. C. Damen, Phys. Rev. **154**, 522 (1967).

[46] C. Huang, X.Liu, L. Kong,W. Lan, Q.Su, Y.Wang, Appl. phys. A **87**, (2007) 781.

[47] B. Santara, B. Pal, and P. K. Giri, Journal of Applied Physics **110**, 114322 (2011).

[48] A. K. Rumaiz, J. C. Woicik, E. Cockayne, H. Y. Lin, G. H. Jaffari, and S. I. Shah, Appl. Phys. Lett. **95**, 262111 (2009).

[49] K. Ando, H. Saito, Z. Jin, T. Fukumura, M. Kawasaki, Y. Matsumoto, H. koinuma, J. Appl. Phys. **89**, 7284 (2001).

[50] F. Gracia, J. P. Holgado, A. Caballero, A. R. Gonzalez-Elipe, J. Phys. Chem. B **108**, 17466 (2004).

[51] M. Ivill, S. J. Pearton, S. Rawal, L. Leu, P. Sadik, R. Das, A. F. Hebard, M. Chisholm, J. D. Budai, D. P. Norton, New. Jour. Phys. **10** (2008) 065002.

[52] L. Chiodo, J. M. G. Lastra, D. J. Mowbray, A. Iacomino, and A. Rubio, Computational Studies of New Materials from Nanostructures to Bulk Energy Conversion Materials, World Scientific (2010).

[53] N. Satoh, T. Nakashima, K. Kamikura and K. Yamamoto, Nature Nanotech. **3**, 106 (2008).

[54] H. Peng and J. Li, J. Phys. Chem. C **112**, 20241 (2008).

[55] Y. Brik, M. Kacimi, M. Ziyad, B. V. Francois, J. Catal. **202**, 118 (2001).

[56] E. I. Solomon, A. B. P. Lever, Inorganic Electronic Structure and Spectroscopy Vol 1 methodology; John Wiley and Sons: New York, (1999).

Chapter 4

Anisotropic super-paramagnetism in cobalt implanted rutile-TiO$_2$ single crystals

4.1 Introduction

The study of magnetism in nano-particles has gained enormous interest in last two decades from technological as well as fundamental perspectives [1]. In nanoscale systems, magnetic nature can be drastically different, compared to a bulk, since surface effects play crucial role in determining this behavior such that properties as diverse as ferromagnetism, anti-ferromagnetism, super-paramagnetism (SPM) or spin-glass(SG) like behavior are observed [1–4]. Among these, SPM is a property that crucially depends on the size of the nano-particle and shows magnetic moment that is proportional to the particle- volume [3]. An individual atom in a nano-sized cluster can exhibit giant magnetic moment (sometimes as high as few thousand μ_B) which is randomly oriented in the absence of external field. The particles are non-interacting, except for a weak dipole interaction which is usually negligible. Thus, an ideal super-paramagnet should exhibit *paramagnetic behavior*, i.e follow Curie - Weiss law, but with a large effective moment and a non-hysteretic $M - H$ curve up to 0 K. However, effects of magneto-crystallinity as well as surface and shape anisotropy alter this behavior such that a real super-paramagnet shows deviations from the Curie-Weiss law at the non-zero temperatures [5]. The super-paramagnetic clusters possess a uniaxial anisotropic direction which is random in direction for each SPM particle. Thus every individual nano-particle has its corresponding easy axes of magnetization.

As the system is cooled through the SPM state, there comes a characteristic temperature called the blocking temperature (T_B). Above T_B, the magnetic moment of the individual SPM particle is oriented randomly like a normal paramagnet, which can rotate freely under the influence of external field. Below T_B, the individual SPM particle has its magnetic moment blocked along its respective easy anisotropy axis. This temperature is prominently seen as a bifurcation of zero field cooled (ZFC) and field cooled (FC) magnetization. Associated with this temperature is an energy barrier U, which is the energy required for the individual magnetic moment to flip its direction along the two easy axes directions. The time for flip is giving by the characteristic equation [3],

$$\tau = \tau_0 exp\left(\frac{U}{k_B T}\right). \tag{4.1}$$

Here τ_0 is the limiting relaxation time, k_B is the Boltzmann constant, T is the temperature and U is the potential barrier. The blocking temperature is affected by individual particle volume and their distribution [6].

SPM behavior has been shown by several transition metals and their alloys when incorporated in non-magnetic host matrices, such as by Co multilayers on Al_2O_3 [6], nano-powdered $CoPt_3$ alloys [7] and Ni nano-particles on SiO_2 [5]. These compounds show a near perfect SPM behavior with a low blocking temperature and a universal scaling behavior [5] in $M - H$ curves.

Incorporating Co in TiO_2, however, has been demonstrated to form a dilute magnetic semiconductor (DMS) system that shows room temperature ferromagnetism [8]. DMS materials, achieved by introducing small concentration of transition metal or non-magnetic material in a semiconductor, exhibit ferromagnetic/ anti-ferromagnetic properties that are useful in spintronic devices. DMS is demonstrated by many systems like Co/Mn substituted in TiO_2, ZnO or Mn doped in narrow band gap semiconductors like GaAs, InAs [9–12] etc.. For Co doped TiO_2, magnetic properties have been investigated, in rutile and anatase forms of bulk as well as thin TiO_2 [13–15] films that were prepared by various methods like pulsed laser deposition, molecular beam epitaxy, magnetron sputtering, metal organic chemical-vapor deposition and sol-gel technique [16, 17]. In spite of extensive studies, origin of observed ferromagnetism in this system is still unclear. Investigations suggest that cobalt ions in thin TiO_2 films exist in a +2 oxidation state forming $Ti_{1-x}Co_xO_2$, which is ferromagnetic in nature [18]. Most of the preparation techniques produce precipitation of cobalt metallic nano-clusters which could also be responsible for this observed ferromagnetism [18]. First principles calculations for Co substituting Ti sites in rutile as well as anatase TiO_2 show creation of Co $3d$ bands at the Fermi energy implying metallicity [19, 20]. Also a net magnetic moment of $\sim 0.6\mu_B$ occurs at the Co site suggesting that Co is in low spin state.

Implantation is a less explored method for introducing magnetism in non-magnetic system. By this technique small concentration of dopants can be introduced, at well defined depth, in the host. Systems produced in this fashion can show many interesting electronic and magnetic properties [21]. GaMnP displays enhanced magnetism with a transition temperature above 300 K [22]. Mixed phases of ferromagnetism and super-paramagnetism have been observed after high fluence ($1.5\text{x}10^{17}$ ions/cm^2) implantation of Cobalt in rutile -TiO_2(001) single crystals [23, 24]. Cobalt doped thin films of TiO_2, prepared by sputtering and various other techniques, show formation of Co clusters [21]. Few studies have also shown SPM behavior in Co thin films on TiO_2 [25]. However, none of these studies have investigated the anisotropic nature of magnetization along different crystallographic directions, or the role of inter-cluster interactions.

The present study investigates the magnetic behavior after Cobalt implantation in rutile $TiO_2(110)$ single crystals. Surprisingly, a super-paramagnetic behavior is observed here instead of the expected ferromagnetic behavior from TiO_2 which is a DMS material. Here a detailed study of magnetic behavior, originating especially from super-paramagnetism, both above and below the blocking temperature, is presented. Interestingly, the super-paramagnetic behavior here is anisotropic in nature, i.e. non-equivalent along the two crystallographic axes. Development of $Ti_{1-x}Co_xO_2$ phase and Cobalt nano-clusters give rise to properties not observed before in SPM or DMS based systems.

4.2 Experimental Details

Commercially available single crystals ($5mm \times 5mm \times 1mm$) of TiO_2 (from Matech) with $<110>$ crystallographic direction perpendicular to the surface were implanted with cobalt ions at room temperature with fluences of 5×10^{16}, 8×10^{16} and 1×10^{17} ions/cm^2. These samples have been labeled here as A, B and C, respectively. In addition, implantation was also carried out at two lower fluences of 1×10^{16} and 3×10^{16} ions/cm^2. Co ions were implanted in TiO_2 with an energy of 200 keV. The penetration depth of Co in TiO_2 has been evaluated using SRIM to be $\sim 90nm$ [26]. The structural modifications have been investigated using x-ray diffraction, both in conventional $\theta - 2\theta$ geometry as well as in grazing angle geometry, on a Bruker diffractometer, using Cu K_α source. For grazing incidence XRD studies, an incidence angle of 2^0 was chosen. Magnetic measurements were performed using a commercial Superconducting Quantum Interference Device (SQUID). Temperature dependence of magnetization (M) has been obtained for zero-field cooling (ZFC) as well as field cooling (FC) conditions in a field of 0.05 T. Magnetization (M) vs. magnetic field (H) measurements have been carried out at various temperatures ranging between 2 and 300 K. As the magnetization from a host lattice and from implanted ions is always considered to be independent in any implanted sample, so the the contribution to magnetization of the former has been subtracted from all the implanted samples. The magnetic measurements have been carried out with H parallel ($H_{||}$) as well as perpendicular ($H_\perp$) to <001> crystallographic direction of the TiO_2 crystals.

4.3 Results and discussion

4.3.1 X-ray diffraction

Fig. 4.1 displays the XRD results from pristine TiO_2 as well as after it is implanted with Co at the fluences of 5×10^{16}, 8×10^{16} and 1×10^{17} ions/cm^2 (samples A,B and C). Fig. 4.1(a) shows a sharp feature at 27^o both prior to and after implantation. With TiO_2 crystals oriented in <110> direction, these features correspond to the [110] TiO_2 planes [27]. These features show slight shift and become little broader upon Cobalt implantation indicating generation of some stress as well as substitutional incorporation of Co in TiO_2 lattice with the formation of $Ti_{1-x}Co_xO_2$ (x $<$ 0.01) at low fluences. These results have been discussed in chapter 3 and in ref. [27]. Fig. 4.1(b) presents the normal XRD (39-50^o) results which show presence of Cobalt clusters at the highest fluence of 1×10^{17} ions/cm^2, not observed for lower fluences. Here, the feature at $\sim$ 47.4^o reflects the hexagonal closed packed (hcp) Cobalt (1011) clusters. Feature at $\sim$ 40.7^o suggests formation of a secondary $CoTiO_3$(210) phase [28]. Development of Cobalt clusters is also reflected by the grazing

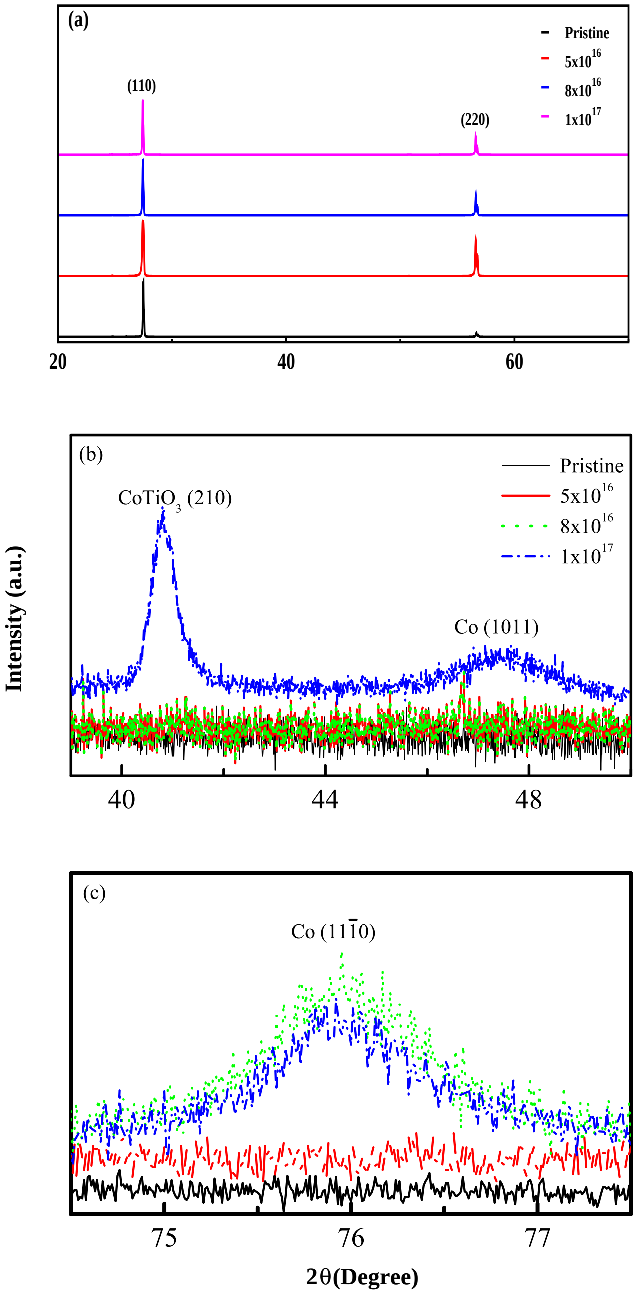

Figure 4.1: (a) XRD in the normal $\theta - 2\theta$ geometry shows (a) [110] and [220] planes of TiO_2(110) for the pristine and after Cobalt ion implantation (b) formation of Co clusters and secondary $CoTiO_3$ phase at the fluence of 1×10^{17} ions/cm^2 (c) Grazing incidence XRD showing Co clusters for 8×10^{16} and 1×10^{17} ions/cm^2.

incidence XRD studies (fig. 4.1(c)) where hcp Co($11\bar{1}0$) is observed at 76^o for samples B and C but not for sample A. Based on the width of hcp-Co Bragg peak, particle size of hcp-Co cluster has been determined to be ∼7 nm. The effect of cluster formation on the magnetic properties is discussed below.

4.3.2 Magnetization vs. Temperature

The temperature variation of magnetization for both pristine as well as implanted samples were measured with magnetic field (H) pointed along two crystallographic directions of TiO_2 viz. <001> ($H_{||}$) and <$1\bar{1}0$> ($H_{\perp}$). Fig. 4.2(a) (inset) displays the ZFC-FC plots for the pristine sample. Though the trends in magnetization are the same, along both the field directions, magnetic moment (M) is higher along $H_{||}$. This suggests $H_{||}$ (<001>) to be the easy (anisotropic)-axis in pristine TiO_2. Below 20 K a downward trend in the ZFC plot is observed which rises again upon further decrease in temperature. Ideally, the pristine sample should be non-magnetic due to the empty d orbital of Ti^{4+}. However, Van Vleck paramagnetism and a weak defect induced magnetic ordering is observed due to the presence of O and Ti type vacancies and other defects [29]. In addition, a small amount of Ti_2O_3 can also contribute to this magnetic moment [30].

For small Co implantation fluences (1×10^{16} and 3×10^{16} ions/cm^2), though there is a slight increase in the magnetization (data not shown), the nature of ZFC-FC curves remain similar to the pristine. At these low fluences, lattice remains paramagnetic with Co ions substitutionally incorporated in the TiO_2 lattice and net magnetic behavior unaltered compared to pristine. However, the magnetic moment is higher when field is along $H_{\perp}$ direction indicating this to be the preferred magnetization direction for Co.

For the Co fluence of 5×10^{16} ions/cm^2 (sample A), a drastically different magnetic nature compared to the pristine is observed. Fig. 4.2(a) shows the ZFC-FC plots for both the field directions. For field along $H_{||}$, a bifurcation in ZFC is noticed at 8 K, while for $H_{\perp}$ this is at 30 K. With increasing fluence, i.e. for sample B and C, the bifurcations shift to much higher temperatures. Fig. 4.2(b) shows the ZFC-FC plots for samples B and C in both field configurations. The nature of splittings in these plots indicate that samples A, B and C show super-paramagnetism, with arrows indicating

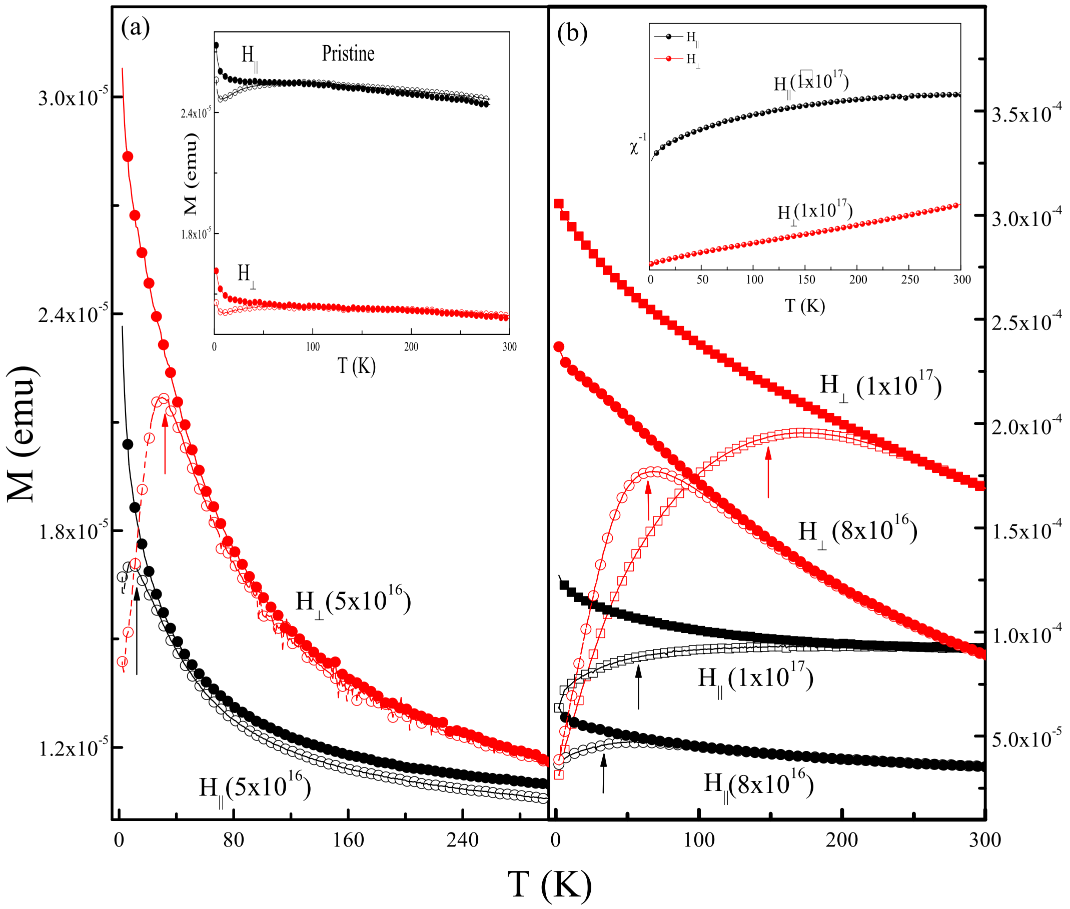

Figure 4.2: ZFC and FC graphs for cobalt implanted TiO_2 at 500 Oe for (a) sample A, inset shows for pristine. (b) samples B and C, inset shows χ^{-1} for sample C. The black and red symbols correspond to field parallel ($H_{||}$) and perpendicular ($H_{\perp}$) to <001> directions of TiO_2 crystal. The arrows indicate the blocking temperatures.

the respective blocking temperatures (T_B). The large increase in T_B with fluence indicates an increase in particle size while the broadening of the transition around T_B indicates a large variance in particle diameters. For all the three samples, $M(T)$ and T_B are considerably higher for field along $H_\perp$ compared to $H_{||}$ (also see table 4.1). At the highest fluence 1×10^{17} ions/cm^2 (sample C), the difference in T_B of 80 K between $H_{||}$ and $H_\perp$, indicates that this system is very anisotropic.

For $H_{||}$ field, magnetization in samples B and C appears nearly constant, with temperature, above T_B. Any decrease in magnetization is much slower than the expected Curie-Weiss like decrease in SPM systems. However for $H_\perp$ field, a decrease in magnetization with temperature is observed which indicates presence of SPM characteristics. Fig. 4.2(b) (inset) shows a plot of inverse susceptibility (χ^{-1}) as a function of temperature, for sample C, along both the field directions. For a SPM system, χ^{-1} should show a linear increase with temperature. However, here this is only observed along $H_\perp$ direction. The x-axis intercept is negative, indicating presence of some antiferromagnetic couplings in the system, similar to the pristine. For $H_{||}$ field, χ^{-1} is almost constant above T_B (fig. 4.2(b) inset).

The ZFC-FC results indicate that in Cobalt implanted samples, $H_\perp$ direction is the easy axis of magnetization. Hence, the magnetic moments of the clusters in this system are rotatable, due to external field and temperature, only when field is along $H_\perp$ direction. In a typical SPM, well below T_B, the ZFC susceptibility increases with increasing temperature, suggesting that more nanoparticles get unblocked and contribute to the susceptibility. Most of the particles get unblocked near T_B and system becomes an SPM for $T > T_B$. In a system of SPM nano-particles, irrespective of field direction all particles get unblocked above T_B and display a Curie-Weiss like behavior, i.e. decrease in magnetization with increasing temperature. Such a behavior is observed, above T_B, in the present study only when the field is along $H_\perp$. For field along $H_{||}$, the magnetization above T_B remains nearly constant with increasing temperature. This suggests that along this direction, only the smaller nano-particles get unblocked above T_B, whereas the larger particles remain blocked. Combined anisotropy due to the Co clusters and $Ti_{1-x}Co_xO_2$ will be responsible for this observation.

4.3.3 Magnetization vs. Field

Above Blocking temperature

Fig. 4.3 shows the magnetization isotherms, above T_B, for Cobalt implanted samples. M-H plots for the pristine TiO_2, at 2 and 300 K, are shown in the inset (of fig. 4.3(a)) for fields along $H_{||}$ and $H_{\perp}$ directions. At 300 K, the magnetization rises linearly as expected for a paramagnetic TiO_2, without attaining any saturation. A small ($<$ 20 Oe) coercivity has also been observed. Moreover, the magnetization is higher along $H_{||}$ (than $H_{\perp}$) indicating this to be the easy axis of magnetization in the pristine rutile TiO_2. Similar behavior is also observed at 2 K. The magnetization curve for Sample A at 100 K along $H_{\perp}$ is shown in fig. 4.3(a) and indicates some saturation- like behavior near 1 T. This curve also displays a very small coercivity of 30 Oe. At this stage the cobalt concentration in TiO_2 lattice is small and consequently the Co induced magnetic moment is comparable to the pristine.

The magnetization plots for samples B and C, at 300 K, are shown in fig. 4.3 for fields along $H_{||}$ and $H_{\perp}$ directions. Both the samples show higher magnetization when the field is along $H_{\perp}$ (than $H_{||}$) indicating, surprisingly, this to be the easy axis of magnetization. Thus, though the easy-axis in pristine is along $H_{||}$, it becomes $H_{\perp}$ for samples B and C. This indicates a reversal in the preferred direction of anisotropy. Moreover for both the samples B and C, the slope of magnetization at low H, is much steeper for fields along $H_{\perp}$ than $H_{||}$. As a result, the near-saturation like behavior is attained faster (at field $\sim$ 0.2 T) in the former case than in the latter case where saturation is achieved at fields around 1 T. Ideally for an SPM system, the M-H isotherms should be reversible [3]. However both samples B and C, show a mild irreversible behavior. For field along $H_{\perp}$, small coercivities of nearly 60 and 90 Oe are observed for samples B and C. Coercivities are smaller along $H_{||}$.

For an SPM system, a plot of M/M_S vs. H/T (M_S is saturation magnetization) should scale into a single universal curve [6]. Here, no scaling has been observed for sample A. Samples B and C also do not show any scaling for field along $H_{||}$. However for $H_{\perp}$ field, interestingly, scaling behavior is displayed (see fig. 4.3(d)). The scaled curves for sample B show that though the scaling exists, there are some deviations. A possible reason can be the existence of long ranged antifer-

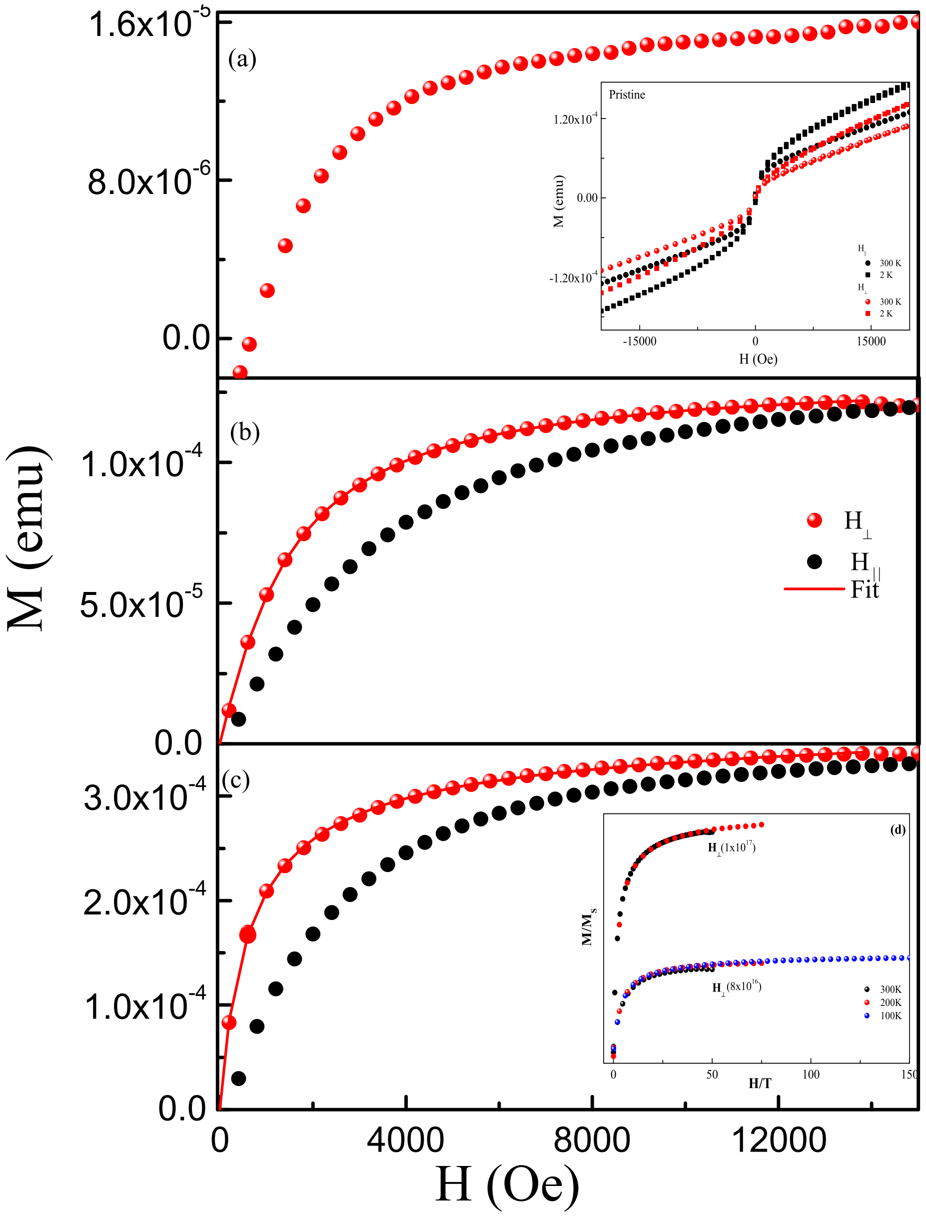

Figure 4.3: Magnetization v/s Field graphs for Cobalt implanted TiO_2 for field along $H_\perp$ (red symbols) and $H_{||}$ (black symbols). The solid curves correspond to fitting to Langevin function with lognormal distribution (eqn 2). In (a) data of sample A corresponds to T = 100 K. Inset shows the magnetization vs field of pristine sample obtained at T = 300 and 2 K, for both field directions. (b) Experimental and calculated (using eqn. 2) M-H plots at T = 300 K for sample B along both field directions. (c) Experimental and calculated (using eqn. 2) M-H plots at T = 300 K for sample C along both field directions. (d) Universal scaling behavior of samples B and C for field along $H_\perp$ at various temperatures.

romagnetic couplings due to the formation of $Ti_{1-x}Co_xO_2$, that results in an effective molecular field which hinders complete SPM-like behavior at this stage. For samples C a nearly perfect scaling is observed indicating a good SPM character. Absence of scaling along $H_{\|}$ can be due to the anisotropic effects that restrict free rotation of magnetic moments of the nano-particles along this direction. The ZFC-FC plots of fig. 4.2 and the magnetization results of fig. 4.3 show that SPM -like behavior is observed only when field is applied along $H_{\perp}$.

In a superparamagnet, there exists a distribution of magnetic moments due to the variations in the particle size of the nanoclusters. Hence, the net magnetization is given as a weighed sum of the Langevin function [31],

$$M(H,T) = \int_0^{\infty} \mu L\left(\frac{\mu H}{k_B T}\right) f(\mu) d\mu \tag{4.2}$$

where $L(x) = coth(x) - 1/x$ is the Langevin function, $f(\mu)$ is the distribution of magnetic moments, given by a log-normal distribution [5],

$$f(\mu) = \frac{1}{\sqrt{2\pi}\mu\sigma} exp\left[-\frac{ln^2(\frac{\mu}{\mu_0})}{2\sigma^2}\right] \tag{4.3}$$

Here μ_0 is the median of distribution and σ is the width of this distribution. The mean magnetic moment μ_M = $\mu_0$exp($-\sigma^2$/2). Assuming all the nano-particles to be spherical, μ_0= $\pi M_S D^3$/6. Here, D is the diameter of particles and $M_S (= 1.56\ u_B)$ is the saturation magnetization of bulk cobalt. The above equation holds only when the SPM particles are isotropic in nature.

In many SPM systems, equation (4.2) has been shown to yield good results for magnetization well above T_B. The fittings for the magnetization curves, using this eqn. (4.2), have been shown in fig. 4.3(b,c) for samples B and C when the fields is along $H_{\perp}$, the easy axis of magnetization. Fittings of the magnetization curves have been utilized to obtain average magnetic moment (μ_M), particle size (D) and standard deviation (σ) and are listed in Table 4.1. With increasing fluence there is a systematic increase in the average magnetic moment as well as particle diameter. In addition, the deviation σ also considerably increases from sample A to C. This is also observed in the ZFC-FC plots, wherein sample A displays a sharper transition while sample C shows a broader transition.

Table 4.1: T_B and parameters obtained by fitting $M - H$ data to the Langevin function are listed for field along $H_\perp$ for samples A, B and C. T_B for field along $H_\|$ is also mentioned

Sample	Fluence (ions/cm^2)	T$_B$ (K) ($H_\perp$)	T_B (K) ($H_\|$)	Particle Size (nm)	σ	Average moment $\mu_M(\mu_B)$
A	5×10^{16}	30	8	2.50	0.3	1261.7
B	8×10^{16}	65	40	3.97	0.64	4562.8
C	1×10^{17}	150	70	4.43	1.25	6285.8

Below blocking temperature

The magnetization curves for the implanted samples below T$_B$, at 2 K, are presented in fig. 4.4. Inset shows the magnetization curves of sample A for both $H_\perp$ and $H_\|$. Small coercivity is observed along both these fields. Magnetization curves observed for the pristine at 2 K are similar to those of sample A. The coercivities are also small. Also as demonstrated by sample A (fig. 4.4 inset), the magnetization in pristine does not saturate even at high fields (2 T) but rather continues to increase, indicating a paramagnet- like behavior.

Fig. 4.4 shows the hysteresis behavior of samples B and C along $H_\|$ and $H_\perp$. For samples B and C, coercivities (H_C) as large as 1500 and 1800 Oe, respectively, are observed for $H_\perp$ field. These coercive fields are nearly 3 times larger than those observed for Fe implanted TiO$_2$ [32], and also considerably larger than those for nano-Cobalt systems prepared by other methods [33]. However H_C obtained by Akdogan $etal.$ [23] for Co implanted TiO$_2$ are considerably higher.

For both samples B and C, the magnetization ($M - H$) plots display a near saturation-like behavior above 1 T (fig. 4.4). Moreover, the slope (dM/dH) here at 2 K is higher than that observed above T$_B$ at 300 K (fig. 4.3(b,c)). A crossover in M between the two field directions (indicated by arrows in fig. 4.4) is also observed at 2 K for both the samples. This suggests an additional contribution to the magnetization at low temperatures and will be discussed below in the section on *anisotropic paramagnetism*. For 1.5 T field, both samples B and C show a near-saturation like behavior with $M_S \sim$ 0.8 and 1.2 μ_B/Co atom, respectively. These values are considerably lower than saturation magnetization (1.56 μ_B/Co atom) for bulk cobalt. Since the presence of isolated Co-atoms or sub-nano few-atom Co clusters will effectively not contribute to the magnetization, this observation suggests presence of some (substituted) Co atoms and small

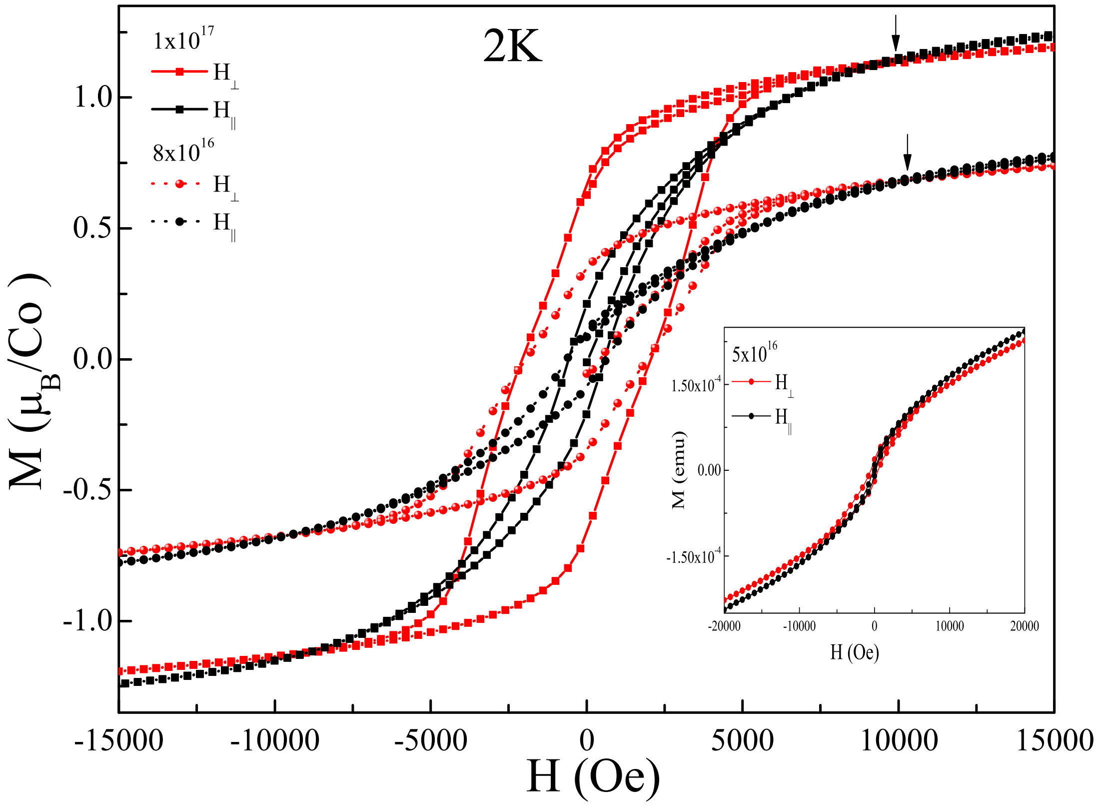

Figure 4.4: M-H curves of samples B and C obtained at 2 K for fields along $H_\perp$ (red symbols) and $H_\parallel$ (black symbols). Arrows indicate cross-over. The inset shows M-H data for sample A at 2 K.

clusters in the TiO_2 lattice, as also shown by XRD results. Nano-dimensional or bigger Co clusters give rise to the observed magnetization and estimates here show that for samples A, B and C nearly 22, 43 and 67$\%$ cobalt atoms, respectively, form such clusters.

Starting from 2 K, the width of hysteresis loop decreases on increasing the temperature, in both field directions for samples B and C. $M - H$ loop for both the samples display trends like a hard ferromagnet, similar to metallic Fe and Co. The hysteresis loop appears like a "parallelogram" for $H_\perp$, indicative of the easy axis of magnetization, but narrow "ribbon-like" for field along $H_\|$, similar to the hard axis.

4.4 Discussion

4.4.1 Anisotropy

Super-paramagnetic region

In the super-paramagnetic regime for $T >> T_B$, effects of uniaxial anisotropy can be neglected and magnetization can be completely described by eqn. (4.2). However as temperature reduces, anisotropy starts to increase. Then the magnetization cannot be described in a simple analytical manner as in eqn. (4.2). For a system of SPM clusters, each with random anisotropy direction, the magnetization is obtained from the Hamiltonian, $\mathcal{H} = E_B + E_{an}$. Here, $E_B = -VM_SHcos(\alpha)$ is the external magnetic field energy for magnetic field H applied in a direction which makes angles λ with anisotropy-axis and α with magnetization (geometry shown in fig. 4.5). M_S is the saturation magnetization and V is the volume of a nanocluster. The anisotropy energy, $E_{an} = -K_\mu V cos^2(\theta)$, depends only on the angle θ between the magnetization and the direction of anisotropy in the particle, K_μ is the anisotropy constant. Morup *et al.* [34] have obtained the z-component of magnetization as an integral over θ and azimuthal angle ϕ, assuming the single nano-particle to have a fixed volume. However in the present study, for a nanocluster with a size distribution of particles, the earlier description has to be modified. The *volume term* now considers a log-normal distribution of particle volumes, $f(V)$, instead of fixed volume for the cluster. Magnetization for a nanocluster is then described as:

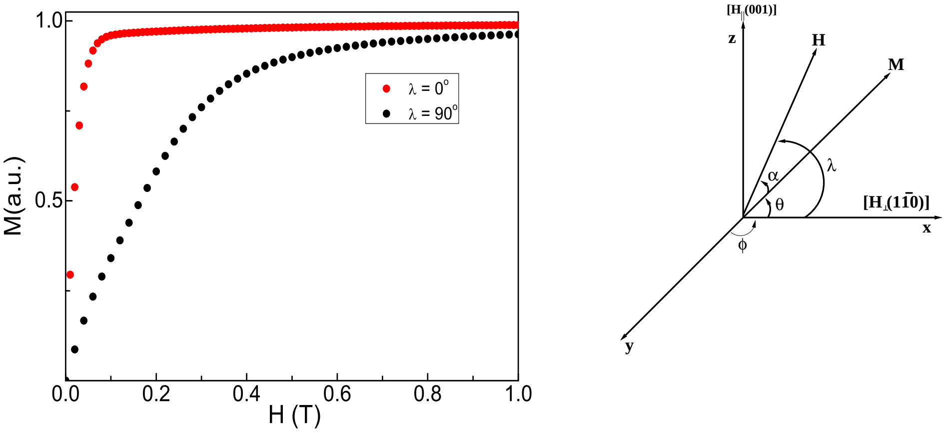

Figure 4.5: M-H curves calculated for a single nanocluster using eqn(4) for magnetic field applied along easy axis, $\lambda = 0^o$ ($H_\perp$) and hard axis, $\lambda = 90^o$ ($H_{||}$) assuming complete saturation of the nanoparticle with anisotopy constant K_{mu} = 5x10^{6}Joules/m^3.

$$M(H, \lambda) = \int_0^\infty M_S < cos(\theta) > f(V)dV \tag{4.4}$$

The term <cos(θ)> is the expectation value of magnetization vector for all possible orientations [34]. For a system of randomly oriented particles, $M(\lambda)$ is integrated from 0 to π to account for all possible directions of applied field. However, in the present study the magnetic moments of the cobalt SPM clusters show preferred orientations along $H_\perp$ and $H_{||}$ directions of TiO$_2$ crystal. Hence calculations have been undertaken by assuming λ = 0 along the easy axis (i.e. $H_\perp$) and λ = π/2 along the hard axis (i.e. $H_{||}$).

Magnetization curves along λ = 0^o ($H_\perp$) and λ = 90^o ($H_{||}$) calculated using eq.(4.4) are presented in fig. 4.5. The behavior of these magnetization curves is very similar and compare very well with the experimental curves presented in fig. 4.4. These results systematically show that the anisotropy directions of the clusters, in the present system, are not entirely random and are effectively along $H_\perp$ and $H_{||}$. The anisotropy, K_μ, has been estimated, using the values of average volume and saturation magnetization, to be 5x10^{6}J/m^3 which is similar to the anisotropy observed in bulk cobalt [35].

Blocked region

Bulk cobalt has a uniaxial anisotropy along the hexagonal c direction which corresponds to the easy axis [13]. The $M - H$ plots of samples B and C (fig. 4.4) suggest that the c axis of the individual cobalt clusters should lie in the $(1\bar{1}0)$ plane of TiO_2 crystal. Similar oriented metallic clusters have also been observed in Fe implanted TiO_2 where $<1\bar{1}0>$ direction ($H_\perp$) of TiO_2 is the easy axis [32]. The anisotropy of the system is given by $K_\mu = M_S H_K/2$, where H_K is the anisotropy field [32]. From $M - H$ plots along the easy and hard axis (fig. 4.4), anisotropy constants have been determined here for samples B and C at 2 K. In both the samples, the saturation along the hard axis ($H_{||}$) is attained at $H_K \sim$ 1.2 T, suggesting anisotropy constant of 2.5 $\times$ 10^5 Joule/m^3 and 5.39 $\times$ 10^5 Joule/m^3 for samples B and C. These values are smaller than the anisotropy constant of 7.5 $\times$ 10^5 Joule/m^3 observed for the bulk cobalt at 5 K [7]. This is due to the presence of some isolated (substituted) atoms and sub-nano clusters in the TiO_2 lattice which also led to (fig. 4.4) lower saturation magnetization for samples B and C, compared to bulk Cobalt.

In switching of the easy axis, from being along $H_{||}$ (<001>) prior to implantation to $H_\perp$ ($<1\bar{1}0>$) after implantation, it is assumed that the anisotropy of Co spins occupying Ti sites play a significant role. To verify this, first principle calculations have been carried out to determine the magneto-crystalline anisotropy energy of $Ti_{1-x}Co_xO_2$ using VASP [36]. The calculations were performed for three spin directions of Co spin: along $H_{||}$, along $H_\perp$ and along <110>. The net magnetic moment ~0.7 μ_B obtained here is lower than 1 μ_B expected for the S=1/2 system, suggesting an itinerant character. Among the three spin configurations, the system has the lowest energy when spin is along $H_\perp$, while energy is highest along $H_{||}$ direction. This is in agreement with the experimental results observed here. The difference in energy, in these two directions, is approximately -0.5 meV/Co i.e. nearly ~5 K. These results indicate that the magnetocrystalline anisotropy of Co in $Ti_{1-x}Co_xO_2$ determines the easy and hard axis and leads to highly anisotropic super-paramagnetism in TiO_2.

Anisotropic paramagnetism

In addition to the anisotropic effects of super-paramagnetic Co clusters, an additional anisotropy from paramagnetic Co ions has also been observed here. In the magnetization isotherms of samples B and C above T_B (fig. 4.3), magnetization is observed to be nearly constant for fields higher than 1 T, especially for field along $H_\perp$. However in the blocked region, at 2 K, an increase in dM/dH for samples B and C is observed (see fig. 4.4). This is in contrast to the usual SPM systems where M remains almost constant with increasing H. A possible reason for this could be the presence of uncompensated paramagnetic Co spins. In addition, a cross over in magnetization between the two field directions (shown by arrow in fig. 4.4) is also observed. The cobalt that occupies Ti sites in TiO_2 lattice should be in a 4^+ state corresponding to the S=1/2 system, as also observed in the first principles calculations carried out here. In S=1/2 system, the single ion anisotropy does not affect the magnetic behavior. The unusual cross-over behavior can be explained qualitatively by considering the presence of Co^{2+} ions, i.e. S=3/2 system. The crossover observed here then arises due to presence of the single ion anisotropy of this 3/2 spin state. Origin of Co^{2+} is via formation of $CoTiO_3$ nanoclusters whose presence in sample C has been observed by XRD (fig. 4.1). In addition, Co^{2+} also exists as Ti_2O_3. XPS studies, discussed in chater 3, have shown that along with Ti^{4+} state, a small percentage of Ti^{3+} also develops for samples B and C and increases with fluence [27]. Still, the main source of Co^{2+} spins here is $CoTiO_3$ and though it has been observed only for sample C, it is likely that smaller amounts will be present in sample B also.

Similar paramagnetic anisotropy has been observed in the magnetization of Co:ZnO thin films [37]. Ney et al. [37,39] have discussed the magnetization in terms of an *effective spin Hamiltonian* with an anisotropy along the crystallographic c axis (referred as z axis) of $Zn_{1-x}Co_xO$ films. Here, effective spin Hamiltonian has been applied to understand the anisotropic paramagnetic behavior observed in fig. 4.4. Remarkably, no crossover was observed when anisotropy was along $\hat{z}$ axis (i.e. along $H_\parallel$: <001>), rather it was observed when $\hat{x}$ direction (along $H_\perp$: $<1\bar{1}0>$) of the spin was considered to be the axis of single ion anisotropy (geometry of present system is shown in fig. 4.5). Hence, a modified S = 3/2 spin Hamiltonian was used here and is discussed below:

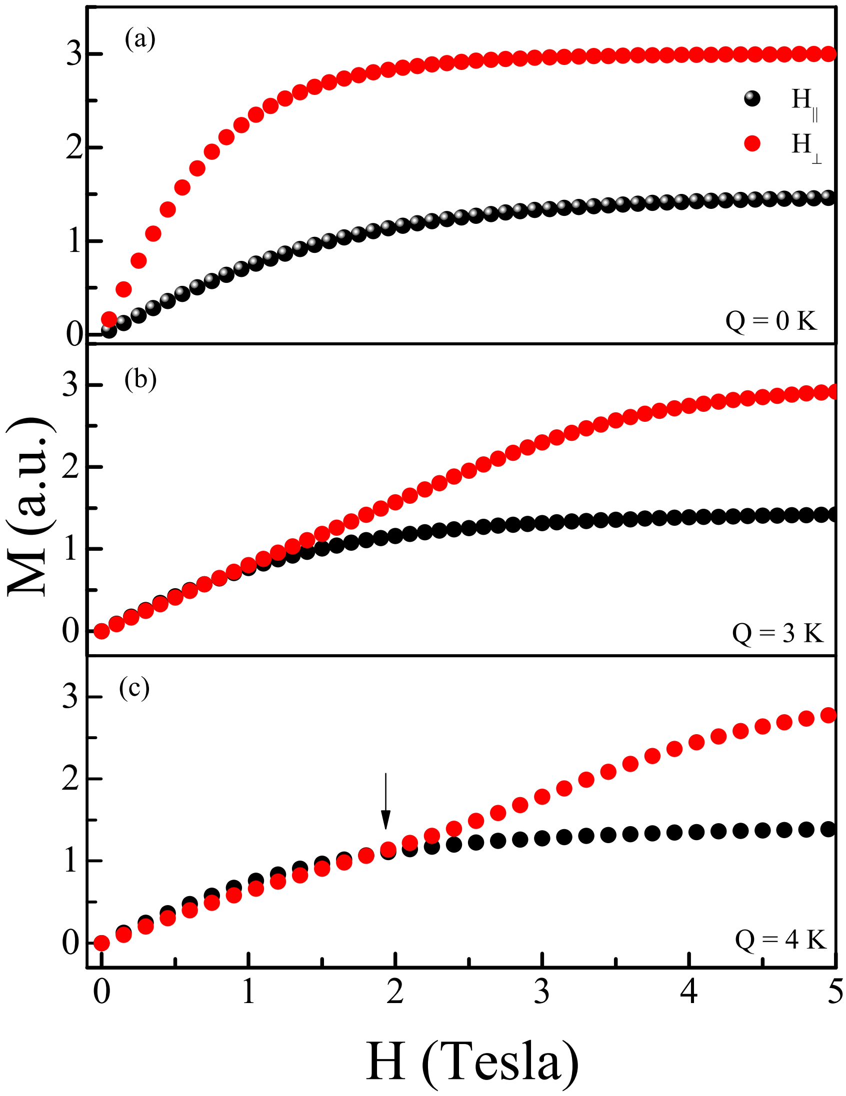

Figure 4.6: Calculated M-H curves at $T = 2$ K for H $\parallel$ $H_{\parallel}$ (black symbols) and H $\parallel$ $H_{\perp}$ (red symbols) using effective spin Hamiltonian of eqn. (5) and different values of zero -field splitting Q. The anisotropy and the cross-over (marked by the arrow) between two field directions observed at $Q = 4$ K are similar to experimental results in fig. 4.4

$$\hat{H}_{spin} = \mu_B g_{\|} H_z S_z + \mu_B g_{\perp}(H_x S_x + H_y S_y) + Q S_x^2, \tag{4.5}$$

Here the magnetic state is characterized by two g factors, $g_{\|}$ (2.238) and $g_{\perp}$ (2.276), and the zero field splitting constant Q. In the above equation, Q corresponds to single ion anisotropy of S=3/2 system, due to Co^{2+}, along the $\hat{x}$ direction. Spin Hamiltonian has been applied to calculate the energy levels of the $S = 3/2$ system $|M_S >= | - 3/2 > \cdots | + 3/2 >$ by using the matrix $< M_S|\hat{H}_{spin}|M_S >$ for H $\|$ $\hat{z}$ (H $\|$ $H_{\|}$) and H $\|$ $\hat{x}$ (H $\|$ $H_{\perp}$). Diagonalization of the matrix provide four eigenvalues along each direction. These energy values $E_{i,a}$ (i : M_S values and $a = H||\hat{z}, \hat{x}$) were used to calculate the magnetization $M = (\partial F/\partial T)_H$ of the magnetic free energy $F = -k_B T ln(Z_{i,a})$ using the partition function $Z_{i,a} = \sum_i e^{-E_{i,a}/k_B T}$.

Fig. 4.6 shows the $M - H$ curves calculated at T= 2 K using the spin Hamiltonian for varying strengths of Q. The strength of zero-field splitting Q was varied from 0 K to 4 K and its role on the anisotropy of the $M - H$ curves was investigated. For $Q = 0$ K the $M - H$ curves calculated for H $\|$ $H_{\|}$ and H $\|$ $H_{\perp}$ show no cross-over. The shape of $M - H$ curves for H $\|$ $H_{\|}$ do not show much change upon increasing Q. On the other hand, the $M - H$ curves for H $\|$ $H_{\perp}$ show a decreasing slope with increasing Q. This becomes responsible for an increase in anisotropy, and a cross-over (marked by the arrow) is seen for $Q = 4$ K. This plot calculated at $T = 2$ K can be compared with the experimental data presented in fig. 4.4 and displays a remarkably similar anisotropic behavior. Moreover, interestingly the effective Hamiltonian calculations for $S = 3/2$ system of Co in TiO_2 here show that the anisotropy is observed when $\hat{x}$ ($H_{\perp}$) direction of the spin is considered to be the axis of single ion anisotropy, unlike the $\hat{z}$ ($H_{\|}$) direction in Co:ZnO system [37].

Dipole and inter-particle exchange interactions

According to Neel-Brown prediction, the super-paramagnetic relaxation time for an assembly of non-interacting particles is given as:

$$\tau = \tau_0 exp\left(\frac{U}{k_B T}\right) \tag{4.6}$$

where τ_0 is a characteristic time of the system which gives a microscopic limiting relaxation time (usually $\tau_0 \sim \ 10^{-9}$ sec). k_B is the Boltzmann constant and U is the potential barrier due to anisotropy. The typical measurement time τ_m is 1-100 sec for DC measurements and is inverse of the measurement frequency for the AC measurements, providing $ln\left(\frac{\tau_m}{\tau_0}\right) \sim 25$ and $U = 25k_BT_B$. U separates the two local minima of the magnetization energy states. Below the blocking temperature T_B of the order of $\frac{U}{25k_B}$ the fluctuations between the two states become long enough to be observable on a laboratory scale. The energy barrier in the presence of a DC magnetic field is give by :

$$U = U_0\left(1 - \frac{H}{H_K}\right)^2 \tag{4.7}$$

Shengqiang where $U_0(= K_\mu < V >)$ is the energy barrier at zero field where K_μ is the uniaxial anisotropy constant, $< V >$ is the average particle volume, $H_K(= 2K_\mu/M_S)$ is the anisotropy field at zero temperature [38] and M_S is the saturation magnetization of the particle. Note that energy barrier U is proportional to $< V >$. The temperature dependent coercivity $H_C(T)$ for a *system of randomly oriented and non interacting particles* displays a behavior like [5]:

$$H_C(T) = H_K\left(1 - \left(\frac{k_BT\ ln\left(\frac{\tau_m}{\tau_0}\right)}{U_0}\right)^{1/2}\right). \tag{4.8}$$

Here $U_0 = K_\mu < V >$ and the Blocking temperature at zero field $T_B^0 = \frac{K_\mu<V>}{k_B\ ln(\tau_m/\tau_0)}$. Then [5]

$$H_C(T) = H_K\left(1 - \left(\frac{T}{T_B^0}\right)^{1/2}\right). \tag{4.9}$$

In the blocked region of a super-paramagnet, in addition to coercivity H_C, the parameter of importance is the reduced remanence (m_R = M_R/M_S). For a system of non-interacting particles with random anisotropy axes, the reduced remanence should be ∼0.5. The values of M_R and H_C are much smaller for field along $H_\parallel$ axis (fig. 4.4), since it corresponds to the hard axis of the clusters. Hence in this section field along $H_\perp$ direction is discussed. With increase in fluence the reduced remanence increases along with the coercive field. At 2 K, sample A shows the lowest m_R of 0.2, while samples B and C show values of 0.47 and 0.55, respectively, for field along the $H_\perp$ direction. The highly reduced remanence in sample A indicates a dominating presence of antiferromagnetic interactions [40] in the system.

Fig. 4.7 plots H_C values (eqn. 4.8) as a function of the reduced temperature $k_BT/K_u < V >$, for samples B and C for the field along the $H_\perp$ direction. Here $< V >$ corresponds to the average volume and has been evaluated using the size(D) of the clusters as mentioned in table 4.1. In order to directly observe the linear relation, inset of fig. 4.7 also displays a plot (eqn. 4.9) of H_C against $T^{1/2}$ for samples B and C. For sample B, a linear relation has been observed up to T $\sim$ 50 K. However above this temperature, deviations occur as T approaches T_B (=65 K). In sample C also, H_C shows deviations beyond $\sim$ 50 K, a temperature which is much lower than its T_B (=150 K). Also, the extrapolation of $H_C(T)$ to 0 yields values of $T_B \sim$ 64 K and 100 K for samples B and C, respectively, which are lower than the observed blocking temperatures. The deviations from linearity imply that some inter-particle interactions in Cobalt clusters are playing an important role. In SPM system, nearest neighbor exchange-interactions as well as long ranged dipolar interactions between nanoparticles are possible and will be explored below.

Using Monte-Carlo (MC) simulations, Kechrakos and Trohidou etal. [41,42] have investigated the role of inter-particle dipole and exchange interactions in determining the coercivity and remanence of the magnetization, in the blocked region, for a system of SPM nano-particles with random uniaxial anisotropic directions. The variations in m_R and H_C have been studied as a function of increasing volume fraction of the magnetic nano-particles. That analysis indicates [41,42] presence of a competition between the dipolar interaction strength, magnetic anisotropy and inter-particle exchange interactions. Further, a large exchange interaction would increase the reduced remanence and coercivity, with increasing concentration, resulting in a complete ferromagnetic alignment of the spins. Similar results have been observed in the present study and are presented in fig. 4.7, where $H_C(T)$ has been shown to increase with fluence, i.e. is higher for sample C than sample B at all temperatures. This indicates that the inter-particle exchange interactions are crucial here. The itinerant nature of the Co occupying Ti sites, can produce this carrier mediated exchange interaction between the clusters. Thus in the present study, a large inter-particle ferromagnetic exchange interactions, in addition to the anisotropy energy of the individual particles is present.

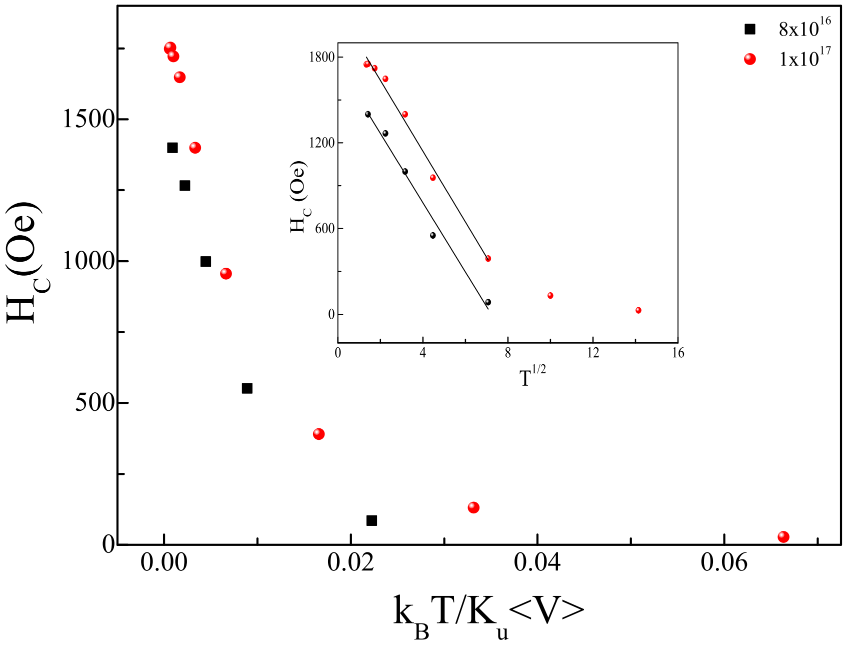

Figure 4.7: H_C as a function of the reduced temperature $k_BT/K_u < V >$, for samples B (square) and C (circle) for the field along the $H_\perp$ direction. Inset displays H_C as a function of $T^{1/2}$ for samples B and C.

Presence of some competing dipolar- interactions has also been observed via ZFC-FC curves. The blocking temperatures can be calculated via eqn. (4.7) for hard axis ($H \ \|$) and also easy axis ($H_{\perp}$) by replacing the -ive sign with a +ive sign in this equation [43]. Thus, the barrier energy is higher when field is along $H_{\perp}$ and smaller when the field is along $H_{\|}$ of the super-paramagnetic particle. Accordingly, T_B is higher along the easy axis $H_{\perp}$ and smaller along the hard axis. Assuming an anisotropic field H_K~10000 Oe, the difference in T_B does not exceed 10 K between $H_{\perp}$ and $H_{\|}$ directions. However in table 4.1, differences as large as 25 K and 80 K for sample B and C, respectively, are observed. The MC results have shown that large increase in T_B with increasing particle sizes indicates inter-particle dipolar interactions [41, 42]. Hence, in the present study Cobalt nanoparticles are undergoing ferromagnetic exchange -interactions as well as dipolar interactions. These interaction play important role in the unblocking of the SPM nano-particles.

4.5 Conclusion

Present study investigates the magnetic properties of single crystals of rutile TiO_2 after they are implanted with Co ions. ZFC- FC curves show presence of super-paramagnetic character above T_B. This SPM behavior, seen due to the development of Cobalt nano-clusters in the host lattice, is surprisingly anisotropic along the crystallographic directions of the crystal. With this anisotropy, SPM behavior is observed only along the $<1\bar{1}0>$ ($H_{\perp}$) direction which behaves as an easy-axis of magnetization, and not along $<001>$ ($H_{\|}$). Analysis with Langevin function -fitting considers a lognormal distribution of cluster sizes and yields a systematic increase in magnetic moment as well as particle volume with fluence, above T_B. For sample C, a linear behavior in inverse susceptibility, higher T_B and a good M/M_S vs. H/T scaling is observed only when field is in $H_{\perp}$ direction. Such anisotropy is very unexpected and shows that though along this $H_{\perp}$ direction magnetic moments are easily rotatable, above T_B, this is not the case along $H_{\|}$ direction where a considerable fraction of spins are *blocked*. Below T_B at T = 2 K, $M - H$ curves show a wide hysteresis loop for field along $H_{\perp}$ suggesting a highly oriented nature of the clusters. The Co nanoclusters possess an *easy* and *hard* axis of magnetization coupled with the magnetocrystalline anisotropy of the $Ti_{1-x}Co_xO_2$.

In addition at T=2 K, surprisingly a crossover in the magnetization for two field directions in sample B and C is observed. The origin of this crossover is the anisotropic paramagnetism arising from the 2+ ionic state of Cobalt in a $S = 3/2$ system. Role of dipole- interactions and inter-cluster exchange interactions have also been discussed.

Bibliography

[1] Alberto. P. Guimarães, Principles of Nanomagnetism, Springer-Verlag, Berlin, (2009).

[2] T. Kaneyoshi, J. Phys. Cond. Mat. **3**, 25, 1991.

[3] C. P. Bean and J. D. Livingston Jour. Appl. Phys **30**, 120 (1959).

[4] K. Binder and A. P. Young Rev. Mod. Phys. **58**, 801 (1986).

[5] F. C. Fonseca, G. F. Goya, R. F. Jardim, R. Muccillo, N. L. V. Carreño, E. Longo, and E. R. Leite, Phys. Rev. B **66**, 104406 (2002).

[6] F. Luis, J. M. Torres, L. M. Garcia, J. Bartolome, J. Stankiewicz, F. Petroff, F. Fettar, J.-L. Maurice, and A. Vaure‘s Phys. Rev B, **65**, 094409 (2002).

[7] F. Wiekhorst, E. Shevchenko, H. Weller and J. Kötzler, Phys. Rev. B **67**, 224416 (2003).

[8] Y. Matsumoto, M. Murakami, T. Shono, T. Hasegawa, T. Fukumara, M. Kawasaki, P. Ahmet, T. Chikyow, S. Koshihara, and H. Koinuma, Science **291**, 854 (2001).

[9] K. Ueda, H. Tabata and T. Kawai Appl. Phys. Lett. **79** 988 (2001).

[10] T. Fukumura, Z. Jin, A. Ohtomo, H. Koinuma and M. Kawasaki J. Appl. Phys. **75** 3366 (1999).

[11] H. Ohno, A. Shen, F. Matsukura, A. Oiwa, A. Endo, S. Katsumoto and Y. Iye, Appl. Phys. Lett. **69** 363 (1996).

[12] K. W. Edmonds, K. Y. Wang, R. P. Campion, A. C. Neumann, N. R. S. Farley, B. L. Gallagher and C. T. Foxon, Appl. Phys. Lett. **81** 4991 (2002).

[13] D. H. Kim, J. S. Yang, K. W. Lee, S. D. Bu, T. W. Noh, S. J. Oh, Y. W Kim, J. S. Chung, H. Tanaka, H. Y. Lee and T. Kawai Appl. Phys. Lett. **81** 2421 (2002).

[14] J. Y Kim, J. H. Park, B. G. Park, H. J. Noh, S. J. Oh, J. S. Yang, D. H. Kim, S. D. Bu, T. W. Noha, H. J. Lin, H. H. Hsieh and C. T. Chen Phys. Rev. Lett. **90** 017401 (2003).

[15] H. Toyosaki, T. Fukumura, Y. Yamada, K. Nakajima, T. Chikyow, T. Hasegawa, H. Koinuma and M. Kawasaki Nature **3** 221 (2004).

[16] Y. Matsumoto, R. Takahashi, M. Murakami, T. Koida, X.-J. Fan, T. Hasegawa, T. Fukumura, M. Kawasaki, S.-Y. Koshihara and H. Koinuma Jpn. J. Appl. Phys. 40 L1204 (2001).

[17] Jianping Xu, Shaobo Shi, Lan Li, Xiaosong Zhang, Yaxin Wang, Ximing Chen, Jianfeng Wang, Liya Lv, Fengming Zhang, and Wei Zhong J. Appl. Phys **107**, 053910, (2010).

[18] D. H. Kim, J. S. Yang, Y. S. Kim, T. W. Noh, S. D. Bu, S. J. Baik, Y. W Kim, Y. D. Park, S. J. Pearton, J. Y. Kim, J. H. Park, H. J. Lin, C. T. Chen, and Y. J. Song Phys. Rev. B **71** 014440 (2005).

[19] W. T. Geng, Kwang S. Kim, Phys. Rev. B **68**, 125203 (2003).

[20] Hongming Weng, Xiaoping Yang, Jinming Dong, H. Mizuseki, M. Kawasaki, and Y. Kawazoe Phys. Rev. B **69**, 125219 (2004).

[21] Y. Xin, J. Lu, P. A. Stampe, and R. J. Kennedy, Appl. Phys. Lett. **88**, 112512 (2006).

[22] M. E. Overberg, B. P. Gila, G. T. Thaler, C. R. Abernathy, S. J. Pearton, N. A. Theodoropoulou, K. T. McCarthy, S. B. Arnason, A. F. Hebard, S. N. G. Chu, R. G. Wilson, J. M. Zavada and Y. D. Park 969 J. Vac. Sci. Technol. B **20**, 969 (2002).

[23] Numan Akdogan, Alexei Nefedov, Hartmut Zabel, Kurt Westerholt, Hans-Werner Becker, Christoph Somsen, Şafak Gök, Asif Bashir, Rustam Khaibullin and Lenar Tagirov J. Phys. D, Appl. Phys. **42**, 115005 (2009).

[24] R I Khaibullin, L R Tagirov, B Z Rameev, Sh Z Ibragimov, F Yildiz and B Aktaş, J. Phys. Cond Mat **16** L443 (2004).

[25] S. R. Shinde, S. B. Ogale, J. S. Higgins, H. Zheng, A. J. Millis, V. N. Kulkarni, R. Ramesh, R. L. Greene, and T. Venkatesan Phys. Rev. Lett. **92**, 16601 (2004).

[26] J. F. Ziegler, M. D. Ziegler, J. P. Biersack, Nucl. Inst. Meth. B **268**, 1818 (2010).

[27] Shalik Ram Joshi, B. Padmanabhan, Anupama Chanda, V. K. Malik, N. C. Mishra, D. Kanjilal and Shikha Varma Appl. Phys. A **122**, 713 (2016).

[28] E. Newnham, J. H. Fang and P. P. Santoro Acta Cryst. **17**, 240 (1964).

[29] M. S. Park, S. K. Kwoo, and B. J. Min Phys. Rev. B **65**, 161201(R) (2002).

[30] L. A. Errico, M. Renteria, and M. Weissmann Phys. Rev. B **72**, 184425 (2005).

[31] R. W. Chantrell, J. Popplewell and S. W. Charles IEEE Trans.on Magn. Vol. Mag-14, 5, 975 (1978).

[32] Shengqiang Zhou, G. Talut, K. Potzger, A. Shalimov, J. Grenzer, W. Skorupa, M. Helm, J. Fassbender, E. imr, S. A. Zvyagin, and J. Wosnitza. J. Appl. Phys **102**, 083907 (2008).

[33] Hongmei Luo, Donghai Wang, Jibao He and Yunfeng Lu J. Phys. Chem. B **109**, 1919 (2005).

[34] M. Hanson, C. Johansson and S. Morup J. Phys. Cond. Mat **5**, 725 (1993).

[35] G. H. O. Daalderop, P. J. Kelly, and M. F. H. Schuurmans Phys. Rev. B **41**, 11919 (1990).

[36] G. Kresse and D. Joubert, Phys. Rev. B **59**, 1758 (1999). J. Phys : Conference Series **568**, 042022 (2014).

[37] A. Ney, T. Kammermeier, K. Ollefs, S. Ye, V. Ney, T. C. Kaspar, S. A. Chambers, F. Wilhelm and A. Rogalev Phys. Rev. B **81**, 054420 (2010).

[38] R. M. Bozorth, Ferromagnetism Van Nostrand, Princeton, NJ, Chap. 18, p. 831 (1956).

[39] A. Ney, K. Ollefs, S. Ye, T. Kammermeier, V. Ney, T. C. Kaspar, S. A. Chambers, F. Wilhelm, and A. Rogalev, Phys. Rev. Lett.**100**, 157201, (2008).

[40] Weili Luo, Sidney R. Nagel, T. F. Rosenbaum and R. E. Rosensweig **67**, 2721 (1991).

[41] D. Kechrakos, K.N. Trohidou, Phys. Rev. B **58**, 18, (1998).

[42] D. Kechrakos, K.N. Trohidou, J. Magn. Magn. Mat. **262** 107 (2003).

[43] Masatsugu Suzuki, Sharbani I. Fullem, Itsuko S. Suzuki J. Magn. Magn. Mat. **322** 3178 (2010).

Chapter 5

Damage Studies of Cobalt Implanted Rutile TiO_2 (110) lattice via RBS/C

5.1 Introduction :

Titanium dioxide (TiO_2) is considered an advanced research material in many applications due to its several fascinating characteristics in fields of photo-catalysis, solar cells, gas sensors, and electrical devices [1–5]. It is a wide band gap semiconductor and displays numerous intriguing aspects through nanoscale designing, band gap engineering, inclusion of dopants and control on point defects. This has stimulated overwhelming activity in many areas including photovoltaics and photocatalysis [6]. Incorporation of magnetic dopants in TiO_2 also reveal many fascinating results encompassing DMS and ferromagnetism [7]. Dopant inclusion, for modulation of characteristics, can proceed via several routes like dye sensitization, synthesis as thin films, formation of nano crystals, incorporation of dopants by chemical methods, etc [4, 8].

Present thesis (chapters 3 and 4) discusses many aspects of surface and bulk modifications, nanostructure formation, phase formations, generation of vacancy states as well as modifications in photo-response and development of anisotropic super-paramagnetism in TiO_2 after inclusion of Cobalt atoms in the TiO_2 lattice upon 200 keV ion implantation. Ion implantation is a well established technique which is extensively used to design hetro-structures with controlled selective area doping [9]. Implantation can also generate point defects and lattice modifications that will alter the material properties. These have variety of implications, beneficial as well as detrimental to the host lattice. Vacancies, point defects and end-of range (EOR) defects for example can control the lifetime of free electron, contribute to the nucleation of nanocrystals, influence phase formation, regulate diffusion as well as lead to accumulation of damage. Annihilation of defects, via recombination, and their agglomeration into energetically stable defect complexes etc. can modify the disorder. Radiation damage develops via concerted effect of displacements of lattice atoms as well as excitations and ionization of target atoms [10]. Understanding the development, distribution and role of defects and damage in the lattice is crucial for describing the observed properties and it can be critical in many applications.

Rutherford back-scattering spectrometry/Channeling (RBS/C) has proved to be a very successful technique for investigating radiation induced defects as well as damage in single crystals. Channeling of the incident ions, within the crystal, reveal information about the defects and their distribution. Lattice imperfections and damage profile can be evaluated from the ion- channeled spectrum by applying the multiple scattering formalism [17].

In this chapter, the techniques of RBS/C and GIXRD have been utilized to study the radiation damage and structural modifications that occur in $TiO_2(110)$ single crystals after they are implanted with various fluences of 200 keV Cobalt ions. The total accumulated damage demonstrates many complex behaviors. At low fluences a buried amorphous layer is observed. This, however surprisingly, recovers through ion induced dynamic activation at higher fluences. Hence, an overall lowering of net accumulated damage with fluence is observed. However, the profiles are complex where a cross-over at 50 nm is observed such that the damage is highest at surface and lowest in deep layer at 1×10^{17} ions/cm^2, but reverse scenario with lowest surface damage and highest damage in deep occurs for 1×10^{16} ions/cm^2. In addition to this cross-over, a valley in the profile is also observed reflecting an intricate damage distribution. The Co-Ti-O phase formation and the strain in the lattice, as presented by GIXRD results, can also be responsible for the damage recovery observed here. Monte Carlo (MC) simulations via SRIM 2013 have also been utilized to obtain the damage distributions in TiO_2. MC simulations underestimate the damage in the surface as well as in deep regions. Damage is also observed to extend far deeper than expected by simulations.

5.2 Experimental :

Commercially available single crystal rutile TiO_2 (110) were implanted at room temperature (RT) with a scanned beam of 200 keV Cobalt ions. To avoid channeling effects the sample was tilted by 7^o off normal to the incident beam. The flux of the ion source was 1.6×10^{13} ions/cm^2.sec. The implantation fluence was varied from 1×10^{16} to 1×10^{17} ions/cm^2. A secondary electron suppression system was used for precise fluence control. The residual pressure in a target chamber during the experiment was 2×10^{-6} mbar. The projected range (R_p) and the longitudinal straggling for cobalt ions in TiO_2 lattice was estimated to be 98 nm and 10 nm, respectively, using SRIM code [12].

After implantation, the sample was taken out of the implantation chamber and loaded in the RBS/C analysis chamber. RBS/C measurements were carried out using 2 MeV He^+ ions from 1.7MV 5SDH-2 Pelletron Accelerator at IUAC. The beam divergence was less than 0.02° and the spot diameter was 1mm. The chamber pressure was 1×10^{-6} Torr. The samples were mounted on a four axis goniometer. Backscattering spectra from random and channeling orientations were obtained for all the samples. With a beam current of 10 nA, the charge of 20 μC was collected during each measurement. The scattering angle was kept at 165° (laboratory coordinates). The resolution of the silicon surface barrier detector was 30 keV. The energy calibration (0.988keV/channel) of the 2K channel analyzer was achieved using a standard unimplanted silicon specimen with a very thin gold film on the surface.

5.3 Results and Discussion :

Fig. 5.1 (inset) shows a RBS spectrum of the pristine (un-implanted) TiO_2(110) crystal. The edges from the Ti and O sub-lattices can be seen in the RBS and are marked in the inset. Fig. 5.1 also shows the random spectra of the 200 keV Cobalt implanted TiO_2 samples. The development of an edge near channel no. 1400, with increasing Co fluence, is due to the incorporation of cobalt in the lattice. At the the highest fluence of 1×10^{17} ions/cm^2, a well developed Cobalt peak is visible at $R_p \sim 98\ nm$ below the surface as also expected from SRIM simulations.

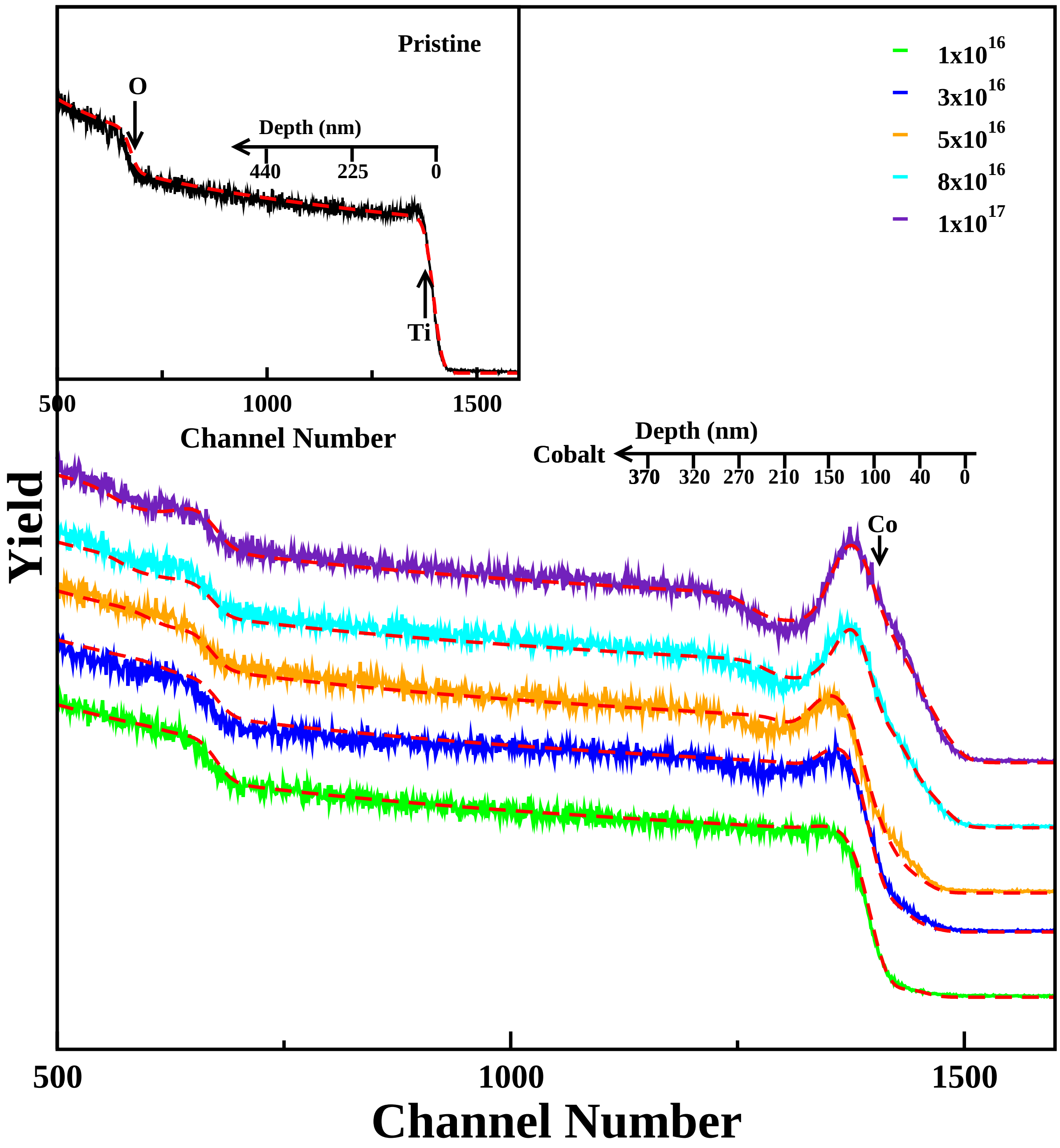

Figure 5.1: 2.0 MeV He^+ Random RBS spectra of pristine (inset) and Co implanted TiO_2 at various fluences. Spectra have been vertically shifted. Depth scale is also shown. Dashed lines are the simulated RBS profiles obtained by SIMNRA.

The dashed lines on the spectra in fig. 5.1 denote the RBS profiles obtained via SIMNRA [13] simulations. In these simulations implanted cobalt ions were considered to have a uniform distribution. The stopping powers of the analyzing He beam from SRIM-code and the detector resolution were also taken into account. The simulations considered four layers where layer 1 is the surface layer of TiO_2 that does not contain any cobalt ions, layer 2 is just below layer 1 and contains a low concentration of implanted ions, layer 3 is the region containing the highest cobalt ions concentration and is located just below layer 2, layer 4 is lowest region (below layer 3) which is stoichiometric bulk TiO_2. The results of the simulations, with the thickness of each layer as well as the concentrations of Ti, O and Cobalt in each layer are presented in table 5.1 and table 5.2.

For the pristine as well at 1×10^{16} ions/cm^2, layer 1 is stoichiometric TiO_2 (table 5.2). At higher fluences some oxygen deficiency is observed. This can be due to the preferential sputtering of oxygen atoms from the surface during irradiation. Furthermore, the thickness of this layer decreases with fluence, with it being about 120 nm at 1×10^{16} ions/cm^2 but only 30 nm at 1×10^{17} ions/cm^2 (table 5.1). Thus, the thickness of the surface layer containing no cobalt atoms decreases, as expected, as the cobalt fluence is increased. Layer 2 contains small (1-7%) cobalt concentration and its thickness is 45 nm at 1×10^{16} ions/cm^2 but 120 nm at other fluences. Layer 3 consists of higher concentration (5-18%) of cobalt ions and its thickness increases with fluence, being 15 nm at 1×10^{16} ions/cm^2 and 270 nm at 1×10^{17} ions/cm^2. Layer 2 and layer 3, together, indicate oxygen deficient lattice at all fluences. This suggests that the oxygen vacancy states are created on the surface as well as in the bulk during Cobalt implantation. Layer 4 is the bulk layer with fully stoichiometric TiO_2. Depth distribution of cobalt concentration, as obtained from the SIMNRA simulations (table 5.1 and table 5.2), is also shown in fig. 5.2 for all the fluences.

Table 5.1: Thickness of all layers as obtained from SIMNRA simulations

Fluence (ions/cm^2)	Layer1	Layer2	Layer3	Layer4
Pristine	—-	—	—	3000 nm
1×10^{16}	120 nm	45 nm	15 nm	3000 nm
3×10^{16}	75 nm	120 nm	30 nm	3000 nm
5×10^{16}	60 nm	120 nm	60 nm	3000 nm
8×10^{16}	30 nm	120 nm	210 nm	3000 nm
1×10^{17}	30 nm	120nm	270nm	3000 nm

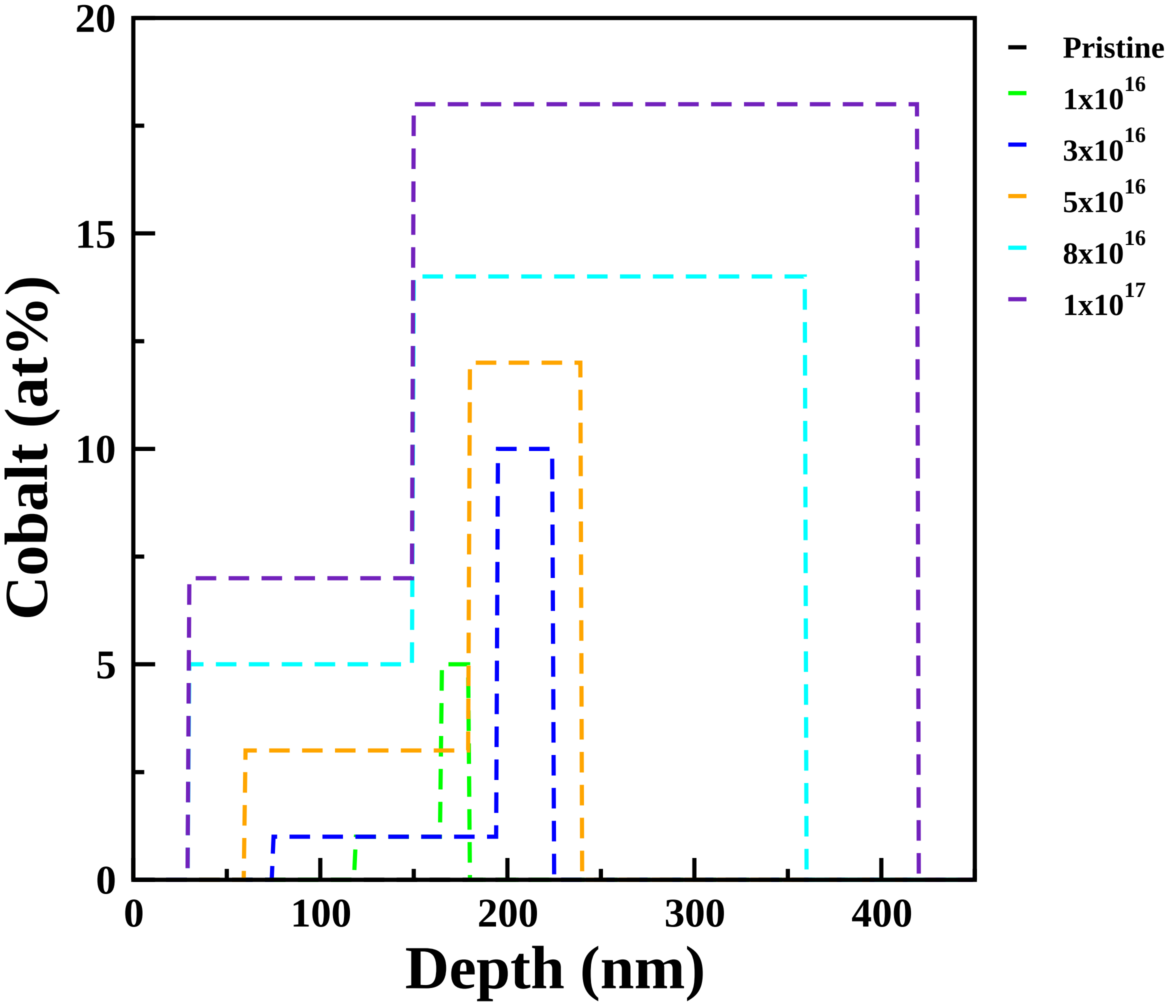

Figure 5.2: Depth distribution of cobalt concentration as obtained from SIMNRA simulations at all the fluences.

Fig. 5.3 shows the (110)-aligned RBS spectra of the Co implanted TiO_2 samples. In order to clearly understand each individual profile and its features, aligned spectra with their corresponding random RBS (from fig. 5.1) are shown separately for pristine and implanted samples in fig. 5.4 and fig. 5.5. The random and channeling spectra from the pristine sample are shown in fig. 5.4. A χ_{min} of 0.028 is observed just below the surface peak suggesting a good crystalline quality of the TiO_2 sample. For the cobalt implanted samples, channeling data (in fig. 5.5) indicates incorporation of disorder in the lattice. After the fluence of 1×10^{16} ions/cm^2 (fig. 5.5(a)), aligned spectrum displays

Table 5.2: Concentrations of elements (Ti, O, Co) in the layers as obtained from SIMNRA simulations

Fluence(ions/cm^2)	Layer1			Layer2			Layer3			Layer4		
	Ti	O	Co	Ti	O	Co	Ti	O	Co	Ti	O	Co
Pristine										0.33	0.67	0.00
1×10^{16}	0.33	0.67	0.0	0.35	0.64	0.01	0.4	0.55	0.05	0.33	0.67	0.00
3×10^{16}	0.40	0.60	0.0	0.40	0.59	0.01	0.3	0.60	0.10	0.33	0.67	0.00
5×10^{16}	0.40	0.60	0.0	0.42	0.55	0.03	0.3	0.60	0.12	0.33	0.67	0.00
8×10^{16}	0.33	0.67	0.0	0.40	0.55	0.05	0.31	0.55	0.14	0.33	0.67	0.00
1×10^{17}	0.42	0.58	0.0	0.40	0.53	0.07	0.32	0.5	0.18	0.33	0.67	0.00

appearance of two broad features P_1 and P_2 at 130 and 250 nm, respectively, below the surface. Former is associated with the presence of Cobalt in the lattice whereas the later corresponds to the development of the damage in the lattice. As shown by simulation results (table 5.1), the region of P_2 does not have cobalt impurity, since the cobalt is only present up to 180 nm below the surface (layer 3) at this stage. With the channeling yield around P_2 being nearly similar to the random RBS (fig. 5.5(a)), the lattice appears to be amorphised in this zone. Beyond P_2 some improvement in the lattice crystallinity is observed.

Features P_1 and P_2 are also observed at higher fluences in fig. 5.5 and appear around 130 ± 10 and 265 ± 50 nm at all the fluences. Though feature P_1 is observed to become sharper and higher with increasing Cobalt ion concentration, P_2 displays some interesting behavior. After 3×10^{16} ions/cm^2 a larger lowering in the channeling yield beyond P_2 (fig. 5.5(b)), compared to in fig. 5.5(a) indicates a scenario of ion induced damage recovery. This improvement in radiation induced damage is surprising and will be discussed later. One notices (table 5.1 and 5.2) that with layer 3 extending 225 nm below the surface at 3×10^{16} ions/cm^2, the region around P_2 will now contain some cobalt ions. For higher fluences, concentration of cobalt in this region further increases (table 5.1 and 5.2). The channeling yield in P_2 region as well as beyond P_2, however, decreases with increasing fluence as seen in fig. 5.3 (and fig. 5.5). This in turn reflects the attenuation of disorder in the lattice with fluence. Ion induced reduction in damage here suggests an influence of dynamic activation processes. This is a surprising result as such processes are usually coupled

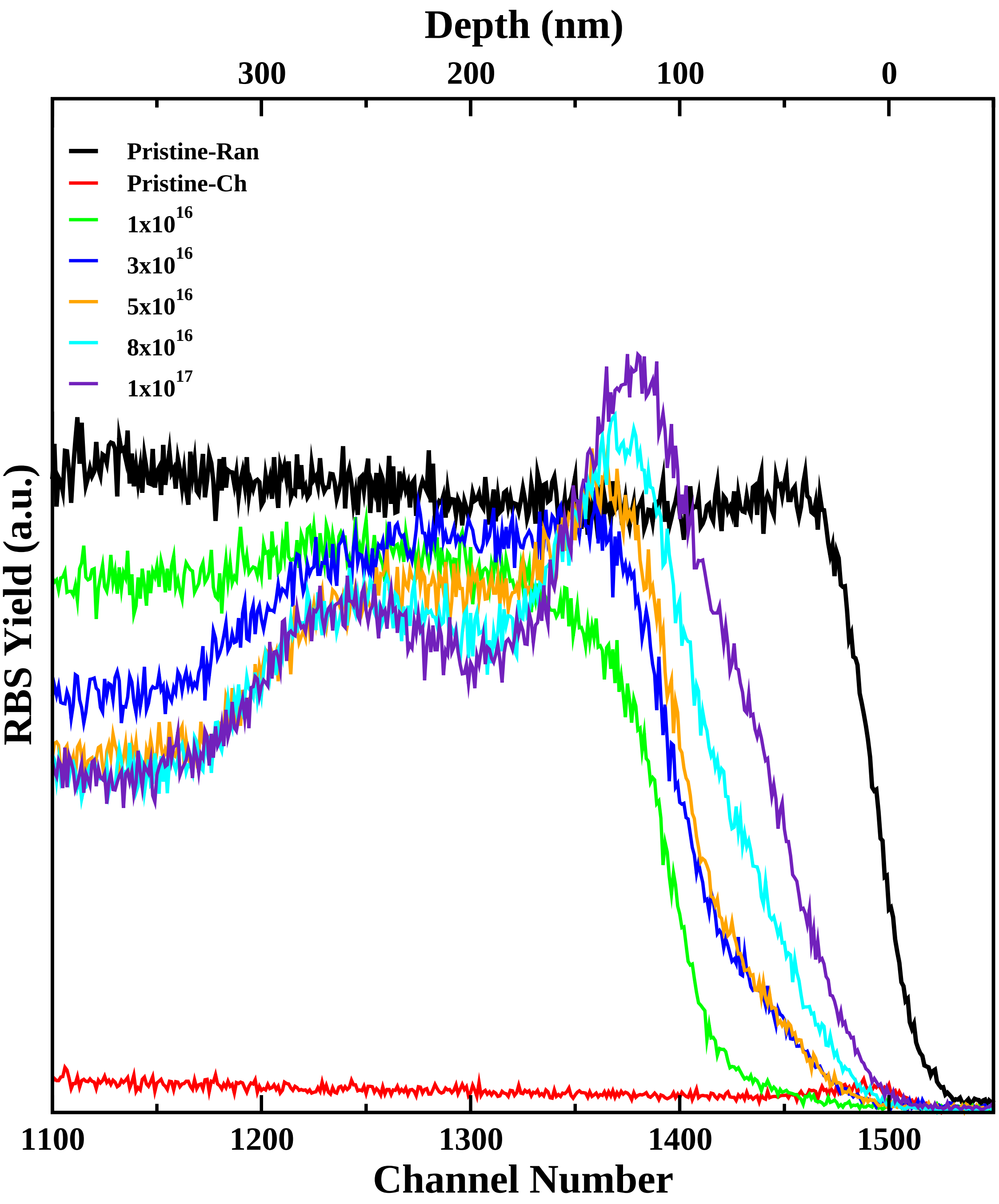

Figure 5.3: Channeled spectra of Co implanted TiO_2 at various fluences. Random RBS and channeled spectra from pristine are also shown in same depth scale.

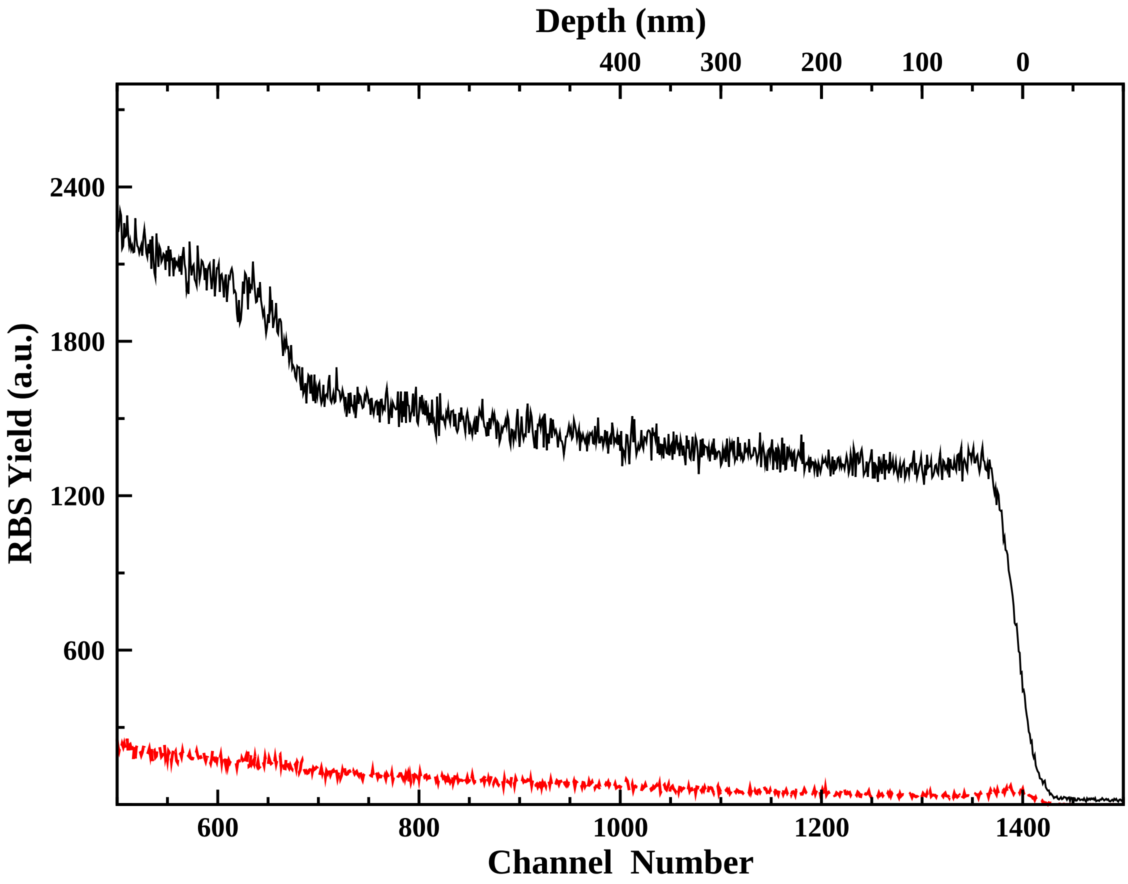

Figure 5.4: Random and channeled spectra for pristine sample

with thermal activity. As discussed below, the dynamic annealing processes are playing a distinct role in the damage recovery of the TiO_2 lattice investigated here.

Damage production in oxides is complicated as it can be produced via many processes like nuclear, electronic, photochemical as well as preferential sputtering of oxygen atoms with the development of a non-stoichiometric lattice. Damage accumulation and transition into the amorphous phase depends on the ion species, temperature and dose [14]. The recovery of damage is also a complex process in oxides exhibiting various stages and processes which might be thermally or dynamically activated. Latter processes involving recombination of point defects, including oxygen/di-vacancy annihilation, enhanced dynamically during irradiation by electronic excitation or nuclear transfer below the displacement threshold pose many intricacies to the understanding

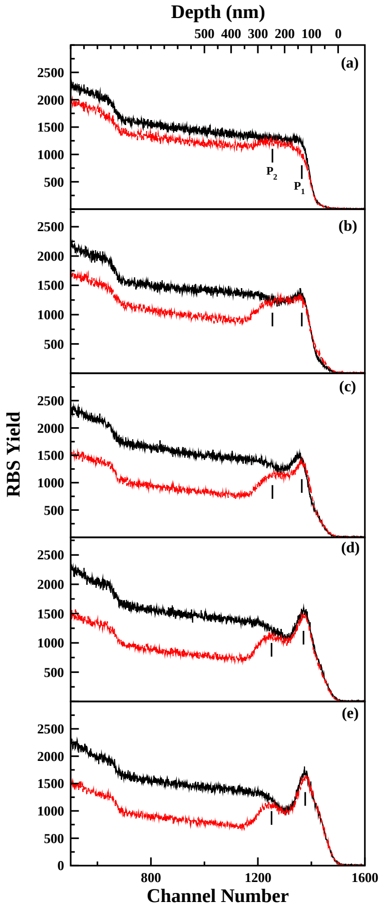

Figure 5.5: Random and channeled spectra after cobalt implantation with fluence of (a)1×10^{16} (b)3×10^{16} (c)5×10^{16} (d)8×10^{16} and (e)1×10^{17} ions/cm^2. Vertical bars are marked at P_1 and P_2.

of damage annihilation [15]. For example, two recovery stages during thermal annealing of amorphous TiO_2 can be lowered by about 200 K due to the radiation induced annealing [16]. Low temperature (77 K) implantation of 260 keV Hg implantation in TiO_2(100) also shows various recovery stages, upon annealing to 293 K, which are induced by dynamical processes [15].

The multiple scattering formalism discussed by Feldman and Rodgers [17] has been utilized to obtain the damage profiles from the RBS/C spectra of fig. 5.4 and fig. 5.5. The stopping power ratio (α) of the incident He ions in the channeling direction compared to the random direction has been considered to be 0.7 [18]. With appropriate corrections to the Scattering cross-sections, the disorder-depth profiles for cobalt implanted TiO_2(110) have been obtained and are shown in

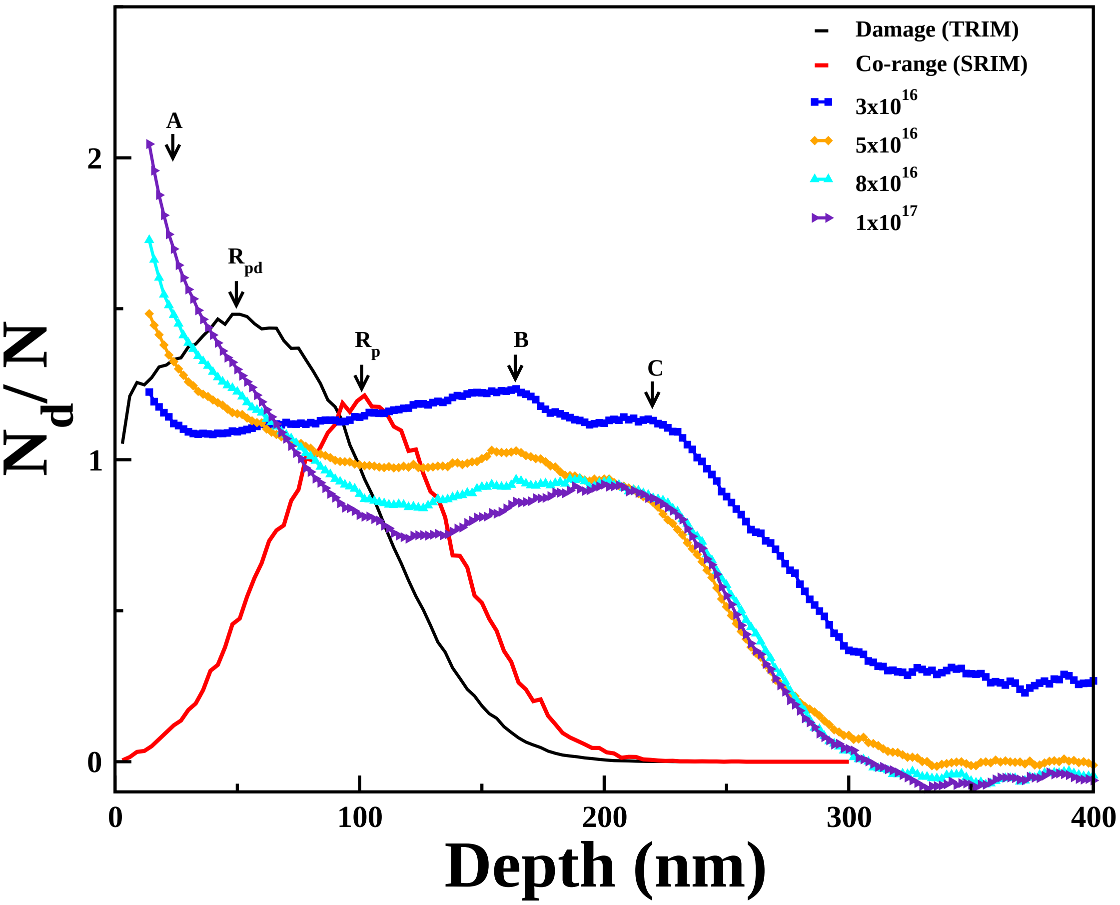

Figure 5.6: Damage profiles for TiO_2 implanted with various fluences of Cobalt. The profiles are extracted from RBS/C data by using the multiple-scattering model. The Damage profile obtained from TRIM shows R_{pd} and Cobalt profile obtained from SRIM shows range R_p of cobalt atoms.

fig. 5.6. The density of the displaced atoms N_d, normalized wrt. the density of the host atoms (N), are shown as a function of depth at all the fluences. It is observed that in TiO_2, the damage accumulates both at the surface and in bulk upon cobalt implantation. The damage profile after 3×10^{16} ions/cm^2 cobalt implantation displays three prominent features: A at the surface, B near the depth of 160 nm, and C near 220 nm (fig. 5.6). MC simulations, performed using SRIM-2013 for 200 keV Co ion implantation in TiO_2, provide the mean-projected range (R_p) for cobalt ions to be 98 nm and the simulated damage profile shows the depth of maximum nuclear energy loss (R_{pd}) at 50 nm (see fig. 5.6). The disorder-profile for 3×10^{16} ions/cm^2 is distinctly different than the

simulated curve. It is remarkably flatter than the simulation and considerably deeper than R$_{pd}$ or R$_p$. With surface showing some excess defects, the top ~ 250 nm of the TiO$_2$ appears amorphised. Interestingly with increasing fluence the damage-profiles also become very different; the disorder on the surface (feature A) increases, but surprisingly the damage in feature B decreases and feature C saturates. There are two more noticeable features of these profiles. One is the presence of *valley* like structure at R$_p$ which becomes deeper with fluence. Another is the cross-over in disorder at 50 nm. For example it is noticed that compared to other fluences, for 1×10^{17} ions/cm^2 though the disorder in the surface 0-50 nm (SR) region is the highest, in the deeper (DR) 50-300 nm region it is lowest (table 5.3). Furthermore for decreasing fluences, the disorder in the SR reduces but it systematically enhances in DR (table 5.3), leading to a distinct cross-over at 50 nm. Room temperature Cobalt implantation of TiO$_2$, thus leads to a very complicated damage accumulation profile. Such complex behavior may be related to the high ionic character of chemical bonds as observed in some oxides [19]. The total number of displacements have been calculated by integrating the density of defects over various depths and are given in table 5.3. As displayed by fig. 5.6, SRIM simulation under-estimates the disorder at the surface as well as in the deeper layers.

Table 5.3: Total displacements in various regions

Fluence (ions/cm^2)	SR 0-50 nm (10^{17}/cm^2)	DR 50-300 nm (10^{17}/cm^2)	Total 0-300 nm (10^{17}/cm^2)
3×10^{16}	1.28	8.27	9.54
5×10^{16}	1.46	6.48	7.94
8×10^{16}	1.60	6.25	7.85
1×10^{17}	1.81	5.93	7.74

SR region is expected to contain mostly isolated point defects. This is also confirmed by XPS studies, discussed in chapter 3, that demonstrate the generation of of oxygen vacancies (Ti^{3+}) upon ion irradiation. In addition to the vacancies, irradiation also produces nanostructures [20, 21] and enhanced roughness on the sputtered surfaces (chapters 3, and 6). Together, they become responsible for the enhanced disorder observed on the surface at high fluences. As presented by (TRIM and SRIM) simulations, SR becomes the sink of vacancies (shown by R$_{pd}$) whereas excess interstitials will be expected towards bulk (near R$_p$) [22]. The damage profiles, as presented here show that MC simulations cannot describe the observed behavior completely. High concentration of vacancies below R$_{pd}$, and creation of defects up to 300 nm below the surface cannot be explained by simulations. Damage observed in regions B and C here, may be caused by presence of Cobalt ions (suggested by table 5.1 and table 5.2) and Ti interstitials. Further, the dynamical annealing processes, as discussed above, can also promote the development of the Co-Ti-O phase, cobalt nano-clusters as well as some End-of-Range (EOR) defects in these regions [23]. Presence of phase formation and nano-clusters upon irradiation has been observed in chapter 3 through XRD and Raman investigation. GIXRD results in fig. 5.7 also indicate the generation phase transition. With A being vacancy rich region, and excess interstitials mostly located in B and C, recombination processes are active in the intermediate (100-150 nm) regions. This is responsible for the lower damage in this region at high fluences. Moreover, phase formations can also produce enhanced point defects, at high fluences, which may diffuse and control the fluence dependent lowering of disorder in this region. Strain, as seen in fig. 5.7, can also influence the activation energy of damage recovery [24].

The structural modifications in cobalt implanted rutile $TiO_2(110)$ single crystals have also been investigated by GIXRD studies. Fig. 5.7 displays high resolution GIXRD spectra from a depth of about 200 nm by keeping the incident angle at 0.8°, w.r.t. the sample surface, during experiment. Pristine sample displays a distinct crystalline feature from TiO_2 (111) plane at 41.6°. After 1×10^{16} ions/cm^2 cobalt implantation, this feature is weak and slightly shifted towards higher angles (41.8°) indicating a generation of compressive stress in the lattice. Presence of oxygen vacancies and cobalt atoms in TiO_2 lattice can generate stress in the lattice [25]. The residual stress due to cobalt implantation have been calculated as [26]:

$$\sigma = -\frac{E}{\nu}\left(\frac{d_s - d_0}{d_0}\right) \tag{5.1}$$

where, E, ν, d_s, d_0, are the young's modulus , Poission's ratio, and interplanar spacing for implanted and pristine surface, respectively. The value for E and ν are respectively 230 GPA and 0.27 for rutile TiO_2 [26]. For 1×10^{16} ions/cm^2, the residual stress is of compressive nature and is

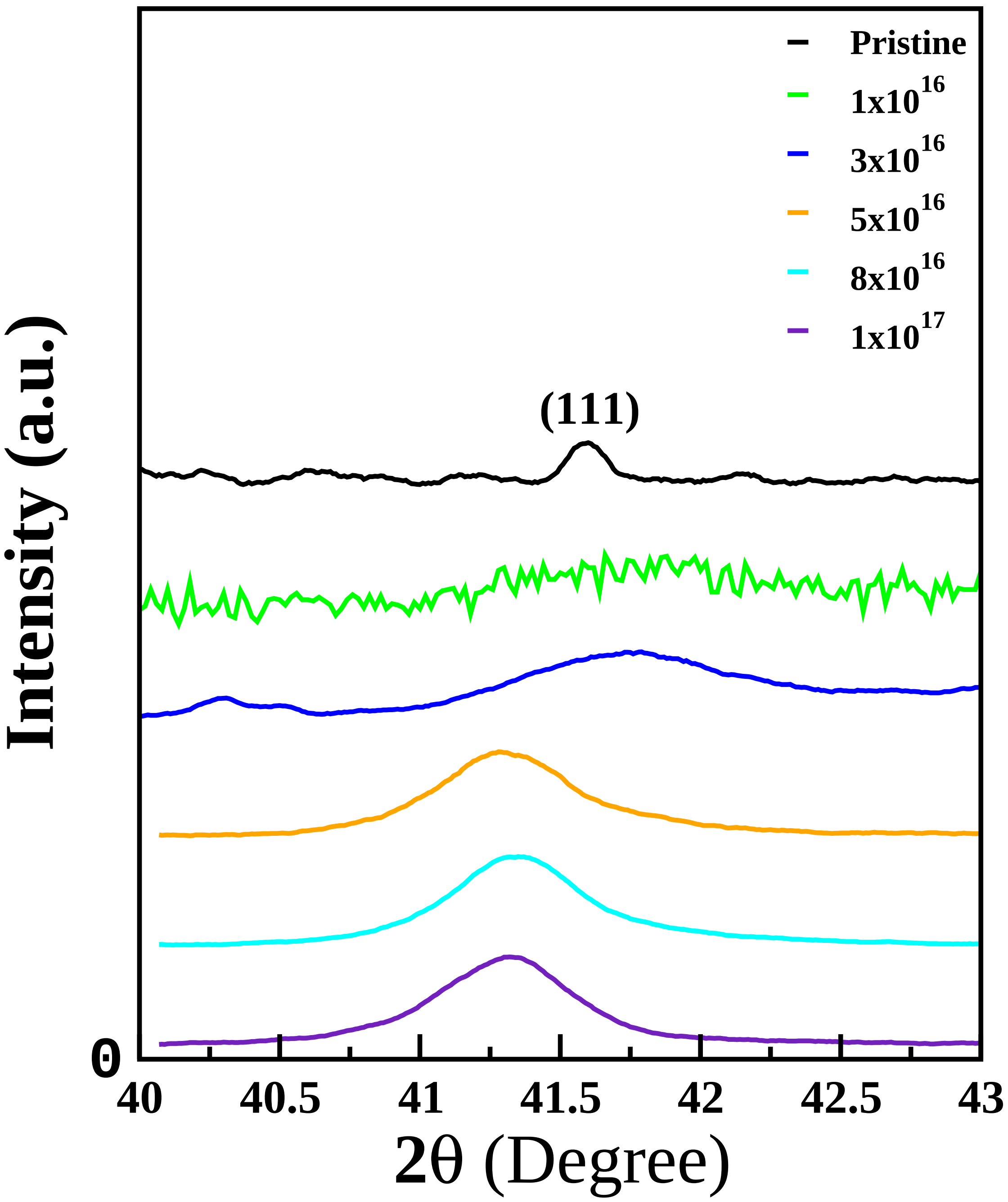

Figure 5.7: GIXRD spectra for pristine TiO_2 and after implantation with various Cobalt fluences are shown.

estimated to be -3.9 GPA. At 3×10^{16} ions/cm^2 also, an increase in angle (41.75°) compared to the pristine causes a compressive stress of -2.9 GPA in the lattice. Surprisingly however, for 5×10^{16} ions/cm^2 and higher fluences, the (111) feature appears at lower angles (41.5°) than pristine indicating development of tensile stress of about 5.92 GPA in the lattice. Hence, there is a transition in the nature of stress which is of compressive type at lower fluences becoming tensile like at larger fluences. Such transitions will be expected to be accompanied by phase formation [25]. In the present thesis, the development of Co-Ti-O type phases have been observed at 5×10^{16} ions/cm^2 in chapters 3. This phase formation may be responsible for the observed transitions. However, presence of new phases in GIXRD were only observed at higher fluences 8×10^{16} and 1×10^{17} ions/cm^2. This may be due to the presence of only small clusters, of new phase, at lower fluences. The variation in FWHM have also been investigated as a function of ion fluence. At 1×10^{16} ions/cm^2 the feature is very broad and weak. This demonstrates formation of a nearly amorphised lattice at this fluence and support the observed RBS/C results (fig. 5.5). At 3×10^{16} ions/cm^2 also the feature is very broad indicating a large inherent disorder, however at larger fluences the feature become narrower suggesting improvement in crystallinity. These results are similar to the trends observed in the damage profiles of fig. 5.6 where an improvement in lattice disorder is observed at higher fluences.

5.4 Conclusion

RBS/C and GIXRD techniques have been utilized to characterize the radiation damage and structural modifications in TiO_2 lattice that are produced after 200 keV cobalt implantation. Multiple scattering formalism has been utilized to extract the depth dependent damage profiles as a function of ion fluence and the results are compared with the MC simulations. RBS/C results indicate amorphization of the TiO_2 lattice at low fluences. However at higher fluences, a reduction in this lattice damage is observed as a function of ion fluence. This recovery is limited to 50-300 nm region and is controlled through ion induced dynamic annealing processes. The surface region on the other hand demonstrates an increased disorder with fluence due to the creation oxygen vacancies, higher rms roughness and nanostructures. The switchover in damage behaviors occurs at a very distinct cross-over point at 50 nm below the surface. In addition, damage profiles also show a valley, or low damage region, created by high recombination of point defects. Formation of Co-Ti-O phase as well as stress in the lattice can also be responsible for the intricate damage profiles observed here. MC simulation (SRIM) result displays a very different damage distribution. It shows a much narrower damage profile and estimates much lower disorder in the surface as well as deep layers.

Bibliography

[1] H. Li, Y. Zhang, S. Wang, Q. Wu, and C. Liu, J. Hazard. Mater. **169**, 1045 (2009).

[2] D. L. Liao and B. Q. Liao, J. Photochem. Photobiol. A **187**, 363 (2007).

[3] L. Zhang, F. Lv, W. Zhang, R. Li, H. Zhong, Y. Zhao,Y. Zhang, and X. Wang, J. Hazard. Mater. **171**, 294 (2009).

[4] U. Diebold, Surf. Sci. Rep. **48**, 53 (2003).

[5] M. A. Fox, M. T. Dulay, Chem. Rev. **93**, 341 (1993).

[6] A. Fujishima and K. Honda, Nature **238**, 37 (1972).

[7] W. T. Geng and Kwang S. Kim Phys. Rev. B **68**, 125203 (2003).

[8] G. Akpan and B. H. Hameed, Applied Catalysis A. General **375**, 1 (2010).

[9] F. Chen, X. L. Wang, and K. M. Wang, Opt. Mater. **29**, 1523 (2007).

[10] Peter Sigmund, Phys. Rev. **184**, 383 (1969).

[11] L. C. Feldman and J. W. Rodgers, J. Appl. Phys. **41**, 3776 (1970).

[12] James F. Ziegler, M. D. Ziegler, and J. P. Biersack, Nucl. Instru. Meth. B **268**, 1818 (2010)

[13] M. Mayer, Nucl. Instrum. Methods Phys. Res. B **332**, 176-180 (2014).

[14] C. W. White, C. J. McHargue, P. S. Sklad, L. A. Boatner, G. C. Farlow, Mater. Sci. Rep. **4 (2,3)**, 41 (1989).

[15] I. Khubeis, R. Fromknecht, S. Massing, and O. Meyer, Nucl. Inst. Meth. B **141**, 332-337 (1998).

[16] R. Fromknecht, O. Meyer, Mater. Chem. Phys. **45**, 50 (1996).

[17] L. C. Feldman and J. W. Rodgers, J. Appl. Phys. **41**, 3776 (1970).

[18] G. S. Sandhu, M. Anjum, S. Cherekdjian, B. K. Patnaik, N. R. Parikh, and M. L. Swanson, Nucl. Inst. and Meth. B **59/60**, 145 (1991).

[19] S. Kim, S. J. Hwang, W. Choi, J. Phys. Chem. B **109**, 24260 (2005).

[20] S. R. Joshi, B. Padmanabhan, A. Chanda, V. K. Malik, N. C. Mishra, D. Kanjilal, and Shikha Varma, Appl. Phys. A. **122**, 713 (2016).

[21] S. R. Joshi, B. Padmanabhan, A. Chanda, I. Mishra, V. K. Malik, N. C. Mishra, D. Kanjilal, and Shikha Varma, App. Sur. Sci. **387**, 938-943 (2016).

[22] Soma Dey and Shikha Varma, Nucl. Inst. and Meth. B **212** , 146-150 (2003).

[23] Yupu Li, R. J. Liu, and Wei-Kan Chu, Phys. Rev. B **57**, 5668 (1998).

[24] H. Abe, S. Yamamoto, H. Naramoto, Nucl. Instr. and Meth. B **127/128**, 170 (1997).

[25] D. Ma, Z. Lu, Y. Tang, T. Li, Z. Tang, Z. Yang, Phys. Lett. A **378**, 25702575 (2014).

[26] Subrata Majumder, D. Paramanik, V. Solanki, I. MIshra, D. K. Awasthi, D. Kanjilal, and Shikha Varma Appl. Surf. Sci **258**, 4122-4124 (2012).

Chapter 6

Scaling Studies of Self-affine Nanostructures on TiO_2 Surfaces via Ion Implantation

6.1 Introduction :

Ion irradiation of metal and semiconductors exhibit numerous technological applications through the formation of nanostructures, hetrostructures, improvement of functional properties, etc. [1–3]. These properties can be easily tuned by controlling the ion parameters and ion- solid interactions in the host lattice [4, 5]. These interactions can produce modifications to the surface and bulk as well as sometimes produce new phases, not observed by simple doping methods [6]. Significantly, these are produced by the instabilities created during sputtering processes via competing processes of erosion, surface diffusion [7] and mass transport [8]. These processes further participate in the generation of many exciting self-organized nano-patterns on the surfaces, such as ripples, nanostructures, hill and valleys, hemi-spherical dots, etc. [4, 5]. For non metals, the normal incident ion irradiation produces interlocking hillocks and depressions on the surface whereas for off normal incidence, quasi periodic ripple patterns, whose orientation depends on the angle of the incident ion beam, are observed [7]. For metals, ripple patterns have been observed even at normal ion incidence conditions [6, 9].

Transition metal oxides have attracted immense attention from fundamental as well as application perspectives [10, 11]. TiO_2 is a wide band gap semiconductor (3.2 eV for anatase and 3.0 eV for rutile) and exhibits many advanced properties with exciting potential in fields like photocatalysis, solar cells, photovoltaics, magnetic storage media, waste water management, bio-implants, etc. [12–15]. In nano-scale also TiO_2 displays many fascinating properties which are, however, severely controlled by the preparation methods [16, 17]. Morphology of nanostructures and their evolution can also influence the properties. Fabrication of nanostructures on clean single crystal surfaces, by ion irradiation, has been shown to be an attractive and simple method which does not involve intricate procedures. The formation of nanostructures and nano-patterns on surfaces here occurs *spontaneously* through the process of kinetic roughening [1, 7, 9, 18]. Such methods present simple routes for the generation of the nanostructures on a large surface area, in a technologically single step. Here, fabrication of nanostructures is stimulated by the competing processes of erosion and diffusion [19–24]. Remarkably the morphology of the nano-patterns, produced by irradiation methods, and their many characteristic distributions (like long range distribution, power spectral density etc.) depend only on the nature of the surface and the ion beam parameters [1, 2, 7, 25–27]. Systematic understanding of these self assembled patterns and their distributions can provide essential knowledge about the relation between the irradiation parameters and the morphologies that they produce.

Surface patterning of oxides or multi-atom surfaces, during ion irradiation, is significantly more complex due to the preferential sputtering of the lighter atoms [19, 28]. On oxides, enhanced sputtering of oxygen leads to the formation of metal rich centers that become the nucleation sites of the nanostructures [29, 30]. In-equivalent surface diffusion along crystallographic axes, on anisotropic $TiO_2(110)$ surface, further complicates the understanding of the surface dynamics during evolution [6].

Scaling studies of surfaces are fundamentally important to understand the underlying phenomenon of surface- evolution under varying conditions. Non- equilibrium growth models encompass the evolution of surfaces for widely different phenomenon like ion irradiation, atom-deposition, growth of tumors, bacterial colonies, etc. [31–33]. Different surfaces can evolve through very different processes, yet their evolution belongs to only a few universality classes that describe the unique and essential properties of the evolution- dynamics. These are usually understood under the framework of *theory of kinetic roughening* [31–33] where a flat surface essentially grows and roughens with time. The *dynamic scaling hypothesis* by Family-Vicsek shows that rms roughness, $\sigma(L,t)$, of such growing surfaces exhibit spatial and temporal scaling behavior [34,35] with exponents that provide insightful knowledge on the universality class to which the surface- evolution belongs. With a variety of ion beam parameters and many surface conditions, understanding the surface- evolution after ion irradiation can be a complex exercise. Scaling studies provide an essential framework in this direction. Many such studies report investigations of nanostructure- patterning as well as surface evolution after ion irradiation with several ion species and energies [20,28,36,37]. There are however no studies that discuss the scaling properties of Cobalt-ion irradiated TiO_2 (110) surfaces.

This chapter discusses the morphological properties of the self assembled nano-patterns generated on the TiO_2(110) surfaces after irradiation with cobalt ions. The scaling behavior of these surfaces have been investigated via height-height correlation and structure factor analysis. The exponents obtained here show that the evolution of the TiO_2(110) surfaces, after ion irradiation, is diffusion-dominated and evolves under the EW universality class.

6.2 Experimental :

Commercially available rutile TiO_2(110) single crystals have been irradiated at room temperature using 200 keV cobalt ions (flux of 1.6×10^{13} ions/cm^{2}sec) with fluences varying from 1×10^{16} to 1×10^{17} ions/cm^2. The average penetration depth of cobalt ions in TiO_2 at 200 keV has been estimated to be 98 nm using SRIM code [38]. Scanning probe microscope, Nanoscope V (Bruker) AFM, has been utilized in tapping mode to investigate the surface topography. AFM images were acquired on various scan areas in ambient conditions and were digitized into 512×512 pixels. Several different regions of cobalt implanted TiO_2 have been scanned at random locations to perform statistical analysis.

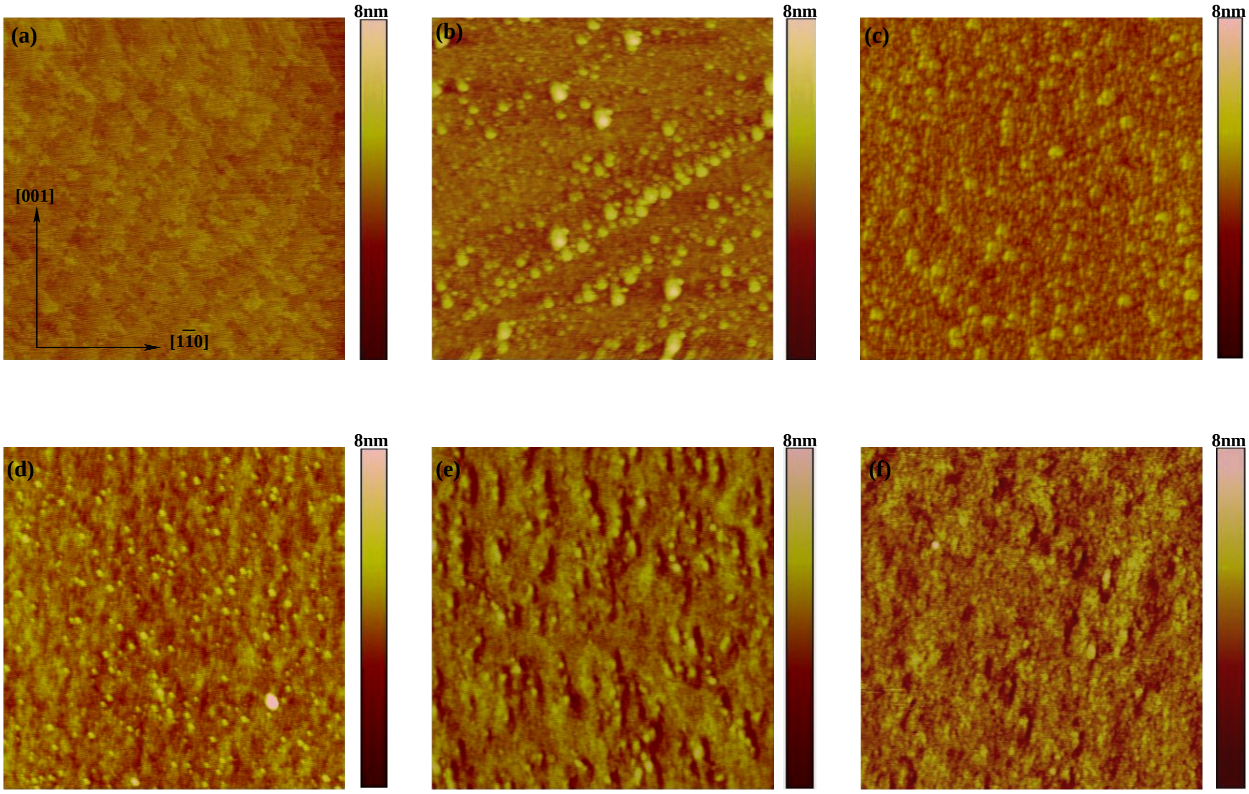

Figure 6.1: AFM images ($2\mu m \times 2\mu m$) of (a) pristine rutile TiO_2 (110) and after cobalt ion implantation with fluence of (b)1×10^{16}, (c) 3×10^{16}, (d) 5×10^{16}, (e) 8×10^{16}, and (f) 1×10^{17} ions/cm^2, respectively. Crystallographic directions are shown on the pristine surface and were kept same for all the samples during irradiation.

6.3 Results and Discussions :

Morphological evolution of single crystal rutile TiO_2 (110) surfaces, both prior to and post cobalt ion irradiation, is shown in fig. 6.1. The topography of pristine surface displays the presence of steps, as expected on rutile TiO_2 surfaces [39]. Evolution of nanostructures on cobalt implanted rutile TiO_2, at various fluences, is shown in fig. 6.1(b-f). The foremost consequence of ion impact on single crystal substrates is to produce adatoms and vacancy clusters [6]. The morphological evolution of the surface during ion implantation takes place due to various competing processes. Erosion of the surface induces instability via curvature dependent sputtering, whereas surface diffusion and adatom diffusion restore equilibrium [6]. The ion induced growth of nanostructures during implantation can be explained by Bradley Harper (BH) theory [7]. The probability of the ejection of the surface atoms during ion implantation is directly proportional to the energy transferred by collision cascade to the surface atoms. The BH model predicts that the total energy deposited and therefore the number of sputtered atoms, is sensitive to the local surface curvature. Surface atoms preferentially get eroded from valleys whereas erosion from the ridges becomes unlikely. This leads to the enhancement of local surface curvature with increase in roughness and formation of self organized nanostructures. In hetro-atomic crystals, like TiO_2, preferential sputtering of light atoms also plays a vital role in the surface evolution [19, 28].

After implantation with a fluence of 1×10^{16} ions/cm^2 (fig. 6.1(b)), the initial nucleation of nanostructures appears to take place at the step edges of TiO_2 surface. This might be due to the presence of kink sites, at the edges, which act as preferential nucleation centers of the nanostructures. This has earlier been observed in MBE grown InP/InGaP surfaces [40]. The diameter distribution of nanostructures (fig. 6.2(a)) shows that about 59% are smaller than 50 nm, though some as large as 150 nm are also observed. After the fluence of 3×10^{16} ions/cm^2, along with the nanostructures, development of a ripple pattern is also noticed. Ripples appear to be aligned along [001] crystallographic direction of rutile TiO_2 surface. The size distribution of the nanostructures at this stage (fig. 6.2(c)) displays that about 65% are smaller than 50 nm. For the fluence of 5×10^{16}, 8×10^{16}, and 1×10^{17}ions/cm^2, nanostructures appear to be aligned along [001] crystallographic direction. Moreover, percentage of nanostructures smaller than 50 nm has increased to 67%, 70% and 87%, respectively. This increase in percentage of smaller size nanostructures (less than 50 nm) with increase in fluence can be attributed to the fragmentation of bigger nanostructures created at lower fluences due to ion irradiation. This leads to a significant enhancement of smaller sized nanostructures at the highest fluences. The average height of the nanostructures (as shown in fig. 6.1)), however, remains nearly same as 1.5, 1.0, 1.1, 1.36 and 1.6±0.2 nm for 1×10^{16}, 3×10^{16}, 5×10^{16}, 8×10^{16}, and 1×10^{17} ions/cm^2, respectively, whereas corresponding rms surface roughness is 0.257, 0.398, 0.418, 0.437m, and 0.438 nm (0.089 for pristine).

The evolution of surfaces during non-equilibrium processes such as ion irradiation, deposition of thin films, etc. is governed by the kinetic theory of roughening [34]. During ion irradiation,

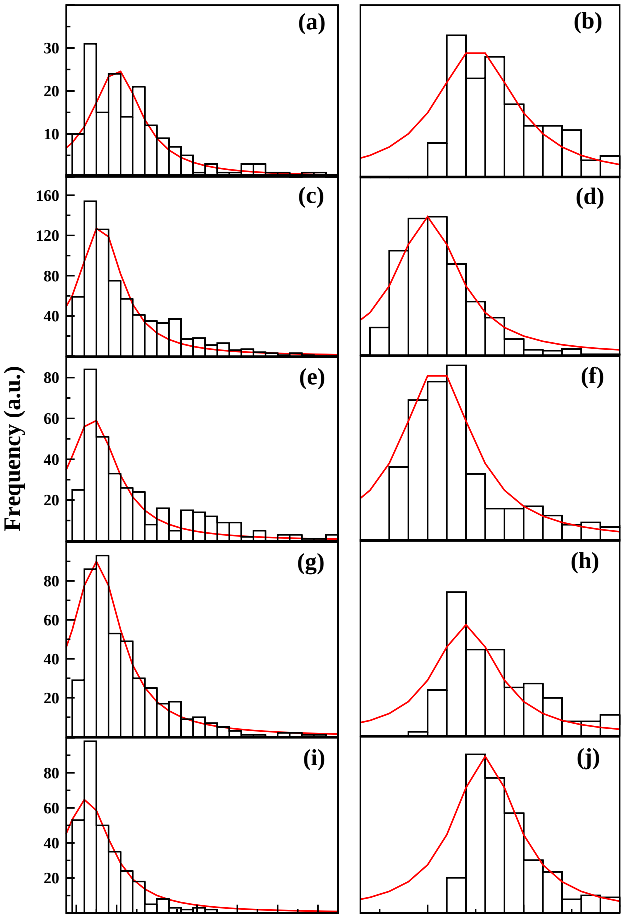

Figure 6.2: Size distribution of nanostructures (Diameter & Height) for (a & b)1×10^{16}, (c & d) 3×10^{16}, (e & f) 5×10^{16}, (g & h) 8×10^{16}, and (i & j) 1×10^{17} ions/cm^2, respectively on cobalt implanted rutile TiO_2 surface. Solid line represents the lorentzian fitting to the distribution.

evolution of nanostructures is assumed to obey *dynamic scaling hypothesis* [34, 35]. All rough surfaces can be characterized by their rms interface width:

$$\sigma = \langle h(x,y) - \langle h(x,y) \rangle \rangle^{1/2} \tag{6.1}$$

where h(x,y) is the height function. Evolution via non equilibrium growth processes is expected to develop self affine surfaces [34, 35] whose rms width scales with time *t* and the length *L* according to Family- Vicsek dynamic scaling hypothesis [41]:

$$\sigma(L,t) = L^{\alpha}\, f(t/L^{\alpha/\beta}) \tag{6.2}$$

where

$$\sigma(L,t) \propto \begin{cases} L^{\alpha} \text{ if } t/L^{\alpha/\beta} \longrightarrow \infty \\ t^{\beta} \text{ if } t/L^{\alpha/\beta} \longrightarrow 0 \end{cases} \tag{6.3}$$

Parameter α is a roughness exponent that characterizes the roughness of the interface [42] whereas parameter β is termed as the growth exponent which identifies the time dependent dynamics of the roughening process. Self affine surfaces display upper horizontal cut off to scaling, described as correlation length ξ, above which the interface width no longer scales as L^{α} and eventually acquires a saturation value σ. Information about the correlation length can be obtained from Eqn-6.3, it increases with time as $\xi \propto t^{1/z}$ where z (= α/β) is the dynamic scaling exponent.

Fig. 6.3 displays the root mean square roughness of the cobalt implanted rutile TiO_2 surfaces as a function of ion fluence. The figure displays that initially the roughness rises for lower fluences but then gets saturated at higher fluences. Using the asymptotic limit of Family Vicsek relation ($\sigma \propto t^{\beta}$ as shown in Eqn-6.3), the dynamic growth exponent β has been evaluated here to be 0.23±0.01. This value of growth exponent is consistent with the numerical simulations of the noisy Kuramoto and Tsuzuki equation [43, 44] along with Edward Wilkinson (EW) growth equation [45]. In this regime, the non linear effects eventually stabilize the surface and surface relaxation takes place by diffusion that belongs to EW universality class.

The equal time HHC function $G(\mathbf{r},t)$ is defined as:

$$G(\mathbf{r},t) = \frac{1}{L}\sum_{\mathbf{r}'} \langle [h(\mathbf{r}+\mathbf{r}',t) - h(\mathbf{r}',t)]^2 \rangle. \tag{6.4}$$

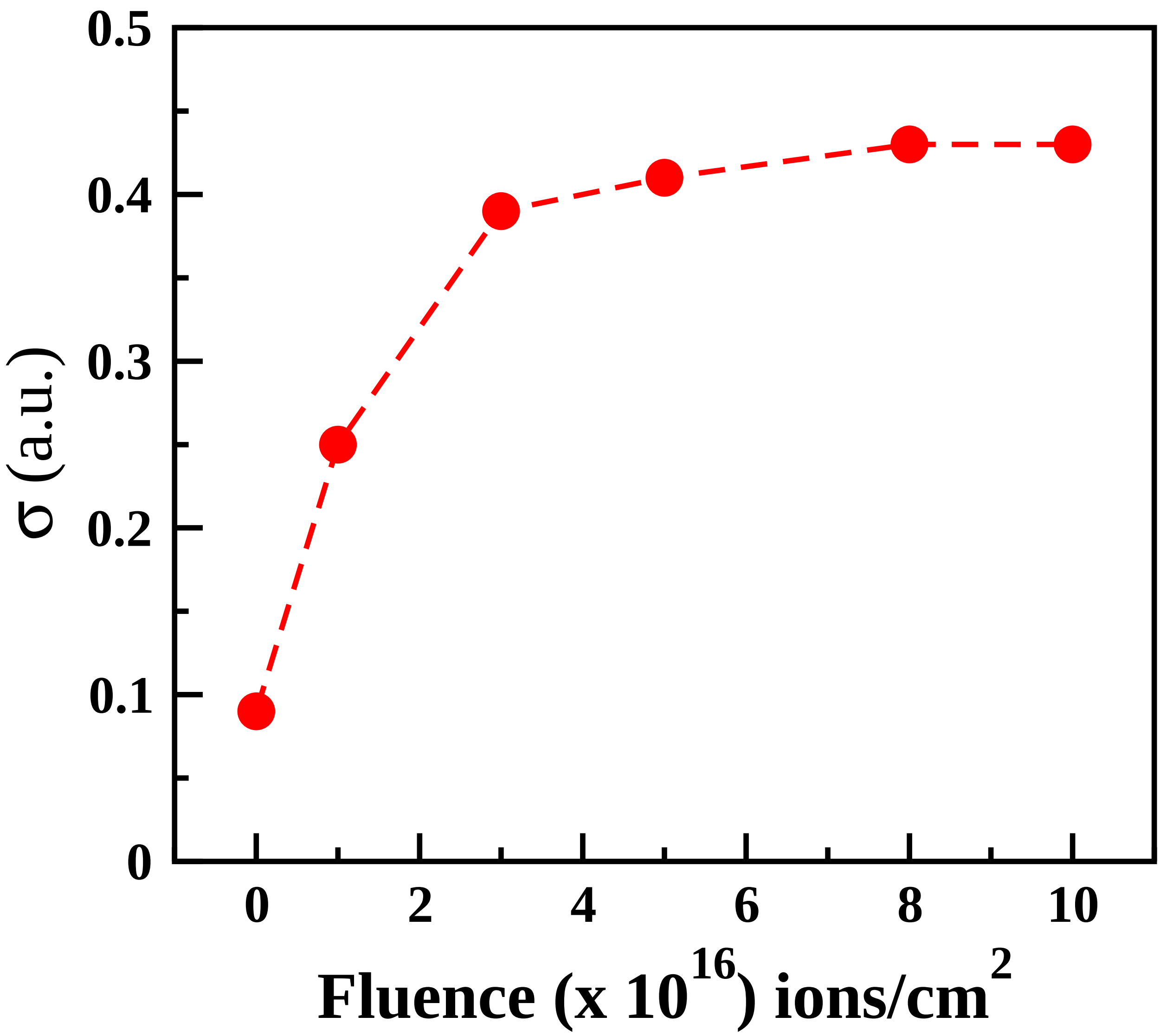

Figure 6.3: Variation of rms roughness (σ) as function of ion fluence, for ion implanted surfaces. Data for pristine sample is also shown.

Here $\mathbf{r}$ is the translational length along lateral direction and $\langle\rangle$ denotes the ensemble average. Under far from equilibrium conditions, noise induced roughening is the major factor for the roughness of the interface [46] and hence the surface morphology appears self affine. In particular, for self affine surfaces, the dynamic scaling hypothesis suggests that the HHC function $G(\mathbf{r})$ has the following scaling form [46]

$$G(\mathbf{r}) \sim \begin{cases} \mathbf{r}^{2\alpha} \text{ if } \mathbf{r} << \xi \\ 2\,\sigma^2 \text{ if } \mathbf{r} >> \xi \end{cases} \tag{6.5}$$

where α is the roughness exponent, ξ is the lateral correlation length and σ is the rms interface width. A large value of α corresponds to a locally smooth surface while a smaller one corresponds to a more locally jagged morphology [34].

Fig. 6.4 displays the HHC function for pristine as well as cobalt implanted TiO_2 surfaces at several fluences. At shorter length scales, the log-log plot of HHC function is a straight line whose slope provides α. At larger length scales, HHC function saturates. The turning point provides the lateral correlation length (ξ) whereas the saturation determines the surface roughness (σ). Location of ξ separates the lower and high length scales in HHC function. Roughness exponent, α, has been estimated here (table 6.1) using height height correlation (HHC) description presented in using Eqn-6.5. The correlation length, ξ, which represents a typical wavelength of fluctuations, on the growing surface, can also be estimated using this technique [9]. ξ have also been estimated via HHC technique and the results are presented in Table-6.1.

Fluence ($ions/cm^2$)	α	ξ (nm)	z	γ
	($\pm$0.02)	($\pm$2)	z	($\pm$0.1)
Pristine	0.90	5.5	3.9	2.0
1×10^{16}	0.70	41.0	3.0	4.0
3×10^{16}	0.77	35.0	3.3	4.0
5×10^{16}	0.85	38.0	3.7	4.0
8×10^{16}	0.94	30.0	4.0	4.0
1×10^{17}	0.82	28.0	3.6	3.5

Table 6.1: Scaling Exponents from height-height correlation (HHC) function and structure factor S(**k**, t).

Pristine surface displays a high value of α (=0.9) suggesting the surface to be smooth. After

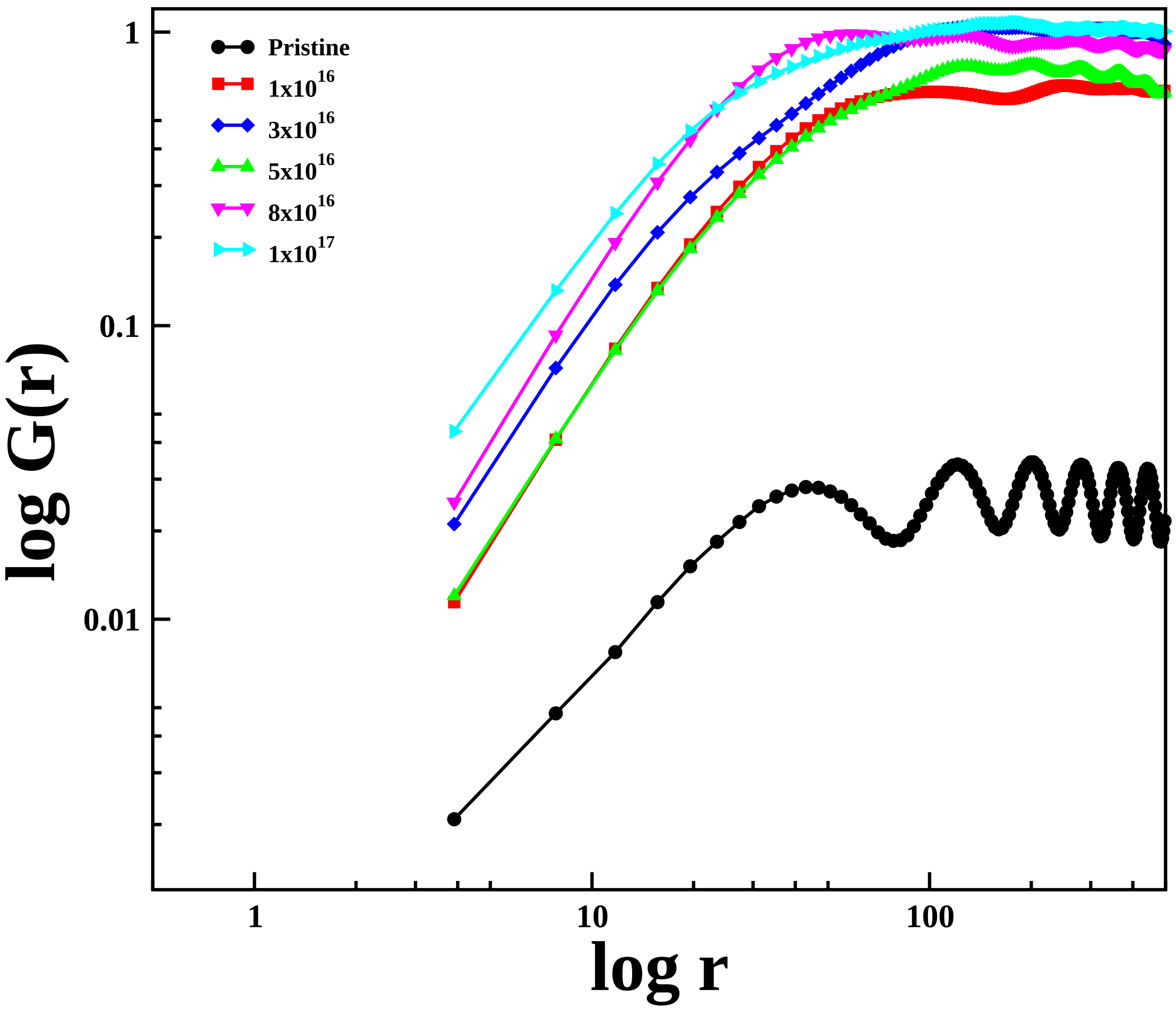

Figure 6.4: Equal time height-height correlation function G(**r**,t) as a function of translational length (**r**), for ion implanted surfaces

a fluence of 1×10^{16} $ions/cm^2$, α decreases to 0.70 due to ion beam induced sputtering which roughens the surface. For higher fluences of 3×10^{16}, 5×10^{16} and 8×10^{16} $ions/cm^2$, α is observed to be 0.77, 0.85 and 0.94, respectively. These values indicate a significant role of ion beam induced diffusion in the evolution of the surfaces. High sputtering becomes responsible for the slight decrease in α (0.82) at the highest fluence. All the values of α here range within 0.7-0.9 (table 6.1). This suggests that the surfaces generated after ion beam irradiation are of self affine ($0.5 < \alpha < 1$) nature [34,35] and their evolution is significantly influenced by diffusion processes. Dynamic exponent z (= α/β) has also been evaluated here and is found to be 3.0-4.0 for the ion irradiated surfaces (table 6.1) again indicating the surface-evolution to be diffusion dominated [47].

Pristine surface being flat displays a small value of ξ. Periodic modulations at large **r**, in HHC, are caused by the steps on the pristine surfaces. An increase in ξ is observed after a fluence of 1×10^{16} $ions/cm^2$ (table 6.1). As ξ contains information related to the lateral dimensions of nanostructures, patterns and periodicities on the surface, increase in ξ reflects the presence of nanostructures on the surface. Lower ξ at higher fluences may be related to the fragmentation of nanostructures with irradiation.

The evaluation of roughness exponent using HHC function can be difficult in the steady state regime, where cross-over effects become important [46]. Structure factor S(**k**, t), however, is not influenced by these problems. It is one of the most appealing technique to study the spatial properties along with the periodicity of the self affine nanostructured surfaces in reciprocal space. The structure factor can be estimated as [46]

$$S(\mathbf{k},t) = \langle \hat{h}(\mathbf{k},t)\hat{h}(-\mathbf{k},t)\rangle \tag{6.6}$$

where $\hat{h}(\mathbf{k},t)$ is the discrete fast Fourier transform of the height at each lattice point about its mean value. The structure factor has a following scaling form

$$S(\mathbf{k},t) = k^{-\gamma}s(\mathbf{k}^{zt}) \tag{6.7}$$

where γ is the structure factor constant. The scaling function s approaches a constant for large argument but behaves differently in the short time limit $x \ll 1$ where it has a form like:

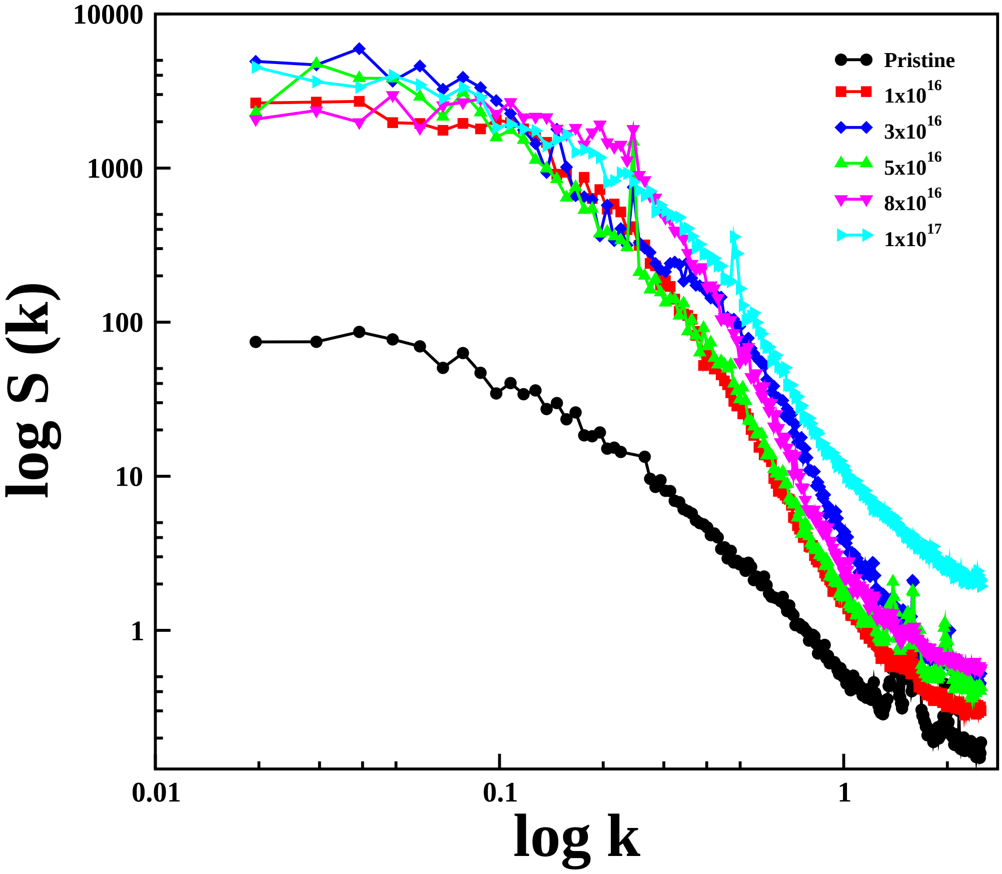

Figure 6.5: Structure factor S(**k**) as a function of spatial frequency (**k**), for ion implanted surfaces.

$$s(x) \sim \left\{ \begin{array}{c} x \text{ if } \gamma \leq z \\ x^{\gamma/z} \text{ if } \gamma \geq z \end{array} \right. \tag{6.8}$$

Fig. 6.5 displays the structure factor, S(**k**, t), for pristine as well ion irradiated TiO_2 surfaces. The structure factor curve can be divided into two distinct regions: the horizontal low frequency part resembles the uncorrelated white noise, while the high frequency region delineates correlated surface structures. The structure factor does not display any prominent peaks in fig. 6.5, thus indicating absence of any dominant periodicities on the irradiated surfaces. Self affine nature of the surfaces is also revealed by the non-appearance of any spatially selected wavelength [48]. The value of γ has been estimated by fitting the higher frequency component of of S(**k**, t) with a power law (table 6.1).

For pristine surface, the value of γ is determined to be 2.0. However, on the ion irradiated TiO_2 surfaces γ of 4.0 is obtained for most of the fluences. Eklund et.al have shown that $\gamma = 4.0$ suggests a diffusion dominated surface evolution [49]. A slightly lower value of $\gamma = 3.5$ at the highest fluence of $1 \times 10^{17}\ ions/cm^2$ indicates some sputtering induced erosion on the surface. Roughness exponents α estimated using γ values are in good agreement with the HHC results.

6.4 Conclusion :

The scaling properties of cobalt implanted rutile TiO_2 surfaces have been investigated here by Height -Height correlation (HHC) as well as Structure factor S(**k**, t) methods. Values of α and γ in conjugation indicate that diffusion is the dominant mode of surface evolution after ion irradiation of TiO_2. Slight decrease in γ at the highest fluence also suggests some role of ion induced sputtering at this stage. Decrease in ξ for higher fluences indicate the fragmentation of the nanostructures. Scaling exponents suggest that these ion irradiated surfaces belong to EW universality class.

Bibliography

[1] F. Frost, A. Schindler, and F. Bigl, Phys. Rev. Lett. **85**, 4116 (2000).

[2] S. Facsko, T. Dekorsy, C. Koerdt, C. Trappe, H. Kurz, A. Vogt, and H. L. Hartnagel, Science **285** 1551 (1999).

[3] S. Arulkumaran, K. Ranjan, G. I. Ng, J. Kennedy, P. P. Murmu, T. N. Bhat, and S. Tripathy, J. Vac. Sci. Technol. B **34**, 042203 (2016).

[4] S. Facsko, T. Dekorsy, C. Koerdt, C. Trappe, H. Kurz, A. Vogt, and H. L. Hartnagel, Science **285**, 1551 (1999).

[5] A. Keller, S. Rossbach, S. Facsko, and W. Miller, Nanotechnology **19**, 135303 (2008).

[6] U. Valbusa, C. Borangno, and F. R. de Mongeot, J. Phys. Condens.Matter **14** 8153(2002).

[7] R. M. Bradley, J. M. E. Harper, J. Vac. Sci. Technol. A **6** 2390 (1988).

[8] D. A. Pearson and R. M. Bradley, J. Phys. COnd. Matt. **27**, 015010 (2015).

[9] S. R. Joshi, T. Bagarti, and S. Varma, Surf. Science **641**, 170, (2015).

[10] A. Fujishima, and K. Honda, Nature **238**, 37 (1972).

[11] Y. Matsumoto, M. Murakami, T. Shono, T. Hasegawa, T. Fukumura, M. Kawasaki, P. Ahmet, T. Chikyow, S. Koshihara, and H. Koinuma, Science **291**, 854 (2001).

[12] X. Chen, and S. S. Mao, Chem. Rev. **107**, 2891 (2007).

[13] M. Qamar, and M. Muneer, Desalination **249**, 535 (2009).

[14] K. S. Ahn, Y. Yan, S. Shet, K. Jones, T. Deutsch, J. Turner, and M. Al-Jassim, Appl. Phys. Lett. **93**, 163117 (2008).

[15] Q. Yu, and C. Cao, J. Nanosci. Nanotech. **12**, (5):3984 2012.

[16] U. Diebold, Surf. Sci. Rep. **48**, 53 (2003).

[17] Yan Wang, Yiming He, Qinghua Lai, Maohong Fan, J. Environmental Sci., **26**, 2139-2177 (2014).

[18] D. K. Avasthi, Y. K. Mishra, D. Kabiraj, N. P. Lalla and J C Pivin, Nanotechnology **18**, 125604 (2007).

[19] V. Solanki, S. Majumder, I. Mishra, P. Dash, C. Singh, D. Kanjilal, and S. Varma, J. Appl. Phys. **115**, 124306 (2014).

[20] V. Solanki, S. Majumder, I. Mishra, S. R. Joshi, D. Kanjilal, and S. Varma, Rad. Eff. Def. Solids. **168**, 518 (2013).

[21] V. Solanki, I. Mishra, S. R. Joshi, P. Mishra, P. Dash, N. C. Mishra, D. Kanjilal, and S. Varma, Nucl. Instr. Meth. Physc. B, **365**, 82 (2015).

[22] D. Paramanik, S. R. Sahoo, S. Majumder, and S. Varma, Vacuum, **84**, 602 (2010).

[23] D. Kabiraj, S. R. Abhilash, L. Vanmarcke, N. Cinausero, J. C. Pivin, and D. K. Avasthi, Nucl. Instr. Meth. Physc. B **244**, 100 (2006).

[24] A. L. Stepanov, Rev. Adv. Mater. Sci. **30**, 150-165 (2012).

[25] S. Facsko, T. Bobek, A. Stahl, H. Kurz, and T. Dekorsy, Phys. Rev. B **69**, 153412 (2004).

[26] M. A. Makeev, R. Cuerno, and A. L. Barabasi, Nucl. Instrum. Methods Phys. Res. B **197** 185 (2002).

[27] P. Sigmud, Phys. Rev. **184** 383 (1969).

[28] S. Majumder, D. Paramanik, V. Solanki, B. P. Bag, and S. Varma, Appl. Phys. Lett. **98**, 053105 (2011).

[29] S. R. Joshi, B. Padmanabhan, A. Chanda, V. K. Malik, N. C. Mishra, D. Kanjilal, and Shikha Varma, Appl. Phys. A. **122**, 713 (2016).

[30] S. R. Joshi, B. Padmanabhan, A. Chanda, I. Mishra, V. K. Malik, N. C. Mishra, D. Kanjilal, and Shikha Varma, App. Sur. Sci., http://dx.doi.org/doi:10.1016/j.apsusc.2016.07.038

[31] J. J. Ramasco, J. M. Lopez and M. A. Rodriguez, Phys. Rev. Lett. **84**, 2199 (2000).

[32] J. Krim and G.Palasantzas, Int. J. Mod. Phys. B **9**, 599 (1995).

[33] G. Palasantzas and J. Krim, Phys. Rev. B. **48**, 2873 (1993).

[34] A.L. Barabsi, H. E.Stanley, *Fractal Concepts in Surface Growth*, Cambridge University Press, **1995**.

[35] F. Family,T. Vicsek, *Dynamics of fractal Surface*, World Scientific, Singapore, **1991**.

[36] G. Carter and V. Vishnyakov, Phys. Rev. B **54** 17647 (1996).

[37] S. Rusponi, G. Costantini, C. Boragno, and U. Valbusa, Phys.Rev. Lett. **81** 2735 (1998).

[38] James F. Ziegler, M. D. Ziegler, and J. P. Biersack, Nucl. Instru. Meth. B **268**, 1818 (2010).

[39] Stefan Fischer, Andreas W. Munz, Klaus-Dieter Schierbaum, and Wolfgang Gopel, J. Vac. Sci. Tech. B **14**, 961 (1996).

[40] Shikha Varma, C.M. Reaves, V.B. Hill, S.P. DenBaars and W.H. Weinberg, Surf. Sci. **24**, 393 (1997).

[41] F. Family and T. Vicsek, J. Phys. A **18**, L75 (1985).

[42] J. Krim and J. O. Indekeu, Phys. Rev. E **48**, 1576 (1993).

[43] K. Sneppen, J. Krug, M. H. Jensen, C. Jayaprakash, and T. Bohr, Phys. Rev. A **46**, R7351 (1992).

[44] F. Hayot, C. Jayaprakash, and C. Josserand, Phys. Rev. A **47**, 911 (1993).

[45] S. F. Edwards and D. R. Wilkinson, Proc. R. Soc. London, Ser. A **381**, 71 (1992).

[46] M. Siegert and M. Plischke, Phys. Rev. E **50** 917 (1994).

[47] D. E. Wolf and J. Villian, Europhys. Lett. **13**, 389 (1990).

[48] Z. J. Liu, N. Jiang, Y. G. Shen, and Y. W. Mai, J. Appl. Phys. **92**, 3559 (2002).

[49] E. A. Eklund and E. J. Snyder, Surf. Sci. **285**, 157 (1993).

Chapter 7

Kinetic Monte Carlo simulations of self organized nanostructures on Ta Surface Fabricated by Low Energy Ion Sputtering

7.1 Introduction :

Non-equilibrium surfaces produced via bombardment with energetic ion beams, often exhibit well ordered patterns having several potential applications [1–3]. The surface morphology, here, develops as a consequence of competition between a variety of processes like roughening dynamics, relaxation processes, generation of defects, material transport etc. [4, 5]. Occurrence of a wide array of surface morphologies complicates the prediction of dominant mechanism controlling their evolution. Non-metallic surfaces generally display hills and depressions for normal incident ion beams [6], while showing quasi-periodic ripple morphology under off-normal conditions [7,8]. For metallic surfaces, ripples develop even at normal incidence [9]. Symmetry breaking anisotropy in surface diffusion can cause these ripples to rotate with substrate temperature [9, 10]. For low energy ion beam induced patterning, although the erosive processes are dominant, enhanced surface diffusion due to the defect mobility also becomes important especially under the low ion-flux conditions [4, 7]. The surface morphology in this scenario is governed by the non-equilibrium biased diffusion current.

Continuum model approach has proved to be a very successful technique in describing the surface evolution but involvement of several complex phenomena make it difficult to relate with the experimental results [11]. An alternative approach is the Kinetic Monte Carlo(KMC) method where the kinetic behavior of the surface is simulated at microscopic level for a discrete surface. During diffusion or sputtering, the surface gets modified in the units of whole atoms, only at the specific site [12]. Various models have been proposed to understand the effect of sputtering related erosion on surface evolution. For instance, in model by Cuerno et.al [13], the local surface morphology has been used to determine the sputtering yield of the surface, while in binary collision approximation, the atom gets removed from the surface with a probability proportional to the energy deposited, in its near surface region, by incoming ions [14–16]. Surface diffusion has been formulated via relaxation of the surface to its minimum energy through a series of atomic jumps with probability that depends upon the energy of the initial and the final state [17]. Thermally activated hopping, where an atom hops over an energetic barrier with a barrier height that depends on the local configuration, has also been considered for studying surface diffusion [14, 16, 18].

In the present article, KMC results are presented in 1+1 dimension for ion beam modified metallic surfaces. Experimentally, the presence of ripple morphology on ion irradiated Tantalum surfaces has been observed [19, 20]. We have developed a model based on earlier work by Cuerno *et. al.* [13] which was not able to describe the surface morphology of ion sputtered metallic Tantalum surface. The Schwoebel effect is found to be important for Tantalum surface, and has been incorporated in our model, by including a weak non-linearity in Hamiltonian for relaxation of diffusing atoms on the sputtered surface. Simulation results, presented here, show that the presence of Schwoebel effect produces the surface morphology and scaling exponents that are consistent with our experimental observations. The scaling exponents indicate that the morphology of ion sputtered Tantalum surfaces may belong to universality class other than Edward-Wilkinson(EW) and Kardar-Parisi-Zhang(KPZ). The paper is organized as follows. In Section 7.2 we describe the KMC model. The experimental details are described in Section 7.3 and in Section 7.4 we discuss the results.

7.2 The Model

In our model we assume that ion irradiation causes the surface to evolve by two dominant processes, namely erosion and surface diffusion. The erosion process consists of the removal of atoms from the surface due to the impinging ions. Ions bombarded on the surface penetrate deep into the substrate releasing energy to the neighboring atoms along the trajectory. If the energy gained by a surface atom is sufficiently large, it gets eroded from the surface. Sputtering yield, $Y(\phi)$, is defined as the number of atoms eroded for every incoming ion at an angle ϕ to the surface normal. It depends on the energy of the ion and local morphology of the interface and, is a measure of the efficiency of the sputtering process [21]. We assume $Y(\phi) = a + b\phi^2 + c\phi^4$, where a, b and c are constant such that $Y(\pi/2) = 0$ and for some critical ϕ_0, $Y(\phi)$ has a maxima. The erosion process brings in an effective negative surface tension that causes the surface to become rough [22].

Surface diffusion, on the other hand, consists of the random migration of surface atoms on the surface such that the surface energy is minimized. Its strength depends on the temperature of the substrate and the binding energy of the atoms. The negative surface tension, during erosion, leads the system towards instability and as a result the system responds to restore stability by surface diffusion [13].

We consider a 1+1 dimensional lattice with periodic boundary conditions. The surface at any instant of time *t* is described by the height $h_i(t)$ at each lattice site $i = 1, \ldots, L$. We consider initially (at time $t = 0$) a flat surface $h_i(0) = \text{const}$. The erosion takes place with probability p while the diffusive process occurs with probability $(1 - p)$ at a randomly chosen lattice site. The surface is evolved by following dynamical rules.

(i) *Erosion:* The particle on the surface at site i gets eroded with a probability $Y(\phi_i)p_e$ where $\phi_i = \tan^{-1}((h_{i+1} - h_{i-1})/2)$ and $1/7 \leq p_e \leq 1$ is the ratio of the number of occupied neighbors to the total number of neighboring sites [21]. The ratio p_e accounts for the unstable erosion mechanism due to the finite penetration depth of the bombarding ions into the eroded substrate [13,22,23].

(ii) *Surface diffusion:* The surface diffusion process is taken into account by nearest neighbor hopping. The hopping rate from an initial state i to a final state f is given by $w_{i,f} =$

$[1 + \exp(\beta \Delta H_{i \to f})]^{-1}$ where $\Delta H_{i \to f} = H_f - H_i$ is the difference in the energy of the states and $\beta^{-1} = K_B T$ where T is the surface temperature and K_B is the Boltzmann constant. The surface Hamiltonian is given by

$$H = \frac{J}{2} \sum_{\langle i,j \rangle} |h_i - h_j|^2, \tag{7.1}$$

where $\langle i, j \rangle$ denotes sum over nearest neighbor sites and J is the coupling strength. Similar relaxation behaviour has been considered by Cuerno *et. al.* [13] to describe the surfaces evolving from initial ripple structure into rough surfaces of KPZ class. Morphology of several other non-metallic surfaces, post ion irradiation, have also been describe sufficiently well by this model [24, 25].

The morphology of metallic surfaces, however, cannot be described by the above model alone. In these cases, a diffusing atom is repelled from the lower step and preferably diffuses in the uphill direction. This Schwoebel effect is controlled by the potential barrier, Schwoebel barrier, and has been considered to be crucial for MBE grown surfaces [17, 26, 27]. Growth models based on MBE studies, have shown that positive Schwoebel effect can be incorporated in the relaxation process Hamiltonian by the inclusion of a quartic term [17]. In the present study, we model the relaxation behaviour on ion sputtered Tantalum metal surfaces by modifying Eq. (7.1) to include the Schwoebel effect in the Hamiltonian:

$$H = \frac{J}{2} \sum_{\langle i,j \rangle} |h_i - h_j|^2 + \epsilon |h_i - h_j|^4. \tag{7.2}$$

Here $0 < \epsilon < 1$ is a nonlinearity parameter which controls the intensity of Schwoebel effect.

In the continuum limit, the evolution of interface height can be described by Langevin equation of following form [11, 13, 17]

$$\partial_t h(x,t) = \nu \nabla^2 h + \lambda \nabla^2 (\nabla h)^2 - D \nabla^4 h - F_0 + \eta(x,t). \tag{7.3}$$

Here $h(\mathbf{x}, t)$ is the interface height at position x and time t, ν is a surface tension coefficient and D is a diffusion coefficient. The first term on the right hand side of Eq. (7.3) describes the curvature dependent erosion [11], while the second term takes into account the surface diffusion driven relaxation [17]. The nonlinear term, $\lambda \nabla^2 (\nabla h)^2$, induces a lateral growth during surface evolution [4]. F_0 incorporates contributions which appears in the equation of motion due to sputtering yield

$Y(\phi)$ e.g. flux, angle of incidence, energy of incoming ions etc., whereas η denotes the fluctuations [13]. The coefficient of the Laplacian term (ν) in Eq. (7.3), plays a key role in the observation of Schwoebel effect. The Schwoebel Barrier is absent when the Lapalacian term is zero (for $\nu = 0$) but becomes positive, with uphill current at the step edges, for $\nu < 0$ [17]. Existence of positive Schwoebel Barrier contributes to the formation of grooves in the surface morphology. In the case of MBE grown surfaces Seigert et.al. have shown that, for a quartic Hamiltonian (as in Eq. (7.2)), the corresponding evolution equation has a positive Schwoebel barrier with $\nu < 0$ [17].

For KMC investigations, of ion irradiated metallic surfaces, diffusion is incorporated via Arrhenius form of thermally activated hopping, $k(E, T) = k_0 exp(-E/K_B T)$, where E includes the nearest neighbor interaction energy (E_n), substrate energy (E_s) as well as the Schwoebel Barrier (E_{sb}) [11, 18, 28]. All these earlier studies, however, considered Schwoebel Barrier to be of a constant energy. In the Hamiltonian approach, as presented in this paper, the non-linear term (ϵ not equal to zero) in Eq. (7.2) controls the Schwoebel Barrier. In addition to not requiring any prior knowledge of various energy parameters e.g. E_n, E_s or E_{sb}, the Schwoebel barrier is not constant but is a function of height difference at step edges. Similar formalism has been discussed for MBE grown surfaces [17,26], but has never been considered in KMC analysis of ion irradiated surfaces. The additional quartic term in Eq. (7.2) is crucial for metallic surfaces as it is responsible for the uphill currents which produce sharp *groove* structures in surface morphology. This generic model, that we have presented here, is not specific to any system and can be considered for any ion irradiated metallic system.

The algorithm for the Monte Carlo simulation is following. A site $1 \leq i \leq N$ is chosen at random and is subjected to follow erosion process with probability p or the diffusive process with probability $1 - p$. If erosion process is chosen, the angle ϕ_i is computed and a particle is eroded with probability $Y(\phi_i)p_e$. On the other hand if diffusive process is chosen, $w_{i,f}$ is computed using the surface Hamiltonian Eq. (7.2) and the new configuration is updated. Time t is incremented by one unit.

7.3 Experimental :

High purity (99.99%) Polycrystalline Tantalum foils were bombarded by 3keV Ar ions under UHV conditions. The angle of incidence for ion beam was 15° w.r.t surface normal and its flux was 10^{13}ions/cm^2. Scanning Probe Microscopy (SPM) studies have been conducted on the surfaces by using Bruker (Nanoscope V) system in tapping mode. The surface roughness after irradiation was found to be 2.0 nm (0.7 nm for pristine). The ensemble average of about 1024 line scans taken from several AFM images, acquired from surfaces irradiated under same conditions, have been utilized for experimental results and estimation of error bars.

7.4 Results and Discussions :

Fig. 7.1 displays an SPM image from a Tantalum surface bombarded by Ar$^+$ ions at fluence of 3.6$\times 10^{16}$ ions/cm^2. A quasi periodic ripple pattern with a wavelength of about 80 nm with ripple wave vector (**k**) parallel to the ion beam direction is observed. The orientation of the ripples is primarily controlled by the direction of ion beam (shown in fig. 7.1). According to Bradley Harper (BH) theory, orientation of ripple wave vector (**k**) depends upon the angle of incidence [22]. It is parallel to the direction of ion beam for incidence angles less than some critical angle, and is perpendicular for grazing incidence. 1-dimensional height profile from the experiment (section marked in fig. 7.1) and from KMC simulations are presented in fig. 7.2.

For KMC simulations, first we study the model that considers erosion and includes relaxation mechanisms via only quadratic term in the Hamiltonian i.e for $\epsilon = 0.0$ in Eq. (7.2). A range of parameters were chosen for simulations and the results are presented in fig. 7.2, for $p = 0.1$, $J_c/K_BT = 0.25$. The height profile shows a periodic structure, usually similar to the morphologies observed for non metallic surfaces [29] where the Schwoebel effects are not essential. Experimental height profile has several sharp peaks and grooves while the simulated profile has only smooth morphology.

Next we examine the model where we consider relaxation of the surface by including both quadratic and quartic terms in the Hamiltonian Eq. (7.2). The nonlinear parameter ϵ is varied

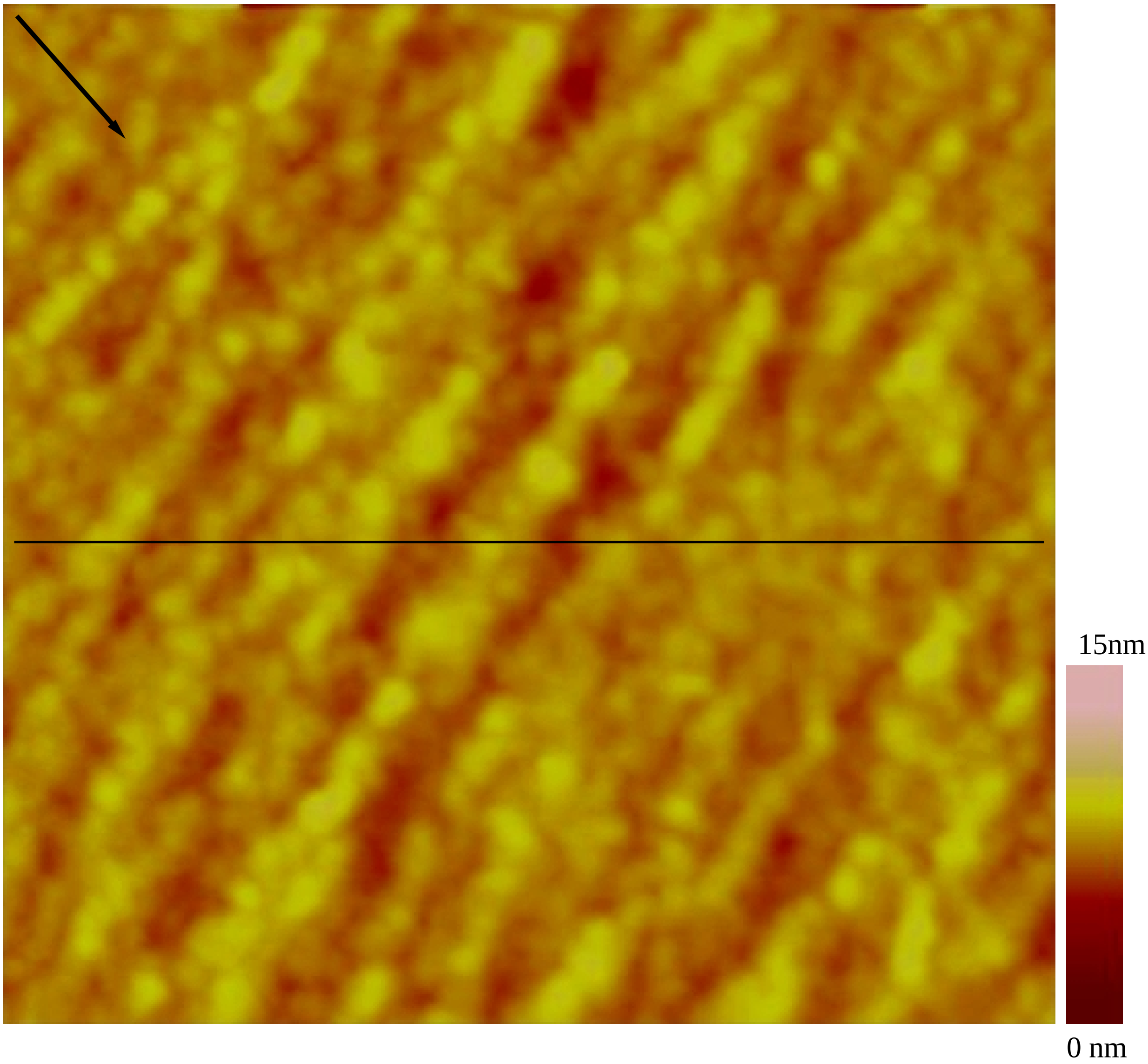

Figure 7.1: Morphology of Tantalum surface: SPM image (500nm×500nm) after ion beam irradiation at a fluence of 36×10^{15}ions/cm^2. The direction of ion beam is shown by the arrow.

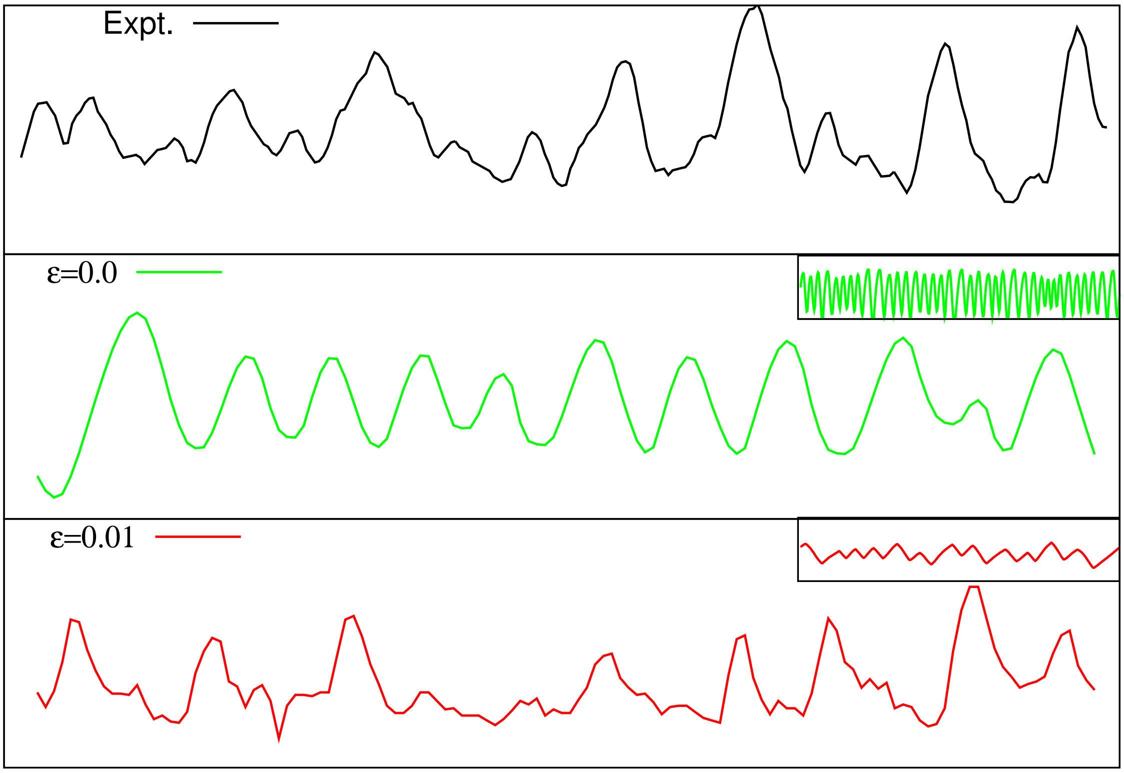

Figure 7.2: Comparison of surface profile(h(x,t)) of experiment with the simulations. The simulated profiles were obtained by KMC model with the parameters $p = 0.1$, $J_c/k_BT = 0.25$ and ϵ=0.0 or 0.01. Inset shows the steady state profile of the surface

between 0.001 and 1.0. The surface morphology with $\epsilon = 0.01$ is presented in fig. 7.2 for $p = 0.1$, $J_c/K_BT = 0.25$. The simulated height profile here, with $\epsilon = 0.01$, displays good agreement with experiments where formation of groove like structures are clearly observed. These features are characteristic signature of positive Schwoebel barrier that force the atom to move in uphill direction by breaking the translational invariance symmetry. A high diffusion rate, as observed here ($p = 0.1$), is expected for metallic surfaces [10]. The steady state height profile for KMC simulations are also shown in fig. 7.2 (inset).

The scaling behaviours and related exponents have also been explored here to investigate the nature of the growing surface. The exponents are useful as they depend on the growth condition and not on the microscopic details of the system. The correlation length ξ, which represents the typical wavelength of fluctuations on the growing surface, also characterizes the phenomenon of kinetic roughening. The width of the surface grows as $W(t) \sim \xi(t)^\alpha$ for roughness exponent α. The scale invariant surfaces lead to scaling laws for correlation functions. The equal time height-height correlation (HHC) function can be written as:

$$G(\mathbf{r}, t) = L^{-1} \sum_{\mathbf{r}'} \langle [h(\mathbf{r} + \mathbf{r}', t) - h(\mathbf{r}', t)]^2 \rangle. \tag{7.4}$$

Here $\mathbf{r}$ is the Translational length along lateral direction of the 1-d lattice and $\langle \cdot \rangle$ denotes the ensemble average. This HHC function has the following scaling form:

$$G(\mathbf{r}, t) = r^{2\alpha} g(r/\xi(t)). \tag{7.5}$$

with $g(x) \sim$ constant for $x \ll 1$ and $g(x) \sim x^{-2\alpha}$ for $x \gg 1$

Fig. 7.3 presents the 1-dimensional height-height correlation function for experiment (using fig. 7.1) as well as KMC simulations. By utilizing the phenomenological scaling function of form $H(r) \sim [1 - \exp(-(r/\xi)^{2\alpha})]$, values of ξ and α have been obtained and are listed in Table-7.1. Although in absence of any Schwoebel effect ($\epsilon = 0.0$), the simulation results are very different from experimental HHC function, after inclusion of Schwoebel effect ($\epsilon = 0.01$) the results are in agreement. These results demonstrate that a small nonlinearity parameter with $\epsilon = 0.01$ is essential for achieving experimentally consistent HHC functional form, ξ and α. This indicates that

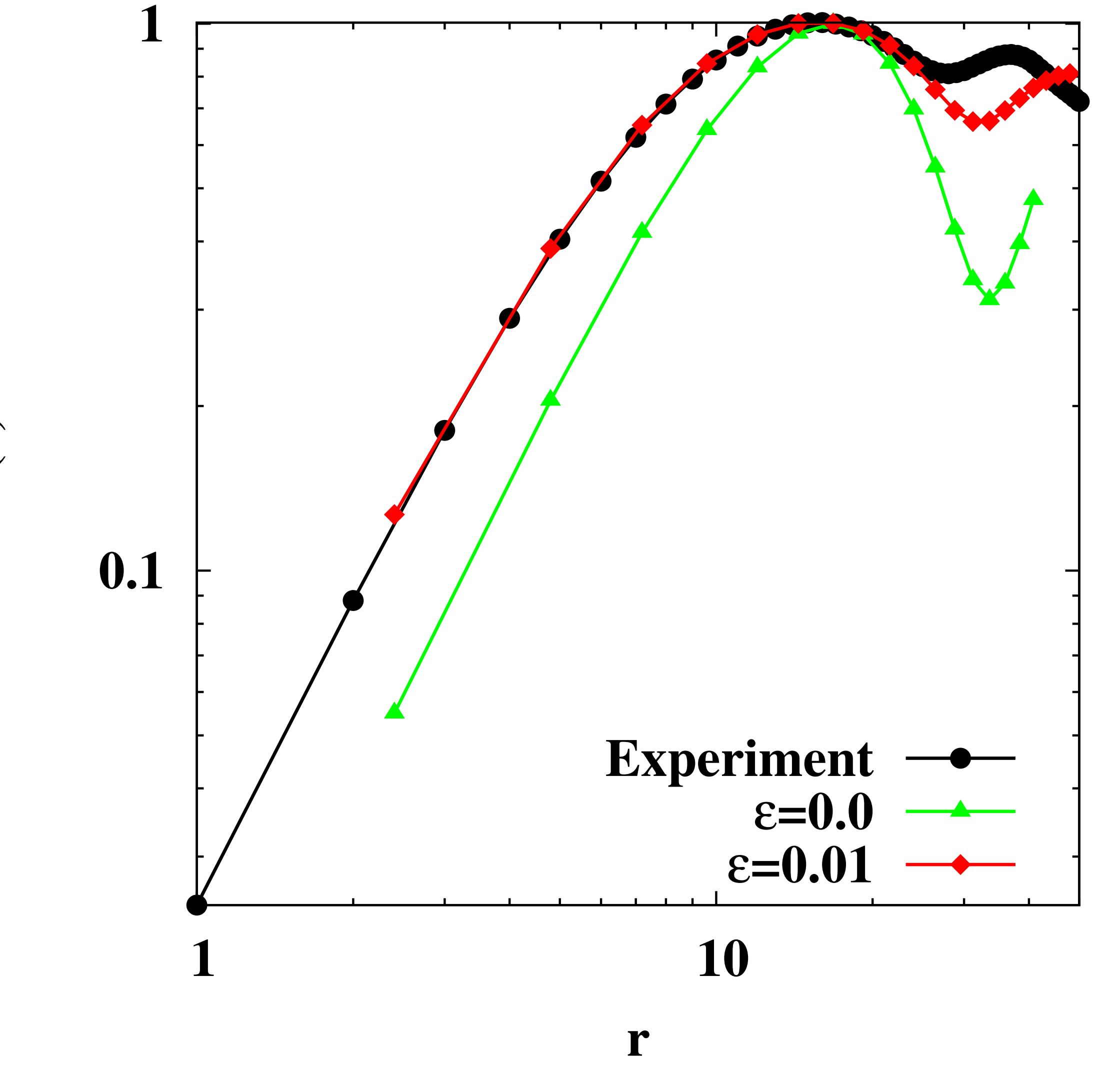

Figure 7.3: Equal time HHC **G(r,t)** as a function of translational distance **r** for experiment. Simulation results are presented (for same parameters as in fig. 7.2) with ϵ=0.0 or 0.01.

Schwoebel effect is necessary for understanding correct growth behaviour on Tantalum surface. Value of α obtained here for KMC simulation, in absence of Schwoebel effect ($\epsilon = 0.0$), is similar to that observed in literature for MBE models with linear Hamiltonian [30, 31].

	α	ξ
Experiment	1.22±0.26	5.66±0.36
$\epsilon = 0.0$	1.63±0.35	2.63±0.50
$\epsilon = 0.01$	1.20±0.07	7.14±0.05

Table 7.1: Roughness exponent α and correlation length ξ.

Obtaining α from G(r,t) can be difficult when the correlation length reaches the system size, specially in the steady state regime. In order to neglect finite size effects α can be computed in $0 \leq r \leq L/2$ regime, where L is the system size. Structure Factor mentioned below does not encounter this problem. The Structure Factor can be defined as [17]:

$$S(\mathbf{k}, t) = \langle \hat{h}(\mathbf{k}, t)\hat{h}(-\mathbf{k}, t)\rangle. \tag{7.6}$$

Here, $\hat{h}(\mathbf{r}, t) = L^{-d/2}\sum_{\mathbf{r}}[h(\mathbf{r}, \mathbf{t}) - \overline{h}]e^{\mathbf{ikr}}$, is the associated correlation function and $\overline{h}$ is the spatial average of h(r,t). This function has the following scaling form:

$$S(\mathbf{k}, t) = k^{-\gamma}s(\mathbf{k}^{zt}). \tag{7.7}$$

with $\gamma = 2\alpha + d$. The scaling function s approaches a constant for large argument but behaves differently in the short time limit $x \ll 1$ where it has form

$$s(x) \sim \begin{cases} x \text{ if } \gamma \leq z \\ x^{\gamma/z} \text{ if } \gamma \geq z \end{cases} \tag{7.8}$$

In fig. 7.4, the steady state structure factor $S(\mathbf{k}) = S(\mathbf{k}, t \to \infty)$ is shown for experiment as well as from KMC simulations The result clearly demonstrate that the non-linear Hamiltonian, with $\epsilon = 0.01$, agrees quite well with the experimental results. For $\epsilon = 0.0$, we observe that $S(\mathbf{k})$ qualitatively differs from the experimental results. The value of exponent γ obtained by linear Hamiltonian is 4.00±0.12 while for nonlinear Hamiltonian, the value is 3.27±0.07. For the ion beam modified Tantalum surfaces, $\gamma = 3.04 \pm 0.06$ has been observed here. This value

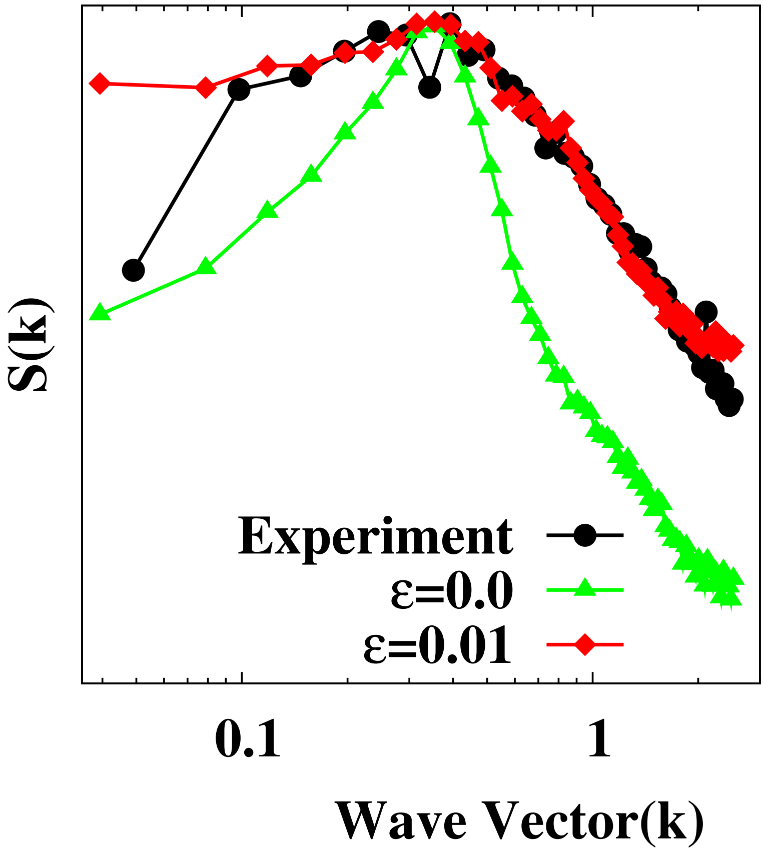

Figure 7.4: Steady state structure factor **S(k)** for experiment. KMC simulation results are presented (for same parameters as in fig. 7.2) with ϵ=0.0 or 0.01.

of γ is not expected from the universality classes of EW or KPZ. Thus the results indicate that positive Schwoebel effect is necessary for understanding the morphological growth of ion sputtered Tantalum surfaces which does not belong to the well known EW or the KPZ class.

7.5 Conclusion :

In Conclusion, we have presented a KMC model to describe the morphology of ion sputtered Tantalum surfaces. We have shown that a positive Schwoebel effect is needed to explain the characteristics of self organized nanostructures observed in the experiment. The Schwoebel effect has been used earlier for MBE growth models. Here, we have shown that, it can also be used for ion sputtered metallic surfaces such as Tantalum. The scaling exponents computed from the simulation and experimental data agrees quite well and indicates the presence of universality class that differs from that of non-metallic surfaces.

Bibliography

[1] Q. Xu, B. Schmidt, S. Pradhan and M. Lipson Nature Letters **39** 325 (2005).

[2] P. G. Eliseev, H. Li, A. Stintz, G. T. Liu, T. C. Newell, K. J. Malloy, and L. F. Lester Applied Physics Letters **77** 262 (2000).

[3] Mark A. Hughes, Yanina Fedorenko, Russell M. Gwilliam, Kevin P. Homewood, Steven Hinder, Behrad Gholipour, Daniel W. Hewak, Tae-Hoon Lee, Stephen R. Elliott, and Richard J. Curry Applied Physics Letters **105** 083506 (2014).

[4] M. A. Makeev, R. Cuerno, and A. L. Barabasi, Nucl. Instrum. Methods Phys. Res. B **197** 185 (2002).

[5] F. Frost, B. Ziberi, T. Hoche, and B. Rauschenbach, Nucl. Instrum. Methods Phys. Res. B **216** 9 (2003).

[6] S. Facsko, T. Dekorsy, C. Koerdt, C. Trappe, H. Kurz, A. Vogt,and H. L. Hartnagel, Science **285** 1551 (1999).

[7] E. Chason, T. M. Mayer, B. K. Kellerman, D. T Mcllroy, and A.J. Howard, Phys. Rev. Lett. **72** 3040 (1994).

[8] G. Carter and V. Vishnyakov, Phys. Rev. B **54** 17647 (1996).

[9] S. Rusponi, G. Costantini, C. Boragno, and U. Valbusa, Phys.Rev. Lett. **81** 2735 (1998).

[10] U. Valbusa, C. Borangno, and F. R. de Mongeot, J. Phys. Condens.Matter **14** 8153(2002).

[11] E.Chason, W.L.Chan J.Phys. Condens. Matter **21** 224016 (2009).

[12] A.L. Barabasi and H.E. Stanley, Fractal Concepts of Surface Growth Cambridge University Press, Cambridge, 1995.

[13] R. Cuerno, H.A. Makse, S. Tomassone, S.T. Harrington, and H.E.Stanley, Phys. Rev. Lett. **75** 4464 (1995).

[14] A.D. Brown, J. Erlebacher, W.-L. Chan, and E. Chason, Phys.Rev. Lett. **95** 056101 (2005).

[15] A. K. Hartmann, R. Kree, U. Geyer, and M. Klbel, Phys. Rev. B **65** 193403 (2002).

[16] M. Stepanova and S. K. Dew, Appl. Phys. Lett. **84** 1374 (2004).

[17] M. Siegert and M. Plischke, Phys. Rev. E **50** 917 (1994).

[18] E. O. Yewande, A. K. Hartmann, and R. Kree, Phys. Rev. B **71** 195405 (2005).

[19] V.R.R. Medicherla, S. Majumder, D. Paramanik, Shikha Varma, Journal of Electron Spectroscopy and Related Phenomena **180** 15 (2010).

[20] Subrata Majumder, Ramarao Medicherla, Dipak Paramanik, V. Solanki, Indrani Mishra, Shikha Varma, Radiation Effects and Defects in Solids **166** 592597 (2011),

[21] Kent Bkgaard Lauritsen, Rodolfo Cuerno, and Hernan A. Makse Phys. Rev. E **54** 3577 (1996)

[22] R.M. Bradley, J.M.E. Harper, J. Vac. Sci. Technol. A **6** 2390 (1988).

[23] R. Cuerno and A.-L. Barabasi, Phys. Rev. Lett. **74** 4746 (1995).

[24] Elliott A. Eklund, R. Bruinsma, and J. Rudnick PRL **23** 1759 (1991)

[25] H.N. Yang, G.C. Wang, and T.M. Lu Phys.Rev. B **50** (1994) 7635

[26] Fereydoon Family and Pui-Man Lam Physica A **205** 272 (1994).

[27] M. Siegert and M. Plischke, Phys. Rev. Lett. **68** 2035 (1992).

[28] M. Strobel, K.H. Heining and T. Michely, Surf. Sci. **486** 136 (2001).

[29] Javier Munoz-Garca, Raul Gago, Luis Vazquez, Jose Angel Sanchez-Garca, and Rodolfo Cuerno PRL **104** 026101 (2010)

[30] D.E. Wolf and J. Villain, Europhys. Lett. **13** (1990) 389.

[31] S. Das Sarma and P.I. Tamborenea, Phys. Rev. Lett. **66** (1991) 325.

Chapter 8

Summary and Conclusion

The present thesis discusses the development of nanopatterns on rutile $TiO_2(110)$ and Tantalum surfaces via ion irradiation technique. The surface evolution of nanostructures on these surfaces is due to the interplay between surface erosion and material transport via diffusion mechanism.

Chapter-1 encapsulates the theory behind pattern formation, interaction of incident ions with the target atoms during ion beam irradiation in conjugation with the significance of these nanostructured surfaces in several fields. Nanostructures have been fabricated on rutile TiO_2 and Tantalum surfaces using ion irradiation technique. The effect of cobalt ion irradiation on rutile $TiO_2(110)$ surface along with its optical and magnetic response have been investigated via several characterization techniques. The details about these characterization techniques have been dicussed in **Chapter 2**.

Chapter 3 presents the development of nanostructures on rutile $TiO_2(110)$ surfaces using ion beam irradiation. $TiO_2(110)$ surfaces have been irradiated with 200 keV cobalt ions, at several fluences. Ion irradiation is a very powerful technique which provides precise control over the concentration of dopants along with wide range of nanopatterns on large surface area, in a single technological step. Ion irradiation leads to the development of Ti^{3+} states or oxygen vacancies which can act as a nucleation sites for the evolution of nanostructures on rutile TiO_2 surfaces. These nanostructures becomes smaller in size due to fragmentation at higher fluences. Development of secondary phases of cobalt such as $Ti_{1-x}Co_xO_2$ and $CoTiO_3$, have also been observed. UV-Vis photoabsorption studies display an enhancement in photoabsorption, 5 times in visible and

1.7 times in UV, in conjugation with the reduction in band gap, after being irradiated with cobalt ions at various fluences. Formation of cobalt clusters, development of Ti rich zones and creation of oxygen vacancy states, during implantation, are crucial for these observations. The enhanced photoabsorption has been attributed to the sp-d exchange interactions between the band electrons and localized d electrons of Co^{2+} ions. These results can have potential applications in photocatalysis.

Chapter 4 deals with the magnetic response of rutile TiO_2 after implantation with 200 keV cobalt ions, at several fluences. The experiments have been performed using Superconducting Quantum Interference Device (SQUID) at various temperatures and fields. The results display a superparamagnetic character instead of room temperature ferromagnetism, as primarily observed for DMS based materials. The magnetic moments have been observed to increase with ion fluence, indicating an increase in the size of cobalt nanoclusters. Scaling studies, above blocking temperature, suggest an anisotropic nature of SPM behavior. Higher magnetization along $H_\perp$ also confirms this to be an easy axis of magnetization for cobalt clusters. Below blocking temperature, a crossover in M-H isotherm, taken at 2K, has been observed which has been attributed to the anisotropic paramagnetism arising from +2 ionic state of cobalt. Role of dipole-dipole and inter-cluster exchange interactions have also been investigated. These results can play a pivotal role in spintronic devices.

Chapter 5 investigates the radiation damage, amorphization and structural modifications that are produced by ion-solid interactions in TiO_2 crystals during 200 keV Cobalt ion implantation. RBS/C and GIXRD have been utilized to evaluate the damage in the host lattice as a function of ion fluence. Multiple scattering formalism has been applied to extract the depth dependent damage distributions in $TiO_2(110)$. The results have been compared with the MC simulations performed using SRIM-2013. RBS/C results delineate a buried amorphous layer at a low fluence. Surprisingly, ion induced dynamic activation produces a recovery in this damage at higher fluences. This improvement interestingly occurs only in deep regions (50-300 nm) where a systematic lowering in damage with fluence is observed. Formation of Co-Ti-O phases and generation of stress in TiO_2 lattice, suggested by GIXRD results, can also be responsible for this improvement in deep regions. In contrast, surface region (0-50 nm) indicates a gradual increase in damage with fluence. Such a switch in the damage behavior creates a cross point in damage profiles at 50 nm. Surface region is a sink of vacancies whereas deep layers are interstitial rich. However, these regions are far separated from each other resulting in an intermediate (100-150 nm) region with a significant dip (valley) in damage which can be characterized by enhanced recombination of point defects. MC simulations present very different results. Simulations do not indicate presence of any valley like structure in the damage profile which extends to only 150 nm, nearly half of the damage widths observed in present study. The complex nature of damage distribution observed here may be related to the high ionic nature of the chemical bonds in the TiO_2 lattice.

Chapter 6 Evolution of cobalt implanted rutile $TiO_2(110)$ surfaces displays development of nanostructures and ripple patterns oriented along a crystallographic direction of the surface. Atomic Force Microscope (AFM) have been utilized to investigate the morphological evolution of TiO_2 surfaces prior and post cobalt ion implantation. Scaling studies have been performed to investigate roughness exponent (α), growth exponent (β), dynamic exponent (z), and structure factor exponent (γ). Scaling exponents suggest that ion irradiated TiO_2 surfaces belong to EW universality class. Ion induced diffusion plays a pivotal role in the evolution of these self affine surfaces created after Cobalt ion irradiation.

Chapter 7 presents the Kinetic Monte Carlo (KMC) simulations to study the surface evolution of Ta surface after 3 keV Ar^+ ion irradiation. The surface displays a self organized ripple pattern with the ripple wave vector oriented along the direction of incident ion beam. To understand the mechanism behind ripple pattern formation on this surface, 1+1 dimensional KMC simulations have been discussed. The line profile of experimentally obtained pattern shows the development of shrap “groove-like” structures which indicates the presence of Schwoebel effect during pattern formation. The model, proposed here, incorporates the effect of Schwoebel barrier by using a non-linear term in the Hamiltonian. The simulation results produce the surface morphology and scaling exponents that are consistent with our experimental observations. These simulation results in conjugation with scaling exponents suggest that the surface evolution of Ta surface, via ion beam irradiation, is also diffusion driven, as observed for TiO_2 surfaces. The scaling exponents, however, indicates that the surface evolution of Ta surface may belong to universality class other than E-W or KPZ class.

Thus, the present thesis discusses the development of nanopatterns on rutile $TiO_2(110)$ and Ta surfaces, using ion beam irradiation technique. The surface evolution of these nanopatterns is due to the competetion between surface erosion and various relaxation mechanism. The scaling studies show that the surface evolution of these self affine surfaces are diffusion driven. On $TiO_2(110)$ surface, preferential sputtering of oxygen atoms leads to the development of metal rich centers which act as nucleation sites for the evolution of nanostructures. Development of nanostructures in conjugation with the formation of secondary phases like $Ti_{1-x}Co_xO_2$, $CoTiO_3$ and Co nanoclusters, after cobalt implantation, also manifests an anisotropic SPM behavior in this system. Scaling studies, above blocking temperature, also display this anisotropy. Presence of clusters, with dipole-dipole interactions along with inter-cluster exchange interactions, plays a significant role in the development of anisotropy in this system. RBS/C studies also display the development of these Co nanoclusters along with an intricate depth dependent damage below the surface. Multiple scattering formalism has been used to investigate the damage distribution which indicates the occurence of dynamical annealing during ion beam irradiation.